Nottingham Geospatial Institute
Department of Civil Engineering
Faculty of Engineering

Kinematic Precise Point Positioning Algorithm Development and Improvements using External Atmospheric Information

By
Brian Jerald Weaver, M.Sc., B.Sc.

Thesis submitted to The University of Nottingham
for the degree of Doctor of Philosophy,
February 2023

This project has received funding from the European Union's Horizon 2020 research and innovation programme under the Marie Skłodowska-Curie grant agreement No 722023

Abstract

Precise point positioning (PPP) is a high-accuracy GNSS positioning technique used to process single-receiver, dual-frequency carrier-phase and pseudorange measurements using precise network-estimated satellite clock and orbit data products, along with optional satellite carrier phase bias and attitude information. The PPP strategy does not require any nearby reference stations and has therefore gained interest in many commercial and scientific industries over the past few decades. However, kinematic PPP can be affected by large positioning errors in the presence of ionospheric scintillation, under strong ionospheric gradients, and during strong tropospheric storm events. Therefore, this thesis aims to develop new methods that incorporate additional external atmospheric information into the positioning model to improve kinematic PPP accuracy under these harsh atmospheric conditions.

Ionospheric scintillation of GNSS signals is caused by plasma density irregularities in the ionosphere and is characterized by rapid phase and amplitude fluctuations of the received signal. In equatorial regions, between ±20° geomagnetic latitude, strong and frequent post-sunset scintillation is common and can amplify positioning errors by several orders of magnitude. However, an increased number of satellites using modernized signals could help to mitigate this impact. Therefore, this thesis evaluates kinematic PPP performance using multi-GNSS processing under low latitude ionospheric scintillation conditions. Compared to GPS-only processing, multi-GNSS configurations using Galileo measurements achieved respective average vertical positioning accuracy and precision improvements equal to 3.4-cm (39.8%) and 1.8-cm (52.7%). In addition, multi-GNSS configurations improved daily respective horizontal and vertical position accuracy and precision by up to 13.0-cm (80.4%) and 13.6-cm (90.4%) during the worst GPS-only processing day.

Although multi-GNSS processing can improve kinematic PPP performance under ionospheric scintillation conditions, a non-mitigated satellite elevation-based stochastic model degrades positioning accuracy when high-elevation satellites are affected by moderate or strong scintillation. Furthermore, scintillation mitigation using receiver tracking error outputs in a modified stochastic model is affected by frequent outages under strong scintillation conditions and has only been demonstrated for single-system processing. Therefore, this thesis develops repaired and normalized multi-GNSS receiver tracking error model outputs to respectively

increase mitigation availability and expand mitigation benefits to non-specialized users that may require a mixed stochastic approach. The proposed techniques were evaluated using GPS+Galileo measurement processing for a common geodetic receiver under moderate and strong low latitude ionospheric scintillation conditions. Relative to a standard elevation-based stochastic model, the mitigated approach improved the daily worst-case 3D kinematic PPP error by 16.6-cm (46.7%) and 13.6-cm (37.4%) for the two best cases, while the average 3D position error for both stochastic methods agreed at the cm-level in all cases.

Tropospheric effects are typically addressed in GNSS processing by *a priori* hydrostatic correction models and estimation of zenith wet delay and horizontal gradient components. However, rapid changes in atmospheric water vapor caused by heavy rainfall can amplify tropospheric asymmetry effects and reduce kinematic PPP accuracy due to tightly constrained tropospheric parameters. Therefore, this thesis develops and evaluates deterministic, partially stochastic, and fully stochastic correction methods that use progressively more GNSS network-estimated tropospheric data under extreme tropospheric storm conditions to improve the achievable kinematic PPP accuracy at user locations. Comparison with the non-corrected model revealed that the fully stochastic approach improved the hourly horizontal and vertical position error by up to 3.2-cm (45.5%) and 10.2-cm (66.2%), respectively, while deterministic and partially stochastic methods improved only the vertical positioning error component.

Increased ionospheric activity for high-elevation satellites can amplify otherwise stable positioning errors in an elevation-based stochastic model unless the stochastic model is modified with user-estimated ionospheric delay information to amplify measurement noise. However, this technique relies on continuous dual-frequency carrier phase measurements that are assumed to be free from cycle slip effects, which is not guaranteed in challenging ionospheric environments due to measurement outages and poor-quality carrier phase data. Therefore, this thesis suggests an alternative stochastic model strategy to amplify measurement noise using the rate of the ionospheric delay computed from external global and regional ionospheric map products that are independent of cycle slips and outages that a GNSS user may experience. For low latitude stations evaluated relative to a standard satellite elevation-based stochastic model, the proposed technique successfully improved maximum 3D kinematic PPP error by up to 15.6-cm (52.5%) when the global ionospheric map product was used. Extreme variability of the experimental 60-second update rate regional ionospheric map data deactivated the modified stochastic approach for 88.8% of epochs which resulted in positioning performance identical to the elevation-based method at the mm-level.

Acknowledgements

The work necessary to complete this PhD was carried out at the Nottingham Geospatial Institute during employment hosted by the University of Nottingham. Funding was fully provided by the TREASURE project as part of the Horizon 2020 initiative under the Marie Sklodowska-Curie Action Innovative Training Network (proposal number: 722023). The TREASURE project also funded international travel for training, research collaboration, and secondment opportunities with project partners.

I first convey gratitude to my supervision team, Dr. Marcio Aquino, Dr. Sreeja Vadakke-Veettil, and Dr. Lei Yang, who guided my early-stage research career, while also coordinating TREASURE project activities and events. I am grateful for the opportunity to study a topic in-depth with support from experts in all aspects of GNSS technology and from prestigious institutions worldwide. Thanks to the financial, research and interpersonal guidance from supervisors and other project partners, I learned many interesting things about foreign cultures, developed close friendships, and greatly enjoyed my time outside my home country.

A special thanks is needed for my primary supervisors who acquired funding and spent years developing and publishing many of the research outcomes that inspired the methods developed throughout this thesis. In addition, my first experience with international travel, and how to deal with the complications that arise, was assisted by valuable inputs from my supervision team and other University of Nottingham staff. For example, prior to my first ever travel to a non-English speaking country, Dr. Marcio Aquino suggested I contact his brother who lived in a nearby city if I needed help with anything. Similarly, Dr. Sreeja Vadakke-Veettil helped with the logistics of international travel prior to my departure from the United Kingdom by reviewing checklists and travel information.

After supervision changes due to retirement and career decisions, Dr. Paul Blunt dutifully replaced both my primary and secondary supervisors from 2020 to 2022 and fulfilled the academic role that is required to submit this thesis. Although high-accuracy positioning algorithm develop was initially beyond his main research area, Dr. Paul Blunt provided excellent academic guidance and review comments during the thesis write-up phase. In addition, many staff changes occurred during this period, likely due to COVID-19 restrictions, enhanced voluntary redundancy offers, and student enrollment, which increases my appreciation for Dr. Paul Blunt's willingness to begin a supervision role for my thesis.

The collaboration with other TREASURE researchers throughout the PhD process was essential to achieve the project goals and outcomes presented in this thesis. Therefore, I acknowledge the helpful discussions and brainstorming with Francesco Darugna regarding GNSS data transmission, Juliana Garrido Damaceno for generating experimental regional ionospheric map data, Hongyang Ma for experimental design and interpolation of regional tropospheric correction data, and both Dimitrios Psychas and Lotfi Massarweh regarding GNSS algorithms and implementations. In addition, it is difficult to express my appreciation for fellow University of Nottingham TREASURE researcher Kai Guo who patiently answered questions regarding ionospheric scintillation and became a close friend and companion during work-related and personal travel.

Dr. Panos Psimoulis is acknowledged for his role as internal assessor and commitment to my lengthy PhD write-up and finalization process. I also thank Dr. Daniel Gillins for first developing my interest in GNSS technology and for the excellent lectures on estimation theory and practical GNSS surveying applications while I was a student at Oregon State University. In addition, I am grateful to Dr. Jihye Park for teaching the complex topic of geodesy, informing me about the TREASURE project positions, and for challenging me to pursue a PhD, even after I initially declined the possibility. I enthusiastically thank my TREASURE secondment hosts, Professor Peter Teunissen, Professor Jihye Park, Professor Sandra Verhagen, and Marcos Guandalini, for graciously meeting with me and discussing research ideas during study periods that lasted up to two months. Thank you to Dr. Christopher Parrish who patiently waited for me to transition from PhD student to a post-doctoral position.

Finally, words do not express my appreciation for the love and support my wife has shown during the pursuit of my PhD by moving to a new country far from family, delaying lifelong dreams, and the many other sacrifices she made for me to graduate. I also thank my family and friends for understanding that my time spent as a busy and sometimes stressed student was valuable and that I missed our time together when work and school became hectic.

Contents

List of Figures

List of Tables

Abbreviations

3D	3-Dimensional
AltBOC	Alternate Binary Offset Carrier
APC	Antenna Phase Center
ARP	Antenna Reference Point
ASCII	American Standard Code for Information Interchange
BDC	BeiDou Coordinate System
BDT	BeiDou Time
C/A	Course/Acquisition
CALIBRA	Countering GNSS high Accuracy applications Limitations due to Ionospheric disturbances in BRAzil
CDMA	Code Division Multiple Access
CGCS	China Terrestrial Reference Frame
CIGALA	Concept for Ionospheric Scintillation Mitigation for Professional GNSS in Latin America
CMR	Compact Measurement Record
CODE	Center for Orbit Determination in Europe
CSRS	Canadian Spatial Reference System
DCB	Differential Code Bias
DIA	Detection, Identification, and Adaptation
DLL	Delay-Locked Loop
DOF	Degrees Of Freedom
DOY	Day Of Year
ECEF	Earth-Centered-Earth-Fixed
EGNSS	European Global Navigation Satellite System
EIA	Equatorial Ionospheric Anomaly
EKF	Extended Kalman Filter
ERP	Earth Rotation Parameters
ESR	Early Stage Researcher

EU	European Union
FDMA	Frequency Division Multiple Access
FLL	Frequency-Locked Loop
GAL	Galileo
GFZ	GeoForschungsZentrum
GIM	Global Ionospheric Map
GLO	GLONASS
GLONASS	Global'naya Navigatsionnaya Sputnikovaya Sistema
GLONASST	GLONASS Time
GPS	Global Positioning System
GPST	GPS Time
GST	Galileo System Time
GTRF	Galileo Terrestrial Reference Frame
IAR	Integer Ambiguity Resolution
IBGE	Brazilian Institute of Geography and Statistics
ICD	Interface Control Documents
IERS	International Earth Rotation and Reference Systems Service
IF	Ionosphere-Free
IGS	International GNSS Service
IMU	Inertial Measurement Unit
INS	Inertial Navigation System
ISB	Inter-System Bias
ISMR	Ionospheric Scintillation Monitoring Receiver
ITN	Innovative Training Network
ITRF	International Terrestrial Reference Frame
JPL	Jet Propulsion Laboratory
MGEX	Multi-GNSS EXperiment
MSCA	Marie Sklodowska-Curie Action
MWWL	Melbourne-Wübbena Wide-Lane
NL	Narrow Lane
NRCAN	Natural Resources CANada
NRTK	Network Real-Time Kinematic
OS	Open Service

PCO	Phase Center Offset
PCV	Phase Center Variation
PLL	Phase-Locked Loop
POINT	Position Orientation INTegration
PPP	Precise Point Positioning
PSD	Power Spectral Density
PZ	Parametry Zemli
RBMC	Network for Continuous Monitoring of GNSS Systems
RCP	Right Circularly Polarized
RIM	Regional Ionospheric Map
RINEX	Receiver INdependent EXchange
RMS	Root Mean Square
RMSE	Root Mean Square Error
ROT	Rate Of TEC
ROTI	ROT Index
RTCM	Radio Technical Commission for Maritime Services
RTK	Real-Time Kinematic
RTN	Real-Time Network
S/A	Selective Availability
SF	Scale Factor
SIS	Signal-In-Space
SPP	Standard Point Positioning
STEC	Slant TEC
SVID	Satellite Vehicle IDentification
TAI	International Atomic Time
TEC	Total Electron Content
TECR	TEC Rate
TECU	TEC Unit
TEQC	Translation, Editing and Quality Check
TREASURE	Training REsearch and Applications network to Support the Ultimate Real time high accuracy EGNSS solution
UNAVCO	University NAVSTAR Consortium

UTC	Coordinated Universal Time
VTEC	Vertical Total Electron Content
WGS	World Geodetic System
WL	Wide Lane
ZHD	Zenith Hydrostatic Delay
ZTD	Zenith Total Delay
ZWD	Zenith Wet Delay

Chapter 1

Introduction

1.1 Global Navigation Satellite System (GNSS) positioning

Human civilization is currently characterized by the Information Age, where rapid technological advancements generate the greatest societal impacts and economic benefits. This latest stage in human development is demonstrated by the progression of Global Navigation Satellite System (GNSS) technologies and the recent expansion of new GNSS constellations over the past few decades. Furthermore, in the 10-year period following 2019, the global number of GNSS-enabled devices is forecasted to increase from 6.4 to 9.6 billion (European GNSS Agency 2019), which will exceed the projected global human population (United Nations 2019). These devices are key components in a variety of industries, where GNSS data are either processed in real-time or after measurements are collected (i.e., post-processed) using stand-alone or differential positioning techniques.

For these reasons, the following first introduces each component of the current multi-GNSS environment and describes the ongoing modernization efforts that enhance GNSS-based capabilities. Then, standard differential positioning techniques and typical accuracies are discussed along with the limitations of differential GNSS measurement processing in the context of specific user applications. Finally, the primary GNSS error sources and techniques to either model, correct, or eliminate these effects are provided.

1.1.1 Multi-GNSS environment and modernization efforts

The current multi-GNSS environment is comprised of the well-known United States' Global Positioning System (GPS) and Russia's GLObal'naya NAvigatsionnaya Sputnikovaya Sistema (GLONASS), along with the recently developed European

Galileo and Chinese BeiDou systems. Both the GPS and GLONASS constellations were developed in the 1970s-80s and declared fully operational by the year 1995, with ground segment infrastructure deployed and at least 24 satellites in orbit to achieve global coverage (McDonald 2002). In the early 2000s, the development of the Galileo and BeiDou GNSS constellations began with the aim to achieve independence from the previously established GPS and GLONASS systems. Galileo additionally aimed to provide a non-military, civilian-based system. By the year 2021, the Galileo and BeiDou constellations were designated as fully operational, while GPS and GLONASS underwent modernization efforts and the previously declining GLONASS system (Revnivykh 2008) recovered to a complete constellation.

The newly established and upgraded constellations offer many benefits to users such as access to new signals centered at lower L-band frequencies, higher signal transmission power (Steigenberger et al. 2018) and positioning augmentation and safety of life services. Ongoing efforts unique to GLONASS propose a transition from frequency division multiple access (FDMA) to code division multiple access (CDMA), which will be consistent with the other global systems. Due to a phased modernization approach, progressively more GPS and GLONASS satellites transmit new signals, while Galileo and BeiDou were developed with modernization benefits in mind and transmit signals at either overlapping or unique frequencies. For example, the GPS constellation overview in Figure 1.1 depicts a combination of both legacy and modernized satellites used simultaneously, where each new generation typically transmits signals centered at new frequencies.

A key feature of modernized GNSS signals is the separation of pilot and data channels that is intended to improve signal tracking performance for GNSS receivers. For this reason, Galileo has recently gained more attention in multi-GNSS studies due to the superior signal noise and multipath performance of the E5 alternate binary offset carrier (AltBOC) signal (Basile et al. 2019; Guo et al. 2016; Lou et al. 2016; Zaminpardaz and Teunissen, 2017) to enhance GNSS signal acquisition and tracking. This modulation technique results in a Galileo E5 signal that occupies a greater frequency band compared to the corresponding GPS L5 signal, as shown in Figure 1.2, which can additionally be tracked as separate E5a or E5b signals depending on the receiver design. Note that although the frequency bands between global systems do not necessarily overlap, similar channel separations into pilot and data components have also been implemented for the newest GPS and BeiDou signals.

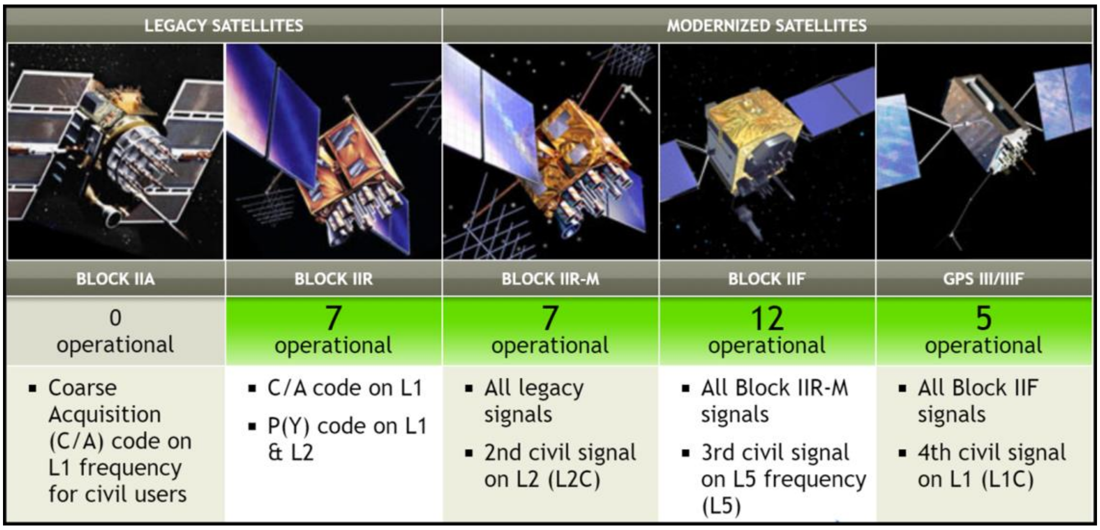

Figure 1.1. Legacy and modernized GPS satellites and transmitted signals, updated June 2022 (source: www.gps.gov/systems/gps).

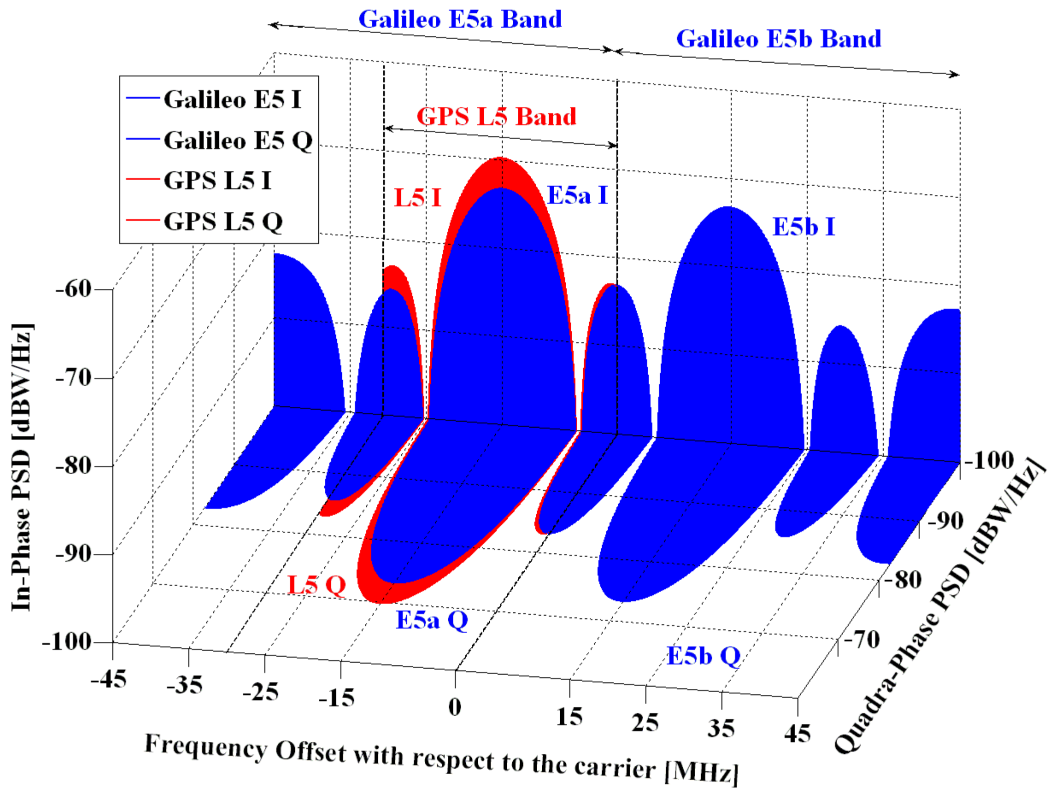

Figure 1.2. In-phase (I) and quadrature (Q) frequency bands for GPS L5 and Galileo E5 signals (source: gssc.esa.int/navipedia).

1.1.2 Differential positioning techniques and limitations

Since the intentional degradation of GPS signals was deactivated in the year 2000 (GPS S/A Announcement 2000), the nominal accuracy of single point positioning (SPP) has been approximately 10 meters due to the meter-level accuracy of pseudorange measurements and the inherent complexity of GNSS error sources (Alkan 2001; Subirana et al. 2013). However, differential positioning techniques that exploit the spatial and temporal correlation of GNSS errors at a reference and nearby user receiver, as shown in Figure 1.3, can achieve positioning accuracy of better than 1 meter (Alkan 2001; Landau et al. 2007). Similar differential positioning accuracy is also possible for between-receiver distances (e.g., baselines) up to several hundreds of kilometers, where correction data transmitted by a network of GNSS receivers replaces the poorly modelled atmospheric error estimation in the user's model.

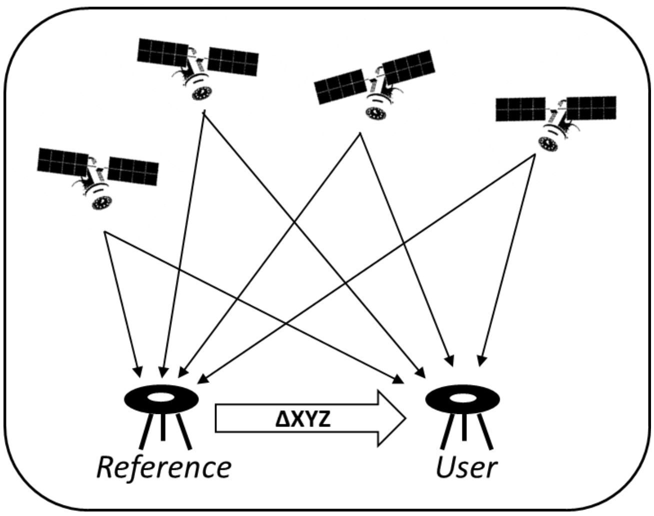

Figure 1.3. Differential positioning approach, where reference station coordinates are constrained to estimate a relative user position.

If high accuracy mm- to cm-level positioning performance is desired, then mm-level precision carrier phase measurements and related ambiguity parameters must be included in the underlying model and algorithms. Ambiguities bias the otherwise highly precise carrier phase measurements and represent an unknown number of integer cycles that occur between signal transmission and reception. After ambiguities are precisely estimated, as either non-integer (float) or integer (fixed) values, carrier phase measurements behave as extremely precise, mm-level precision, pseudorange measurements (Kouba 2015).

A large number of carrier phase ambiguities can weaken the positioning model, as more unknown parameters must be estimated. However, for a network of receivers that use between-receiver baselines to form double-differenced code and carrier phase measurements, the unknown ambiguities can be estimated then set as integers to strengthen the overall model. In post-processing mode, integer ambiguities are estimable for: long baselines up to thousands of km with nominal mm-level daily positioning accuracy (Hill et al. 2009; King and Williams 2009); medium-length baselines less than one hundred km with cm-level accuracy using less than one hour of measurements (Eckl et al. 2001; Schwarz 2008); short baselines less than tens of km with cm-level accuracy for epoch-wise fixed solutions (Bouin et al. 2009; Han and Rizos 2000; King 2009; Larson et al. 2007).

Relative positioning is also used for cm-level accuracy real-time kinematic (RTK) positioning, where integer ambiguities can usually be estimated after a short convergence period of only a few epochs for short baselines (Dai 2000; Dai et al. 2007; Han 1997). For the standard RTK user, the error residual in the rover-reference double-differenced observation increases with increased baseline length due to the atmospheric variations along the baseline, which decreases the success rate of instantaneous integer ambiguity resolution. In this case, a regional real-time network (RTN) of GNSS reference stations can be used to estimate and transmit real-time atmospheric correction information to users in a technique known as network-RTK (NRTK). Aside from the costly deployment of RTN infrastructure, correction quality rapidly decreases outside the reference station domain and is therefore not suitable for precise positioning at a global scale (Rizos 2007).

For the many applications that require centimeter-level positioning accuracy in real-time and are located outside the reference network coverage, differential RTK and NRTK approaches are not feasible. For example, precision agriculture activities such as seed-transplanting, variable-rate fertilization and pesticide management require positioning better than 10-cm and may be applied to areas larger than several hundred square kilometers (Gebbers and Adamchuk 2010; Lan et al. 2017). Bathymetric, topographic and gravimetric surveys that rely on cm-level positioning of respective echo sounder, lidar, and gravimeter instruments are conducted over areas of more than millions of square kilometers (Madore et al. 2018; Roman and

Childers 2013; Smith and Roman 2010). Precision maritime navigation, positioning of ocean structures, satellite radar altimetry-derived sea-surface mapping and offshore geological hazard and tectonic plate monitoring are fundamentally challenging as reference stations are often not available or too expensive to build (Evans et al. 2022; Chen et al. 2021; Chadwell and Spiess 2008; Kato 2005; Picot et al. 2003).

With these critical applications and challenges in mind, a high-accuracy positioning method able to achieve cm-level accuracy at a global scale without a relatively dense network of reference stations is necessary to enable GNSS positioning for a greater variety of users. A global non-differential technique would also reduce the potential propagation of reference station errors and costs associated with the deployment and maintenance of Continuously Operating Reference Station (CORS) networks. In the following, primary GNSS error sources are provided to give a background on the challenges that must be addressed to achieve accurate GNSS positioning.

1.1.3 Primary GNSS error sources

The overall GNSS error budget in Figure 1.4 is comprised of major error sources related to the troposphere, ionosphere, satellite orbit, receiver and satellite clock offsets, and hardware bias effects. These primary errors must be addressed using sophisticated error modelling, specialized estimation techniques, mathematical elimination, or other external corrections to achieve high-accuracy GNSS positioning. Therefore, these error sources and the modelling strategies that are typically used for GNSS processing are described in the following:

- **Tropospheric delays.** The troposphere is an atmospheric layer that extends from the earth's surface to an altitude of approximately 60-km. The delayed propagation of GNSS signals through the troposphere is typically separated into zenith hydrostatic delay (ZHD) and zenith wet delay (ZWD) components that respectively represent the dry atmosphere and water vapor (Solheim et al. 1999). Thus, the zenith total delay (ZTD) is the summation of both the hydrostatic and wet delay components. The ZHD can be modelled to mm-level accuracy if accurate temperature, pressure, and humidity data are available locally. In the absence of local atmospheric data, global ZHD models are used, with residual ZHD errors absorbed by ZWD parameters estimated by the GNSS user at each epoch.

Tropospheric delays in the zenith direction can be converted to the slant direction for each receiver-satellite link using empirical mapping functions. The slant hydrostatic delay is typically used as *a priori* GNSS observation corrections, while the slant wet delay is more difficult to model and requires the GNSS user to estimate it as part of their functional model. Typical hydrostatic delay models include the Hopfield and Saastamoinen models (Colombo 2006; Hopfield 1969; Jensen and Ovstedal 2008; Saastamoinen 1973), while typical mapping functions include the Niell function (Niell 1996), the Global and Vienna functions (Boehm et al. 2006), and the University of New Brunswick function (Leandro et al. 2006). These mapping functions are empirical models and assume a symmetric troposphere effect surrounding the user receiver. Additional horizontal gradients can be estimated by the user to address the asymmetric nature of the troposphere (Bar-Sever et al. 1998). In most weather conditions, the horizontal gradient is tightly constrained in time and the resulting estimated values are quite small, at a nominal mm-level.

- **Ionospheric effects.** The ionosphere is an atmospheric layer that extends from about 60-km above earth's surface up to several thousand kilometers in altitude. GNSS signals that pass through this region are affected by the atmospheric free electron density, which is highly dynamic due to ionization and recombination of particles during respective day and night periods. Proportional propagation speed of GNSS signals in the GHz frequency band can be used to eliminate first-order ionospheric effects that account for more than 99.9% of the total ionospheric effect (Hoque and Jakowsi 2008). Thus, dual-frequency code and carrier phase measurements are typically used to form respective combined ionosphere-free measurements that are affected by less than 0.1% of the original ionospheric effect. The minor contribution of second- and third-order ionospheric effects is typically ignored, as the maximum respective range errors at zenith are below 2-cm and 2-mm (Bassiri and Hajj 1993; Hoque and Jakowski 2007).

  Single-frequency receiver users typically use *a priori* ionospheric delay models to correct measurements, such as the vertical Total Electron

Content (TEC) maps (Hernandez-Pajares et al. 2009; Noll et al. 2009) produced by International GNSS Service (IGS) associate analysis centers. Alternatively, ionospheric model parameters estimated by ground control networks are broadcast as part of each satellite's navigation message and can generally reduce ionospheric range errors by approximately 50-60% (Prieto-Cerdeira et al. 2014; Hoque and Jakowski 2015). Hence, low-cost single-frequency devices commonly apply ionospheric corrections to measurements using the Klobuchar (1987) model, a modified Klobuchar model or the NeQuick model (Hochegger et al. 2000; Nava et al. 2008), with model parameters broadcast by respective GPS, BeiDou and Galileo satellites (Yang et al. 2020).

- **Hardware biases.** GNSS code and carrier phase measurements are affected by instrumental delays due to the signal propagation medium and hardware components of satellites and receivers. For example, simply increasing the cable length of a receiver antenna affects the absolute receiver pseudorange bias at the mm-level (Defraigne et al. 2014; Dyrud et al. 2008). Due to the hardware used at the signal's origin and reception, hardware biases are specific to each satellite, each frequency, and each measurement type.

Combinations of dual-frequency GNSS measurements are often formed to mathematically eliminate or isolate individual parameters using the scaled difference of measurements observed at each frequency. The resulting combined observables then become biased by the scaled difference of the original individual signal biases, i.e., the so-called differential code bias (DCB) in the case of combined code measurements. IGS clock and GIM products are estimated using unique combinations of GNSS measurements and are therefore contaminated by satellite DCB offsets. These satellite DCBs can be safely neglected if the same functional model and signals are used by both the network and user. Otherwise, in the case of single-frequency or uncombined measurement processing, the user must apply network estimated DCB corrections (e.g., from the IGS) to retrieve unbiased code measurements. Carrier phase bias products were recently developed and made available by some IGS analysis centers to assist with single-receiver integer ambiguity resolution.

- **Receiver clock offset.** An internal GNSS receiver clock typically uses a quartz crystal oscillator that is a few orders of magnitude worse, in terms of both accuracy and stability, than the atomic clocks used by GNSS satellites. Thus, standard GNSS users are not directly synchronized with respective GNSS time scales unless an expensive external atomic clock is utilized, which is rarely the case as the resulting GNSS receivers would not be affordable. Thus, the receiver clock offset is typically either introduced as an unknown parameter as part of the position estimation procedure or eliminated mathematically using between-satellite differencing of GNSS observations.
- **Satellite orbits and clock offsets.** Satellite orbit and clock information is available in real-time via the navigation message that is broadcast by satellites in respective GNSS constellations. Broadcast satellite orbits are provided at an approximate meter-level accuracy, while broadcast clock data are around 5-ns accuracy. Broadcast orbit and clock data are typically updated several times per day, with less frequent updates for other navigation message information, to provide GNSS users the information needed to estimate a coarse position. More precise satellite orbit and clock products are also available from GNSS data analysis centers for either enhanced real-time or post-processing applications. These precise products are discussed in more detail in the following section as they are a critical input to non-differential GNSS positioning techniques.

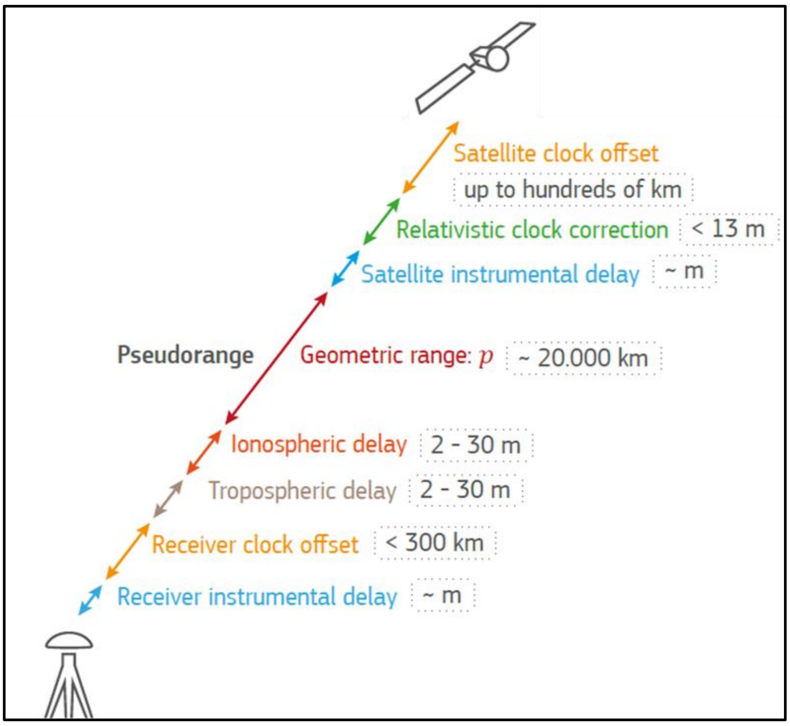

Figure 1.4. Primary GNSS error sources and nominal magnitudes (European GNSS Agency 2018).

In the next section, details related to non-differential GNSS measurement processing are given, in the context of single-receiver positioning. This requires specialized treatment of the primary GNSS error sources and the incorporation of additional error models. Then, a review on integer ambiguity resolution methods for single-receiver GNSS users is given. Benefits and capabilities for single- and multi-GNSS processing using non-differential techniques are also discussed.

1.2 Precise Point Positioning (PPP)

Precise Point Positioning (PPP), also known as "absolute" or "stand-alone" positioning, is a GNSS positioning technique used to process single-receiver, multi-frequency carrier-phase and pseudorange measurements (Malys and Jensen 1990; Zumberge et al. 1997). In a PPP model, shown in Figure 1.5, satellite orbit and clock information estimated by a global network of GNSS reference stations enables high-accuracy user positioning at a global scale, with nominal centimeter-level accuracy under ideal conditions (Kouba and Heroux 2001). Additional satellite carrier phase bias and attitude products estimated by a reference network can further enhance the performance of standard PPP (Loyer et al. 2021; Liu et al. 2021).

The characteristic undifferenced measurements used by the PPP user distinguish the technique from relative positioning methods and permits accurate and precise single-receiver positioning, as only measurements from a single receiver are required by the GNSS user. Conceptually, PPP constrains the positions of orbiting satellites, while differential techniques constrain the position of reference stations located on or near the earth's surface. Single Point Positioning (SPP) similarly uses an undifferenced approach but with pseudorange measurements only (i.e., without the carrier phase) and broadcast orbit information to achieve nominal 1- to 3-meter respective horizontal and vertical positioning accuracy using a multi-GNSS configuration (Choi et al. 2015). Therefore, PPP is characterized by both the precise carrier phase measurements and global network-estimated precise satellite products incorporated in the user's non-differential positioning model. Additionally, PPP performance can be further enhanced using carrier phase-based pseudorange smoothing (e.g., Geng et al. 2019; Basile et al. 2019) based on time-differenced measurements (Hatch 1982) which improves the precision of the relatively noisy pseudorange observations. However, pseudorange smoothing is not applied in this thesis, as the new processing strategies and algorithms are developed for real-time applications, where the user only has access to GNSS measurement data at the current and previous epochs of each continuous satellite observation arc.

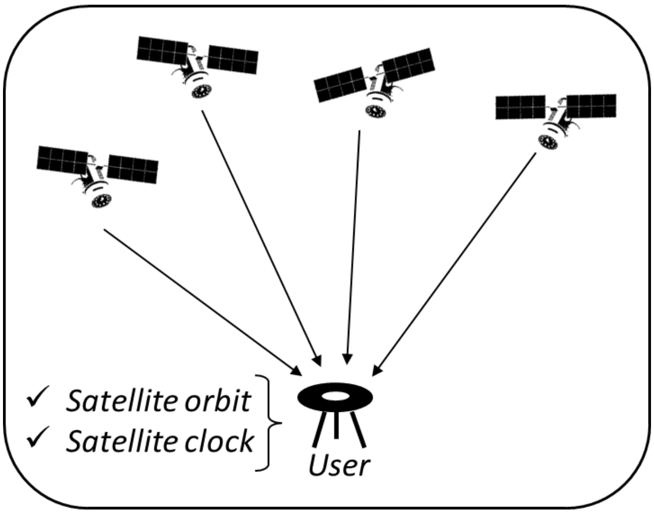

Figure 1.5. Precise point positioning approach, where precise satellite orbit and clock products estimated by a GNSS reference network are provided to a single-receiver dual-frequency user.

To fully describe the PPP approach, the following first provides the basic functional model components needed for standard PPP processing. Additional error models that affect single-receiver users are also discussed. Afterward, the precise satellite orbit and clock products that are critical external inputs to the PPP user's processing are discussed in detail. Advances in integer ambiguity resolution for PPP are given. Lastly, the positioning performance for single- and multi-GNSS PPP is provided to highlight the excellent accuracies that can be achieved by PPP users and enhancements using multi-GNSS processing.

1.2.1 Single receiver positioning

Traditional PPP uses a single GNSS receiver that can observe dual-frequency carrier-phase and pseudorange measurements to estimate the receiver position components and clock offset, tropospheric ZWD and one ambiguity parameter per observed satellite (Kouba and Heroux 2001). Models are typically used to approximate the tropospheric ZHD, with remaining tropospheric effects absorbed by the ZWD component. First-order ionospheric delays that account for more than 99.9% of the total ionospheric delay (Hoque and Jakowsi 2008) are eliminated using combined ionosphere-free observables (Leick 1995). The remaining unknown satellite parameters in the PPP user's model are then fixed to precise network-estimated satellite orbit and clock products. Consequently, traditional PPP addresses each of the primary GNSS error sources using dual-frequency measurements from a single GNSS receiver, along with advanced modelling techniques and precise satellite orbit and clock information.

Although this PPP model and estimation strategy can achieve excellent precision, high-accuracy PPP requires state-of-the-art corrections that represent complicated satellite, signal, timing, and site displacement effects. Relative positioning with short baselines normally neglects many of these effects due to the elimination of common errors observed by two receivers using between-satellite and between-receiver differencing operations. For PPP however, the single-receiver user is responsible for applying the following *a priori* corrections and strategies (see Figures A.1-A.5 in Appendix A for the effects on PPP positioning performance):

- **Antenna phase center (APC).** The phase center of both satellite and receiver antennas are offset from their respective nominal phase centers and require phase center offset (PCO) corrections to locate signals relative to the respective transmission and reception points. For example, satellite orbits that are modelled referenced to the satellite center of mass and the receiver antenna reference point (ARP) do not correspond to the true phase centers. In addition, the mm-level absolute antenna phase center variation (PCV) of satellite and receiver antennas must also be corrected using products derived from precisely calibrated experiments (Schmid et al. 2007). These PCO and PCV corrections are contained in files provided by the IGS for both the IGS08 and IGS14 reference frame realizations: ftp://ftp.igs.org/pub/station/general/. From these receiver and satellite antenna models, individual measurement corrections can be obtained using observed receiver-satellite geometries.

- **Phase wind-up.** Signals transmitted from GNSS satellites are formed by right hand circularly polarized (RHCP) radio waves. A rotation about the vertical axis of either the observer or satellite changes the observed carrier phase by a fraction of the full cycle amount, up to one whole cycle. The phase wind-up correction, given by Wu et al. 1993, is applied in the IGS products and therefore must be applied to maintain compatibility with IGS orbit and clock products.
- **Solid earth tides.** Contrary to intuition, the solid Earth crust deforms daily up to the decimeter-level due to gravitational interactions of nearby celestial objects. These site displacements are modeled by spherical harmonics which can be truncated at the second order term to provide 5-mm level precision. Thus, the total correction is a function of gravitational parameters, station coordinates, time, and the unit vector between the station and planets (IERS 1989).
- **Polar tides.** The relationship between the Earth’s spin axis and crust is not fixed and causes variations of the Earth’s poles with respect to the mean poles. Pole tide corrections for station latitude, longitude, and height are calculable with respect to the mean pole values (IERS 2010). The polar tide corrections are applied in the development of IGS products and must also be applied at user locations to maintain network-user consistency.

- **Ocean loading.** The ocean tidal load on the pliable earth crust results in periodic deformations up to 5 cm and must be corrected for sites closer than 1000 km to the nearest coastline. The ocean load can be modeled accurately using the summation of 11 tidal wave parameters, each dependent on astronomic and site-specific parameters (IERS 2010). The following online service provides parameters used in the correction model for given user location as input: http://holt.oso.chalmers.se/loading/.
- **Earth rotation parameters (ERP).** These parameters contain pole position, time conventions, and precession and nutation information to enable transformation between terrestrial and inertial reference frames. If a GNSS user fully constrains IGS orbit and clock products, then position estimates are directly related to the ITRF conventions that define the reference frame. If the user desires sub-daily ERP in an inertial reference frame, then sub-daily ERP variations must be considered (Kouba 2002).
- **Relativity.** GNSS positioning is affected by gravitational induced curvature of the transmitted signal along the propagation path (i.e., general relativity) and a frequency shift caused by satellite motion (i.e., special relativity). The propagation effects are normally neglected for relative positioning techniques but can cause decimeter-level errors if not corrected in absolute positioning methods (Zhu and Groten 1988; Ashby 2003). The relativistic satellite motion effects are corrected prior to launch by modifying the satellite clock base frequency according to a nominal circular orbit. Remaining periodic effects due to orbit eccentricity are corrected internally by the GNSS user using satellite-receiver geometry and standard definitions for the speed of light and gravity constants.

Next, the external satellite orbit and clock products that enable high-accuracy PPP at a global scale are discussed. The techniques used to generate and apply these satellite products are provided, with nominal accuracies. Because these products impose constraints on the PPP user, care is taken to explain the development and use of the satellite orbit and clock data.

1.2.2 External satellite products

Satellite orbit and clock products that enable PPP are estimated by GNSS networks, independent of the GNSS user. GNSS satellite orbit determination begins by assimilating gravitational, radiation and thrust forces that act on each satellite (Montenbruck and Gill 2000; Motenbruck et al. 2002). Then, a model is constructed using GNSS measurements from a reference station network and using highly stable orbital dynamics to solve for the unknown force parameters (Beutler et al. 2003).

Satellite clock parameter estimation similarly uses a GNSS ground station network to form non-differential ionosphere-free observables of pseudorange and carrier phase measurements (Hauschild and Montenbruck 2009). However, before this final estimation step, absolute receiver clock offsets are approximated using pseudorange-only measurement processing with clock constraints to eliminate rank deficiencies (Defraigne and Bruyninx 2000; Defraigne and Bruyninx 2007). The approximated clock offsets are then incorporated in the ionosphere-free model, where carrier-phase measurements regulate the between-epoch relative accuracy of the estimated ionosphere-free clock parameters (Hauschild and Montenbruck 2009).

For nearly three decades, the IGS has published high-precision satellite orbit and clock products. These products are created by combining outputs from international associate analysis centers such as: Center for Orbit Determination in Europe (CODE), GeoForschungsZentrum (GFZ), Jet Propulsion Laboratory (JPL), Natural Resources Canada (NRCAN), and others. Improved products and product variety are periodically made available due to an increase in analysis center contributors, better error modelling, and multi-GNSS processing strategies.

The latest IGS product qualities, in terms of root mean square (RMS) error, and properties for GPS satellites are given in Table 1.1. All non-broadcast orbit products are at least 5-cm accuracy with a 15-minute sampling interval and are considered suitable for PPP. The final products provide the best accuracies and sample intervals but have the longest latencies of approximately two weeks. Rapid products are available only 1-2 days after observation with similar quality as the final products but suffer from a worse 5-minute clock sampling interval. These trends continue for ultra-rapid products, especially for the predicted products that are available in real-time but are not suitable for PPP due to the relatively poor clock accuracy of 3-ns.

Table 1.1. Properties of IGS satellite products.

Type		Accuracy	Latency	Updates	Sample Interval
Broadcast	orbits	~100 cm	Real-time	–	daily
	clocks	~5 ns			
Ultra-rapid (predicted)	orbits	~5 cm	Real-time	6-hour UTC intervals	15 minutes
	clocks	~3 ns			
Ultra-rapid (observed)	orbits	~3 cm	3 – 9 hours	6-hour UTC intervals	15 minutes
	clocks	~150 ps			
Rapid	orbits	~2.5 cm	17 – 41 hours	17 UTC daily	15 minutes
	clocks	~75 ps			5 minutes
Final	orbits	~2.5 cm	12 – 18 days	every Thursday	15 minutes
	clocks	~75 ps			30 seconds

Note: Adapted from https://igs.org/products/. Accuracies reported are RMS.

Satellite clock product precision is also reported by the IGS and is typically better than the Table 1.1 RMS accuracies by at least a factor of two. This indicates that small biases exist among analysis center outputs, likely due to slightly different processing and modelling strategies. However, these discrepencies can be neglected if products are consistently used from the same analysis center.

The PPP user measurement interval rarely aligns exactly with the Table 1.1 network-derived product intervals and therefore interpolation to the user measurement epochs is required. Commonly applied satellite orbit interpolation techniques are better than 1-cm accuracy, largely due to well-defined and stable orbital dynamics (Yousif and El-Rabbany 2007). Simple between-epoch linear interpolation of satellite clocks is suitable due to the 30-second original sampling interval. Interpolation below approximately 5-second intervals offer negligible positioning improvement (Bock et al. 2009).

The single-receiver PPP user that relies on the information illustrated in Table 1.1 introduces parameter constraints in their functional model. For example, because the IGS precise orbits are defined in the IGS global reference frame (e.g., the ITRF), PPP users that apply these products become directly constrained to the underlying reference frame (Kouba 2015). This automatic placement of the PPP users relative to an inherited global reference frame is a key benefit of the method, as the whole reference system contributes constraints to the user's estimation position. For comparison, relative positioning techniques constrain the unknown estimated user location relative to the position of a single reference station that may not be accurately positioned within the reference frame desired by the user.

Consistency between network and user models must be maintained to estimate user parameters that are free from unknown biases. This is especially true for the IGS clock products that are estimated relative to dual-frequency ionosphere-free observables (Kouba and Springer 2001; Defraigne and Bruyninx 2007). The resulting ionosphere-free satellite clock products contain DCBs related to the signals used in the network's functional model, e.g., P1-P2 for GPS satellites. Therefore, the IGS clock products are directly compatible only with an ionosphere-free user model where the same satellite DCBs are absorbed in the satellite clock parameters. If individual signals are processed in an undifferenced and uncombined model, or if a different signal such as GPS L1C/A is used, then satellite code bias products are required to correct the corresponding raw pseudorange measurements (Jefferson et al. 2001; Leandro et al. 2007). For standard PPP, satellite phase biases are absorbed by the estimated ambiguity parameters resulting in non-integer (i.e., float) ambiguities. Although integer ambiguities are not used in this thesis, integer ambiguity resolution for PPP is described in the next section.

In addition to the IGS products given in Table 1.1, real-time satellite clocks and other corrections are provided by a variety of public and commercial augmentation services (European GNSS Agency 2020). These services typically constrain ultra-rapid and rapid satellite orbits from the IGS, then estimate satellite clocks using a reference station network to replace the poor quality IGS real-time clocks. Then, real-time products are transmitted to users via geostationary communication satellites or the internet using data protocols such as the Radio Technical Commission for Maritime Services (RTCM) or Compact Measurement Record (CMR) standards.

In the context of PPP, studies typically simulate real-time positioning performance using final satellite clock products that have better accuracy than real-time counterparts. However, improvements to real-time multi-GNSS satellite clock estimation and error modeling are approaching the accuracy of IGS final products (Gong et al. 2018; Lou et al. 2015; Shi et al. 2018; Zuo et al. 2021). Therefore, throughout this thesis, none of the aforementioned real-time services or products are used and positioning results are post-processed using final satellite products.

1.2.3 Integer ambiguity resolution

Carrier phase measurements are inherently ambiguous due to an unknown number of integer cycles that occur between signal transmission and reception. Thus, carrier phase measurements are biased by a number of unknown integer cycles that are commonly represented by ambiguity parameters in the GNSS positioning model. If these carrier phase ambiguities can be precisely estimated or resolved as integer values, then the corresponding carrier phase measurements behave as extremely precise pseudorange measurements with nominal mm-level precision (Laurichesse et al. 2011; Kouba 2015).

Differential positioning commonly uses double differenced carrier phase observations to remove most of the errors common to receivers and satellites. This includes mathematical elimination of non-integer bias effects that would otherwise destroy the integer nature of the carrier phase ambiguities. Thus, double-differenced GNSS processing can easily resolve integer ambiguities to strengthen the positioning model. However, as noted previously, differential processing is not an option for a wide variety of GNSS applications that use only a single receiver.

Integer ambiguity resolution (IAR) for non-differential GNSS models has recently gained interest, with a focus on non-differential alternatives to the precise double-differenced processing technique (Laurichesse 2010; Laurichesse 2011; Odijk et al. 2016; Odijk et al. 2017; Teunissen et al. 2010). The methods to estimate integer ambiguities for a single-receiver GNSS user can be separated into observation- or state-space techniques (Odijk et al. 2016). In the observation-space, combinations of code and carrier phase measurements are used to identify and resolve integer ambiguities. Therefore, integer ambiguity resolution applied in a PPP user's model is considered an observation-space technique, commonly named PPP-AR or PPP-IAR. In the state-space, combinations of the fundamental GNSS model parameters are used instead of measurement combinations to perform integer ambiguity resolution (Teunissen and Khodabandeh 2015). This is the reason state-space techniques are commonly referred to as PPP-RTK, where the GNSS model is non-differential (i.e., PPP) and simultaneously enables integer ambiguity resolution of uncombined carrier phase measurements (i.e., RTK).

Although observation- and state-space techniques are conceptually different, both methods require complete consistency between the network and user models, with satellite orbit and clock information made available to the user. If no further modifications are applied, then the GNSS user's processing becomes identical to a standard PPP model, i.e., with non-integer ambiguities. However, both PPP-IAR and PPP-RTK techniques estimate then provide additional information that is incorporated in the user's model to enable single-receiver IAR. For PPP-RTK, network-estimated clock, phase bias and code bias parameters are necessary to achieve integer ambiguity resolution for the user's undifferenced and uncombined measurements. This approach also optionally provides ionospheric delay information to the user. For observation-space techniques, the user resolves their ionosphere-free ambiguities using network-estimated satellite orbit, clock, and phase bias information (Wubbena et al. 2005; Laurichesse 2010; Laurichesse and Mercier 2007). Remaining parameters, such as the satellite code bias, are then eliminated in the observation-space if the network and user use identical GNSS models.

A critical difference between these single-receiver integer ambiguity resolution techniques is the flexible parameterization of network-estimated information in the PPP-RTK approach that can additionally provide ionospheric data to the user. For example, if accurate ionospheric information is given to the PPP-RTK user, e.g., from a regional GNSS reference network, then fast and reliable positioning that is comparable to double-differenced RTK models can be achieved (Psychas and Verhagen 2020). If network-estimated ionospheric delays are not available, then the PPP-RTK user can estimate slant ionospheric delays, which may be useful for atmospheric studies or other applications. Another advantage of the PPP-RTK approach is that the underlying GNSS model consists of uncombined measurements that are less noisy than the alternative ionosphere-free combined measurements.

In terms of real-time positioning applications, RTK and NRTK users require reference station observations at each epoch to form double-differenced observables. This process is quite intensive from a data transmission perspective and is especially problematic when a GNSS user is operating with limited bandwidth, e.g., in a remote area with poor data coverage. Therefore, PPP-RTK is an appealing alternative to traditional RTK and NRTK methods, as reference station observations are not needed by the PPP-RTK user. Additionally, some network-estimated PPP-RTK parameters are quite stable in time and can be updated less frequently to further reduce bandwidth requirements (Wübbena et al. 2014).

A small number of IGS analysis centers have adopted strategies that enable observation-space PPP-IAR, while PPP-RTK is primarily limited to commercial and research applications. Additional data currently available for PPP-IAR are satellite wide-lane bias products. These products are usually quite stable over short time periods and are therefore typically made available by GNSS analysis centers on a daily basis. In this thesis, it should be noted that the standard PPP strategy is used, without satellite bias products or PPP-RTK strategies, as the objectives focus on post-convergence PPP performance. Also, the extreme atmospheric conditions that are studied typically amplify position errors by several factors, or even orders of magnitude in some cases, while PPP-IAR and PPP-RTK models are nearly identical to the standard PPP model, in terms of accuracy, after the initial convergence period (Ma et al. 2020).

The benefits of PPP from the single- and multi-GNSS processing perspectives are given next. Examples are provided to demonstrate the achievable positioning performance using single- and multi-GNSS configurations under a variety of conditions. Comparisons between single- and multi-GNSS positioning show the typical performance improvements that can be achieved when GNSS measurements from more than one system are used by the GNSS user.

1.2.4 Benefits of single- and multi-GNSS PPP

Standard PPP was initially developed to efficiently analyze large networks of GPS measurements and reduce the computational burden compared to standard double-difference methods (Zumberge et al. 1997; Blewitt 2008). Additionally, PPP users are not required to establish a reference station. For comparison, relative positioning users are restricted by reference station logistics, feasibility, and expenses (Bisnath and Gao 2009).

In a standard PPP model, users only need to receive network-estimated precise satellite orbit and clock data which requires less bandwidth compared to relative positioning that uses raw measurements of a reference station (Wubbena et al. 2005). Real-time applications greatly benefit from the inherently scalable PPP model due to every user receiving the same satellite-dependent data transmitted from the service provider. For the same reason, only a sparse network of a few dozen globally-distributed reference stations is required to estimate precise satellite products which can achieve comparable quality to the IGS rapid and final products (Hauschild and Montenbruck 2009). Thus, PPP is suitable for service at a global scale, even in remote regions or open-ocean environments where reference stations are thousands of kilometers away from users (Geng et al. 2010b).

Under ideal conditions, and after an initial convergence period, static and kinematic GPS-only PPP can reach respective mm- and cm-level horizontal positioning accuracy with approximately double the horizontal positioning error in the vertical direction (Geng et al. 2010a; Heroux et al. 2004; Soycan 2012). These advantages have encouraged the development of many PPP-enabled commercial (Dixon 2006; Leandro et al. 2011; Tavasci et al. 2021), scientific (Gregorious 1996; Leandro et al. 2007; Píriz et al. 2008; Shi et al. 2008; Teferle et al. 2007) and public (Jia et al. 2014; Tetreault et al. 2005) software and services.

Multi-GNSS PPP incorporates measurements from combinations of GNSS constellations that have global coverage, namely, GPS, GLONASS, Galileo, and Beidou, in a single-receiver PPP model. When compared to GPS-only processing, multi-GNSS models strengthen the overall positioning and estimation quality, especially if GPS satellite coverage or the measurement quality is poor (Cai and Gao 2007; Cao et al. 2010; Gjevestad et al. 2007). For example, benefits of using a nearly complete Galileo constellation are discussed by Xia et al. (2019), where the addition of Galileo E1/E5a measurements to GPS and GPS+GLONASS based models improved kinematic PPP accuracy by more than 25% and 10%, respectively. Furthermore, Dabove et al. (2020) compared GPS-only with GPS+GLONASS+Galileo combined processing in a multi-GNSS kinematic PPP model and showed improvements of up to 51% and 46% in the respective positioning accuracy and initial convergence time in the presence of strong ionospheric activity at high latitudes. Multi-GNSS studies currently focus on resolving measurement biases, using low noise multi-frequency combinations and integer ambiguity resolution.

1.3 Limitations of PPP

Despite the numerous advantages of single- and multi-GNSS PPP, positioning quality may degrade if conditions are not ideal. While non-mitigated positioning errors are always problematic, real-time PPP users that operate far from reference stations and infrastructure and are typically unable to use control (i.e., reference) points to independently validate their position. For comparison, NRTK users can normally occupy a control point or create a new baseline by changing reference stations to assess their accuracy. Therefore, careful consideration must be given to situations where PPP quality is unreliable.

Increased activity in earth's troposphere and ionosphere can increase GNSS-related errors and reduce positioning estimation quality. These atmospheric effects are commonly separated into tropospheric and ionospheric signal propagation delays and ionospheric scintillation effects. In this thesis, the distinction between the effects of tropospheric and ionospheric layers is used, with further separation of ionospheric scintillation effects as it is characterized by the rapid phase and amplitude fluctuations of the received signal. The following explains specific cases that worsen PPP performance and are addressed using innovations developed in this thesis.

1.3.1 Ionospheric scintillation

Strong and frequent post-sunset scintillation is common in the equatorial/low latitude regions between ±20° geomagnetic latitude due to the Equatorial Ionospheric Anomaly (EIA) effect (Spogli et al. 2013). Although strong scintillation may occur more frequently in the presence of geomagnetic storms, the CODE GIM in Figure 1.6 shows that large ionospheric gradients are frequent at equatorial regions. Strong scintillation has been demonstrated to cause frequent receiver loss of signal lock and amplify kinematic PPP errors by several orders of magnitude compared to quiet ionospheric conditions (Pi et al. 2017; Luo et al. 2018; Marques et al. 2018, Guo et al. 2019; Vadakke Veettil et al. 2020).

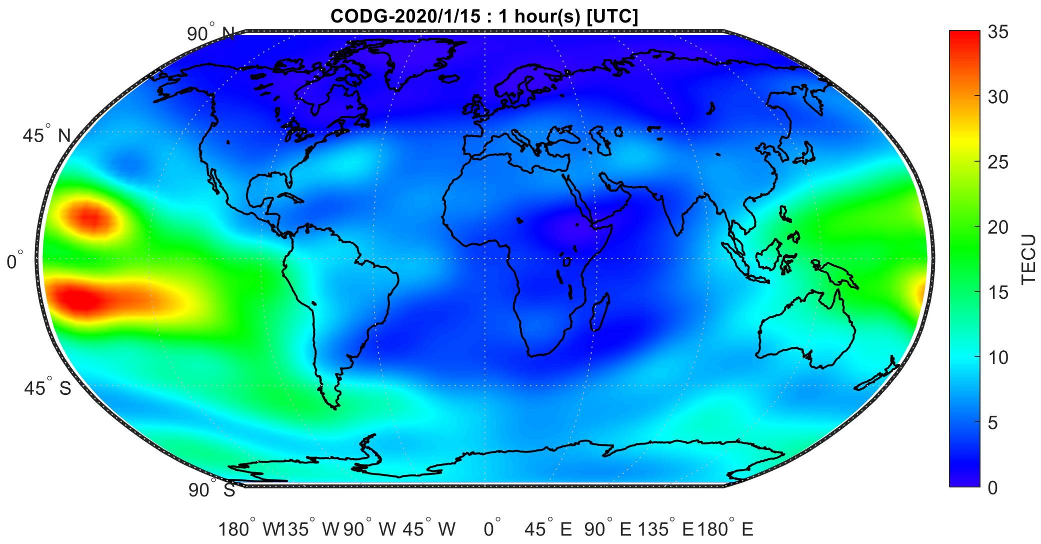

Figure 1.6. CODE GIM on January 15, 2020 at 01:00 UTC, with EIA ionization crests visible as dark red regions near the antemeridian (180° W).

Studies frequently characterize scintillation using the amplitude and phase scintillation indices (Briggs and Parkin 1963; Basu et al. 2002; Aquino et al. 2005; Sreeja et al. 2011; Spogli et al. 2013; Marques et al. 2018; Vadakke Veettil et al. 2020) and, as the result of correlation analyses, the rate of total electron content index (ROTI) (Pi et al. 1997; Juan et al. 2017). Mitigation of ionospheric scintillation effects is typically achieved using modifications to the stochastic model (Aquino et al. 2009; Park et al. 2017; Silva et al. 2010; Weng et al. 2014) or functional model (Zhang et al. 2014; Vani et al. 2019). Additionally, enhanced model error detection and quality control algorithms have been shown to mitigate scintillation effects (Zhang et al. 2014; Luo et al. 2020). However, mitigation techniques are typically not applied to multi-GNSS processing and are challenging to use for non-specialized GNSS receivers (Sreeja et al. 2011).

1.3.2 Ionospheric delay

The ionosphere-free combinations of individual GNSS measurements that are fundamental for standard PPP processing effectively eliminates ionospheric information that may otherwise be useful to the GNSS user. Fortunately, PPP users typically compute biased ionospheric delay for each receiver-satellite link using geometry-free combinations of individual GNSS measurements as part of cycle slip detection and repair algorithms (Cai et al. 2013; Liu et al. 2011). The time-difference of this ionospheric delay was innovatively used by Luo et al. (2022) in a modified stochastic model that uses the ionospheric rate to amplify the basic elevation-based measurement noise. However, this method fails if carrier phase cycle slips are not detected or remain uncorrected, as cycle slips artificially increase the otherwise precise ionospheric rate (Cai et al. 2013). This limitation is especially problematic during periods of increased ionospheric activity, as cycle slips are more frequent and can be further amplified in the presence of geomagnetic storms. In these cases, GNSS measurements are assigned noise values that are not realistic.

1.3.3 Tropospheric storms

Tropospheric delay is typically estimated in the GNSS functional model as a slowly changing time-dependent parameter. In most weather conditions, it can be well-estimated using PPP, as the ZWD is only a single parameter modelled as being common to all measurements using empirical mapping functions (Boehm et al. 2006; Niell 1996). However, in extreme weather events, such as tropospheric storms, the tropospheric delay could change rapidly and exhibit azimuthal asymmetry. As a result, ZWD estimation accuracy could become worse and, therefore, worsen PPP accuracy.

The PPP user typically does not have access to an immediate meteorological database to mitigate the situation, as in the NRTK domain. Moreover, standard regional tropospheric corrections that are available to NRTK users are supplied deterministically (e.g., without uncertainty data) as frequency independent terms. This limits the PPP user's potential to develop a stochastic application of the network-estimated tropospheric information, where the user's tropospheric time constraints are allowed to vary.

1.4 Research objectives

Due to the challenges identified in Section 1.3, this thesis develops strategies to improve single- and multi-GNSS PPP performance using atmospheric information, provided externally to the PPP user, in order to restore nominal PPP accuracy levels under non-ideal conditions. Within this scope, background on the TREASURE project is required to identify the motivation for using external information. The TREASURE project was led by the University of Nottingham and was comprised of

9 beneficiaries, 21 associated partners, and 13 early-stage researchers enrolled as PhD students. The TREASURE project was funded by the EU Horizon 2020 framework as a Marie Sklodowska-Curie Action (MSCA), part of the Innovative Training Network (ITN). The focus of the project was on training the students through secondments and interactions with the industry to achieve the ultimate real-time GNSS solution for Europe. The TREASURE project was divided into sub-topics such as receiver tracking error, ionospheric and satellite orbit modelling, among other interests.

The purpose of this research aims to incorporate the outcomes from other TREASURE project tasks into improved PPP algorithms, as shown in Figure 1.7. External ionospheric and tropospheric information in Figure 1.7 was generated through collaborations with Juliana Garrido Damaceno and Hongyang Ma, respectively. Collaboration with Kai Guo regarding new tracking error model outputs occurred in parallel with the Figure 1.7 workflow, though none of the products were used in this thesis. Additional details on processing techniques and roles in Figure 1.7 are given in corresponding sections in Chapter 5. Although the initial development of methods involved collaboration within the TREASURE project, the strategies and results presented throughout this thesis are the original work of the author.

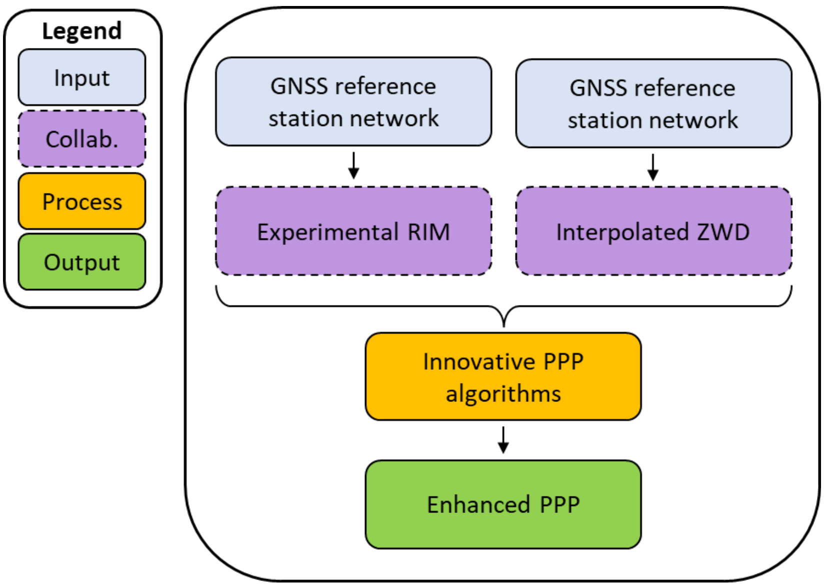

Figure 1.7. Workflow of TREASURE project collaborations as sources for external regional ionospheric map data and interpolated tropospheric correction data used as inputs to new PPP algorithms.

To pursue the objectives, the following key tasks were identified and addressed throughout this thesis:

- Develop methods to improve kinematic PPP performance under adverse tropospheric and ionospheric conditions using external information that is not available to a standard PPP user.
- Demonstrate single- and multi-GNSS PPP accuracy, reliability and precision improvement under strong low-latitude ionospheric scintillation conditions using modernized Galileo signals.
- Mitigate ionospheric scintillation effects for a non-specialized multi-GNSS PPP user in a mixed stochastic model.
- Develop strategies to process and show the benefits of a troposphere-corrected PPP model using deterministic and stochastic corrections to mitigate tropospheric storm effects.
- Develop a revised PPP model that uses regional and global ionospheric information in an efficient manner to improve positioning performance under large ionospheric gradients.
- Implement the above solutions in the University of Nottingham POINT software, where algorithms can be further expanded by future researchers.

1.5 Thesis structure

This thesis contains six chapters which are organized as follows. After the current chapter, Chapter 2 reviews previously developed methods for crucial multi-GNSS PPP algorithms and techniques. Then ionospheric scintillation characterization, tracking error models and positioning mitigation techniques are discussed. Afterward, strategies that use correction information for both tropospheric and ionospheric delays are presented. Finally, conclusions related to each experiment are given and innovative contributions for this thesis are discussed, along with future research opportunities.

Chapter 3 introduces the University of Nottingham POINT software architecture and capabilities. This chapter also provides details on the estimation processing strategy. Contributions to the software for this thesis are also given.

Chapter 4 presents and discusses results on the evaluation of kinematic multi-GNSS PPP under low latitude ionospheric scintillation. Then, multi-GNSS mitigation methods are developed and results are evaluated with respect to a standard elevation-based stochastic model.

Chapter 5 proposes troposphere-corrected and ionosphere-weighted PPP models that improve positioning performance under adverse conditions. The development and quantitative evaluation of deterministic, partially stochastic and fully stochastic tropospheric corrections is presented. Then, a new modified stochastic model is developed to amplify measurement uncertainty based on the ionospheric delay rate computed using global and regional ionospheric map products.

Although both Chapters 4-5 contain experiments related to the ionosphere, the organization is based on the type of information provided to the PPP user. In Chapter 4, new processing strategies specifically target ionospheric scintillation effects using multi-GNSS processing and receiver tracking error characteristics. Therefore, this content is provided separately from Chapter 5, which incorporates ionospheric and tropospheric correction information into new algorithms, as opposed to the receiver properties that are used in Chapter 4.

Chapter 6 summarizes the key outcomes and highlights the contributions of this thesis. Quantitative support for the innovations developed herein is also given. Future research tasks are also presented with the aim of building on the results of this thesis.

Chapter 2

Externally Aided PPP

2.1 Introduction

Other than precisely estimated satellite orbit and clock products, standard PPP users operate without any additional external information. Therefore, changes in atmospheric conditions that affect PPP performance typically remain unknown to users and there is no opportunity to mitigate these errors. Hence, this chapter first reviews general algorithms and techniques used for PPP and multi-GNSS processing. Developments on integer ambiguity resolution for single-receiver PPP users using external bias products is also reviewed. Then, the challenging tropospheric and ionospheric conditions that affect PPP performance are presented in detail. The techniques that will be shown to improve the deteriorated positioning under these adverse atmospheric effects are given last.

2.2 Current advances in PPP

In this section, the methods that enable high-accuracy single-receiver positioning are introduced using an undifferenced and uncombined functional model that relates absolute unknown parameters to GNSS observations. Then, crucial measurement combinations that define the functional PPP model are presented in terms of the combined original unknown parameters. Furthermore, advances and strategies in multi-GNSS processing and methods to detect model errors that would otherwise degrade positioning accuracy are discussed. Finally, integer ambiguity resolution techniques for single-receiver GNSS users are given.

2.2.1 Fundamental raw measurement model

Many different linear combinations of GNSS measurements can be formed to isolate, eliminate, or emphasize specific parameters in the observation model (Hauschild 2017). Combined observables can either amplify or reduce the resulting observable noise due to the error propagation law (Ghilani 2017) and are used for various positioning algorithms and quality control analyses that can enhance positioning performance.

For an undifferenced and uncombined GNSS positioning model, it is helpful to first separate frequency-independent parameters from frequency-dependent ones, where frequency-independent terms for both code and carrier phase measurements grouped as a single parameter G_r^s for satellite s and receiver r at a single epoch are:

$$G_r^s = \rho_r^s + c \cdot dt_r + m_{r,ZWD}^s \cdot T_{ZWD} + m_{r,(G_N,G_E)}^s \cdot T_{(G_N,G_E)} \tag{2.1}$$

where $\rho_r^s = \sqrt{(X^s - X_r)^2 + (Y^s - Y_r)^2 + (Z^s - Z_r)^2}$ represents the geometric distance between satellite (X^s, Y^s, Z^s) and receiver (X_r, Y_r, Z_r) with precise satellite positions fixed to network-estimated orbit products; c denotes the unimpeded speed of light (i.e., in vacuum); $dt_r = t_r - t^s$, where t_r and t^s represent respective receiver and satellite clocks and dt_r denotes the associated receiver clock offset after the network-estimated satellite clock biases are removed; T_{ZWD} represents the absolute tropospheric zenith wet delay multiplied by a mapping function $m_{r,ZWD}^s$ that converts from the zenith to slant direction (Leandro et al. 2006); finally, $T_{(G_N,G_E)}$ denotes north and east gradients multiplied by their respective $m_{r,(G_N,G_E)}^s$ mapping functions, which convert the tropospheric zenith wet delay to azimuthal dependent components (Chen and Herring 1997). The dry tropospheric delay component is modelled (Saastamoinen 1972), mapped to slant directions, then applied as measurement corrections and is therefore not shown in Equation 2.1.

Next, the Equation 2.1 frequency-independent parameter (G_r^s) and remaining frequency-dependent parameters, transmitted on frequency j, can be used to express undifferenced and uncombined pseudorange (p) and carrier phase (φ) measurements as:

$$p_{r,j}^s = G_r^s + \frac{\mu}{f^2} \cdot I_{r,1}^s + c \cdot b_{r,j}^s + e_{r,j}^s \tag{2.2}$$

$$\varphi_{r,j}^{s} = G_r^s - \frac{\mu}{f_j^2} \cdot I_{r,1}^{s} + \lambda_j \cdot B_{r,j}^{s} + \lambda_j \cdot N_{r,j}^{s} + \epsilon_{r,j}^{s}$$

where $I_{r,1}^{s}$ represents the first-order ionospheric delay of the first frequency (j = 1); $b_{r,j}^{s} = b_{r,j} - b_j^s$ and $B_{r,j}^{s} = B_{r,j} - B_j^s$ denote respective code and carrier phase hardware delays, where $b_{r,j}$ and $B_{r,j}$ are receiver delays and b_j^s and B_j^s are satellite delays, with b and B parameters expressed in meters and cycles, respectively; $N_{r,j}^{s}$ represents the integer carrier phase ambiguity, in cycles, that is multiplied by wavelength λ_j, in meters; finally, $e_{r,j}^{s}$ and $\epsilon_{r,j}^{s}$ denote respective code and carrier phase measurement noise, assumed to be normally distributed with a zero mean. The frequency index j is an integer value that corresponds to the individual GNSS signal, where GPS L1 and L2 signals, for example, are assigned respectively as $j = 1$ and $j = 2$.

Higher-order ionospheric effects that account for ionospheric refraction depending on the planetary magnetic field are neglected in Equation 2.2, as maximum effects are typically below a few centimeters of range error (Bassiri and Hajj 1993; Hoque and Jakowski 2007). Note that the ionospheric effect advances the carrier phase and is thus represented in Equation 2.2 using a sign opposite of the ionospheric coefficient for the code measurements. The ionospheric coefficient μ/f_j^2, where $\mu = 40.3 \cdot TEC$, relates the ionospheric delay of a reference frequency (i.e., $I_{r,1}^{s}$) to any other frequency based on the total electron content. Note that Equation 2.2 is rank deficient for $j \leq 2$, i.e., the number of unknown parameters exceeds the number of measurements, due to linear dependencies between the $b_{r,j}^{s}$ and $B_{r,j}^{s}$ hardware delays and other unknown parameters.

2.2.2 Essential measurement combinations

Linear combinations of the Equation 2.2 raw carrier phase and pseudorange measurements at an epoch can be generalized for measurements transmitted on frequency j in the form:

$$o_{r,c}^{s} = \sum_{j=1}^{n} \left(\alpha_j \cdot \varphi_{r,j}^{s} + \beta_j \cdot p_{r,j}^{s} \right) \tag{2.3}$$

where α_j and β_j are signed, real-valued scale factors applied to respective carrier phase and pseudorange measurements that create the combined observable $o_{r,c}^{s}$. Note that the Equation 2.3 form is adapted from the parameterization given by Hauschild (2017). If the Equation 2.2 code and carrier phase measurements are substituted in Equation 2.3, then unknown parameters become linear combinations of the original uncombined parameters, as depicted in Equation 2.4 below.

$$\begin{aligned} & o_{r,c}^{s} = \\ & \Sigma\left(\alpha_j + \beta_j\right) \cdot G_r^s + \\ & \Sigma\left(-\alpha_j + \beta_j\right) \cdot \frac{f_1^2}{f_j^2} \cdot I_{r,1}^s + \\ & \Sigma\left(\alpha_j \cdot \lambda_j \cdot B_{r,j}^s + \beta_j \cdot c \cdot b_{r,j}^s\right) + \\ & \Sigma\left(\alpha_j \cdot \lambda_j \cdot N_{r,j}^s\right) + \\ & \Sigma\left(\alpha_j \cdot \epsilon_{rj}^s + \beta_j \cdot e_{r,j}^s\right) \end{aligned} \tag{2.4}$$

The unknown parameters of combined observables in Equation 2.4 are clearly functions of the α_j and β_j coefficients. Although the α_j and β_j coefficients may be any real number, the existence of some parameters completely depends on combination of these coefficients. For example, the scale factor which controls the existence of the first order ionospheric delay is defined in Equation 2.5 for n frequencies.

$$SF_{Iono} = \sum_{j=1}^{n}\left(-\alpha_j + \beta_j\right)\frac{f_1^2}{f_j^2} \tag{2.5}$$

The ionosphere-free combination introduced in Section 1.2 is a special case of Equation 2.5 that is formed when carefully selected coefficient values α_j and β_j satisfy the conditions: $SF_{Iono} = 0$ and $j > 1$. This is critical for standard PPP users that rely on only the precise satellite orbit and clock products provided by the IGS, without any *a priori* ionospheric information. Equation 2.6 presents the ionosphere-free combination coefficients for dual-frequency carrier phase and pseudorange measurements.

$$\begin{aligned} & \alpha_1 = +\frac{f_1^2}{f_1^2 - f_2^2};\ \alpha_2 = -\frac{f_2^2}{f_1^2 - f_2^2} \\ & \beta_1 = \alpha_1;\ \beta_2 = \alpha_2 \end{aligned} \tag{2.6}$$

The Equation 2.6 coefficients evaluated in Equation 2.5 confirm that the ionospheric parameter of Equation 2.4 is mathematically eliminated for carrier phase and pseudorange measurements. At the same time, the evaluations of $\Sigma\left(\alpha_j\right) = \Sigma\left(\beta_j\right) = 1$

in Equation 2.4 indicates that the combination preserves geometry parameters. Therefore, the geometric range, absolute receiver clock offset and tropospheric parameters that are contained within Equation 2.1 are identical before and after the combination, as each parameter is independent of the measurement frequency.

The ionosphere-free carrier phase observable, i.e., $\varphi_{r,IF}^{s} = \alpha_1 \cdot \varphi_{r,1}^{s} + \alpha_2 \cdot \varphi_{r,2}^{s}$, can be reconstructed by substituting the Equation 2.6 coefficients in Equation 2.4 to obtain:

$$\varphi_{r,IF}^{s} = G_r^s + \lambda_{IF} \cdot \left(N_{r,IF}^{s} + B_{r,IF}^{s}\right) + \epsilon_{r,IF}^{s} \tag{2.7}$$

where $\lambda_{IF} = \alpha_1 \cdot \lambda_1 + \alpha_1 \cdot \lambda_2$ represents the ionosphere-free wavelength; $N_{r,IF}^{s} = \alpha_1 \cdot N_{r,1}^{s} + \alpha_2 \cdot N_{r,2}^{s}$ denotes the (integer) ionosphere-free ambiguity; $B_{r,IF}^{s} = \alpha_1 \cdot B_{r,1}^{s} + \alpha_2 \cdot B_{r,2}^{s}$ denotes the ionosphere-free hardware bias; finally, $\epsilon_{r,IF}^{s} = \alpha_1 \cdot \epsilon_{r,1}^{s} + \alpha_2 \cdot \epsilon_{r,2}^{s}$ represents the combined measurement noise. If satellite carrier phase hardware bias information is not available, then a single-receiver user must re-parameterize $\widetilde{N}_{r,IF}^{s} = N_{r,IF}^{s} + B_{r,IF}^{s}$ to remove the associated linear dependency. Although the resulting ambiguity parameter becomes estimable, it is no longer an integer and must be estimated as a biased non-integer real (e.g., float) value. However, the biased ambiguity term remains time-constant due to relatively stable satellite hardware biases.

The combined dual-frequency ionosphere-free pseudorange observable, i.e., $p_{r,IF}^{s} = \beta_1 \cdot p_{r,1}^{s} + \beta_2 \cdot p_{r,2}^{s}$, can be reconstructed by substituting the Equation 2.6 coefficients in Equation 2.4 to obtain:

$$p_{r,IF}^{s} = G_r^s + c \cdot b_{r,IF}^{s} + e_{r,IF}^{s} \tag{2.8}$$

where $b_{r,IF}^{s} = \beta_1 \cdot b_{r,1}^{s} + \beta_2 \cdot b_{r,2}^{s}$ represents the combined hardware bias; and $e_{r,IF}^{s} = \beta_1 \cdot e_{r,1}^{s} + \beta_2 \cdot e_{r,2}^{s}$ denotes the combined measurement noise. An obvious linear dependency exists in Equation 2.8 due to both the terms $c \cdot dt_r$ (see Equation 2.1) and $c \cdot b_{r,IF}^{s}$ containing the same coefficient. Therefore, if satellite hardware bias information is not available, then the single-receiver user must re-parameterize $\widetilde{dt}_{r,IF} = dt_r + b_{r,IF}^{s}$ to remove the associated rank deficiency. Furthermore, if the $b_{r,IF}^{s}$ parameter of Equation 2.8 is expanded following Equation 2.2, then the respective ionosphere-free receiver and satellite code hardware delays become differential code biases (DCBs) comprised of the original absolute code biases scaled by β_j coefficients. Precise satellite clock products provided by the IGS similarly absorb ionosphere-free satellite DCBs in the estimated clock parameters. Therefore, satellite DCB corrections are not required in Equation 2.8 if the PPP user processes the same raw measurement combinations that were used to generate the satellite products, as these DCBs are consistently absorbed by the $\widetilde{dt}_{r,IF}$ parameter.

The scale factor which controls the existence of the geometric range, clock offsets, and tropospheric delay parameters contained within G_r^s is defined in Equation 2.9 for n frequencies.

$$SF_{Geo} = \sum_{j=1}^{n} (\alpha_j + \beta_j) \tag{2.9}$$

Geometry-free combinations are a special case of Equation 2.9 and are formed when coefficient values α_j and β_j satisfy the condition $SF_{Geo} = 0$, if $j > 1$. Therefore, the frequency difference between two measurements of the same type eliminates geometry. The coefficients that simultaneously remove geometry ($SF_{Geo} = 0$) and preserve ionospheric parameters ($SF_{Iono} = 1$) are presented in Equation 2.10 for dual-frequency measurements. Note that the pseudorange coefficients β_1 and β_2 in Equation 2.10 have an opposite sign as the carrier phase coefficients to preserve consistently positive ionospheric parameters.

$$\begin{aligned} &\alpha_1 = +\frac{f_2^2}{f_1^2 - f_2^2};\ \alpha_2 = -\frac{f_2^2}{f_1^2 - f_2^2} \\ &\beta_1 = \alpha_2;\ \beta_2 = \alpha_1 \end{aligned} \tag{2.10}$$

The combined dual-frequency geometry-free pseudorange observable, i.e., $p_{r,GF}^s = \beta_1 \cdot p_{r,1}^s + \beta_2 \cdot p_{r,2}^s$, can be reconstructed by substituting the Equation 2.10 coefficients in Equation 2.4 to obtain:

$$p_{r,GF}^s = I_{r,1}^s + c \cdot b_{r,GF}^s + e_{r,GF}^s \tag{2.11}$$

where $I_{r,1}^s$ denotes the ionospheric absolute propagation delay of the first signal; $b_{r,GF}^s = \beta_1 \cdot b_{r,1}^s + \beta_2 \cdot b_{r,2}^s$ represents the combined hardware bias; and $e_{r,GF}^s = \beta_1 \cdot e_{r,1}^s + \beta_2 \cdot e_{r,2}^s$ denotes the combined measurement noise. The re-parameterization $\tilde{I}_{r,1}^s = I_{r,1}^s + c \cdot b_{r,GF}^s$ allows a single-receiver user to estimate slant ionospheric delays that are biased by geometry-free pseudorange hardware delays. It is worth noting that the IGS routinely provides global ionospheric map (GIM) products that are estimated along with geometry-free DCBs of satellites and reference station receivers.

Linear combinations of raw measurements create observables that have new apparent signal properties, namely, frequency, wavelength and noise. If measurements are assumed to be uncorrelated and have identical errors, then errors propagate as the square-root of the scaled squared sum of individual measurement component errors due to error propagation law. Therefore, the noise properties of combined observables are either amplified or attenuated relative to the original measurements. Thus, the combined stochastic behavior of the ionosphere-free observables in Equations 2.7 and 2.8 is amplified by about three times the original measurement noise, i.e., $\sqrt{\Sigma(\alpha_1^2 + \alpha_2^2)}$, for GPS L1 and L2 signals. Similarly, the geometry-free observable in Equation 2.11 is amplified by approximately 1.7 times the raw measurement noise.

2.2.3 Integer ambiguity resolution

Combinations of individual carrier phase measurements are often referred to as narrow- and wide-lane, depending on respective shorter and longer combined wavelengths relative to the original raw measurements. For example, respective narrow- and wide-lane carrier phase combinations for GPS L1 and L2 measurements have combined wavelengths equal to approximately 11- and 86-cm. Incremental integer ambiguity resolution methods benefit from wide-lane combinations, where it is easier to first resolve a longer wavelength observable's ambiguity as an integer value. Afterward, the solved integer wide-lane ambiguities assist the integer resolution of the shorter wavelength narrow-lane ambiguities.

The cascade from wide- to narrow-lane integer ambiguity resolution is commonly used for PPP-IAR to enable ambiguity-fixed positioning for PPP (i.e., for single-receiver, ionosphere-free) users. This process requires further modifications to the standard PPP model to separate receiver clock offset parameters into code and phase clock components, which removes receiver code bias effects from the ambiguity parameters. In addition, satellite phase bias products estimated by GNSS reference networks must also be included in the PPP-IAR model to restore the wide-lane ambiguities to integer values. The resulting narrow-lane ambiguities can then be de-correlated and solved using the LAMBDA method (Teunissen et al. 1995). Additional details regarding integer ambiguity resolution and the LAMBDA method are provided in Appendix E.

2.2.4 Combined multi-GNSS processing

In the current multi-GNSS environment, positioning and navigation users have access to more than 100 satellites of the combined GPS, GLONASS, Galileo and BeiDou constellations, with signals transmitted across many shared and some unique frequencies. However, these systems were developed and are maintained by various national organizations that use different timing datums. For example, GPS Time (GPST) was synchronized with International Atomic Time (TAI) at the first epoch of Coordinated Universal Time (UTC) in the year 1980 (IS-GPS-200G 2012). Similar synchronizations also formed GLONASST (ICD GLONASS 2008), GST (OS-SIS-ICD 2021) and BDT (BDS-SIS-ICD 2013); the respective reference times used in GLONASS, Galileo and BeiDou systems. These definitions and respective UTC offsets are commonly used to convert multi-GNSS measurements to a consistent system time, such as GPST, with time variations between datums estimated at each epoch.

In addition to timing offsets, GNSS constellations also broadcast satellite positions relative to a variety of Earth-Centered-Earth-Fixed (ECEF) reference frames, where each frame is defined by different geodetic constants, ellipsoid parameters, and reference epochs. The WGS-84, PZ-90, GTRF and BDC/CGCS frames are used for respective GPS, GLONASS, Galileo and BeiDou systems. Transformation parameters enable conversions to various ITRF realizations, with nominal mm-level accuracy, for frames that are not already aligned to the ITRF. Thus, multi-GNSS processing typically uses ITRF coordinates after any necessary transformations are applied to establish a consistent reference frame.

Multi-GNSS positioning with measurements from more than one system in the same model is affected by intra-system and inter-system biases, where “intra” refers to the between-satellite biases within the same system and “inter” refers to between-system biases. Inter-system biases (ISBs) complicate the positioning model due to residual differences in constellation time benchmarks and changes in signal paths inside receivers, resulting in system-dependent hardware delays (Liu et al. 2019). A single receiver clock offset estimated along with daily time-constant ISB parameters is one strategy for multi-GNSS processing (Li et al. 2015). Alternatively, receiver clock offset parameters separated for each system can sufficiently absorb the ISBs (Lou et al. 2016). In the following discussion, the latter strategy is applied.

Therefore, the ionosphere-free pseudorange and carrier phase observables in Equation 2.7 and Equation 2.8 can be rewritten to include multi-GNSS measurements in the form:

$$\begin{aligned} p_{r,IF}^{s,GNSS} &= \rho_r^s + dt_r^{GNSS} + \Sigma\left(m_r^s \cdot T_{W,G_N,G_E}\right) + e_{r,IF}^s \\ \varphi_{r,IF}^{s,GNSS} &= \rho_r^s + dt_r^{GNSS} + \Sigma\left(m_r^s \cdot T_{W,G_N,G_E}\right) + \lambda_{IF}^{GNSS} \cdot \widetilde{N}_{r,IF}^s + \epsilon_{r,IF}^s \end{aligned} \tag{2.12}$$

where $dt_r^{GNSS} = \widetilde{dt}_r + ISB^{(GNSS-GPS)}$ represents system-dependent receiver clock offsets that absorb ISBs relative to GPST in the biased ionosphere-free clock term ($\widetilde{dt}_r$); λ_{IF}^{GNSS} denotes the system-dependent ionosphere-free wavelength, in meters; and all other parameters are identical to previous definitions. Note that the frequency-dependent ionosphere-free coefficients in Equation 2.6 must be evaluated to compute pseudorange and carrier phase measurement scale factors for each Equation 2.12 system.

The multi-GNSS PPP functional model in Equation 2.12 estimates the following unknown parameters: three receiver coordinate components, tropospheric zenith wet delay, two horizontal tropospheric delay gradients, one receiver clock offset for each GNSS constellation and one real-valued (float) ambiguity per satellite. The degrees of freedom (DOF), or redundancy, in Equation 2.12 is computed by differencing the number of estimated unknown parameters, $s + g + 6$, and observations, $s \cdot 2$, at each epoch, where s is the number of satellites and g is the number of GNSS constellations. Therefore, single-GNSS and triple-GNSS processing require at least seven and nine satellites, respectively, to enable per-epoch least-squares solutions. For filter-based estimation typically used in PPP, the dynamic model constraints enable solutions at all epochs, regardless of measurement availability. However, poor model redundancy and satellite geometry can reduce estimated parameter accuracy before ambiguities are precisely estimated, causing poor least-squares-minus-Kalman-filter quality control and terminating the model error detection algorithms.

2.2.5 Model error evaluation and cycle slip detection methods

All carrier phase positioning models presented thus far assume that ambiguity parameters are time-constant and continuous. However, undetected cycle slips introduce biased measurements in the positioning model, while noisy measurements reduce the precision of the estimated parameters. Undetected cycle slips are a major problem for PPP, where the converged solution is tightly constrained to the assumed time-constant ambiguity parameters, estimated using carrier phase measurements at a millimeter noise level. If a cycle slip occurs, then the affected ambiguity is no longer time-constant and must be reinitialized to a new value. Therefore, carrier phase measurement cycle slips are critical model errors that must be addressed to maintain high-accuracy positioning.

The Melbourne-Wübbena wide-lane (MWWL) combination (Melbourne 1985; Wübbena and Hannover 1985) is commonly used to monitor carrier phase cycle slips and is a critical component of model error detection algorithms (Blewitt 1990; Cai et al. 2013; Liu et al. 2011). The dual-frequency MWWL combination is presented in Equation 2.13 as the difference of narrow lane ($\beta_{NL,j}$) pseudorange and wide lane ($\alpha_{WL,j}$) carrier-phase measurements.

$$\alpha_{WL,j} = \frac{f_j}{f_1 - f_2}; \beta_{NL,j} = \frac{f_j}{f_1 + f_2} \tag{2.13}$$

$$o_{MWWL} = [\alpha_{WL,1} \cdot \varphi_1 - \alpha_{WL,2} \cdot \varphi_2] - [\beta_{NL,1} \cdot p_1 + \beta_{NL,2} \cdot p_2]$$

The MWWL combined observable in Equation 2.13 can be expanded using Equation 2.4 to obtain:

$$\begin{aligned} o_{MWWL} &= \lambda_{WL} \cdot N_{WL} + \\ &\lambda_{WL} \cdot (B_1 - B_2) - c \cdot (\beta_{NL,1} \cdot b_1 + \beta_{NL,2} \cdot b_2) + \\ &\alpha_{WL,1} \cdot \epsilon_1 - \alpha_{WL,2} \cdot \epsilon_2 - \beta_{NL,1} \cdot e_1 - \beta_{NL,2} \cdot e_2 \end{aligned} \tag{2.14}$$

where λ_{WL} denotes the wide-lane wavelength and $N_{WL} = N_1 - N_2$ represents the integer wide-lane ambiguity as the difference between ambiguities of individual measurements. It is apparent that o_{MWWL} is indeed both ionosphere- and geometry-free, as related parameters are eliminated by the combination and do not appear in Equation 2.14. Moreover, the MWWL combination in Equation 2.14 simplifies to $o_{MWWL} = N_{MWWL}$, where $N_{MWWL} = \lambda_{WL} \cdot N_{WL} + bias + noise$ is simply the wide-lane ambiguity biased by both carrier-phase and pseudorange hardware delays. Therefore, if hardware biases are assumed to be time-constant over short intervals, then cycle slips that independently affect either N_1 or N_2 create a discontinuity in the N_{MWWL} time-series. Thus o_{MWWL} is a useful cycle slip detection indicator. It is worth noting that o_{MWWL} receives noise contributions from both narrow-lane pseudorange and wide-lane carrier phase components. Thus, the combined noise is mostly controlled by the relatively noisy pseudorange measurements. This is indeed true, even though narrow-lane noise is actually reduced by about 30%, i.e., $\sqrt{\beta_{NL,1}^2 + \beta_{NL,2}^2} = 0.71$, and wide-lane noise is amplified by about 5.7 times, i.e., $\sqrt{\alpha_{WL,1}^2 + \alpha_{WL,2}^2} = 5.74$, for GPS L1 and L2 signal measurements having identical noise properties on each frequency.

The total electron content rate (TECR) is an additional quality control metric that can be used to monitor carrier phase cycle slips. This technique uses the Equation 2.10 coefficients to construct a geometry-free carrier phase observable that contains only the slant ionosphere and the scaled difference between biased dual-frequency ambiguities. This observable uses only precise carrier phase measurements, which results in an extremely precise cycle slip detection metric. If hardware biases are assumed to be time-constant over short intervals, then cycle slips that independently affect either N_1 or N_2 create a discontinuity in the TECR time-series can be used to detect and repair cycle slips (Liu 2011). Furthermore, a second-order time-difference of the phase-based TEC (i.e., rate of TECR) eliminates trends in the TECR time-series, which is especially beneficial during intervals having increased ionospheric activity (Cai et al. 2013). In addition, recursive time-averaging can reduce the MWWL ambiguity noise to further aid cycle slip detection (Cai et al. 2013). Thus, simultaneous monitoring of the MWWL ambiguity and time-differenced TECR combinations can efficiently detect carrier phase cycle slips, uniquely resolve cycles slips on individual signals, and be used to repair carrier phase measurements to improve positioning performance.

Detection-identification-adaptation (DIA) algorithms enable robust detection of model errors by checking if measurement residuals agree with formal errors (Teunissen 1998 and Petovello 2003). In a DIA algorithm, the detection step computes a normalized test statistic t_i for i measurements that can be expressed as

$$t_i = \left| \frac{v_i \cdot P_i^{-1}}{\sqrt{v_i \cdot P_i^{-1}}} \right| \tag{2.15}$$

where v_i represents the measurement residual and P_i denotes the corresponding formal error along the residual variance co-variance matrix diagonal elements. Note that model errors are assumed to follow a zero-mean, Gaussian distribution. Model errors are identified if the test statistic exceeds a pre-defined threshold that is equal to a certain number of standard deviations away from the mean value. Finally, if at least one measurement exceeds the threshold, then the model is adapted by removing the outlier and the estimation is re-processed. For carrier phase measurements, this is typically accomplished by reinitializing the related ambiguity parameter with a large parameter noise value.

2.3 Ionospheric scintillation

This section first presents the characteristics of ionospheric scintillation along with the challenges of positioning under scintillation effects. Typical scintillation environments and geographic locations are discussed, along with the associated degradation of high-accuracy positioning performance. Then mitigation techniques are presented in order to provide details on methods that are later developed in this thesis and used for subsequent multi-GNSS processing.

2.3.1 Characterization

Scintillation of GNSS signals is caused by plasma density irregularities in the ionosphere (Kintner et al. 2001) and is characterized by rapid phase, amplitude and carrier-to-noise density ratio (C/N0) fluctuations of the received signal (Sreeja 2016). The S_4 index given by Briggs and Parkin (1963) in Equation 2.16 characterizes amplitude scintillation levels and is defined as the standard deviation of the received signal power or intensity (I) normalized to its mean value over a 60-second interval:

$$S_4 = \sqrt{\frac{\langle I^2 \rangle - \langle I \rangle^2}{\langle I \rangle^2}} \tag{2.16}$$

where $\langle \cdot \rangle$ denotes the mean operator.

The σ_φ (sigma-phi) index characterizes phase scintillation severity and is defined as the 60-second standard deviation of the received carrier phase detrended using a high pass filter with a fixed 0.1-Hz cut-off frequency to sharpen the high-frequency phase data (Yeh and Chao-Han 1982; Van Dierendonck et al. 1993). These scintillation indices are output by specialized ionospheric scintillation monitoring receivers (ISMRs) and are commonly used to illustrate scintillation conditions, typically classified as weak, moderate and strong (Aquino et al. 2005; Briggs and Parkin 1963; Basu et al. 2002; Sreeja et al. 2011; Spogli et al. 2013; Marques et al. 2018; Veettil et al. 2020). If raw high-frequency (e.g., 50- or 100-Hz) post-correlation in-phase (I) and quadrature (Q) component data are recorded by the receiver and made available, then spectral properties can be estimated at shorter intervals (Guo et al. 2021). Alternatively, if ISMR data are not available, then the rate of total electron content index (ROTI) can effectively represent an approximation of overall scintillation levels (Pi et al. 1997; Juan et al. 2017).

Scintillation occurrence is highly variable both temporally and spatially due to complex interactions between solar radiation and earth's magnetic field (Hunsucker and Hargreaves 2003). On a global scale, scintillation maximums are well-known to occur at high (polar) and low (near equatorial) geomagnetic latitudes (Basu et al. 2002). However, high latitude scintillation is mainly influenced by geomagnetic storms, while strong and frequent post-sunset scintillation is common in the equatorial regions between ±20° geomagnetic latitude due to the Equatorial Ionospheric Anomaly (EIA) (Spogli et al. 2013).

This post-sunset scintillation effect is caused by ionospheric plasma density irregularities produced by interactions between Earth's electric and magnetic fields (Basu et al. 2002). Near Earth's geomagnetic equator, electric and magnetic fields are approximately perpendicular, which causes a "fountain effect" as free electrons move vertically (i.e., perpendicular to the electric and magnetic fields) through the ionosphere and are deposited at approximately ±15-20-degrees geomagnetic latitude regions. For these reasons, polar/auroral scintillation studies usually coincide with specific geomagnetic storm events (Mitchell et al. 2005; De Franceschi et al. 2008; Meggs et al. 2008; Prikryl et al. 2011a; Kinrade et al. 2012), while equatorial studies normally overlap with local times where scintillation is most intense (Spogli et al. 2009; Li et al. 2010; Prikryl et al. 2011b; Veettil et al. 2020).

2.3.2 Effects on GNSS positioning

Strong scintillation is indicated by large values of the aforementioned scintillation metrics, which have been shown to amplify kinematic PPP errors by several orders of magnitude compared to non-scintillation conditions (Pi et al. 2017; Luo et al. 2018; Marques et al. 2018, Guo et al. 2019; Vadakke Veettil et al. 2020). Frequent loss of lock, cycle slips and increased noise accompany strong scintillation conditions due to worse signal tracking performance, especially for the carrier phase (Skone et al. 2001; Doherty et al. 2003; Sreeja et al. 2012). Furthermore, poor satellite geometry can occur if many noisy measurements are removed from the estimation process by model error detection algorithms (Marques et al. 2018). Scintillation effects on modernized GNSS positioning performance were observed and evaluated for the GPS L2C signal (Marques et al. 2016), BeiDou constellation (Luo et al. 2018), and combined GPS+GLONASS (Marques et al. 2018) and GPS+GLONASS+Galileo (Dabove et al. 2020) processing. These studies demonstrated average vertical positioning accuracy of about 20- to 50-cm using multi-GNSS and modernized signals under scintillation. However, strong scintillation conditions can amplify positioning errors to many times larger than the average (i.e., overall) error at an individual epoch. For this reason, it is important to consider the worst-case positioning error in an ionospheric scintillation environment.

2.3.3 Mitigation strategies

Several strategies were developed in recent years to improve scintillation-affected positioning performance. For example, if scintillation is detected by monitoring the dual-frequency slant ionospheric rate (Cai et al. 2013), then the affected satellites can simply be removed from the estimation process until scintillation metrics return to their nominal levels. However, this is not a robust strategy because remaining satellite geometry may suffer and dilute the estimation precision (i.e., DOP amplification). Even if multi-GNSS processing is applied to increase the number of satellites, poor satellite geometry may occur if many satellites are affected by scintillation simultaneously. Lastly, a standard satellite elevation-based stochastic model applied to either single- or multi-GNSS processing may not be realistic when high-elevation satellites are affected by ionospheric scintillation, as satellites observed in the zenith direction are modeled as having the most precise measurements in the elevation-based strategy.

For these reasons, the mitigation of scintillation effects at the receiver tracking loop level or within positioning algorithms is preferred. Receiver tracking improvements were demonstrated using enhanced Kalman filter-based phase lock loop (PLL) tracking algorithms (Humphreys 2005; Susi et al. 2017), assisted by frequency lock loop (FLL) processing (Zhang and Morton 2009) and with *a priori* in-phase filtering (Xu et al. 2015). Scintillation mitigation can also be achieved by using: a scintillation-sensitive stochastic model (Aquino et al. 2009; Silva et al. 2010; Weng et al. 2014); enhanced model error detection and quality control algorithms (Zhang et al. 2014; Luo et al. 2020); regional TEC information with a robust stochastic model (Park et al. 2017); and functional model re-parameterization to absorb scintillation-induced range errors combined with Aquino et al. (2009) and Zhang et al. (2014) methods (Vani et al. 2019).

The modified least squares stochastic model presented in Aquino et al. (2009) and Silva et al. (2010) successfully mitigated high latitude scintillation effects using Conker et al. (2003) receiver tracking error model outputs. This method assumed that phase and amplitude scintillation effects would be adequately represented in the receiver PLL and delay-locked loop (DLL) tracking error variances computed using Conker models. However, this technique is only valid when the scintillation is in the low or moderate level. Strong amplitude scintillation, namely $S_4 > 0.7$, frequently encountered at low latitudes restricts the Conker model output availability due to the model mathematical expression limitation, which originates from an assumption that the amplitude scintillation follows the Nakagami-m (1960) distribution. Therefore, more reliable tracking error models were developed by Moraes et al. (2014) using the α-μ distribution by Yacoub (2007) to extend the tracking error variance computation capabilities. Sreeja et al. (2020) demonstrated improved kinematic PPP horizontal and vertical positioning accuracies using α-μ distribution based tracking error variances in a modified stochastic model under low latitude scintillation conditions. However, the α-μ approach improved 3D positioning errors by 1- to 3-cm relative to the Conker method, in terms of RMS computed over 4-hour intervals affected by strong scintillation. It was reported that this is mainly due to the inaccurate parameter estimation of the α-μ distribution.

Due to the relatively small improvements between stochastic mitigation methods, the Conker model was used as the basis for algorithm development throughout this thesis. The Conker model for the DLL and PLL tracking error variance of respective GPS pseudorange (C/A) and carrier phase signals within the L1 frequency band are:

$$\sigma^2_{DLL,L1} = \frac{B_{DLL} \cdot d \cdot [1 + \left(\eta_{DLL} \cdot SN0 \cdot (1 - 2 \cdot S^2_{4,L1})\right)^{-1}]}{2 \cdot SN0_{L1} \cdot (1 - S^2_{4,L1})} \tag{2.17}$$

$$\sigma^2_{PLL,L1} = \frac{B_{PLL} \cdot \left[1 + \left(2 \cdot \eta_{PLL} \cdot SN0_{L1} \cdot \left(1 - 2 \cdot S^2_{4,L1}\right)\right)^{-1}\right]}{SN0_{L1} \cdot \left(1 - S^2_{4,L1}\right)} + \frac{\pi \cdot T}{k \cdot f_n^{p-1} \cdot \sin\left((2 \cdot k + 1 - p) \cdot \pi \cdot (2 \cdot k)^{-1}\right)} + oscillator\ noise \tag{2.18}$$

where the receiver-specific parameters B_{DLL} and B_{PLL} are respective one-sided DLL and third-order PLL bandwidths, in hertz; d is the correlator spacing, in chips; $SN0 = 10^{0.1 \cdot (C/N0)}$ is the fractional signal-to-noise density ratio that uses the ratio of the received signal power to the noise threshold $C/N0$; η_{DLL} and η_{PLL} are respective DLL and PLL pre-detection integration times, in seconds; S_4 is the signal-dependent amplitude scintillation index; T is the 1-Hz phase noise spectral strength; p is the phase power spectral density (PSD) slope; k is the PLL loop order; and finally, f_n is the PLL natural frequency, in hertz. In the case of ISMR data, the scintillation parameters in Equations 2.17 and 2.18 are estimated internally by the 50- or 100-Hz raw data and are reported in output files. In addition, receiver tracking loop parameters can be assumed or provided from receiver manufacturer specifications. It can be observed in Equation 2.18 that the PLL variance is the summation of scintillation error, thermal noise, and oscillator noise components.

The respective chips- and radians-squared base units of $\sigma^2_{DLL,L1}$ and $\sigma^2_{PLL,L1}$ converted to units of meters and cycles are:

$$\sigma_{DLL,L1}(meters) = \sqrt{\sigma^2_{DLL,L1}} \cdot F_{DLL,L1} \tag{2.19}$$

$$\sigma_{PLL,L1}(cycles) = \sqrt{\sigma^2_{PLL,L1}} \cdot F_{PLL}$$

where $F_{DLL,L1} = 293.0523$ meters per chip for GPS L1C/A; and $F_{PLL} = (2 \cdot \pi)^{-1}$ cycles per radian for carrier phase signals. Therefore, the units in Equation 2.19 are consistent with pseudorange and carrier phase measurements and can be used to form a modified stochastic model, as recommended by Aquino et al. (2009).

2.4 Atmospheric delays and mitigation

High-accuracy GNSS positioning separates atmospheric error components into tropospheric and ionospheric categories. In general, *a priori* measurement corrections from advanced modelling outputs can be applied to reduce the receiver-satellite line-of-sight range effects. This section presents the methods and challenges involved in generating and using atmospheric corrections for high-accuracy GNSS positioning.

2.4.1 Troposphere error modelling and correction

Tropospheric delays can typically cause meter-level range biases for GNSS measurements in the zenith direction, with effects amplified up to tens of meters in slant directions. Therefore, tropospheric effects are a major constituent of the overall GNSS error budget and must be modelled, estimated or corrected to achieve high-accuracy positioning. Fortunately, the hydrostatic (or dry) tropospheric delay component can be accurately modelled to remove about 90% of the total effect (Saastamoinen 1972; Leandro et al. 2006). The remaining wet tropospheric delay depends on atmospheric water vapor and is difficult to model due to high spatial and temporal variability. For this reason, wet tropospheric delay is typically estimated in the zenith direction, then scaled by elevation-dependent mapping functions that convert from the zenith to slant directions (Niell 1996). These mapping functions are symmetrical for an individual receiver and therefore assume identical azimuthal behaviour for satellites at a constant elevation angle.

Asymmetrical tropospheric conditions become more evident during severe weather events that are accompanied by rapid changes in atmospheric water vapor, e.g., heavy rainfall due to storms or typhoons (Ma and Verhagen 2021). Therefore, precise positioning applications are recommended to estimate azimuthal-dependent horizontal gradients along with the standard zenith wet delay parameter (Bar-Sever et al. 1998). Horizontal linear models that separate the tropospheric asymmetry in to north-south and west-east gradients (Chen and Herring 1997) tend to have worse performance under abnormal tropospheric conditions (Douša et al. 2016; Masoumi et al. 2017). Therefore, severe weather events, especially with asymmetrical tropospheric conditions, may threaten high-accuracy GNSS positioning applications.

Furthermore, Ma et al. 2021 demonstrated in simulation that inadequate tropospheric modelling resulted in worse PPP integer ambiguity resolution success rates during storm events.

2.4.2 Ionospheric error modelling and estimation

Although the well-known ionosphere-free linear combinations in Equation 2.7 and Equation 2.18 mathematically eliminates the first-order ionospheric delay, the combined measurement noise is amplified. Furthermore, the ionosphere-free functional model eliminates 99.9% of the ionospheric delay along the receiver-satellite path (Hoque and Jakowsi 2008), which may be important for applications such as atmospheric monitoring. Fortunately, some GNSS network analysis centers estimate ionospheric information and provide gridded data products to users. These products are then made available as either Global Ionospheric Map (GIM) or Regional Ionospheric Map (RIM) data sets depending on the spatial density of the underlying GNSS reference network. The most common GIM product is provided by the IGS which combines the independent output GIM products from various analysis centers (Hernández-Pajares et al. 2009). However, it is preferred to use all external data products from the same provider to eliminate inconsistencies that may arise.

Regardless of the extents covered, both the RIM and GIM maps typically contain vertical TEC (VTEC) values and corresponding uncertainty at uniform time intervals and regular spatial resolution. The VTEC data provided to users normally originates from slant TEC (STEC) that is estimated by a GNSS reference station network. Then, STEC is projected to vertical using a mapping function that models the ionospheric effect at the height of a representative layer, or layers, within the atmosphere (Mannucci et al. 1998). However, the STEC estimation is non-trivial and commonly uses the Equation 2.11 geometry-free combination that enables biased estimation of the slant ionospheric delay for a single, dual-frequency receiver. The re-parameterization of the ionospheric parameter in Equation 2.11 contains both the original absolute satellite and receiver hardware delays in Equation 2.2 and measurement bias terms. Carrier phase measurements are also affected by unknown ambiguity parameters. Therefore, a so-called ‘carrier to code levelling’ process is often used to assimilate pseudorange and carrier phase measurements in the same functional model (Ciraolo et al. 2007). In this approach, the mean difference between geometry-free pseudorange and carrier phase measurements is estimated for each continuous arc of an observed satellite. The resulting high-precision geometry-free carrier phase observable can then be levelled (e.g., offset removed) to create a theoretically unbiased slant ionospheric parameter.

As shown by Park et al. (2017), RIM data can offer better spatial and temporal resolutions and can improve relative (i.e., double-differenced) positioning performance when compared with conventional GIM processing. Although post-processing was used by Park et al. (2017), forecasted TEC, on the order of seconds to minutes, has been developed to enable real-time ionosphere-corrected positioning applications (Grzesiak et al. 2018). However, forecast quality worsens during the post-sunset hours at low latitudes due to increased ionospheric temporal variation. Furthermore, ionospheric corrections are considered primarily in relative positioning studies (Paziewski and Sieradzki 2020), while single-receiver techniques such as PPP are often overlooked. For example, the spatial and temporal variation of the ionospheric delay could be used to enhance the measurement stochastic model (Luo et al. 2022). Therefore, one aim of this thesis is to demonstrate positioning improvements by incorporating standard GIM and custom RIM data in a single-receiver PPP model.

2.5 Methods and innovations developed in this thesis

In this thesis, single- and multi-GNSS algorithms and processing methods were developed to improve kinematic PPP performance. In particular, multi-GNSS PPP was evaluated under ionospheric scintillation, with and without the mitigation strategies applied. New methods to enable mitigated processing for a non-specialized receiver affected by strong ionospheric scintillation is shown to improve worst-case positioning errors. Additional methods were developed to provide external information to process troposphere-corrected and ionosphere-weighted PPP. The innovative troposphere-corrected methods include a fully stochastic approach, where network-estimated tropospheric corrections and correction precisions are used to improve kinematic PPP performance during a storm event. The new ionosphere-weighted technique successfully uses GIM data in a modified stochastic model to improve low-latitude kinematic PPP performance, especially for the worst-case error epochs.

2.5.1 Multi-GNSS ionospheric scintillation mitigation

Ionospheric scintillation threatens high-accuracy GNSS applications and exacerbates positioning challenges at high and low latitudes and during space weather events (Pi et al. 2017; Luo et al. 2018; Marques et al. 2018, Guo et al. 2019; Vadakke Veettil et al. 2020). In Section 4, multi-GNSS combinations of GPS, GLONASS and Galileo were processed and evaluated under low latitude ionospheric scintillation conditions. Then, the Conker et al. (2003) model for the GPS L1C/A DLL and PLL that were originally developed for GPS signals were extended to multi-GNSS processing. The resulting multi-GNSS tracking error variances were then used in a more realistic stochastic model, following a modified approach of Aquino et al. (2009).

2.5.2 Ionosphere-weighted positioning

Harsh ionospheric conditions are frequently encountered at low latitudes due to regular occurrences of strong TEC gradients. In Section 5, a PPP model is developed using ionospheric-weighted GNSS measurements that rely on GIM and RIM data products as inputs to a modified stochastic model. Low latitude GNSS observations are processed and evaluated using both a standard satellite-elevation-based weighting and the modified approach to improve PPP performance under highly active ionospheric conditions. The results presented herein were developed in collaboration with Juliana Garrido Damaceno of the Istituto Nazionale di Geofisica e Vulcanologia (INGV) of the TREASURE project, who generated the RIM that is used as an external input to the positioning model.

2.5.3 Troposphere-corrected positioning

For high accuracy GNSS positioning, the troposphere is typically separated into dry and wet components, with horizontal gradients also optionally estimated. After the dry delay is modelled, the remaining zenith wet delay and gradient parameters are typically estimated using tight constraints. Although this strategy is reasonable under normal conditions, weather events require an updated processing method that accommodates rapid changes in the wet delay. In Section 5, external troposphere corrections and correction precisions are estimated by a GNSS reference network and made available to PPP users. Then, the *a priori* tropospheric wet delay information is applied and positioning performance is evaluated using deterministic, partially stochastic, and fully stochastic corrections. The results presented herein were developed in collaboration with Hongyang Ma of Delft University of Technology, as part of the TREASURE project, who interpolated the precise corrections at the user station locations.

2.6 Summary

This chapter first reviews the state-of-the-art methods for single-receiver positioning, namely the PPP functional model, linear measurement combinations and model error detection algorithms. Ionospheric scintillation is presented along with the effects on high accuracy positioning and mitigation strategies. Positioning methods that use external atmospheric delays are introduced, namely strategies that include tropospheric correction and ionospheric weighting for high-accuracy processing. Finally, an overview of the methods developed throughout this thesis is given.

Chapter 3

POINT Software

3.1 Introduction

The Position Orientation INTegration (POINT) software was originally developed for positioning and attitude determination using low-cost GPS and inertial sensors (Hide et al. 2007). POINT was developed using the object-oriented C++ programming language and contains many processing modules. Over the past decade, various researchers at the University of Nottingham have developed the POINT software for processing single- and multi-constellation GNSS measurements in a PPP configuration. Although other modules exist, the algorithms in this thesis were developed in the POINT PPP processing framework. The program is capable of processing multi-frequency, multi-constellation RINEX observation files and is based on Kalman filter processing. Version control for the program is done using an online GitLab repository. As is the case for other GNSS measurement processing engines, external products are required to use as inputs to the complex error models needed to resolve a user position.

This chapter begins with a brief description of the main features of the POINT software. Then, the estimation filter is described in detail to relate measured pseudorange and carrier phase observations to unknown parameter states. Afterward, the default POINT software performance is presented to demonstrate achievable positioning results under ideal conditions. Finally, the contributions developed for this thesis are presented.

3.2 Overview of main features

The source code for POINT is available in a private online repository hosted by GitLab (via https://gitlab.com/DfAC/POINT); a version control tool which automatically tracks code changes among project collaborators. This thesis contributed manuals and documentation to configure GitLab and link the POINT project to a local computer. The release version of POINT is protected by the project manager inside the master branch, while all other developers contribute to POINT in separate branches and later merge changes to the master branch. Because this online version control allows easy access to source code files for GitLab users that have been granted access, the changes to POINT developed in this thesis can be used by other researchers in the future.

The POINT software overview in Figure 3.1 depicts the external products introduced in Sections 1.2.1 and 1.2.2 as inputs to the PPP processing of GNSS observations contained within an input RINEX file at a single epoch. After inputs are stored and a user-defined configuration file is read, a least-squares estimation is carried out using ionosphere-free least squares to find an approximate receiver position and receiver clock offset. The estimated position is used to compute initial receiver-satellite unit vectors (i.e., geometry) that enable the application of *a priori* measurement corrections in the following step. For example, the receiver and satellite PCV corrections are functions of receiver-satellite geometry, while some measurement weighting strategies are functions of respective satellite elevation angles. Next, measurement uncertainties are computed using the modeled measurement noise and are propagated using user-defined linear combination coefficients. The next step in POINT is to estimate unknown parameter states, including positioning components, using a Kalman filter that links the functional measurement model to a time-dynamic model of the estimated states. Finally, at each epoch, POINT outputs the estimated parameter states and covariance, pre- and post-fit measurement residuals, model error detection results and other log files. The middle and right columns in Figure 3.1 are repeated for each epoch of the input RINEX file to refine the estimated states.

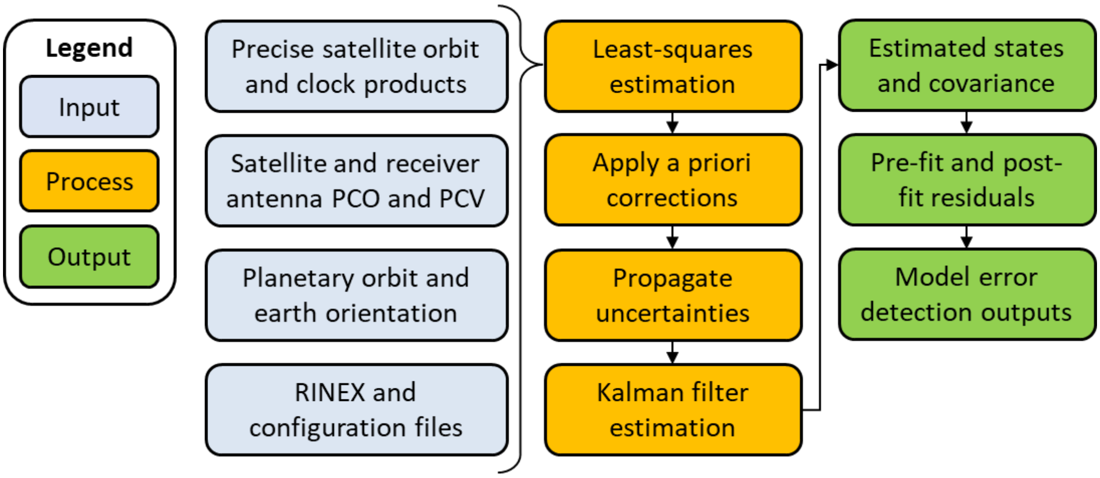

Figure 3.1. POINT software overview for PPP processing at a single measurement epoch, organized by inputs (left column), processing (middle column), and outputs (right column).

3.3 Kalman filter implementation

The Kalman (1960) filter (see Welch and Bishop 1995) was described by Levy (1997) as “navigation’s integration workhorse”. Although this description normally applies to inertial navigation systems (INS) that use GNSS-aided inertial measurement unit (IMU) devices, a model that uses only GNSS measurements can also benefit from Kalman filtering. In this GNSS-only case, the Kalman filter optimally integrates pseudorange and carrier phase measurements using *a priori* information regarding unknown parameter states, namely the carrier phase ambiguities and positioning components. The Kalman filter process is summarized in Figure 3.2, where initial state and covariance estimates are required to pre-populate the filter. Afterward, a time update predicts state and covariance estimates forward in time. Then predications are corrected using measurements at a given epoch. The prediction-correction cycle is repeated at the next epoch, where new measurements are available, to output optimal estimates of unknown parameter states and covariance. In the POINT software, a Kalman filter is implemented following Figure 3.2 to integrate GNSS measurements for PPP processing.

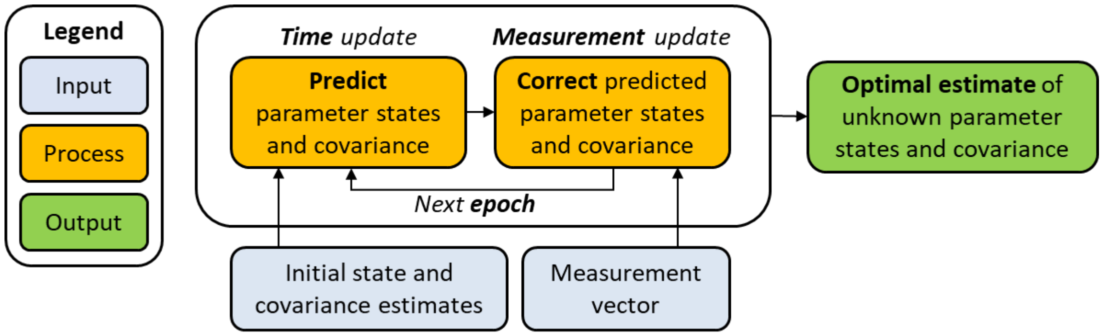

Figure 3.2. Overview of the Kalman filter algorithm, characterized by time updates (predictions) and measurement updates (corrections) to estimate optimal unknown parameter states and covariance, organized by inputs (bottom row), processing (center box), and outputs (right box).

The Kalman filter first requires that initial estimated unknown parameter states and associated covariances are configured in the state vector $\hat{x}_0$ and covariance P_0 matrix. In POINT, initialization of the state vector ($\hat{x}_0$) is done using ionosphere-free least squares estimation of pseudorange measurements at the first epoch. The block-diagonal initial covariance matrix (P_0) is populated by the Table 3.1 default initial uncertainty values. One receiver clock offset parameter is included in the functional model for each system, with each initialized using large uncertainty values, as the receiver clock is assumed to be low-quality compared to the atomic clocks used by GNSS satellites. Ambiguity parameters are also initialized with large initial uncertainties because the pseudorange-based state vector initialization excludes carrier phase measurements and because ambiguities are difficult to estimate precisely until accumulated carrier phase measurements are available.

After initialization, parameter states $\hat{x}_k^-$ and covariances P_k^- are predicted at epoch k using the state transition matrix Φ_k and process noise Q_{k-1} (i.e., process uncertainty) in Equation 3.1.

$$\begin{aligned} \hat{x}_k^- &= \Phi_k \cdot \hat{x}_{k-1}^+ \\ P_k^- &= \Phi_k \cdot P_{k-1}^+ \cdot \Phi_k^T + Q_{k-1} \end{aligned} \tag{3.1}$$

At this stage, and for remaining PPP processing without inertial measurements or other navigation sensors, the state transition matrix Φ is an identity matrix. The process uncertainty matrix Q is block-diagonal with entries at elements corresponding to the Table 3.1 process uncertainty values. Note that the 60-second GNSS measurement processing used throughout this thesis simplifies the Table 3.1 process uncertainty units to meters-squared per minute.

The values contained within the process uncertainty matrix (Q) control how the estimated unknown parameters evolve over time. For example, in kinematic PPP, where the receiver is not stationary, the estimated three-dimensional positioning components do not have time constraints, i.e., $Q_{X,Y,Z} \approx \infty$, while static processing completely constrains the positioning components, i.e., $Q_{X,Y,Z} = 0$. Thus, kinematic PPP is independent of previously estimated positioning components, while static PPP accumulates upon the previous position estimation. In other words, positioning components estimated using kinematic and static configurations are respectively unlinked and linked in the time domain. Ambiguity parameters are modelled as time-constant, unless a cycle slip is detected, in which case the associated ambiguity is reinitialized with a large process uncertainty value. Estimated tropospheric components related to the zenith wet delay and horizontal gradients are tightly constrained in time because the atmospheric water vapor and asymmetry effects are assumed to be quite stable over short time periods.

Table 3.1. Default values for initial and process uncertainties of the ionosphere-free PPP functional model in the POINT software.

Functional model component	Description	Initial uncertainty [m]	Process uncertainty [m^2/epoch]
Position	3D receiver position (X, Y, Z)	$1{\cdot}10^3$	$1{\cdot}10^{10}$ for kinematic 0 for static
Receiver clock offset	Clock error of the receiver with respect to GPS time	$1{\cdot}10^5$	$1{\cdot}10^5$
Troposphere	Tropospheric zenith wet delay	1	$1{\cdot}10^{-5}$
Troposphere gradients	Tropospheric horizontal (north, east) gradient components	0	$3{\cdot}10^{-6}$
Carrier phase ambiguities	Ambiguity parameters for carrier phase observations	$1{\cdot}10^5$	0 without cycle slip $1{\cdot}10^5$ with cycle slip
Ionosphere	Eliminated by ionosphere-free combination	-	-

The next step of the Kalman filter algorithm is to compute the Kalman gain K_k, which optimally controls the weight given to measurements and predicted state parameters. This innovative intermediate step links the time-dynamic and measurement models and directs the filter solution either toward or away from predictions or measurements. For details on the derivation of K_k, readers are directed to the excellent summary by Welch and Bishop (1995). In short, the Kalman gain derivation aims to weight the measurement and dynamic model components to minimize the *a posteriori* error covariance.

$$K_k = P_k^- \cdot H_k^T \cdot (H_k \cdot P_k^- \cdot H_k^T + R_k)^{-1} \tag{3.2}$$

The new parameters in Equation 3.2 are related to the measurement model, where H_k is the design matrix and is populated by the PPP functional model coefficients (columns) for each measurement (rows); and R_k is a diagonal matrix containing the variance of the measurement noise. The elements of R_k are computed at each epoch using modelled measurement noise values, typically set to 30-100-cm and 2-5-mm for respective code and carrier phase measurements in the zenith direction. Sinusoidal amplification of R_k elements is then applied using satellite elevation angle in what is commonly named an elevation-based stochastic model. In the POINT software, and throughout the following sections, R_k contains the propagated measurement uncertainties computed using Equations 2.7 and 2.8 for ionosphere-free combinations of dual-frequency GNSS measurements amplified by a sinusoidal satellite elevation-based scale factor (Mohammed 2017).

After the prediction (Equation 3.1) and Kalman gain (Equation 3.2) steps are complete, the corrected parameters in the $\hat{x}_k^+$ state vector are estimated using Equation 3.3, where observed measurements z_k and measurement predictions $H_k \cdot \hat{x}_k^-$ from the dynamic model are optimally combined using the Kalman gain. The difference $z_k - H_k \cdot \hat{x}_k^-$ in Equation 3.3 is the measurement innovation, or pre-fit residuals, which reflects the discrepancy between observed and predicted (computed) measurements. In comparison, post-fit residuals are expressed as $z_k - H_k \cdot \hat{x}_k^+$ and are typically computed after Equation 3.3 to assess the overall internal agreement between the measurements and model.

$$\hat{x}_k^+ = \hat{x}_k^- + K_k \cdot (z_k - H_k \cdot \hat{x}_k^-) \tag{3.3}$$

The final step of a single Kalman filter iteration is shown in Equation 3.4, where the corrected unknown parameter covariance P_k^+ is estimated and used in Equation 3.1 at the next epoch. In Equation 3.4, the predicted covariance P_k^- is propagated using the design matrix H_k and Kalman gain K_k. The corrected covariance P_k^+ is computed as the difference between the predicted and propagated covariance. Note that because the Kalman filter is designed to minimize the covariance, the values in P_k^+ tend to approach zero after a sufficient number of epochs are processed and, if no model errors are encountered, unknown parameter estimation becomes more precise over time.

$$\begin{aligned} P_k^+ &= P_k^- - K_k \cdot H_k \cdot P_k^- \\ &= (I - K_k \cdot H_k) \cdot P_k^- \end{aligned} \tag{3.4}$$

The standard Kalman filter estimates the state of linear discrete-time processes, i.e., $z_k - H_k \cdot \hat{x}_k^-$. However, in many applications a non-linear relationship exists between estimated states and measurements. Therefore, the POINT software uses an Extended Kalman filter (EKF), where state and measurement vectors are linearized about respective current mean values. The linearization process given in Equation 3.5 is analogous to a Taylor series expansion that uses non-linear functions f and h to respectively relate approximate states ($\tilde{x}_k$) and measurements ($\tilde{z}_k$) to actual values. The corresponding state transition (Φ) and design (H) matrices then become Jacobian matrices and contain partial derivatives of the respective non-linear functions.

$$\begin{aligned} \tilde{x}_k &= f(\hat{x}_{k-1}) \\ z_k &= h(\tilde{x}_k) \end{aligned} \tag{3.5}$$

In the Equation 3.5 linearized form, the measurement update to compute corrected state estimates in Equation 3.3 replaces $z_k - H_k \cdot \hat{x}_k^-$ with $z_k - \hat{z}_k$, which represents observed-minus-computed measurements. After linearization, the standard Kalman filter equations become usable for a non-linear model, as is the case for the PPP model.

Note that while the measurement uncertainty R_k approaches zero in Equation 3.2, the unknown parameter estimation in Equation 3.3 becomes more heavily weighted by the measurements. Conversely, while the estimated parameter uncertainty approaches zero, the dynamic model predictions in Equation 3.3 begin to outweigh measurements. For these reasons, PPP is affected by an initial convergence time of the estimated positioning error components where relatively noisy pseudorange measurements contribute more towards the position estimation in the initial epochs of processing. During this convergence, ambiguity parameters become progressively more precise due to the associated extremely precise carrier phase measurements and process uncertainty time constraints. The PPP model is informed of the carrier phase precision by configuring a low noise (i.e., large weight) relative to the pseudorange measurements. After a certain convergence period, which is typically 30- to 60-minutes, the precise ambiguity estimates cause the parameter covariance to approach zero and the dynamic model predictions begin to control the solution. In this case, the converged solution becomes almost entirely controlled by the carrier phase measurements due to the nearly infinite precision of the time-constant estimated ambiguities.

3.4 Default software performance and configuration

The achievable performance for POINT PPP processing is presented in this section to demonstrate the nominal accuracy and precision that can be obtained under ideal conditions using both kinematic and static configurations. Performance evaluations also establish that implementations of *a priori* error models and estimation procedures within POINT are accurate and are suitable for PPP processing.

Prior to processing and evaluation, the POINT software must be configured to process GNSS measurements using the implemented models and estimation strategies. The default POINT software configuration for GPS-only processing presented in Table 3.2 is used throughout this thesis unless otherwise noted.

The settings in Table 3.2 were used to process 8 hours of dual-frequency GPS L1 and L2 pseudorange and carrier phase measurements for station PPTE using static PPP mode. Although this station is located near the equator, the atmospheric conditions at the time of observation were relatively calm. Positioning errors were evaluated against the estimated position at the final epoch of a 24-hour static processing session output from the Canadian online PPP tool (CSRS-PPP) as reference. Therefore, small position errors indicate that the POINT outputs and processing strategies are consistent with an alternative publicly available software. The horizontal and vertical positioning component time series in Figure 3.3 shows that all positioning components converge to and remain below 5-cm error after 18 minutes of processing. Positioning accuracy and precision are respectively represented by the mean and standard deviation of the Figure 3.3 time-series. These values were computed after one hour of processing to exclude the large errors that occur before convergence is achieved. In the static PPP case, all positioning components achieve 1- to 9-mm accuracy and precision, apart from a slightly worse 1.9-cm vertical accuracy.

Table 3.2. Default POINT software configurations and estimation strategies for GPS-only PPP processing.

GNSS processing	Configurations/strategies
Constellation: signals	GPS: L1P, L2P
Functional model	Ionosphere-free combination
Measurement rate	60-sec
Elevation cutoff threshold	10-deg
Estimation process	Extended Kalman filter
Measurement weighting	Elevation based (see Mohammed 2017)
Satellite/receiver antenna corrections	PCO/PCV corrections: igs14_2108.atx
Satellite orbit and clock	IGS MGEX CODE products
Differential code bias	CODE P1C1 DCB product, if L1P not available
Receiver clock	Estimated as white noise
Receiver coordinates	Kinematic: white noise Static: time-constant
Zenith dry troposphere	A-priori Saastamoinen (1972) model using UNB3 mapping function (Leandro et al. 2006)
Zenith wet troposphere	Estimated as random walk using UNB3 mapping function
Azimuthal wet troposphere	Gradients estimated with Chen and Herring (1997) model
A priori pseudorange precision	L1P/L2P: 1.0/1.0 meters
A priori carrier phase precision	L1/L2: 0.03/0.03 cycles
Additional corrections applied	Phase windup; solid earth tide; polar tides; shapiro delay
Model error detection	MWWL and TECR cycle slip detection and DIA algorithm (Blewitt 1990; Cai et al. 2013)
Carrier phase ambiguities	Float (non-integer)

The same data were then re-processed using a kinematic configuration, where the estimated positioning parameters were not constrained in time with all other settings identical to the static processing configuration. The kinematic positioning error time-series in Figure 3.4 shows that an initial convergence time to reach below 10-cm positioning error is reasonable threshold to use for kinematic processing in POINT. In this case, the initial horizontal positioning errors reach and remain below 10-cm after 48 minutes of processing. It is important to note that the same number of parameters are estimated in both static and kinematic configurations. However, Figure 3.4 shows that the estimated position is less precise using kinematic mode due to fewer constraints applied to the estimated parameters. Indeed, the mm-level static processing precision in Figure 3.3 increases up to 5.6-cm using kinematic settings and appears as increased noise in the positioning error time-series. Although the kinematic configuration time-series exhibits more noise, the mean positioning error is approximately cm-level for kinematic processing, indicating that the estimated positioning components are free from any large or persistent biases.

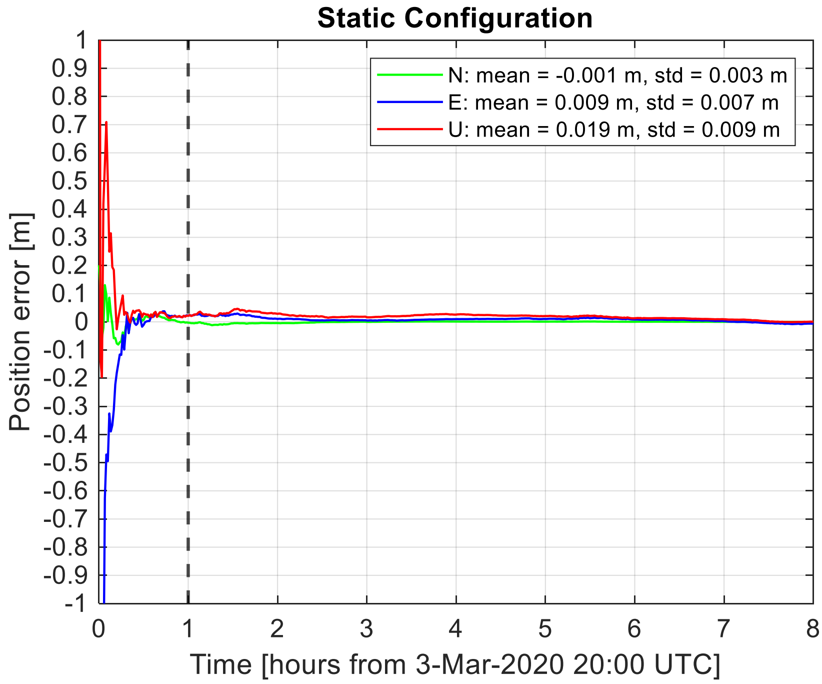

Figure 3.3. Achievable north (green), east (blue), and up (red) positioning error components using the standard static PPP configuration in the POINT software.

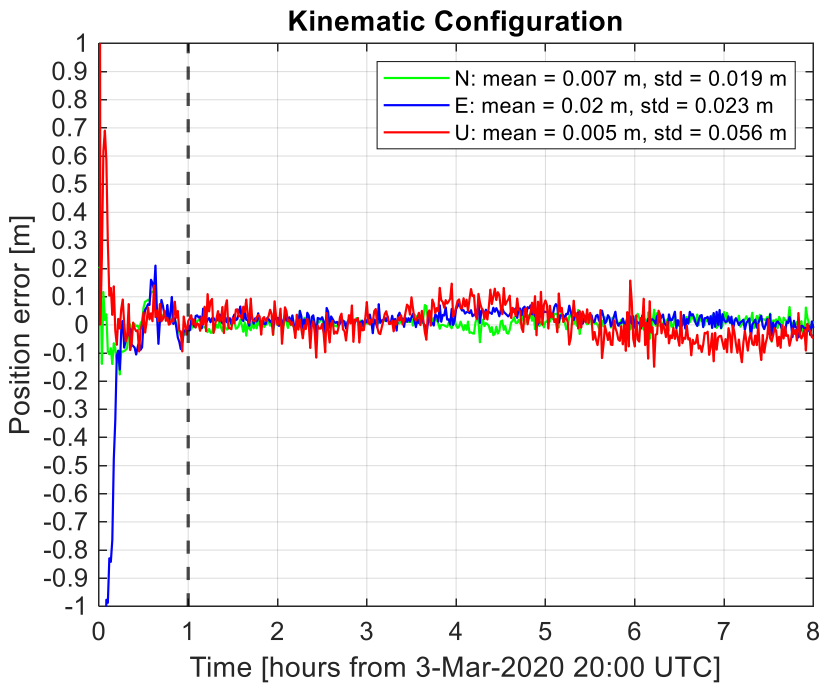

Figure 3.4. Achievable north (green), east (blue), and up (red) positioning error components using the standard kinematic PPP configuration in the POINT software.

Post-fit measurement residuals indicate the internal model agreement between the observed and computed measurements. Pseudorange residuals are shown in Figure 3.5 for kinematic processing corresponding to the Figure 3.4 time-series. The non-zero mean value indicates that a small bias exists between the measurement and dynamic models. However, this bias only affects the model before initial convergence is achieved, prior to the precise estimation of the ambiguity parameters. If the model is accurate, as indicated by the excellent Figure 3.3 and Figure 3.4 positioning error performance, then the meter-level standard deviation represents the overall propagated pseudorange noise for all satellites. Note that the Figure 3.5 post-fit measurement residuals are for satellites from 10-degrees in elevation to zenith. Thus, Figure 3.5 shows the overall measurement precision, in terms of measurement-model agreement, for a variety of measurement qualities.

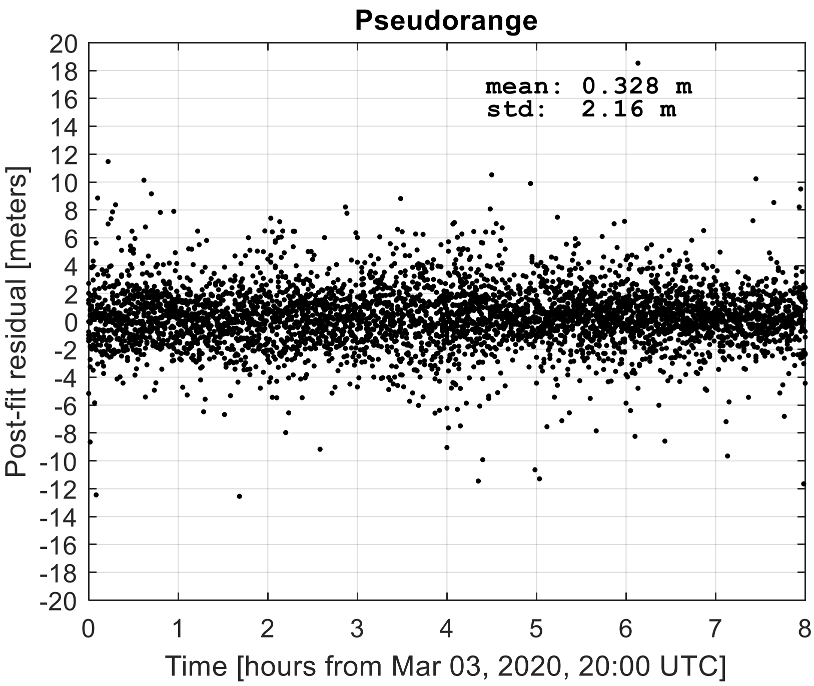

Figure 3.5. Kinematic PPP pseudorange measurement post-fit residuals for 8-hours of GPS L1 and L2 processing at station PPTE under nominally ideal conditions.

Carrier phase residuals shown in Figure 3.6 for kinematic processing have an approximate zero mean value. This indicates excellent agreement between the measurement and dynamic models due to the low *a priori* carrier phase noise and time-constrained ambiguity parameters. The 0.08-cycle (e.g., 1.1-cm for GPS L1) standard deviation represents the overall propagated carrier phase noise for all satellites during the observation interval. Note that the y-axis limit of Figure 3.6 converted from units of cycles to meters is equal to ±14-cm. This range is more than

100-times smaller than the corresponding pseudorange post-fit residual axis scale in Figure 3.5, demonstrating the far superior noise properties of the carrier phase measurements.

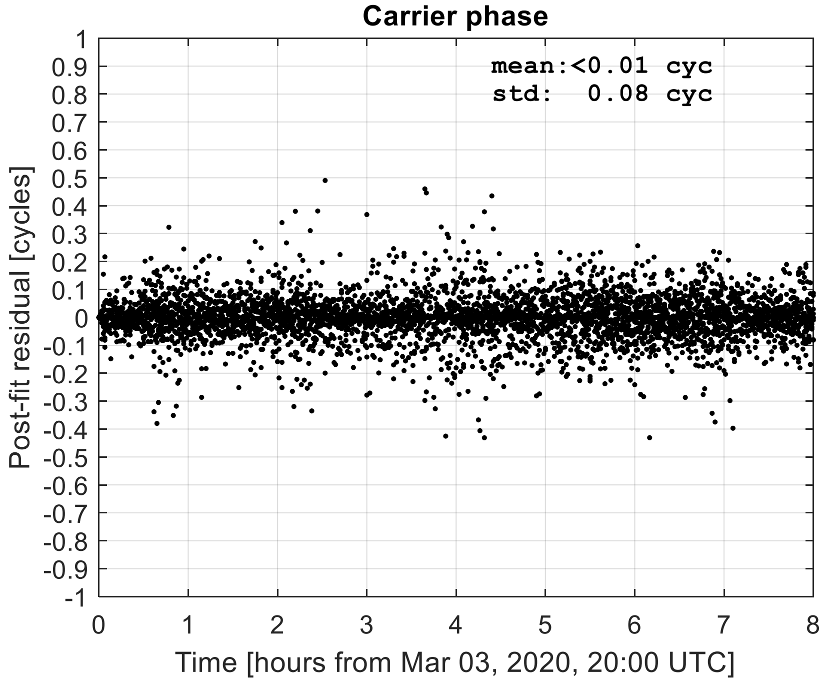

Figure 3.6. Kinematic PPP carrier phase measurement post-fit residuals for 8-hours of GPS L1 and L2 processing at station PPTE under nominally ideal conditions.

3.5 Software contributions for this thesis

Although many GNSS processing engines exist and are freely available, the University of Nottingham version of the POINT software was developed and used since October of 2017, at the start of the TREASURE project (see Appendix B for details), to process GNSS data and generate the results presented in this thesis. During this period of study, new processing capabilities were implemented and bugs were fixed in the POINT software. These additions and improvements are summarized by the following:

- **New scintillation-sensitive stochastic model.** Developed and implemented scintillation-sensitive measurement weighting using modified Conker et al. (2003) tracking error model outputs following the Aquino et al. (2009) approach. The new stochastic model was implemented for multi-GNSS processing and was enabled for GPS, GLONASS and Galileo measurements.

- **Troposphere-corrected PPP.** Developed and implemented *a priori* measurement corrections for external tropospheric data. Existing methods to import measurement corrections were updated to include zenith tropospheric delay correction information and correction precision. New processing options and corresponding implementations enabled tropospheric-corrected PPP using correction precisions in the dynamic model as process noise values.
- **Ionosphere-weighted PPP.** Implemented regional ionospheric map (RIM) correction processing for ionosphere-corrected PPP. Existing GIM methods were used and updated for RIM processing. For example, a new method was implemented so that if an ionospheric pierce point is outside the RIM extents, then the satellite is removed (i.e., corrections are not available) from the affected epoch. This was not previously available for GIM processing, as ionospheric corrections are available for nearly all locations globally.
- **Model error detection.** Implemented separate thresholds that allow either more or less strict outlier detection depending on if a measurement is a pseudorange or carrier phase. Furthermore, a new method was developed that allows more than one outlier to be rejected in the DIA algorithm before issuing a complete ambiguity reset. Prior to this development, complete ambiguity re-initializations were frequent in any epoch with more than one satellite identified as having a bad ambiguity value.
- **Dynamic stochastic model.** Created a new processing option to replace missing tracking jitter values with other weighting functions, per satellite or per epoch. Otherwise, tracking error model output outages would remove measurements from the affected satellite and significantly reduce the measurement availability and thus the positioning performance.
- **Galileo processing.** Corrected an error where up to approximately 17% of the total available Galileo satellites were excluded from processing. This was due to an error in the implementation of a POINT measurement class derived from GPS measurement processing. Additionally, approximate satellite and receiver PCO/PCV corrections were enabled for the Galileo constellation by using GPS corrections as a replacement while antenna calibrations for

Galileo are underway. The same strategy was implemented for GLONASS processing when antenna corrections were found to be unavailable.

- **Satellite products.** Implemented RINEX version 3.04 (http://acc.igs.org/misc/rinex304.pdf) satellite clock products. This enhancement replaced the previous limited capabilities of RINEX version 2.00 satellite clock files that restricted processing in POINT to before the year 2020.
- **MWWL estimation.** Implemented a pseudo-observation of the MWWL ambiguity as an estimated state parameter. This strategy enabled better monitoring of the MWWL ambiguities and a systematic approach to check for cycle slips in a multi-GNSS environment. However, the additional MWWL observable is a linear combination of input measurements and therefore does not contribute any new information to the estimation process.
- **Output files for analysis.** Implemented new logging files that write output data to describe the status/properties of new algorithms. For example, the propagated measurement uncertainties at each epoch for each satellite are output, along with the stochastic modeling method and model error detection statuses. Also, errors that occur while parsing measurements were removed from the general log file and are stored in a separate file, if enabled in the input configuration file. Furthermore, many new output files were implemented to monitor the health of carrier phase ambiguities.
- **Instructions to compile POINT.** Developed instruction manuals to compile the POINT software and uploaded documents to the online repository. For new researchers that are not familiar with POINT, a step-by-step guide on how to configure the development environment is essential.

3.5.1 Scintillation mitigated stochastic model

The scintillation mitigation strategy is implemented in POINT according to the Figure 3.7 pseudocode. In this framework, tracking error model outputs (i.e., tracking jitter in Equation 2.19) represents the uncertainty of measurements from each satellite and at each epoch. Furthermore, because measurement uncertainties are computed outside the POINT software, new methods were implemented to read an external data file that is queried for each measurement following the Figure 3.7

sequence. If an external uncertainty value is not available, and the dynamic stochastic model feature is enabled, then the uncertainty is replaced by either constant or elevation-based weighting factors multiplied by the nominal measurement precision in the zenith direction. The mitigation methods and multi-GNSS development are provided in more detail in Section 4.3.

```
while measurement epochs available
      for each GNSS constellation
            for each satellite
                  for each measurement
                        get tracking jitter uncertainty
                        if uncertainty is not available
                              compute replacement uncertainty
                        end
                  end
                  propagate uncertainties
            end
      end
loop
```

Figure 3.7. Pseudocode for scintillation mitigation strategy using tracking jitter data in an improved stochastic model.

3.5.2 Improved atmospheric-dependent PPP

The troposphere-corrected processing strategy in the Figure 3.8 pseudocode is implemented in POINT. In this framework, both pseudorange and carrier phase measurements are corrected for standard *a priori* dry tropospheric delay and wet tropospheric delay estimated by a regional GNSS reference network. If the PPP user assumes that the corrections contain unknown errors, then a new residual wet tropospheric delay parameter is estimated. Furthermore, if the stochastic properties of the corrections are available, then the process noise of the estimated residual wet tropospheric delay is set equal to the correction uncertainty multiplied by a scale factor. A detailed description of the algorithm and various approaches available to the PPP user are presented in Section 5.3.

```
while measurement epochs available
      for each satellite
            for each measurement
                  dry tropospheric delay correction
                  wet tropospheric delay correction
            end
      end
      estimate residual wet tropospheric delay
      process noise = a*(correction precision)
loop
```

Figure 3.8. Pseudocode for tropospheric-corrected processing.

The ionosphere-weighted processing strategy in Figure 3.9 is implemented in POINT and modifies the stochastic model for GNSS measurements. This strategy uses ionosphere-free pseudorange and carrier phase measurements that are weighted according to the rate of TEC as computed via external ionospheric map products. In this approach, ionospheric VTEC is mapped from the vertical to slant direction using a mapping function (Mannucci et al. 1998), then measurement uncertainty is amplified by a TECR-dependent function. Afterward, weighting values are assigned as the inverse of the measurement noise. Internal DCB corrections that are normally required to use ionospheric products are assumed to be time-constant over short time intervals and are therefore eliminated by the between-epoch difference when TEC rate is computed. The resulting modified stochastic model contains a standard elevation-based measurement noise amplification component along with a new ionospheric amplification component. Details on the algorithm development and strategy are presented in Section 5.2.

```
while measurement epochs available
      for each satellite
            query ionospheric TEC map
            for each measurement
                  map vertical TEC to slant
                  compute TECR
                  compute modified measurement noise
                  assign measurement noise value
            end
      end
loop
```

Figure 3.9. Pseudocode for ionosphere-weighted processing.

3.5.3 Improved model error detection

This study uses the dual-frequency cycle slip evaluation methods presented in Section 2.2.4. The MWWL ambiguities are computed at each epoch, for each usable satellite, as a combination of dual-frequency code and carrier phase measurements. To summarize the algorithm, the change in a MWWL ambiguity from the previous epoch to the current epoch is compared to the variation of the MWWL ambiguity (i.e. the standard deviation) in the previous four epochs. If the current MWWL ambiguity exceeds this variation multiplied by a pre-defined scale factor, then the estimated ionosphere-free ambiguity for that satellite is reinitialized with a large process noise. For MWWL ambiguities with fewer than three epochs of previous data available, the standard deviation is set as equal to one MWWL cycle, a relatively conservative value. The ionospheric TECR is calculated using a geometry-free combination of dual-frequency carrier phase measurements. Then, the same process applied on the MWWL ambiguities is used to check per-satellite TECR. When the between-epoch TECR difference is larger than the scaled TECR variation of the previous epochs and the minimum TECR is greater than 0.2 (a change of ~3.2 cm of delay for GPS L1), a cycle slip is declared and the ionosphere-free ambiguity of the affected satellite is reset.

After the dedicated cycle slip algorithms are complete, a detection-identification-adaptation (DIA) algorithm (Teunissen 1998 and Petovello 2003) evaluates post-fit measurement residuals, normalized by variance-covariance matrix elements, against a pre-defined threshold. If a cycle slip is detected, then the biased carrier phase ambiguity will be reset and the corresponding measurement will contribute to a precise parameter estimation using a new ambiguity value. Thus far, a preliminary Bayesian algorithm was implemented in POINT to enhance MWWL and TECR cycle slip detection. This strategy relies on the improved stochastic model following the Aquino et al. (2009) approach to validate cycle slips using a more realistic *a priori* uncertainty of the cycle slip metrics. Although further development of the new method is needed, the model error detection strategies presented herein are crucial elements of PPP processing that enable high-accuracy and reliable performance.

3.6 Summary

In this chapter, the POINT software is introduced and the estimation process is discussed in detail. Default initialization and processing values are provided for the PPP functional model. The default software performance in both kinematic and static

PPP configurations is presented to demonstrate the quality of POINT outputs and to present the standard configurations used for the GPS-only processing. Then, developments and contributions to the POINT software in support of this thesis are presented and discussed. Overviews of the developed algorithms are presented using pseudocode implemented in the POINT software. All results shown in the subsequent chapters are generated using the aforementioned methods and techniques implemented in the POINT software. Additional details on the development of each method are provided in the following chapters.

Chapter 4

Results on Ionospheric Scintillation Evaluation and Mitigation

4.1 Introduction

This section exploits the advantages of the increased model redundancy available in a multi-GNSS Precise Point Positioning (PPP) model and the high-power, low noise Galileo E5 signal to reduce kinematic PPP errors caused by ionospheric scintillation. Ionospheric scintillation monitoring receiver (ISMR) data deployed at a low-latitude station named as PRU2 in the following sections was used to characterize scintillation conditions and as inputs for the mitigation strategy. This station is located at Presidente Prudente (22.1°S, 51.4°W) in Brazil and is affected by low-latitude post-sunset scintillation that causes large positioning errors even during the solar cycle minimum. GNSS data recorded by a nearby geodetic receiver in March 2019 and March 2020 were used to evaluate the horizontal and vertical positioning performance on 57 days, processed using GPS-only, GPS+GLONASS, GPS+Galileo, and GPS+GLONASS+Galileo configurations, with or without scintillation mitigation. Estimated coordinates were evaluated in terms of reliability, accuracy and precision.

4.2 Evaluation of multi-GNSS PPP under low-latitude scintillation

This section evaluates kinematic PPP performance for GPS-only and multi-GNSS configurations using GPS, GLO and GAL measurements under low-latitude post-sunset scintillation conditions, to exploit the advantage of the AltBOC modulated Galileo E5 signal and the improved model redundancy from multi-GNSS processing. The motivation of this contribution is to show the benefits of having GAL measurements in a multi-GNSS PPP model under the effects of low latitude ionospheric scintillation. Experiments were inspired by previous studies that highlight the benefits of GPS+GLO at low latitudes (Marques et al. 2018), GPS+GLO+GAL at high latitudes (Dabove et al. 2020) and general performance improvements using GAL measurements in a multi-GNSS model (Xia et al. 2019). Data and methodology are described in the next section, followed by the results and discussions section, where GPS-only and multi-GNSS results are evaluated in terms of reliability, accuracy and precision performance. Conclusions and future work are discussed in the final section.

4.2.1 Data and approach

This study uses ionospheric scintillation indices recorded in March 2019 at station PRU2 by a Septentrio PolaRxS model receiver, and multi-GNSS measurement data for March 2019 and March 2020 from a geodetic station PPTE. Both stations are located in Presidente Prudente, Brazil, as shown in the top panel of Figure 4.1, where strong ionospheric scintillation is frequently observed. The bottom panel of Figure 4.1 shows that the stations PPTE and PRU2 are separated by approximately 280 meters. It can be observed from the tracking jitter maps proposed by Sreeja et al. (2011) that the scintillation conditions may be similar over large regions up to a few degrees of ionospheric pierce point latitude. Therefore, the two stations in Figure 4.1 are assumed to be separated by a close enough distance that the two receivers experienced nearly identical ionospheric conditions at the same time. Station PRU2 (22.12203°S, 51.40708°W) is part of the CIGALA (Concept for Ionospheric Scintillation Mitigation for Professional GNSS in Latin America)/CALIBRA (Countering GNSS high Accuracy applications Limitations due to Ionospheric disturbances in BRAzil) network and is used to identify scintillation levels on GPS, GLO and GAL signals. Station PPTE (22.11990°S, 51.40853°W) is part of the Brazilian Institute of Geography and Statistics (IBGE) Network for Continuous Monitoring of GNSS Systems (RBMC), with daily 15-sec GPS+GLO+GAL RINEX data freely available to download from the IBGE website (https://www.ibge.gov.br/en). Station PPTE is used to evaluate kinematic PPP performance.

Results were obtained using a multi-GNSS PPP functional model implemented in the University of Nottingham POINT software (Hide et al. 2007; Mohammed 2017), with GPS L1/L2, GLO R1/R2 and GAL E1/E5 code and carrier phase measurements. A Kalman filter configured for kinematic processing is used to estimate high-accuracy coordinates under post-sunset scintillation conditions. The process that produces frequent low-latitude ionospheric scintillation is described in Section 2.3. The amplitude and phase scintillation indices described in Section 2.3.1 are used to characterize scintillation conditions as weak, moderate and strong levels to verify that the positioning errors coincide with local post-sunset scintillation level at the low latitude station.

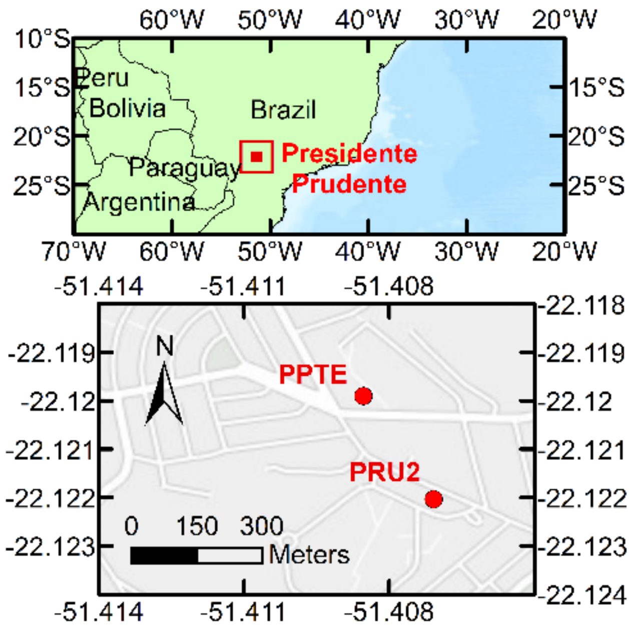

Figure 4.1: Project region (top) and station location (bottom) maps with scintillation data from station PRU2 and multi-GNSS measurements from PPTE.

The S_4 index given by Briggs and Parkin (1963) characterizes amplitude scintillation levels and is defined as the standard deviation of the received signal power normalized to its mean value over a 60-second interval. The σ_φ index characterizes phase scintillation severity and is defined as the 60-second standard deviation of the received carrier phase after it is detrended using a high pass filter. These scintillation indices are commonly used to classify scintillation levels (e.g., Aquino et al. 2005; Sreeja et al. 2011; Marques et al. 2018) and are described in more detail in Section 2.3.

The 60-second interval S_4 and σ_φ values recorded on GPS L1C/L2C, GLO R1C/R2C and GAL E1B/E5a signals for PRU2 were extracted from a monthly ASCII ISMR file generated by the online ISMR Query Tool (Vani et al. 2017). A 10° satellite elevation angle cut off was applied on the scintillation indices to match the elevation threshold applied in PPP processing. This method enabled scintillation data analysis for all satellites used for PPP. A larger elevation cut off angle is typically preferred, as multipath effects may amplify scintillation impact for low elevation satellites. In this study, scintillation conditions are characterized by using one month of data in March 2019 to reduce the multipath contribution to the S_4 and σ_φ values. If only a few sequential days were used instead, then the approximate half-daily orbital periods of the satellites would otherwise repeat multipath effects that could be mistaken as ionospheric scintillation. Furthermore, it is assumed that multipath effects are weak compared to ionospheric scintillation due to the reference station located in open-sky conditions and deployment of a choke ring antenna that reduces multipath effects. A derived scintillation index, the corrected S_4, was calculated by subtracting the ambient noise component from the total S_4, as described in the Septentrio (2015) PolaRxS Application Manual, and is hereby referred to as S_4. The elevation filtered S_4 and σ_φ values were then used to classify the scintillation levels, based on the International Telecommunication Union (2016) recommendation, as weak, moderate or strong, which is shown in Table 4.1.

Table 4.1. Scintillation classification using the International Telecommunication Union (2016) recommendations.

Scintillation category	Received signal amplitude (S_4) or phase (σ_φ) scintillation index
Weak	Value ≤ 0.3
Moderate	0.3 < Value ≤ 0.6
Strong	Value > 0.6

In the months of March 2019 and March 2020, 31 (DOYs 60-90) and 30 (DOYs 61-73 and 75-91) daily 15-sec RINEX files, respectively, were downloaded for station PPTE. The files were preprocessed with the GFZ gfzrnx toolbox (Nischan 2016) to create a new 60-sec sampling rate by decimating GPS L1/L2, GLO R1/R2 and GAL E1/E5 RINEX files. Legacy GPS signals were used, as few GPS satellites had the L5 signal available. These modified RINEX files were windowed with UNAVCO's *TEQC* (unavco.org) software to begin at 20h UTC and end at 04h UTC the following day to allow PPP convergence prior to post-sunset scintillation occurrences that begin at approximately 00h UTC (21h local time). A total of 58 combined and windowed RINEX files were formed, with the latest files in March 2019 and March 2020 on DOY 89-90 and 90-91, respectively, and without a missing DOY 74 RINEX file in March 2020. These 58 RINEX files were processed by the University of Nottingham POINT software in kinematic PPP mode using a forward extended Kalman filter (EKF) for the following four configurations: GPS, GPS+GLO, GPS+GAL, and GPS+GLO+GAL. The Kalman filter equations, along with details on GNSS data processing using the EKF, are available in Verhagen and Teunissen (2017) and Section 3.3 of this thesis. International GNSS Service (IGS) Multi-GNSS Experiment (MGEX) precise satellite orbit and clock products were used to correct GNSS measurements and constrain the positioning solutions to the global International Terrestrial Reference Frame (ITRF). After a quality control check, the DOY 68-69 file in March 2019 was excluded and the remaining 57 files were used for the performance evaluation. In addition to model error detection algorithms described in Table 3.2, additional corrections and strategies applied to the PPP processing specific to this experiment are shown in Table 4.2.

Table 4.2. GNSS processing models and strategies for the evaluation of low-latitude scintillation-affected PPP.

GNSS processing	Configurations/strategies
Constellations: signals	GPS: L1C/A, L2P; GLO: R1P, R2P; GAL: E1B/C, E5
Satellite antenna PCO/PCV	From igs14_2038.atx
Receiver antenna PCO/PCV	From igs14_2108.atx, GPS used for GAL
A priori pseudorange precision	GPS L1C/L2P: 0.3/0.3 m GLO R1P/R2P: 1.0/1.0 m GAL E1B/E5: 0.3/0.05 m
A priori carrier phase precision	GPS L1/L2: 0.01/0.01 cycles GLO R1/R2: 0.03/0.03 cycles GAL E1/E5: 0.01/0.01 cycles

A 24-hour duration GPS+GLO RINEX file, recorded at a 15-sec epoch interval, for station PPTE was submitted to the Canadian Spatial Reference System (CSRS) online service for static PPP processing on March 03, 2019, on a weak to moderate scintillation day, for which the scintillation influence on static PPP is considered negligible, to estimate high-accuracy "ground truth" reference coordinates. Therefore, for all analyses hereafter, positioning errors estimated at

PPTE are defined as differences between the final epoch of static CSRS-PPP estimated coordinates on March 03, 2019 and kinematic POINT-PPP estimated local north, east and up directions.

In this study, horizontal convergence is defined as the absolute value of the north and east positioning component errors below 10-cm for at least 10 epochs and the maximum-minus-minimum error in these 10 epochs is also below 10-cm. Vertical convergence uses the up positioning component with a 20-cm threshold and is evaluated using the same criteria as horizontal convergence. The initial average horizontal and vertical convergence times along with the standard deviation (std) for the remaining 29 files in March 2019 and 28 files in March 2020 are summarized in Table 4.3. It can be observed from Table 4.3 that solutions are converged, on average, prior to the start of post-sunset scintillation at approximately 00h UTC. All multi-GNSS configurations improved the average initial convergence time compared to GPS-only processing, with less daily variation as shown by the lower standard deviation values, likely due to improved satellite geometry. For the same reason, Table 4.3 shows that GPS+GLO+GAL processing performed best with the fastest horizontal and vertical convergence and superior daily stability.

Table 4.3. Initial horizontal and vertical convergence time statistics for 57 RINEX files, from 20h to 04h UTC the next day, in March 2019 and March 2020.

	Horizontal convergence (minutes)		Vertical convergence (minutes)	
Processing strategy	Mean	Std	Mean	Std
GPS	44	21	39	17
GPS+GLO	34	13	28	13
GPS+GAL	28	11	27	13
GPS+GLO+GAL	26	08	25	11

The kinematic PPP performance for all the files with non-converged horizontal and vertical GPS-only epochs after 2-hours of processing are evaluated in terms of horizontal and vertical reliability, accuracy, and precision. GPS-only data with 100% converged horizontal or vertical epochs after 2-hours of processing are excluded from analysis, along with the subsequent multi-GNSS configurations, as the objective is to highlight the benefits of multi-GNSS when GPS-only processing is not adequate. Reliability is defined as the availability of converged epochs, accuracy is computed as the mean of hourly root mean square error (RMSE) of the positioning errors and precision is calculated as the mean of the hourly positioning error standard deviation for each day. These criteria are used in the following section to evaluate horizontal and vertical kinematic PPP performance and demonstrate multi-GNSS improvements relative to GPS-only processing.

4.2.2 Single- and multi-GNSS performance

Amplitude and phase scintillation indices from 20h to 04h UTC on each day in March 2019 were used to generalize pre- and post-sunset scintillation conditions. At the studied location, local sunset is at approximately 22h UTC and post-sunset scintillation typically begins by UTC midnight (i.e., 00h UTC) each day. Figure 4.2 shows hourly strong and moderate scintillation occurrences per-system, normalized by the total number of occurrences for each respective classification. Although scintillation data were recorded during the solar cycle minimum, the local EIA phenomenon increases the likelihood of strong and moderate scintillation occurrence during post-sunset hours, a clear feature in Figure 4.2. Note that scintillation indices in Figure 4.2 are evaluated together, for each classification, as moderate correlation ($R^2 = 0.54$) was found between the S_4 and σ_φ values using a linear fit. In other words, more than 50% of the variability for a single scintillation index can be explained by a linear relationship between each index.

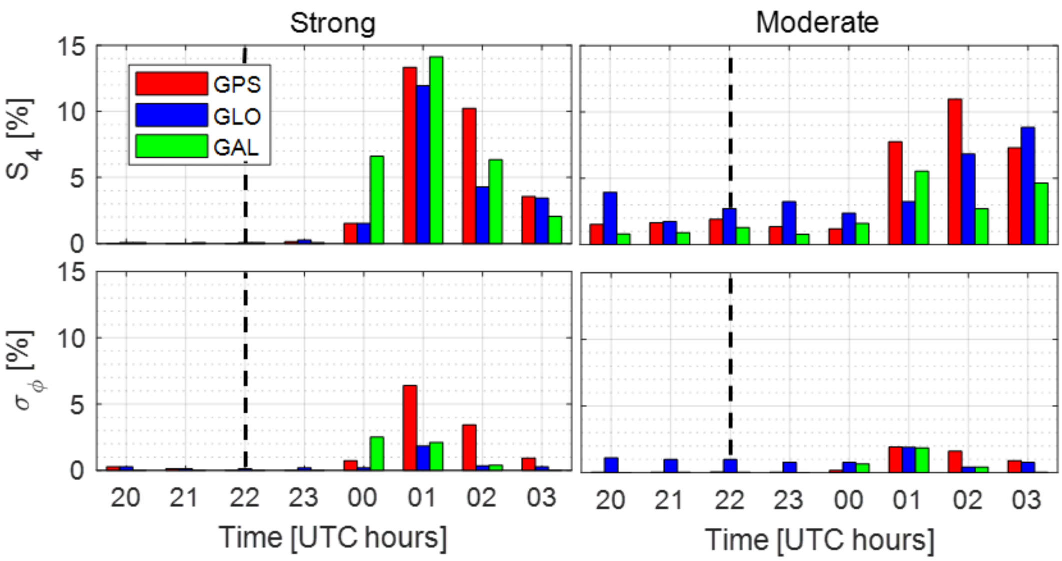

Figure 4.2: Strong (left column) and moderate (right column) amplitude (top row) and phase (bottom row) scintillation occurrences between 20h-04h UTC, normalized by the total number of respective strong or moderate combined amplitude and phase scintillation occurrences, for GPS (red), GLO (blue), and GAL (green) satellites on DOYs 60-90 in March 2019. Approximate sunset time represented by dashed line.

The strong and moderate scintillation occurrences identified from 00h to 04h UTC in Figure 4.2 are 86.8% and 77.7% of the respective total occurrences in each category, which further supports the post-sunset scintillation trend. Strong and moderate amplitude scintillation respectively represents 80.2% and 85.0% of all strong and moderate scintillation occurrences, indicating an environment dominated by amplitude scintillation when the Table 4.3 classification thresholds are used. This indicates that the received signal power fluctuates more frequently than the phase, which is likely due to the nearly vertical ionospheric angle of incidence for satellites observed near the equator. Frequent amplitude Strong amplitude and phase scintillation occur most frequently on GPS, GLO and GAL satellites from 01h to 02h UTC, with decreased activity in each of the following hours, while moderate scintillation conditions remained relatively constant from 01h to 04h UTC.

The vertical positioning component error time series in Figure 4.3 are for each of the four different configurations on days in March 2019 that have GPS-only epochs that do not meet the vertical convergence threshold. Note that horizontal positioning components are not used in Figure 4.3, as the up component is the most affected by scintillation. Prompt initial convergence was achieved prior to the increased scintillation activity at approximately 00h UTC. Vertical positioning accuracy was better than 20-cm for 98% of all cases from 21h to 23h UTC, i.e., after initial convergence and prior to the occurrence of post-sunset scintillation. Figure 4.3 shows worse positioning performance from approximately 00h to 04h UTC, with many epochs exceeding the 20-cm convergence criteria, poor accuracy and decreased precision. The largest vertical error magnitudes of 0.82-m and 2.85-m were recorded on DOYs 60-61 and 61-62, respectively, for GPS-only processing and are highlighted respectively by black and magenta lines in Figure 4.3 to compare against other days. The single-system GPS-only configuration in Figure 4.3 has the worst positioning performance, with vertical position errors exceeding 50-cm, while dual- and triple-system processing is more stable. Therefore, the worst-case days, in terms of maximum positioning error for GPS-only processing, were selected to show detailed evaluations and improvements achieved using the multi-GNSS configurations.

The corresponding strong and moderate amplitude and phase scintillation indices for signals in the same frequency spectrum used for positioning are shown in Figure 4.4. Increased scintillation activity from 01h to 02h UTC in Figure 4.4

corresponds to the same time period when the maximum positioning errors were observed. Thus, it is concluded that the worse positioning performance that typically begins at approximated 00h UTC is caused by increased ionospheric scintillation activities. Daily variations in the number of strong and moderate scintillation occurrences can be observed in Figure 4.4, which explains the daily positioning performance variations, even for sequential days.

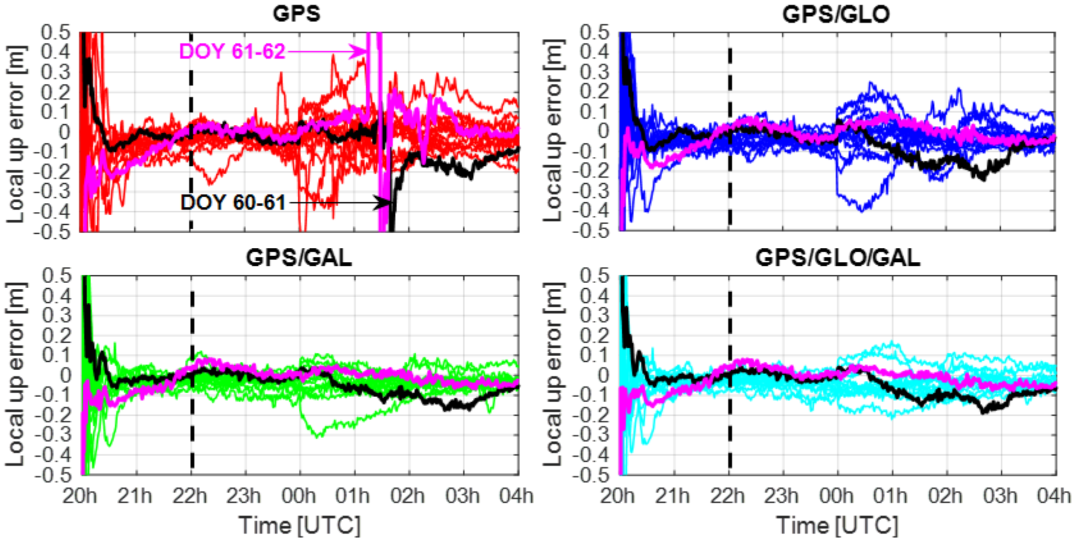

Figure 4.3: Vertical kinematic PPP error from 20h to 04h UTC for GPS (red), GPS/GLO (blue), GPS/GAL (green), and GPS/GLO/GAL (cyan) processing on post-sunset (dashed line) days in March 2019 identified with non-converged GPS-only epochs, with the two worst-case GPS-only days on DOYs 60-61 (black) and 61-62 (magenta) annotated.

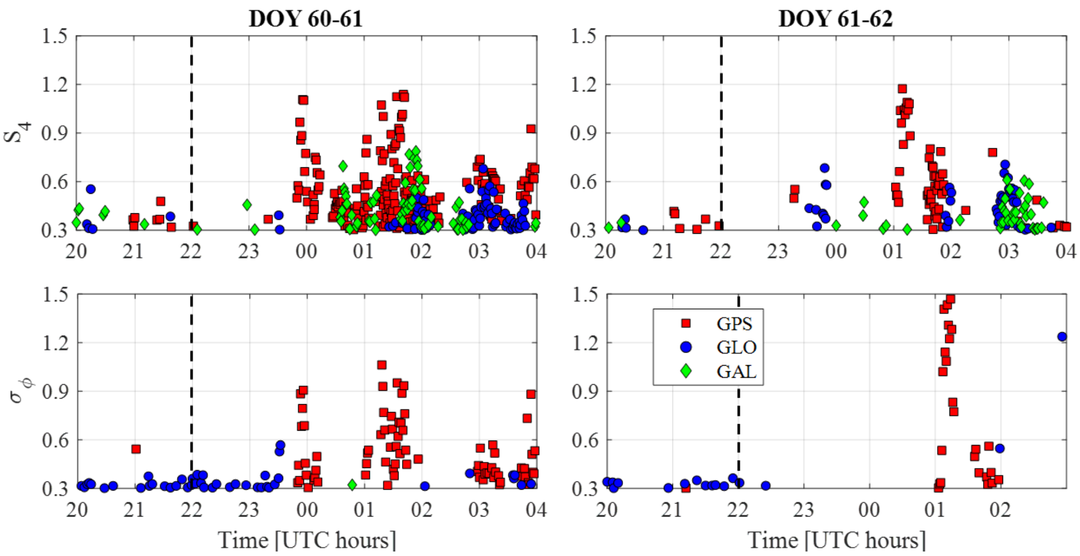

Figure 4.4: Strong and moderate (index ≥ 0.3) amplitude (top row) and phase scintillation (bottom row) from 20h to 04h UTC on DOYs 60-61 (left column) and 61-62 (right column), March 2019 for GPS L1 (red), GLO R1 (blue), and GAL E1 (green) signals. Local sunset time is indicated by the black dashed line.

Performance metrics and multi-GNSS improvements for the horizontal and vertical positioning components on DOYs 60-61 and 61-62 in March 2019 are summarized in Table 4.4 and Table 4.5 respectively to demonstrate multi-GNSS benefits compared with worst-case GPS-only processing. Data from 20h to 22h UTC were excluded to avoid initial convergence errors that are not related to the post-sunset scintillation occurrences. For these two DOY intervals, Table 4.5 shows that multi-GNSS processing improved the respective horizontal and vertical positioning reliabilities, in terms of converged epochs, by up to 24.4% and 27.0% with respect to GPS-only processing. For example, on DOY 61-62 in 2019, all multi-GNSS configurations were 100% reliable, i.e., all epochs met the convergence criteria, while 83.7% and 87.0% of GPS-only epochs were not converged for respective horizontal and vertical components. For the same period, the respective horizontal and vertical positioning accuracy also improved by up to 88.5% and 80.4%, with precision improvements up to 92.9% and 90.4%, using the multi-GNSS configurations. These improvements are defined as the percentage difference between GPS-only processing and respective multi-GNSS configurations for each performance metric.

Table 4.4. Horizontal and vertical positioning reliability, accuracy, and precision on DOYs 60-61, March 2019.

	Horizontal/vertical performance		
System(s)	Reliability [%]	Accuracy [cm]	Precision [cm]
GPS	78.7/80.4	6.6/10.0	4.0/5.3
GPS+GLO	100./88.7	3.8/8.6	1.4/3.0
GPS+GAL	100./100.	4.2/6.8	1.1/2.4
GPS+GLO+GAL	100./100.	4.2/7.0	1.1/2.3

Table 4.5. Horizontal and vertical positioning reliability, accuracy, and precision on DOYs 61-62, March 2019.

	Horizontal/vertical performance		
System(s)	Reliability [%]	Accuracy [cm]	Precision [cm]
GPS	83.7/87.0	13.1/16.2	11.8/15.0
GPS+GLO	100./100.	2.4/4.0	1.1/2.1
GPS+GAL	100./100.	1.5/3.2	0.9/1.5
GPS+GLO+GAL	100./100.	1.8/3.4	0.8/1.4

Unreliable horizontal or vertical GPS-only solutions with non-converged epochs were identified for 25 and 26 intervals, respectively, out of the 57 intervals processed for March 2019 and 2020, with the start DOY for each identified file provided in Figure 4.5. The process used to evaluate the performance for the representative intervals described above was repeated for the cases identified with unreliable GPS-only performance. Although positioning reliability varies day-to-day due to the scintillation conditions, GPS-only processing was the least reliable configuration for 92.0% and 84.6% of horizontal and vertical cases, respectively. The least reliable single-day solutions, both horizontally and vertically, were for GPS-only processing and contained up to 31.6% and 62.1% non-converged epochs, respectively. The GPS+GLO+GAL configuration improved horizontal and vertical reliability in every case, except for four GPS+GLO and two GPS+GAL cases that were less reliable than GPS-only, with negative improvements when positioning errors exceeded the convergence criteria by up to 20-cm for consecutive epochs, while the related GPS-only epochs remained converged.

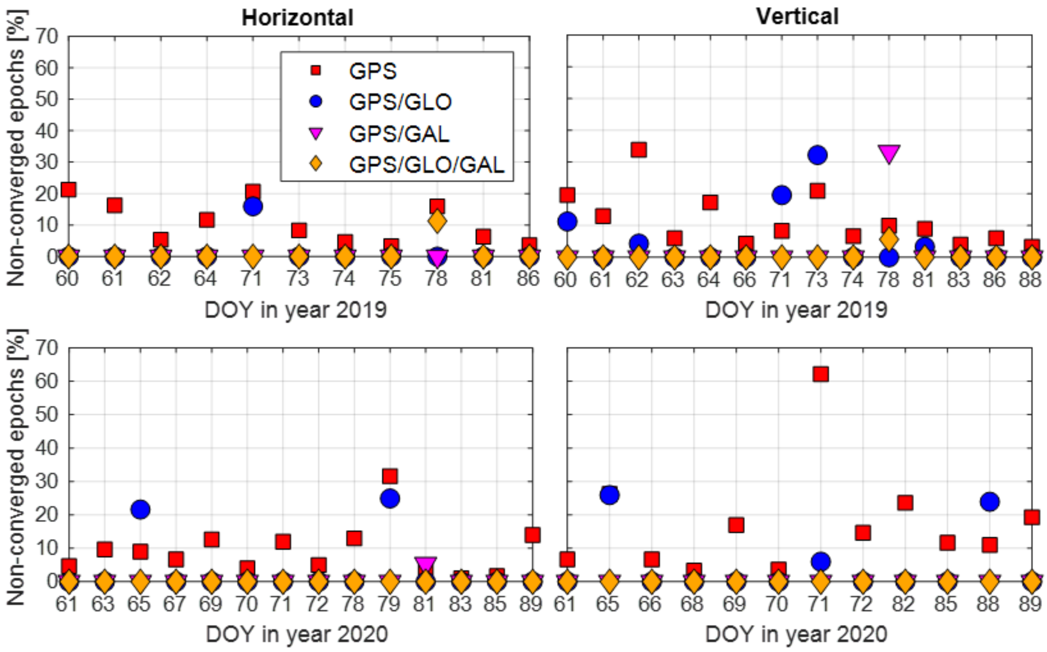

Figure 4.5: Daily non-converged horizontal (left column) and vertical (right column) epochs (units: %), after 2-hours of processing, for March 2019 (top row) and March 2020 (bottom row).

Table 4.6 summarizes the overall horizontal and vertical reliability for each configuration, in terms of the average percentage of converged epochs on days with degraded GPS-only positioning. The total number of epochs evaluated after the initial convergence interval and on days with non-converged GPS-only epochs is equal to 5400 and 6840 epochs in March 2019 and 2020, respectively. Therefore, the

Table 4.6 horizontal GPS-only reliability equal to 90.9% corresponds to approximately 1117 non-converged epochs for horizontal components. In Table 4.6, it is shown that improvements were achieved for all multi-GNSS configurations, on average, with greater improvement in the vertical direction. Configurations using Galileo measurements achieved similar horizontal and vertical improvements of approximately 10% and 14%, respectively. The GPS+GLO configuration achieved less average horizontal and vertical improvement than the GPS+GAL and GPS+GLO+GAL configurations, with approximately half the amount of vertical improvement compared to the combinations using Galileo measurements.

Table 4.6. Average percentage of reliable (i.e., converged) epochs and improvement with respect to GPS-only processing for each multi-GNSS configuration, for days in March 2019 and March 2020 with degraded GPS-only positioning.

	Reliable epochs [%]		Improvement [%]	
Systems	Horizontal	Vertical	Horizontal	Vertical
GPS	90.9	86.9	(ref)	(ref)
GPS+GLO	97.7	93.1	7.6	7.2
GPS+GAL	99.8	99.2	9.8	14.2
GPS+GLO+GAL	99.5	99.8	9.5	14.8

This reliability improvement for the multi-system configurations indicates that the relatively unstable GPS-only kinematic PPP processing can be improved under moderate to strong low-latitude scintillation conditions by using multi-GNSS processing. In addition, a key factor to improve kinematic PPP reliability under low-latitude scintillation is to use multi-GNSS processing with Galileo measurement data. Configurations that used the modernized Galileo E1 and E5a signals consistently outperformed GPS-only and GPS+GLONASS configurations. Aside from the outlier on DOY 78 in 2019, the GPS+GAL configuration had similar reliability as the GPS+GLONASS+Galileo processing. This indicates that the advanced Galileo signals are better suited to improve positioning reliability in a multi-GNSS model as opposed to using legacy GLONASS signals.

Hourly horizontal and vertical RMSE are provided for files with degraded GPS-only solutions in March 2019 (Figure 4.6) and 2020 (Figure 4.7) to illustrate daily positioning accuracy. The RMSE magnitudes are represented in color from 0-cm to the respective 10-cm horizontal and 20-cm vertical convergence criteria thresholds. Both horizontal and vertical positioning accuracies tend to degrade starting at approximately 00-01h UTC, with more frequent large errors for GPS-only processing. For all data represented in Figures 4.6 and 4.7, 8 GPS-only, 3 GPS+GLO, 1 GPS+GAL and 1 GPS+GLO+GAL samples were greater than 10-cm of error, while for vertical data, 11 GPS-only, 3 GPS+GLO, 1 GPS+GAL and 0 GPS+GLO+GAL samples were greater than 20-cm of error. Therefore, the multi-GNSS configurations achieved better horizontal and vertical accuracies, with fewer hours affected by large positioning errors and with greater benefit from the GAL configurations.

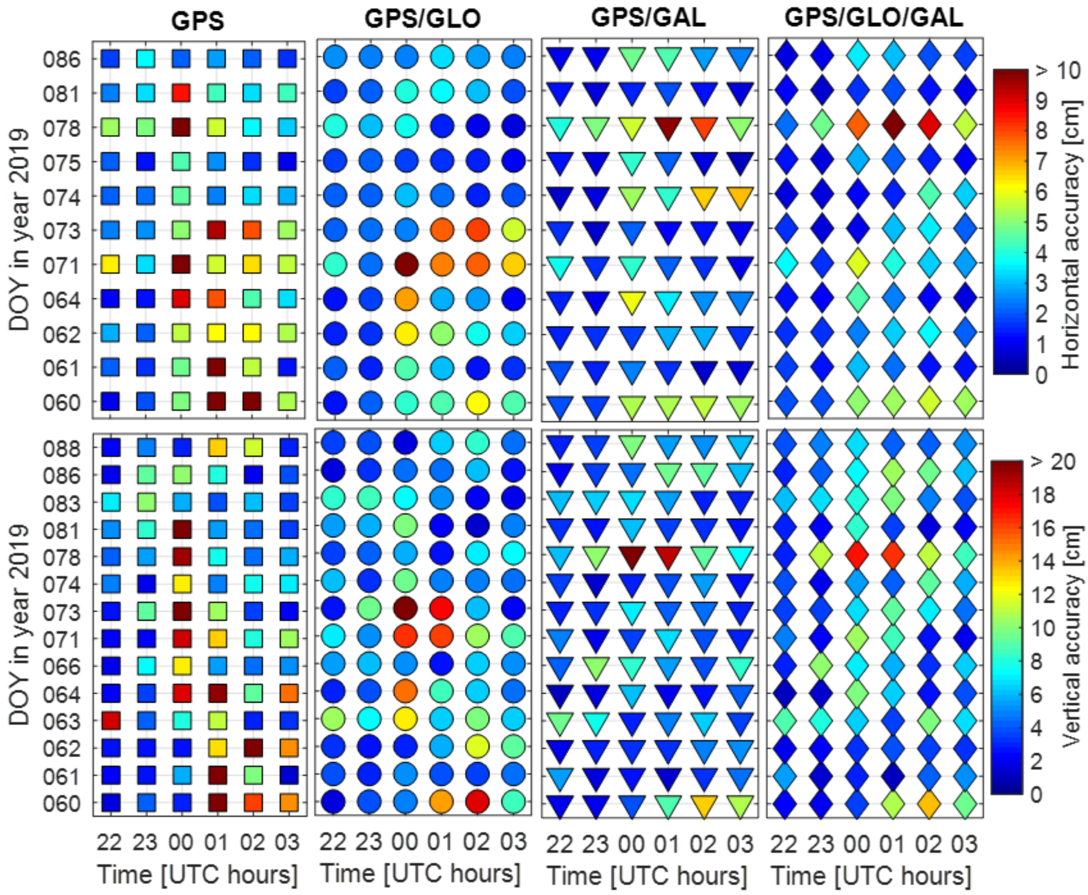

Figure 4.6: Hourly horiztonal (top row) and vertical (bottom row) RMS (units: cm) for days in March 2019 with degraded GPS-only positioning.

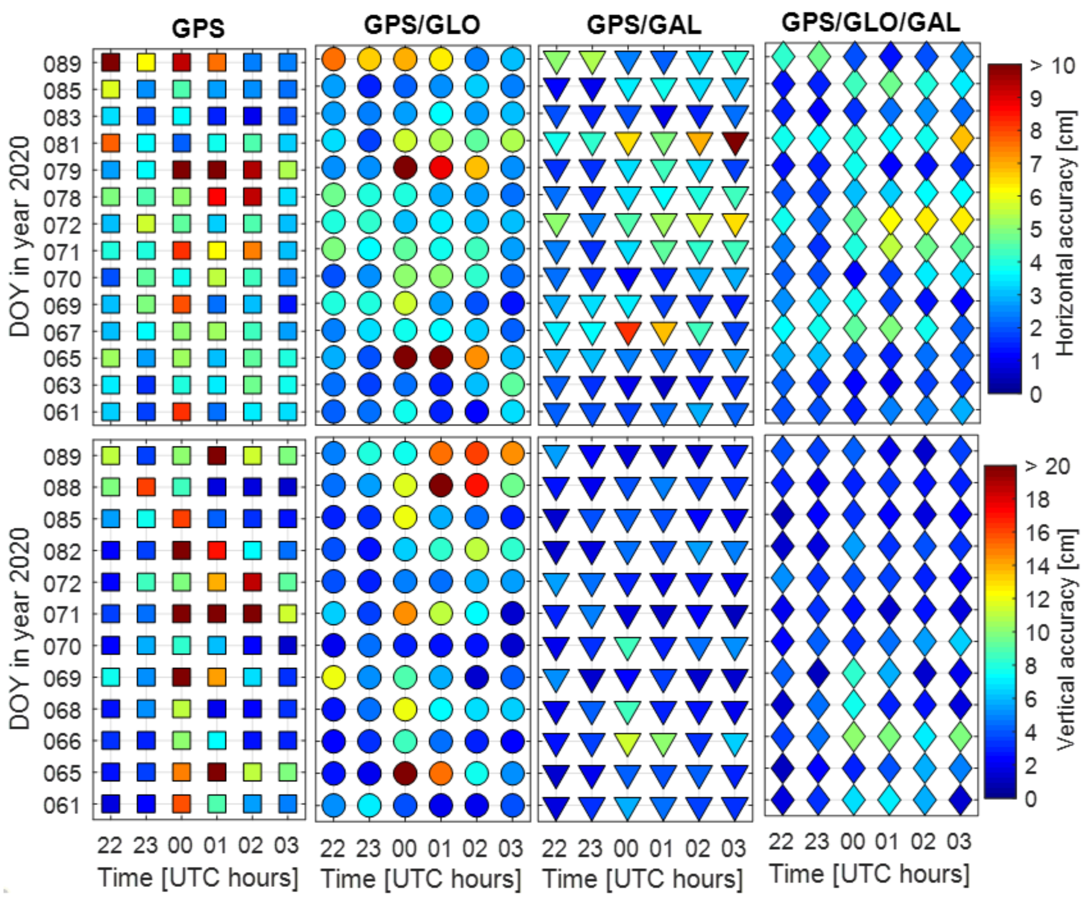

Figure 4.7: Hourly horiztonal (top row) and vertical (bottom row) RMS (units: cm) for days in March 2020 with degraded GPS-only positioning.

Daily accuracy improvements are summarized in Table 4.7, where improvements were computed for multi-GNSS configurations, with respect to GPS-only, using the daily mean of the hourly RMSE data. All multi-GNSS configurations improved positioning accuracy, on average, by up to 36.6% horizontally for GPS+GLO+GAL and 39.8% vertically for GPS+GAL. The mean horizontal and vertical improvements achieved with GPS+GLO processing were approximately half of the best improvement using GAL configurations, which indicates better overall positioning accuracy when the PPP model includes GAL measurements.

Table 4.7. Improvement statistics for daily RMSE, with respect to GPS-only, for days in March 2019 and March 2020 identified as having degraded GPS-only positioning.

	Mean accuracy improvement [%]	
Systems	Horizontal	Vertical
GPS+GLO	20.1	18.8
GPS+GAL	31.3	39.8
GPS+GLO+GAL	36.6	35.9

Hourly horizontal and vertical standard deviations, hereby representative of precision, are provided for days with non-converged GPS-only epochs in March 2019 (Figure 4.8) and 2020 (Figure 4.9) to illustrate daily positioning precision from 23h to 04h UTC. Precision magnitudes are represented in color from 0-cm to one quarter of the respective horizontal and vertical convergence criteria thresholds. Both the horizontal and vertical precision tend to degrade starting at approximately 00-01h UTC, with more frequent variation for GPS-only and GPS+GLO configurations and in the vertical direction. For all horizontal data represented in Figures 4.8 and 4.9, 32 GPS-only, 11 GPS+GLO, 4 GPS+GAL and 3 GPS+GLO+GAL samples were worse than 2.5-cm of precision, while for vertical data, 33 GPS-only, 10 GPS+GLO, 2 GPS+GAL and 3 GPS+GLO+GAL samples were worse than 5-cm of precision. Therefore, the multi-GNSS configurations achieved better horizontal and vertical precision, with fewer hours affected by large fluctuations of the positioning errors and with major benefit from the GAL configurations.

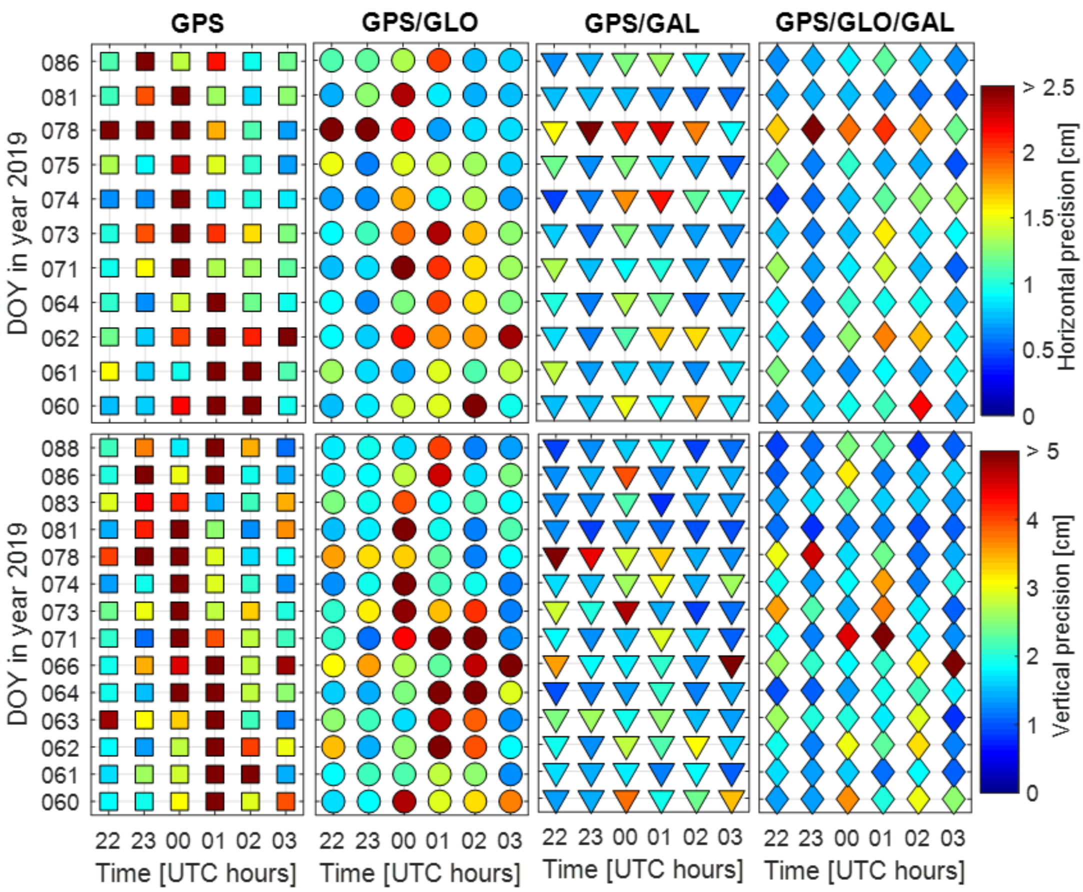

Figure 4.8: Hourly horizontal (top row) and vertical (bottom row) precision (units: cm) for days in March 2019 with degraded GPS-only positioning.

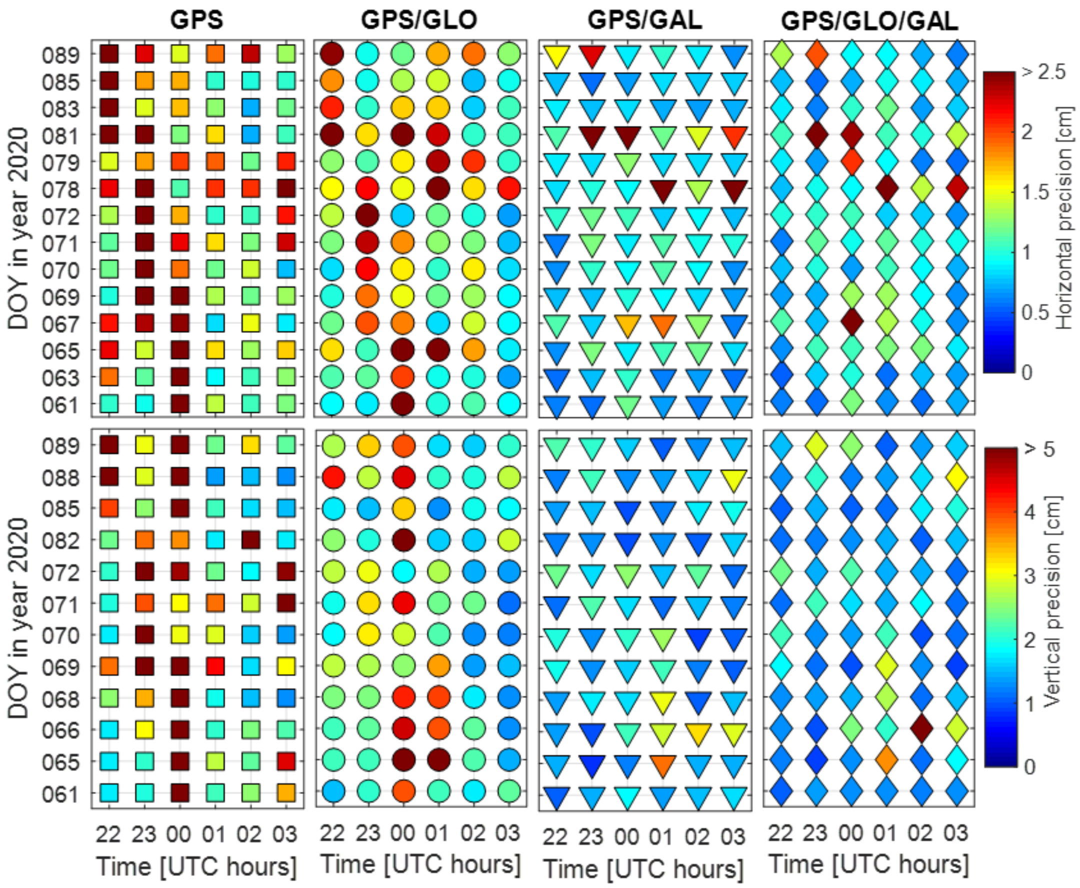

Figure 4.9: Hourly horizontal (top row) and vertical (bottom row) precision (units: cm) for days in March 2020 with degraded GPS-only positioning.

Daily precision improvements are summarized in Table 4.8, where improvements were computed for multi-GNSS configurations, with respect to GPS-only, using the mean of the hourly standard deviation data on each day. All multi-GNSS configurations improved horizontal and vertical positioning precision, on average, by approximately 28% for GPS+GLO and 50% for GPS+GAL and GPS+GLO+GAL configurations. The mean improvements achieved with GPS+GAL and GPS+GLO+GAL configurations were nearly identical (~2% difference), while GPS+GLO achieved approximately 20% less improvement compared to GAL configurations. This suggests that GPS+GAL can offer sufficient precision improvement, with only a minor GLO contribution in the GPS+GLO+GAL configuration. Additionally, the lower overall variability for configurations using Galileo measurements, as indicated by the standard deviation in Table 4.8, indicates that GPS+GAL and GPS+GLO+GAL offer improved repeatability in terms of positioning component precision than that achieved using GPS+GLO processing.

Table 4.8. Mean of daily precision improvement with respect to GPS-only processing, computed as the mean of hourly horizontal and vertical standard deviation data from 23h to 04h UTC, for days with non-converged GPS-only processing.

	Horizontal precision improvement [%]		Vertical precision improvement [%]	
Systems	Mean	Std	Mean	Std
GPS+GLO	28.1	20.6	27.9	23.3
GPS+GAL	48.7	19.7	52.7	14.9
GPS+GLO+GAL	49.7	16.8	51.2	18.4

The Table 4.9 statistics of the number of usable GPS, GLO, GAL and combined GPS+GLO, GPS+GAL and GPS+GLO+GAL satellites recorded at station PPTE per 60-sec epoch were computed for DOYs 60-90 in March 2019, from 20h to 04h UTC the next day, demonstrate the increased number of satellites available for multi-GNSS processing. At least 14 and at most 28 satellites were identified as usable for GPS+GLO+GAL processing at a single epoch, while the maximum number of usable GPS, GLO and GAL satellites were 12, 9 and 9, respectively. It can be observed from Table 4.9 that approximately 9 GPS, 6 GLO and 6 GAL satellites were available for positioning on average, while the combined GPS+GLO+GAL configuration averaged about 21 satellites.

Table 4.9. Statistics of usable satellites for single- and multi-system configurations from 20h to 04h UTC on DOYs 60-90 in March 2019.

System(s)	Mean	Max	Min
GPS	8.6	12	6
GLO	5.9	9	4
GAL	6.4	9	3
GPS+GLO	14.5	20	10
GPS+GAL	15.1	20	10
GPS+GLO+GAL	21.0	28	14

For the multi-GNSS functional model used in this study and the number of usable satellites at the time of the kinematic PPP processing, the GPS+GLO+GAL model redundancy was at least 5, at most 19 and on average 12. In the same period, the maximum and average GPS-only model redundancies were 5 and 2, respectively, while the average dual-system redundancies were approximately 7, due to a similar number of usable GLO and GAL satellites. Therefore, GPS-only processing is more sensitive to ionospheric scintillation, as a single scintillation-affected satellite is a larger proportion of the total number of satellites. Furthermore, if satellites affected by scintillation are identified and removed, then GPS-only processing is more likely to suffer from amplified dilution of precision due to the low number of usable satellites relative to multi-GNSS configurations.

The improved model redundancy for multi-GNSS configurations enables better estimation of unknown parameters and identification of model errors, where measurement outliers are rejected with less impact on the solution reliability. This explanation supports the positioning improvements achieved with the multi-GNSS configurations under the low latitude scintillation conditions. Further improvements for GPS+GAL and GPS+GLO+GAL configurations are likely a result of the increased signal transmission power and low noise properties of GAL signals (Basile et al. 2019; Guo et al. 2016; Lou et al. 2016), which offer further benefits for multi-GNSS processing with GAL measurements. These improvements using GAL combinations were achieved despite a similar average number of available GLO satellites.

4.2.3 Remarks

Low latitude ionospheric scintillation conditions recorded at station PRU2 (22.12203°S, 51.40708°W) were used to verify local post-sunset scintillation conditions at nearby station PPTE (22.11990°S, 51.40853°W) in Presidente Prudente, Brazil. Multi-GNSS GPS+GLO, GPS+GAL and GPS+GLO+GAL measurement configurations were processed for data recorded at station PPTE to evaluate kinematic PPP performance under scintillation with respect to GPS-only processing. Horizontal and vertical reliability, accuracy and precision evaluations of the four processing strategies revealed degraded GPS-only positioning at post-sunset hours and positive improvement, on average, for all multi-GNSS configurations for all evaluation metrics compared to GPS-only processing.

The respective average of daily reliability, accuracy and precision improvements were: 14.8% using GPS+GLO+GAL, 39.8% using GPS+GAL and 52.7% using GPS+GAL configurations. For example, the GPS+GAL configuration achieved 52.7% average vertical precision improvement relative to GPS-only, while the comparable GPS+GLO processing achieved only 27.9% average improvement. The maximum overall improvements were all in the vertical direction and all multi-

GNSS configurations achieved average positive improvement both horizontally and vertically for each performance metric. Therefore, multi-GNSS processing under low-latitude ionospheric scintillation conditions offers excellent improvement to the otherwise low-quality GPS-only processing, especially in the vertical direction. GPS+GAL and GPS+GLO+GAL improvements were comparable for all evaluation metrics, with a 5.3% daily improvement difference at most. For accuracy and precision, GPS+GLO processing provided up to 20% less improvement achieved by the corresponding GAL configurations. Thus, combinations using GAL measurements had better average improvement relative to both GPS-only and GPS+GLO configurations.

Improved multi-GNSS performance is supported by the increased number of usable satellites, which improved the multi-GNSS model redundancy. The increased improvements observed for GPS+GAL compared with GPS+GLO processing, for a quite similar number of usable satellites, on average, is assumed to be due to the superior noise properties of the Galileo E1 and modernized E5 signal.

The increased number of satellites available in a multi-GNSS model may have a negative impact if the number of satellites affected by strong scintillation also increases. Therefore, the following section focuses on the development and implementation of multi-GNSS scintillation mitigation techniques (Aquino et al. 2009; Silva et al. 2010; Luo et al. 2020; Vadakke Veettil et al. 2020) and processing scintillation-affected data for a non-specialized GNSS receiver.

4.3 Mitigation of low-latitude ionospheric scintillation for multi-GNSS PPP

This section uses low-latitude GNSS measurement data from geodetic station PPTE in March 2019 and from nearby station PRU2, a Septentrio PolaRxS ionospheric scintillation monitoring receiver (ISMR), in March 2015. Station PRU2 scintillation monitoring files were additionally used to characterize scintillation levels and as the inputs to the Conker et al. (2000) tracking error model to mitigate single- and multi-GNSS processing in March 2015 and March 2019, respectively, using the Aquino et al. (2009) modified stochastic model approach. Note that Section 4.2.1 describes both stations PPTE and PRU2 in detail and shows that the stations are separated by less than 300-meters. In addition, mitigated multi-GNSS processing for station PPTE uses a subset of the March 2019 data in Section 4.2 identified as having strong scintillation.

Modifications to the Conker et al. (2000) receiver tracking error model input parameters were developed and applied to repair tracking jitter outages that are especially frequent under strong scintillation conditions. In this section, the term "outages" represents missing receiver tracking error model outputs, as opposed to missing GNSS measurement data that is caused by tracking loop failure. The receiver-specific tracking error model parameters in Equation 2.17 and Equation 2.18 were set to: 0.25- and 15-Hz for respective DLL and PLL bandwidths, 0.04-chips for the correlator spacing, 0.1- and 0.01-seconds for respective DLL and PLL pre-detection integration times, 3.04-Hz for the PLL natural frequency, and 3 for the PLL loop order. These values are consistent with those used for Septentrio receivers as part of other scintillation studies (Aquino et al. 2009; Sreeja et al 2011; Sreeja et al. 2012; Vani et al. 2019). Remaining tracking error model parameters needed to compute the tracking jitter were output by the receiver.

Repaired tracking jitter and satellite elevation-based stochastic models are evaluated for station PRU2 affected by strong low latitude ionospheric scintillation beginning at approximately UTC midnight on March 15, 2015. The Aquino et al. (2009) modified stochastic model approach, using Conker et al. (2000) tracking jitter for GPS L1 and L2 measurements, was then used to mitigate scintillation effects on kinematic PPP performance for respective GPS-only and GPS+Galileo processing at station PRU2 in March 2015 and station PPTE in March 2019.

4.3.1 Receiver tracking error model repair

The Conker et al. (2000) receiver tracking error models can only be applied to estimate tracking jitter variance under weak-to-moderate scintillation levels, where $S4 < 0.707$, due to the characterization of the Nakagami-m (1960) probability density function, of which the amplitude scintillation is assumed to obey. The scintillation indices in Figure 4.10 demonstrate more frequent Conker et al. (2000) model outages (i.e., the GNSS signal is intact but Conker et al. (2000) outputs are not available) under particularly strong scintillation for satellites above 10-degrees in elevation observed at station PRU2 from March 14, 16h UTC, to March 15, 08h

UTC, 2015, a case of a strong scintillation day. In Figure 4.10, outages occur for both the DLL and PLL tracking error if the GPS L1 signal-to-noise ratio is unavailable, for DLL outputs if S4 < 0.707, and for PLL outputs if the phase spectral slope of the detrended phase is unavailable or if the phase scintillation index is greater than 1.5. In total, the outages in Figure 4.10 correspond to 2.1% and 2.3% of respective Conker et al. (2000) DLL and PLL outputs being unavailable for the GPS L1 signal, even though the receiver did not lose lock for 91.8% of outages.

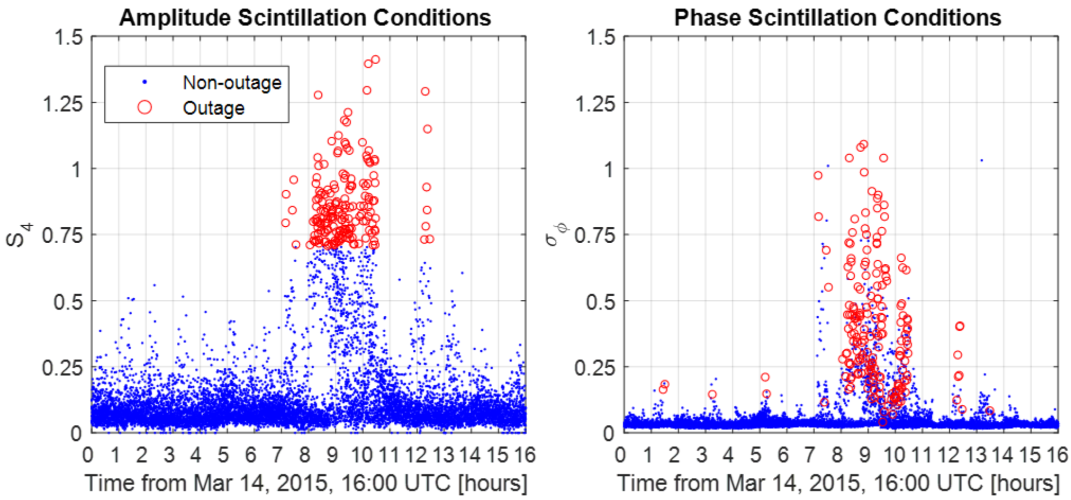

Figure 4.10. Station PRU2 GPS L1C/A signal amplitude (left) and phase (right) scintillation indices (blue filled circles) and corresponding Conker et al. (2000) tracking jitter outages (red non-filled circles) from March 14, 2015 (16h UTC) to March 15, 2015 (08h UTC).

Mitigation of ionospheric scintillation effects on GNSS-based positioning can be achieved using a modified stochastic model that represents more realistic measurement uncertainty (Aquino et al. 2009). However, the identified tracking error model outages result in an incomplete stochastic model due to the missing measurement quality information. Thus, thresholds and limits were assigned to Conker et al. (2000) parameters and inputs to enable tracking jitter that would otherwise be unavailable.

Missing signal-to-noise ratio values for GPS L1 and L2 signals were set to 10% less than the respective minimum signal-to-noise ratio in the outage epoch. Thus, the repaired signal-to-noise ratio values normally correspond to the largest tracking jitter noise values in an epoch when other model parameters are similar. A maximum S4 limit for L1 and L2 signals was assigned as 0.685, with missing values set equal to the maximum limit, to maintain strong amplitude scintillation and reduce quadratic tracking jitter growth effects near the model limit. Although it seems this

S4 limit may impose a strict threshold on the tracking jitter outputs, the tracking error model is exponentially dependent on the signal-to-noise ratio, which is not modified other than occasional repairs.

Phase spectral slope data were limited to respective minimum and maximum values equal to 1.15 and 3.0, with missing data assigned the maximum limit value to reduce the modelled scintillation component. Phase scintillation index values were limited to 1.5, as larger values were assumed to be unreliable. These limits were applied to model parameters that have a quadratic relationship to the tracking jitter outputs and normally have less effect than the exponential relationship between tracking jitter and signal-to-noise values. In other words, the tracking jitter outputs are much more sensitive to signal-to-noise values, rather than scintillation indices or other model parameters.

With these modifications to the original Conker et al. (2000) model, both DLL and PLL tracking jitter data were made available for all L1C/A and L2P data at all epochs. Therefore, a 100% activation rate for stochastic model mitigation was made possible, as opposed to the approximate 54% activation rate by Liu et al. (2020) when the L2C signal was substituted for L2P in order to gain better tracking jitter output stability. The following gives details on the repaired model performance and compares tracking jitter noise relative to measurement noise modelled using satellite elevation to amplify reference noise values.

4.3.2 Stochastic model comparison

The variability of Conker et al. (2000) model outputs depend primarily on the signal-to-noise ratio and scintillation indices for each signal due to respective exponential and quadratic relationships within the model. According to Figure 4.11, the overall GPS L1C/A signal quality is superior to the L2P signal, with respective mean CN0 values equal to 46.5- and 33.2-dB-Hz. Furthermore, the highly variable L2P signal-to-noise ratio varies between 45.3- to 3.3-dB-Hz, while the worst L1C/A signal faded to only 27.3-dB-Hz. Thus, the L2P signal tracking jitter is frequently modelled as high-noise relative to the L1C/A signal, even when scintillation components are removed from the Conker et al. (2000) model. This is due to the exponential relationship between the signal-to-noise ratio and tracking jitter in Equations 2.17 and 2.18 of the Conker et al. (2000) tracking error model. If the

Figure 4.11 CN0 data are available to the user, then a stochastic model using only signal-to-noise data can replace the typical satellite elevation-based model (Wieser and Brunner 2000). However, the Conker et al. (2000) model includes additional scintillation and thermal noise components and is therefore likely better suited for environments affected by ionospheric scintillation.

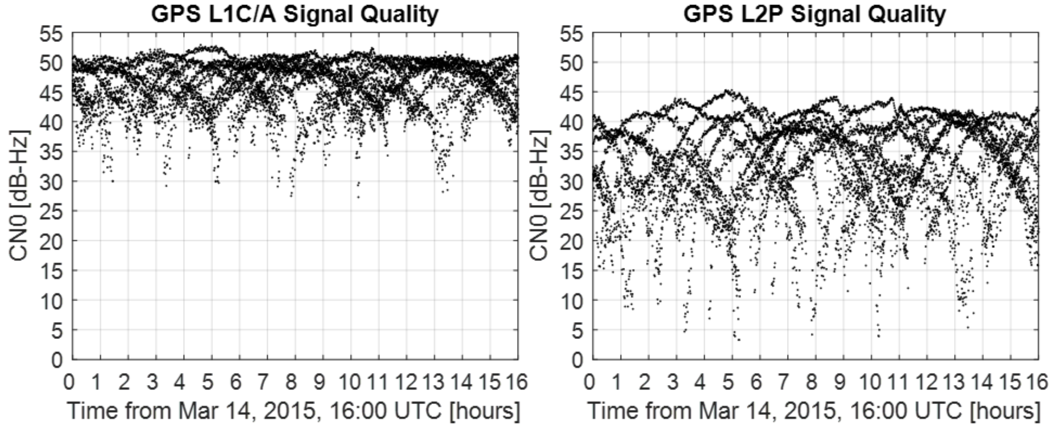

Figure 4.11. Station PRU2 GPS L1C/A (left) and L2P (right) signal quality represented by signal-to-noise ratio values for satellites above 10-degrees in elevation from March 14, 2015 (16h UTC) to March 15, 2015 (08h UTC).

The large L2P noise amplification, relative to the superior GPS L1C/A signal, is more prominent in the Figure 4.12 tracking jitter, computed with scintillation components included in the Conker et al. (2000) model. Note that a logarithmic scale is used to view the large range of tracking jitter values for the L2P signal. The respective median DLL and PLL jitter ratio (L2:L1) for Figure 4.12 data, equal to 6.0 and 1.5, shows that both code and carrier phase measurements are modelled with overall amplified L2P signal noise relative to the L1C/A signal. Therefore, the Conker et al. (2000) tracking error model appropriately assigns higher noise values to the GPS L2P signal that is more susceptible to ionospheric scintillation (Kintner et al. 2007; Jiao and Morton 2015).

However, the larger DLL jitter ratio, with respect to the PLL jitter, indicates better overall modelled carrier phase measurement noise stability regardless of frequency. Consequently, the PLL tracking jitter is more frequently modelled with noise characteristics similar to a standard satellite elevation stochastic model that applies equal noise for each measurement type. For comparison, the DLL tracking jitter is more frequently modelled with unequal noise properties on each frequency, with approximately six times more L2P noise than that of the L1C/A signal. This amplification of L2 signal jitter with respect to the L1 signal can reach more extreme levels as the modelled tracking jitter values increase. For example, the approximate 30-cm L1 signal DLL jitter in Figure 4.12 corresponds to around 10-meters of L2 signal DLL jitter, which is more than thirty times larger than the L1 signal jitter. Lastly, the increased spread that accompanies large tracking jitter values indicates that the highly variable underlying scintillation indices and signal-to-noise ratio values produce rapid fluctuations in the modelled measurement noise.

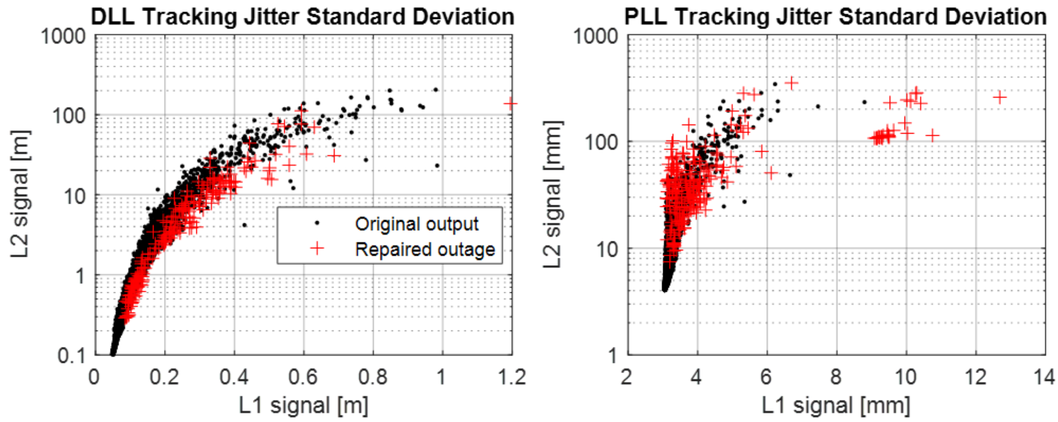

Figure 4.12. Station PRU2 GPS L1C/A and L2P signal Conker DLL (left) and PLL (right) tracking jitter for available (black circles) and repaired (red crosses) input data.

Satellite elevation angle and tracking jitter stochastic model statistics are presented in Table 4.10 and Table 4.11. The ionosphere-free propagated (L_{IF}) pseudorange and carrier phase measurement noise for combined GPS L1C/A and L2P signals use Equation 2.6 coefficients propagated according to the root-squared sum of the individual jitter components. For the elevation-based approach, the reference noise value was set to equal 30-cm and 0.01-cycles (approximately 2-mm) for respective code and carrier phase measurements regardless of the measurement frequency. Reference noise values were then amplified by the elevation-based stochastic model scale factors equal to the inverse sine of minimum and maximum satellite elevation angles; 10.0-, and 90-degrees, respectively. The mean and median of individual and combined signal noise are also provided along with the 95th percentile noise, defined as *n*% probability of randomly selected data being less than or equal to the *n*th percentile value. Note that the 95th percentile was computed using measurement noise data for satellites above 50-degrees in elevation (2144 samples) to compare stochastic models of assumed high-quality measurements. In terms of overall representative statistics, the mean tracking jitter values in Table 4.10

and Table 4.11 are skewed toward the extreme upper limit values. Therefore, median values are also presented to represent the most common measurement noise values for each stochastic method.

Table 4.10. GPS L1C/A, L2P and propagated ionosphere-free (L_{IF}) pseudorange measurement noise statistics for satellite elevation angle and tracking jitter stochastic models.

	Elevation-based noise [m]			Tracking jitter noise [m]		
Statistic	L1C/A	L2P	L_{IF}	L1C/A	L2P	L_{IF}
Mean	0.64	0.64	1.92	0.12	2.73	6.95
Median	0.51	0.51	1.52	0.09	0.54	1.38
Minimum	0.30	0.30	0.89	0.05	0.10	0.26
Maximum	1.73	1.73	5.15	1.20	205.27	522.58
95th percentile*	0.39	0.39	1.15	0.08	0.32	0.83

*Note: Percentile computed for satellites above 50-degrees in elevation.

The minimum propagated code measurement noise for the elevation-based approach in Table 4.10 is more than three times larger than the propagated tracking jitter noise. This difference in lower boundaries is due to the less precise 30-cm reference noise applied to the elevation-based noise amplification method. At the upper limit, the maximum L2P tracking jitter (205.27-m) is the primary component of the corresponding 522.58-m propagated noise which is more than 100 times larger than the maximum elevation-based propagated noise. Thus, the mean propagated tracking jitter is 3.6 times larger than the elevation-based method even though the 30-cm reference noise is at least three times larger than the minimum tracking jitter for individual signals.

The Table 4.10 median propagated tracking jitter (1.38-m) is comparable to the same elevation-based statistic (1.52-m) which indicates agreement between stochastic models in terms of the most common modelled noise values. However, median tracking jitter noise for individual L1C/A and L2P signals are 5.6 times smaller and 1.1 times larger, respectively, than the corresponding elevation-based values. Therefore, the apparent agreement between stochastic models is largely due to the similar median L2P noise values and the Equation 2.6 coefficients used for error propagation in the ionosphere-free combination. This indicates that the *a priori* zenith reference noise value amplified by the elevation-based scale factor is frequently in agreement with the corresponding tracking jitter noise for the L2P signal, while the upper noise limits of the tracking jitter method are the source of the large average differences. Indeed, the 95th percentile statistics also show similar agreement for individual and propagated L2P signal noise between stochastic methods, with overly pessimistic elevation-based L1C/A signal noise compared to the tracking jitter approach.

For carrier phase measurement noise statistics in Table 4.11, the measurement noise modelled using satellite elevation angle is less than the tracking jitter method for nearly all individual and ionosphere-free propagated noise values, aside from the mean L1C/A signal noise that is 28.1% larger than the comparable tracking jitter value. The median individual L1C/A and L2P signal tracking jitter and propagated noise are within 10.0% of corresponding elevation-based noise values, which indicates overall frequent agreement between stochastic models. On the other hand, the worse agreement for maximum propagated noise and individual L2P signal noise shows that the tracking jitter approach applies more extreme noise amplification at the upper noise limit, as was the case for the DLL tracking jitter noise.

Table 4.11. Individual and propagated ionosphere-free (L_{IF}) GPS L1C/A, L2P signal carrier phase measurement noise statistics for satellite elevation angle and tracking jitter stochastic models.

	Elevation-based noise [mm]			Tracking jitter-based noise [mm]		
Statistic	L1C/A	L2P	L_{IF}	L1C/A	L2P	L_{IF}
Mean	4.1	5.2	14.7	3.2	9.2	24.2
Median	3.2	4.2	11.7	3.1	4.6	12.7
Minimum	1.9	2.4	6.9	3.0	4.0	11.3
Maximum	11.0	14.1	39.6	12.7	351.9	895.9
95th percentile*	2.4	3.1	8.8	3.1	10.6	27.4

*Note: Percentile computed for satellites above 50-degrees in elevation.

The individual signal 95th percentile carrier phase measurement noise in Table 4.11 shows relatively good agreement between stochastic models for the L1C/A signal, to below 1 mm, while the tracking jitter noise for the L2P signal is up to 3.4 times larger than the elevation-based counterpart. Therefore, for relatively high-elevation satellites, the elevation-based method may overestimate the L2P signal precision, i.e., underestimate the L2P signal noise, compared to the tracking jitter approach. Thus, variability in the propagated ionosphere-free carrier phase measurement noise is almost entirely due to the stochastic model differences for the

L2P signal, even for satellites observed at high elevations. These differences can be explained by the nearly identical *a priori* measurement noise values (e.g., 0.01-cycles) assigned to both the L1C/A and L2P signals in the elevation-based approach, while the tracking jitter method models the L2P signal as having more noise relative to the L1C/A signal.

The large differences between the elevation-based and tracking jitter-based stochastic methods destroys consistency that is needed to evaluate both techniques in the positioning domain. For this reason, the 95th percentile tracking jitter values in Table 4.10 and Table 4.11 were used as *a priori* zenith reference noise values in the elevation-based approach for individual L1C/A and L2P signals. This approach adjusted the elevation-based method to the 95th percentile tracking jitter-based code and carrier phase measurement noise for satellites above 50-degrees in elevation. Therefore, the resulting 3D positioning error time-series in Figure 4.13 uses similar measurement noise characteristics for satellites observed at high elevation regardless of the stochastic model.

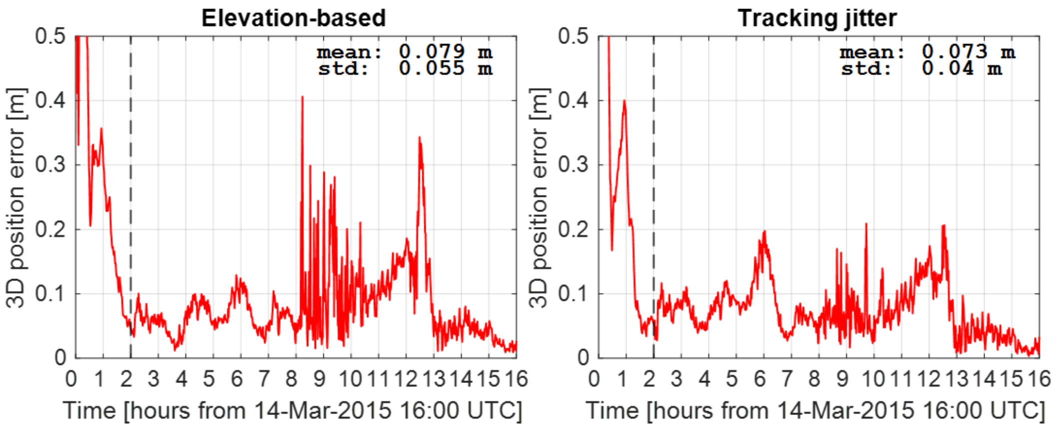

Figure 4.13. Station PRU2 3D kinematic PPP error using elevation-based (left) and tracking jitter (right) stochastic models from March 14, 2015 (16h UTC) to March 15, 2015 (08h UTC).

After the initial positioning convergence period, the 3D positioning error for both stochastic methods are only separated by up to 5.3-cm until strong scintillation conditions begin at approximately 00h UTC on March 15. Thus, the overall post-convergence mean and standard deviation of the 3D position error for both methods are in agreement at the mm- and cm-level, respectively. However, when the tracking jitter approach is used under strong scintillation (i.e., 00h to 05h UTC on March 15), the maximum 3D position error is reduced by nearly 50%, from 40.6-cm to 20.9-cm, compared to the elevation-based model. The tracking jitter method additionally improves 3D positioning error by 13.6-cm (39.7%) at 04:30 UTC (i.e., 12h 30m after the start of processing), which is the second worst epoch for elevation-based processing.

The ionospheric scintillation mitigation properties of the tracking jitter approach can be more easily understood by the Figure 4.14 carrier phase measurement noise time-series for an individual satellite, SVID 3. In Figure 4.14, the satellite ascends to above 60-degrees in elevation at 01:29 UTC, on March 15, and reaches a maximum elevation equal to 68.9-degrees at 02:17 UTC. During this period, the satellite elevation angle is larger than all other satellites and is therefore assigned a relatively small 15.5% measurement noise amplification using the elevation-based stochastic model. In contrast, the scintillation-sensitive tracking jitter method amplifies the nominal pre-scintillation L2 signal measurement noise from 4.3-mm up to 29.1-mm during the same period, which is more realistic given the strong scintillation scenario.

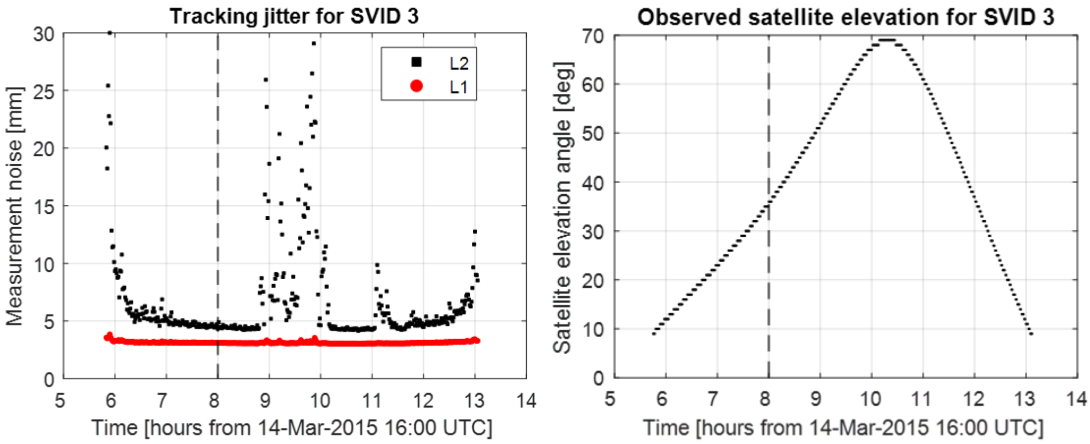

Figure 4.14. Station PRU2 L1 (red circles) and L2 (black squares) carrier phase measurement noise modelled using PLL tracking jitter (left) and satellite elevation angle (right) for GPS SVID 3 under strong ionospheric scintillation beginning after 00h UTC on March 15 (black dashed line).

Thus, high elevation satellites are not immune to ionospheric scintillation effects (Luo et al. 2018) and are especially problematic for elevation-based stochastic models when scintillation occurs for satellites observed at high elevation angles. Conversely, if only low elevation satellites are affected by scintillation, then the elevation-based stochastic approach may provide adequate measurement noise amplification for affected satellites to achieve high-accuracy positioning. For these reasons, mitigated and non-mitigated positioning may achieve similar performance under certain conditions even though the elevation-based approach does not aim to mitigate ionospheric scintillation effects.

To enable multi-GNSS scintillation-mitigated processing, Conker et al. (2000) tracking error models that are updated to use scintillation indices and signal-to-noise ratio values for Galileo E1 and E5a signals. This approach uses data extracted from ISMR files that is provided for Galileo satellites. The tracking jitter repair methods developed for GPS signal processing were extended to Galileo signals. Receiver tracking loop parameters and PLL oscillator noise were fixed to the same values for both GPS and Galileo processing.

4.3.3 Relative tracking jitter approach

The transfer of ISMR-based scintillation data to other locations was first proposed using regional tracking jitter maps (Sreeja et al. 2011b) due to consistent scintillation outputs at multiple locations (Sreeja et al. 2011a). However, non-ISMR users that aim to incorporate tracking jitter data do not operate at the same precision as ISMRs, which are designed to resist ionospheric scintillation. Furthermore, non-ISMR users typically do not have access to the internal tracking loop parameters that define the measurement noise characteristics of tracking error model outputs.

Missing tracking jitter data may occur in the presence of model outages, or when tracking jitter map products are queried outside the extents provided. These cases eliminate satellites that would otherwise be useable for positioning estimation, as the mitigated stochastic model is not available for all measurements. To address this concern, a mixed stochastic approach using a combination of mitigated and non-mitigated models has been used previously (Elmas 2013; Luo et al. 2020). However, common satellite elevation-based and tracking jitter mitigated stochastic models are not compatible in all cases. Therefore, an innovative alternative representation of tracking jitter data is developed in this section to enable incorporation of ISMR-based tracking jitter for non-ISMR users and to improve the mixed stochastic model for multi-GNSS positioning.

The first step to ensure compatibility between stochastic methods is the normalization of tracking jitter data with respect to the minimum (i.e., most precise) value in each epoch for each signal. This normalization replaces the original tracking jitter values with relative values, where the most precise value is scaled to equal 1.0

and the remaining values are scaled relative to the minimum value. A single epoch is provided in Table 4.12, with GPS SVID 1 having the lowest DLL and PLL tracking jitter out of all other satellites in the epoch, primarily because it has the largest signal-to-noise ratio (51.5 dB-Hz) of all satellites in the epoch. Coincidentally, the same satellite is also at the maximum elevation angle (64.3-degrees) of all GPS satellites in the epoch.

Table 4.12. Original, normalized, and scaled GPS L1 DLL and PLL tracking jitter for station PRU2 on 14-Mar-2015 01:18 UTC.

	Original		Normalized		Scaled	
SVID	L1 DLL [m]	L1 PLL [mm]	L1 DLL [-]	L1 PLL [-]	L1 DLL [m]	L1 PLL [mm]
1*	0.055	3.047	1.000	1.000	1.113	2.117
3	0.068	3.056	1.231	1.003	1.369	2.124
4	0.145	3.341	2.629	1.097	2.925	2.322
7	0.273	3.446	4.956	1.131	5.514	2.395
9	0.136	3.141	2.473	1.031	2.751	2.182
11	0.085	3.076	1.533	1.010	1.706	2.137
16	0.163	3.182	2.961	1.044	3.294	2.211
23	0.064	3.057	1.164	1.003	1.295	2.124
31	0.151	3.156	2.733	1.036	3.041	2.193
32	0.078	3.067	1.416	1.007	1.575	2.132

Note: *minimum tracking jitter noise used for normalization

The tracking jitter normalization effect can be observed in Table 4.12, where DLL and PLL values for SVID 1 values are equal to 1.0, as it is the most precise. All other DLL and PLL values are scaled using values greater than 1.0, as they are relatively less precise than SVID 1. From Table 4.12, it can be observed that the least precise DLL tracking jitter noise, i.e., SVID 7, is nearly five times larger than the most precise one, while the largest PLL tracking jitter noise is only 13.1% larger than the most precise PLL tracking jitter noise in the epoch. This is in agreement with the findings in the previous section, where GPS L1 tracking jitter was found to be relatively stable, especially for the PLL.

After normalized tracking jitter values are computed, the tracking jitter must be made consistent with satellite elevation-based stochastic model outputs in order to use both stochastic models together. This process first amplifies the code and carrier phase reference noise values using the elevation-based stochastic model applied to the maximum elevation angle observed in each epoch. In Table 4.12, this corresponds to an 11.3% noise amplification of the original 1.0-meter and 0.01-cycle respective code and carrier phase measurement reference noise values, as the maximum GPS satellite elevation angle in the epoch is only 64.3-degrees. Then, the normalized tracking jitter values are multiplied by the amplified elevation-based noise to scale the respective DLL and PLL tracking jitter relative to the most precise elevation-based noise values. As an example, the minimum normalized L1 PLL tracking jitter in Table 4.12 is equal to 1.0 prior to scaling and 2.117-mm after scaling. This is because the 2-mm elevation-based reference noise was amplified by 11.3% and then multiplied by the normalized PLL tracking jitter value.

Scaling the normalized tracking jitter essentially configures the lower noise boundary of the stochastic model because the most precise modelled noise values are used as an upper precision limit. However, the consistency between stochastic models at the upper noise boundary must also be addressed. In the previous section, it was shown that the GPS L2 signal can be modelled with several hundred times more noise using the tracking jitter approach when compared to the satellite elevation-based model. Therefore, the final step of the proposed relative tracking jitter technique replaces large noise values with the absolute maximum noise from the elevation-based model. This corresponds to the minimum satellite elevation angle, which is configured by a satellite elevation mask used for PPP processing. In this case, a 10-degree satellite elevation mask was used. The elevation-based measurement noise amplification factor for a satellite observed at 10-degrees in elevation is equal to 5.76. Therefore, if a normalized and scaled tracking jitter noise value exceeds this limit, then it is assigned the limit value (i.e., 5.76 times the respective code and carrier phase reference noise values in the zenith direction).

The relative tracking jitter data presented in Figure 4.15 shows the modelled stochastic properties of individual Galileo and GPS satellites for individual signals observed at station PPTE on March 7, 2019. For the Galileo E5a signal in Figure 4.15, the maximum noise limit is enforced for 92.3% of epochs from 23:31 UTC (March 7) to 00:10 UTC (March 8) due to large tracking jitter values exceeding the maximum elevation-based noise. During the same interval, the Galileo E1 signal experiences minor noise amplification up to 3.4-mm using the tracking jitter approach, while the corresponding elevation-based noise is more than 6-mm. In this case, where the elevation-based noise is larger than the tracking jitter noise, the stochastic properties of the Galileo E1 signal are assigned equal to the tracking jitter noise.

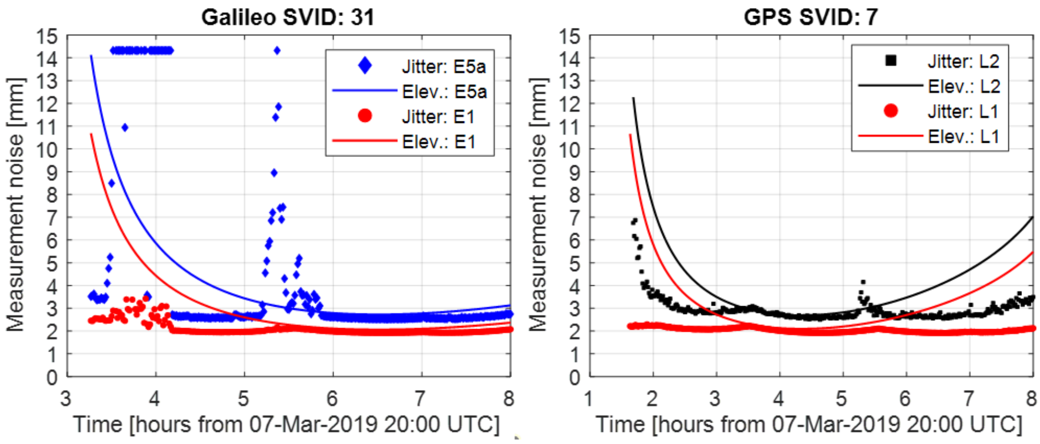

Figure 4.15. Relative tracking jitter (markers) and elevation-based (lines) carrier phase measurement noise for a Galileo (left) and GPS (right) satellite observed at station PPTE on March 7, 2019 (DOY 066).

An advantage of the relative tracking jitter method, using normalization then scaling, is evident in Figure 4.15 at the beginning and end of the GPS SVID 7 observation arc. During these periods, the elevation-based noise rapidly increases while tracking jitter noise remains at low values for the GPS L1 signal. It is assumed that the signal-to-noise ratio is a reasonable indicator of the true measurement noise and can be used to evaluate the two stochastic methods. Therefore, the stable measurement noise modelled by the tracking jitter approach is unnecessarily amplified by the elevation-based model, as the minimum GPS L1 signal-to-noise ratio in the entire arc is 39.5 dB-Hz. For comparison, the corresponding GPS L2 signal-to-noise ratio is below this minimum value for 51.5% of epochs in the arc, indicating that the true noise for the GPS L1 signal measurements is likely much lower than the GPS L2 signal.

Another noteworthy period in Figure 4.15 is from 01:33 UTC to 03:00 UTC (March 8) for the Galileo satellite and from 23:31 UTC to 23:59 UTC (March 7) for the GPS satellite; note that hour 4 corresponds to 00:00 UTC on March 8. In these respective intervals, the Galileo and GPS satellites are at the maximum elevation of all satellites in each epoch. Therefore, the normalization and scaling steps of the relative tracking jitter technique can be observed in Figure 4.15, where the tracking jitter and elevation-based measurement noise are aligned when the respective satellites are at maximum elevation. This alignment between the stochastic models ensures consistency when, for example, tracking jitter values are not available for a non-specialized GNSS receiver that aims to mitigate ionospheric scintillation effects using a tracking jitter-based modified stochastic model.

4.3.4 Mitigated multi-GNSS performance

The six intervals in Figure 4.16 were identified as having the most frequent strong scintillation occurrences (S4 > 0.5) in March 2019. In Figure 4.16, the local sunset time begins at approximately UTC midnight (00:00 UTC), with relatively calm scintillation conditions prior to the post-sunset interval. Note that the same 10-degree elevation mask was applied to the scintillation index data to be consistent with the following positioning estimation. Starting at approximately UTC midnight, strong scintillation becomes more frequent and is severe enough to cause tracking jitter outages in each of the six intervals in Figure 4.16. However, tracking jitter outages occur for approximately one hour during the DOY 061-062 interval, while the DOY 060-061 interval required repairs during a six-hour period. Therefore, both scintillation strength and duration are varied in the selected intervals.

Kinematic PPP using GPS L1C/A and L2P with Galileo E1C and E5 measurements for the six intervals in March 2019, beginning at 20:00 UTC, was processed for elevation-based (non-mitigated) and tracking jitter (mitigated) stochastic models. Note that the Table 4.2 configurations were used with nominal code measurement noise set equal to 1.0-meter for all satellites. The resulting 3D positioning error time-series in Figure 4.17 and Figure 4.18 shows that the maximum post-convergence errors occur when the elevation-based stochastic model is used. Note that individual positioning error components are provided in Appendix D for each configuration. In terms of overall performance, the mean post-convergence 3D error improved when the tracking jitter stochastic model was used for five of the six intervals, with a 1.2-cm mean error increase (-14.0% improvement) during the DOY 066-067 interval. For the remaining intervals, mean 3D positioning error improved by at least a mm-level and up to 3.3-cm (36.3% improvement). Thus, the mitigated GPS+Galileo positioning accuracy is either consistent with the elevation-based approach or achieves cm-level improvement, in terms of overall 3D post-convergence, kinematic PPP accuracy under moderate to strong low-latitude ionospheric scintillation conditions. However, it will be shown next that the tracking jitter approach offers excellent improvement in terms of the single-epoch worst-case position, relative to the standard elevation-based method.

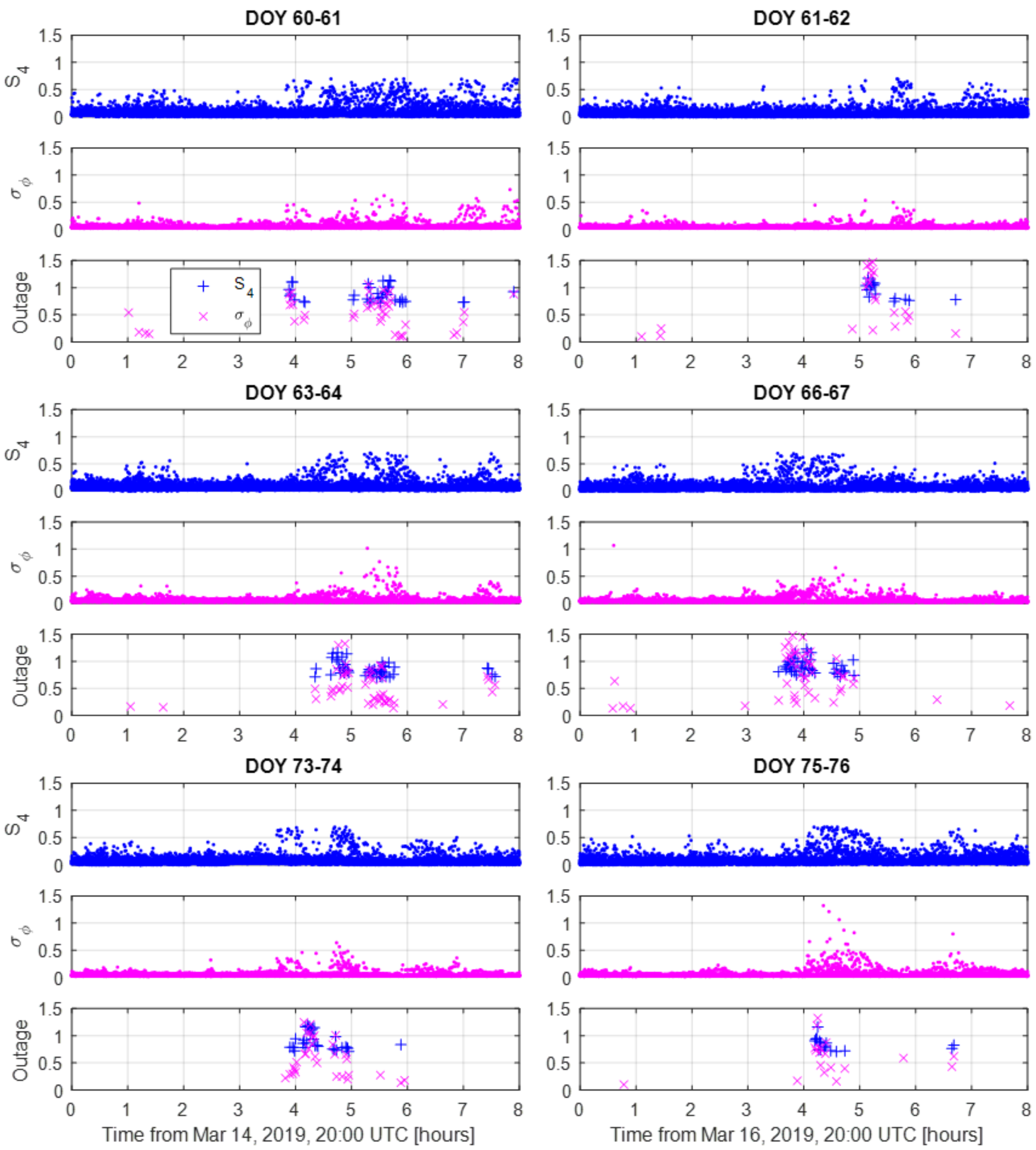

Figure 4.16. Station PRU2 GPS L1C/A and Galileo E1C signal amplitude (blue circles) and phase (magenta circles) scintillation indices and corresponding Conker et al. (2000) tracking jitter outages (blue plus and magenta cross markers, noted in top-left legend) during six intervals beginning at 20:00 UTC in March 2019 identified as having strong scintillation.

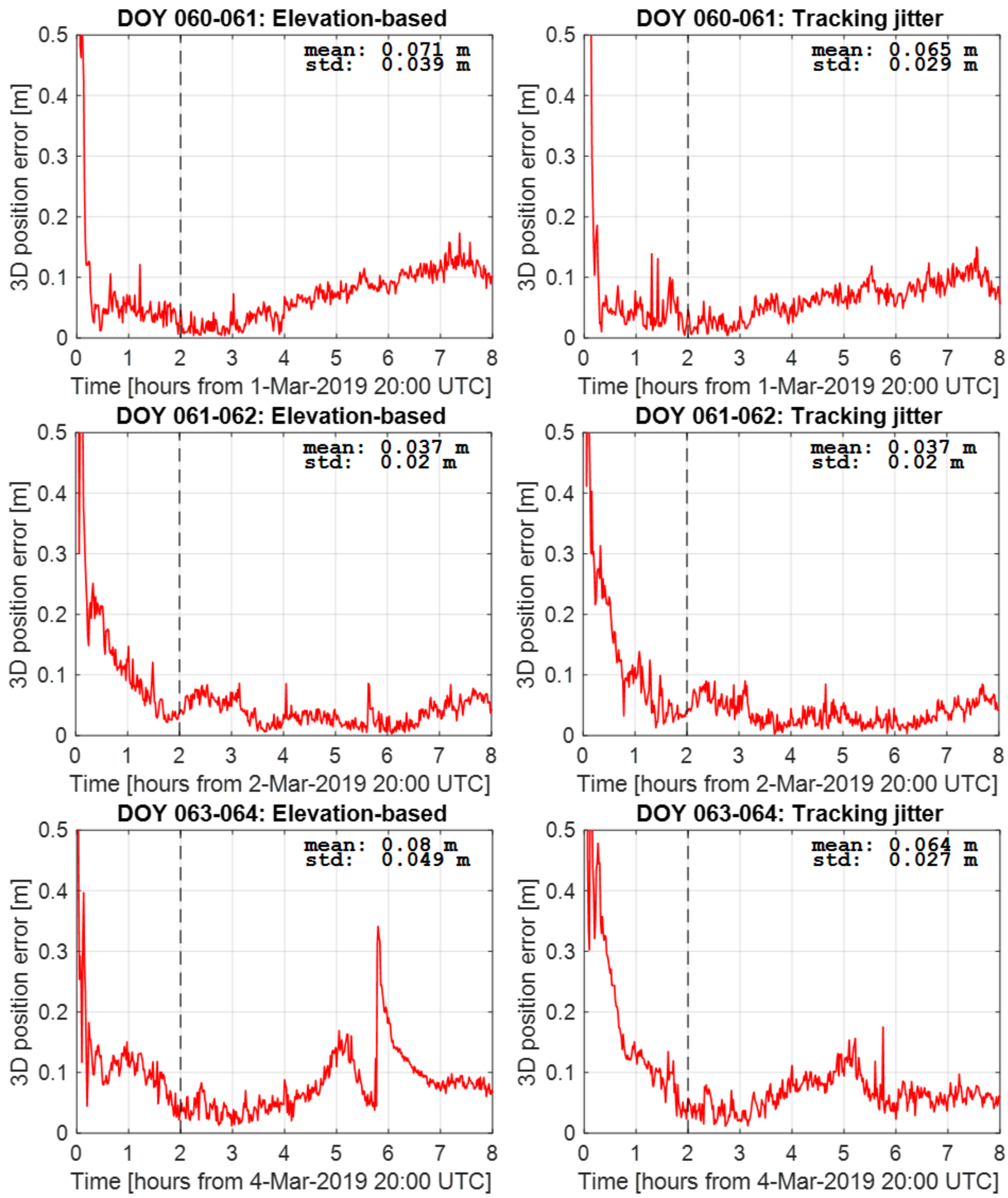

Figure 4.17. Elevation-based (left) and tracking jitter (right) stochastic models used for kinematic PPP processing of GPS+Galileo measurements observed at station PPTE on DOYs 060-061, 061-062, and 063-064 beginning at 20:00 UTC.

The remarkable performance of the modified tracking jitter approach is highlighted during the DOY 063-064 interval in Figure 4.17 and the DOY 066-067 interval in Figure 4.18, where respective maximum 3D positioning error improved by 16.6-cm (46.7% improvement) and 13.6-cm (37.4% improvement) relative to the elevation-based method. The sudden increase in the elevation-based 3D positioning error on DOY 063-064, after approximately 5-hours from the start of processing, is due to multiple ambiguity reinitializations for three satellites. In this case, ambiguity parameters for GPS satellites SVID 6 and SVID 7 are reinitialized in a single epoch due to low-quality post-fit measurement residuals, which resulted in subsequent ambiguity reinitialization for Galileo satellite SVID 1 in the same epoch. For the tracking jitter approach at the same epoch, only a single ambiguity parameter is reinitialized for GPS satellite SVID 28. Based on the superior 3D positioning performance for the tracking jitter approach in Figure 4.17, it can therefore be concluded that the ambiguity reinitializations for the elevation-based method were incorrect and weakened the positioning model. Furthermore, the evaluation of post-fit measurement residuals relative to the corresponding modelled measurement noise is more successful when the elevation-based stochastic model is replaced with the new tracking jitter technique. Thus, it can be concluded that the tracking jitter technique estimates the true measurement noise better than the elevation-based approach under ionospheric scintillation conditions.

Mitigated processing using the new tracking jitter technique additionally improved the maximum 3D position error by 9.7-cm (31.0% improvement) and 4.7-cm (29.5% improvement) during the respective DOY 073-074 and DOY 075-076 intervals. Similar positioning performance was achieved during the DOY 060-061 and DOY 061-062 intervals regardless of the stochastic model, with respective worst-case mitigated 3D error better than the non-mitigated by 2.3-cm and 0.6-cm. Thus, the tracking jitter mitigation method does not simply shift the worst-case positioning error to a new epoch and is consistent with an elevation-based stochastic approach in the absence of large positioning errors.

In terms of precision, the standard deviation of the converged 3D positioning error was 2-mm worse (-4.3% improvement) for the tracking jitter method during the DOY 066-067 interval and identical at the mm-level during the DOY 061-062 interval relative to the elevation-based approach. The remaining intervals improved positioning precision by at least 25.6% (on DOY 060-061) and up to 44.9% (on DOY 063-064), when the tracking jitter method was used. Therefore, mitigated GPS+Galileo processing can at least achieve comparable precision as the elevation-based approach, with the potential for large improvements when elevation-based processing is otherwise not adequate.

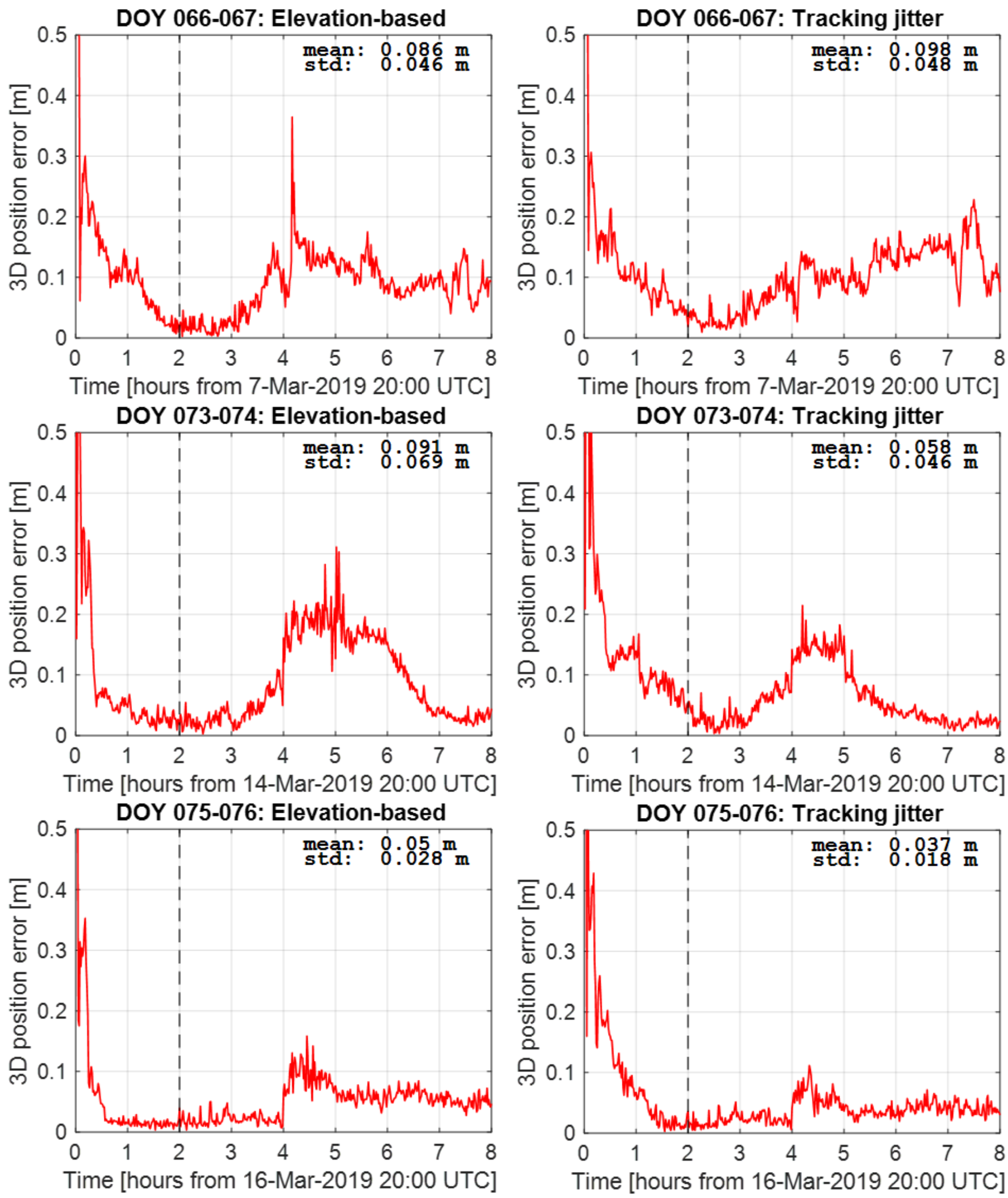

Figure 4.18. Elevation-based (left) and tracking jitter (right) stochastic models used for kinematic PPP processing of GPS+Galileo measurements observed at station PPTE on DOYs 066-067, 073-074, and 075-076 beginning at 20:00 UTC.

4.3.5 Remarks

To evaluate scintillation-mitigated multi-GNSS kinematic PPP performance, GPS L1C/A and L2P with Galileo E1C and E5 measurements for the six intervals in March 2019, beginning at 20:00 UTC, were processed for elevation-based (non-mitigated) and tracking jitter-based (mitigated) stochastic models. The station selected for positioning estimation is a non-specialized GNSS receiver located within a few hundred meters from a specialized ISMR that was used to characterize scintillation conditions. Moderate to strong amplitude and phase scintillation conditions were observed during each of the evaluated periods.

The nearby ISMR outputs were used in the Conker et al. (2000) tracking error models with a modified stochastic approach (Aquino et al. 2009) to mitigate ionospheric scintillation effects. First, the tracking error model outputs were extended to use Galileo signals that were in similar frequency bands as were used in PPP processing. Next, tracking error model limits were applied to make tracking jitter-based ionospheric mitigation techniques usable for all epochs. Innovative normalization and scaling methods were developed and applied to create relative tracking jitter. This process enabled compatibility between the tracking jitter and elevation-based stochastic models so that a mixed stochastic approach could be applied to the non-specialized receiver.

In all six cases, the maximum 3D positioning error for the modified tracking jitter method was better than the elevation-based approach, with up to 46.7% improvement in the best case. The post-convergence maximum 3D positioning error for the mitigated technique improved by 16.6-cm (46.7% improvement) and 13.6-cm (37.4% improvement) relative to the elevation-based method in the two best cases. The modified tracking jitter technique resulted in a reinitialization for a single ambiguity parameter at the worst single-epoch on DOY 063-064, while the elevation-based approach reinitialized multiple ambiguities. These reinitializations increased the nominal 5-10-cm 3D positioning error to more than 30-cm for the elevation-based method, while the maximum tracking jitter error remained below 20-cm in the same interval. In addition, it was found that these reinitializations were caused by disagreement between the post-fit measurement residuals and the measurement noise estimated by the stochastic models. Therefore, it is concluded that the measurement noise modelled using the tracking jitter approach is more realistic in some scenarios.

Four of six intervals achieved at least 25.6% precision improvement, in terms of the standard deviation of the post-convergence 3D positioning error time-series, when the tracking jitter method was used. In the best case, the tracking jitter approach improved precision by up to 44.9%. Remaining intervals had similar precision regardless of the stochastic method at an approximate mm-level. For these reasons, it is concluded that the modified tracking jitter approach at least offers similar 3D positioning precision as the elevation-based method and achieves better stability compared to the otherwise unreliable elevation-based method.

In terms of overall performance, represented by the mean 3D positioning error, the mitigated GPS+Galileo positioning accuracy was consistent with the elevation-based approach at an approximate cm-level. The reliability, represented by the standard deviation of the 3D positioning error, improved by at least 25.6% for five of the six evaluated intervals when the mitigated GPS+Galileo configuration was used, with only 2-mm worse reliability for the remaining interval. These improvements indicate that multi-GNSS processing under some low-latitude scintillation conditions can be further enhanced, in terms of maximum error reduction, when a scintillation-sensitive stochastic model is used, even for a non-specialized GNSS user.

In the future, the repaired tracking jitter and relative approach would benefit from evaluation under additional scintillation conditions, including geomagnetic storms and at high latitude. Additional non-ISMR users may benefit from the new stochastic technique that enables a mixture of elevation-based and tracking jitter methods. For example, if these techniques are implemented in tracking jitter maps, then ionospheric scintillation mitigation coverage may be extended to additional users or for low-cost receivers such as smartphones that may otherwise use a less-realistic stochastic model under ionospheric scintillation conditions.

4.4 Summary

The evaluation of multi-GNSS PPP performance resulted in average horizontal and vertical reliability, accuracy and precision improvements of at least 8.3%, 18.8% and 27.9%, respectively, for GPS+GLONASS processing. Configurations involving Galileo achieved the greatest overall improvements: 19.8% vertical reliability for GPS+GLONASS+Galileo, 39.8% vertical accuracy for GPS+Galileo, and 52.7% vertical precision for GPS+Galileo. Both configurations where Galileo measurements were included provided similar improvements for all evaluation metrics and consistently outperformed GPS-only and GPS+GLONASS processing. The reason for multi-GNSS improvements over the single-system GPS-only processing is due to the increased model redundancy for multi-GNSS processing. It was observed that the configurations using Galileo measurements achieved the best average improvement over GPS-only processing and were up to 20% better than the GPS+GLO configuration, despite GLO and GAL constellations having a nearly identical average number of usable satellites.

A new technique to repair tracking jitter outputs for a specialized scintillation monitoring GNSS receiver successfully enabled activation of a modified stochastic model for all epochs and improved the maximum 3D kinematic PPP error by approximately 50% under strong low-latitude ionospheric scintillation conditions for GPS-only processing. The same methods were then used to extend the repaired mitigation techniques to Galileo E1 and E5a signals. Relative tracking jitter was developed using normalization and scaling to configure the lower measurement noise limit to be compatible with a common elevation-based stochastic model. This method was then applied to mitigate ionospheric scintillation effects on kinematic PPP using GPS+GAL for a non-specialized GNSS receiver relative to elevation-based processing.

The new mitigation technique improved the worst-case (i.e., single epoch) 3D positioning error up to 46.7% in one case where post-fit measurement residuals had better agreement with the tracking jitter noise, which resulted in more accurate ambiguity reinitialization for the tracking jitter method. Improvement in positioning precision, in terms of the 3D positioning error standard deviation, was at least 25.6% for four of the six evaluated periods when the tracking jitter method was used. In terms of overall performance, the average 3D positioning error was in agreement at a nominal cm-level regardless of the stochastic method used. Thus, the mitigation technique is best suited to improve positioning precision and reduce worst-case positioning errors when an elevation-based stochastic model is otherwise unreliable.

Chapter 5

Results on PPP with Atmospheric Corrections

5.1 Introduction

This chapter develops ionosphere-weighted and troposphere-corrected processing methods and evaluates kinematic PPP performance with respect to the standard cases. Although strategies developed herein aim to enhance real-time GNSS applications, precise satellite orbit and clock products are used as substitutes for real-time data products that can be estimated with comparable precision as the precise products when multi-GNSS processing is used (Li et al. 2015). The target scenarios focus on severe weather events, such as increased ionospheric activity in a scintillation-affected low-latitude region and a tropospheric storm at a mid-latitude region. To achieve these objectives, the new methods are developed and evaluated separately for troposphere- and ionosphere-related studies. Regarding the ionosphere sections, RIM data generated from a low-latitude GNSS reference station network in Brazil and GIM data were used to compute TEC rate as input to a modified stochastic model. After biases are properly dealt with, standard and ionosphere-weighted kinematic PPP models were evaluated under highly active ionospheric conditions. For troposphere-corrected processing, precise ZWD corrections were generated from a network of GNSS reference stations affected by a tropospheric storm event in the Netherlands. The ZWD corrections were then interpolated at user locations and kinematic PPP performance was evaluated using correction strategies that rely on progressively more information provided by the reference network.

5.2 Ionosphere-weighted positioning

This section evaluates positioning performance using a modified kinematic PPP stochastic model that relies on global and regional ionospheric map data for GNSS reference stations located in Brazil. Chapter 2 presents the challenges and strategies associated with using external ionospheric data to support high-accuracy positioning. To study the performance of ionosphere-weighted PPP, global and regional ionospheric products were used to compute between-epoch ionospheric delay gradients. Then, the resulting change in the ionospheric state was incorporated into a modified stochastic model. The resulting ionosphere-weighted configurations were evaluated under moderate to low latitude ionospheric activities to study positioning accuracy in terms of maximum and average positioning performance.

5.2.1 Global and regional ionospheric map data at low latitudes

The Brazilian Institute of Geography and Statistics (IBGE) Brazilian Network for Continuous Monitoring of the GNSS Systems (RBMC) RINEX data archive was used by Juliana Garrido Damaceno, of the Istituto Nazionale di Geofisica e Vulcanologia (INGV) as part of the TREASURE project, to generate a low-latitude RIM product from 01h to 23h UTC on DOY 015 in the year 2020. Figure 5.1 shows that the seven IBGE reference stations used to create the RIM are located in the north-eastern region of Brazil and are within ±15-degrees latitude from the geomagnetic equator. The RIM coverage is approximately centred on the State of Piaui, Brazil (8°S, 42°W) with a grid spacing of 1-degree in both latitude and longitude. The RIM extents cover longitudes from 55°W to 29°W and latitudes from 17°S to 6°N with an update rate equal to 60-seconds.

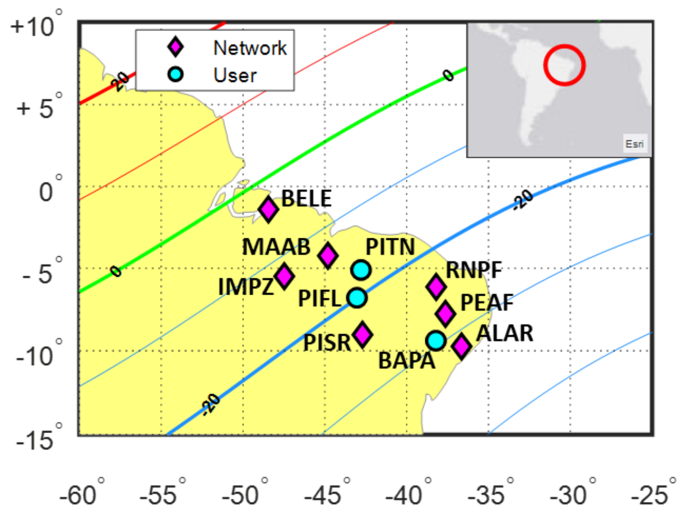

Figure 5.1. Experiment region (top-right inset) and locations of IBGE reference stations (magenta diamonds) used to generate the RIM product for user stations (cyan circles), relative to the geomagnetic equator (green contour) and EIA ionization crests located near ±20-degrees geomagnetic latitude (annotated contours).

The region studied is affected by harsh ionospheric conditions due to the low-latitude location and corresponding EIA effects. Typical ionospheric scintillation conditions for the region are discussed in Chapter 4, which demonstrated that daily moderate to strong ionospheric scintillation occurs frequently. In Figure 5.2, it is shown that the beginning of the UTC day is relatively calm, with the onset of large ionospheric gradients starting at approximately 12h UTC. According to the hourly GIM data shown in Appendix F, these gradients are especially strong in the zenith direction during the post-sunset hours, at approximately 19h UTC. For the hours prior to and immediately after this critical time, the absolute ionospheric delay and associated gradients reach respective maximum values in the day.

The vertical TEC (VTEC) values contained within the external ionospheric maps are provided at uniform time intervals and grid spacing at a representative ionospheric height equal to 350- and 450-km for respective RIM and GIM products. Therefore, for each satellite and epoch, VTEC was calculated using bilinear interpolation of the grid points closest in time and space to the location where the receiver-satellite line-of-sight vector intersects the grid defined by each product. The computed VTEC was then mapped to slant TEC (STEC) for each receiver-satellite link using the well-known Mannucci et al. (1998) mapping function.

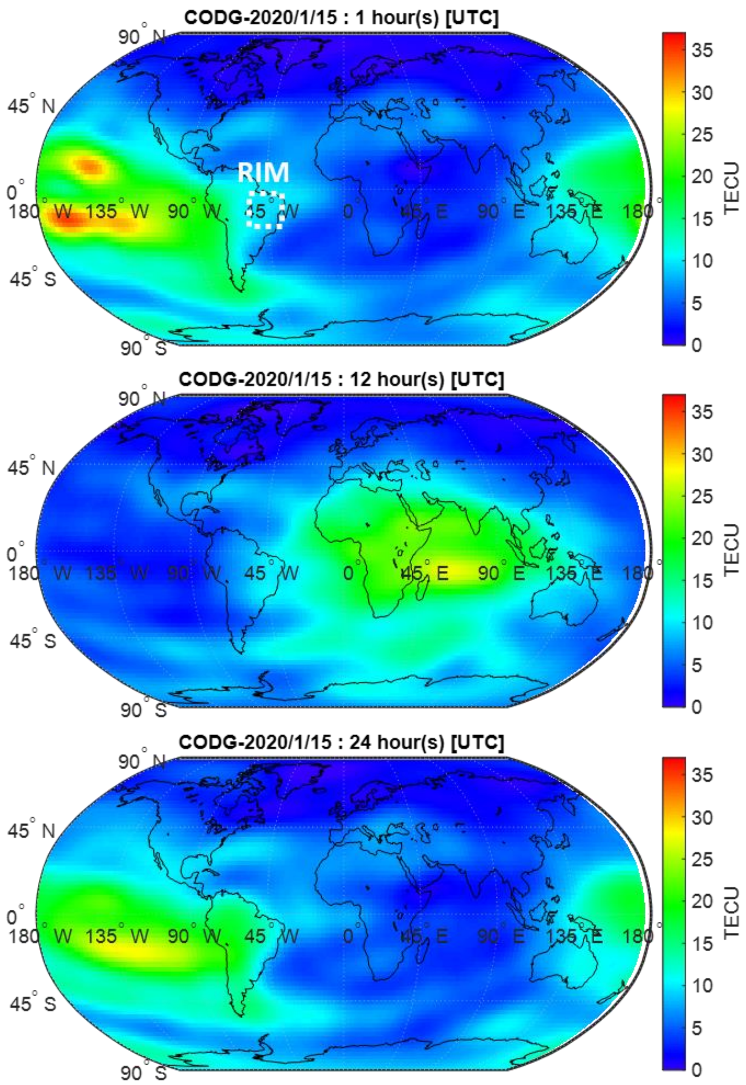

Figure 5.2. CODE GIM product interpolated to a uniform 2.5-degree grid on DOY 15 in 2020 at 01h (upper), 12h (middle) and 24h (lower) UTC. The color scale represents TEC units within each grid cell and the approximate RIM extents are indicated by the white dashed box

Station PITN receiver-satellite links were used to compute the Figure 5.3 GPS L1 signal slant ionospheric delay time-series for GIM and RIM products. According to Figure 5.3, the GIM product contains less per-epoch variation relative to the RIM. This relative time stability of the GIM product data can be seen as smooth curves in the Figure 5.3 time-series for each satellite. The maximum single-epoch ionospheric delays in Figure 5.3 are 11.658- and 8.285-m, respectively, for GIM and RIM products. This difference is absolute maximum ionospheric delay is likely due to a higher 20-degree satellite elevation cutoff limit being used for the generation of the RIM product, compared to the 10-degree elevation threshold applied for the GIM product. In addition, the experimental RIM product relies only on GNSS measurements from within a relatively small region, while the GIM product incorporates GNSS reference stations on a global scale.

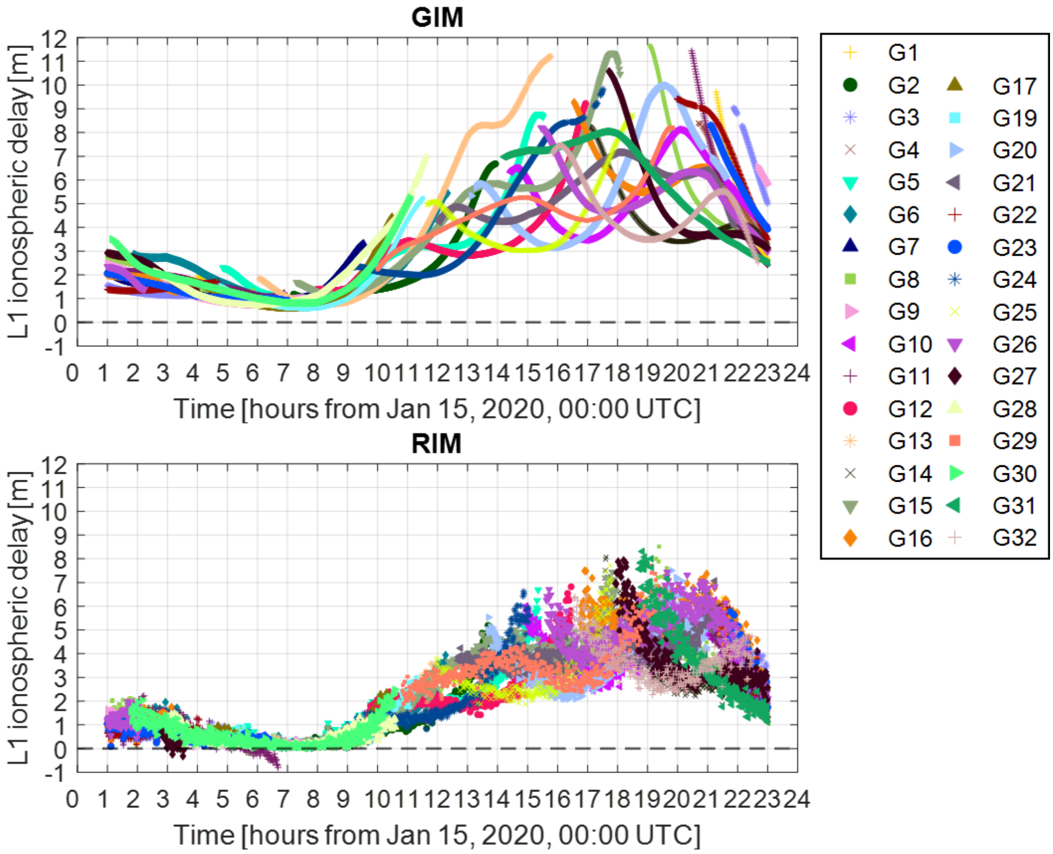

Figure 5.3. GPS L1 signal slant ionospheric delay using CODE GIM (upper) and experimental RIM (lower) products for all satellites above 10-deg in elevation (satellites are assigned unique colors) observed at station PITN from 01h to 23h UTC on DOY 015 in 2020.

Outages for the RIM data occur for 2.27% of epochs and are counted when the RIM-computed STEC is either unavailable, due to a satellite's location below the map extents, or if a negative VTEC value is encountered. Slant ionospheric delays were available for all satellites at all epochs using the GIM data, while 540 slant delays were not available using the RIM. For example, although station PISR is within the RIM extents, a valid slant delay for some satellites above a 20-degree elevation mask failed to be computed because the pierce point coordinates were outside the map extents. This can be explained by the location of station PISR being located less than 10-degrees in latitude away from the southern boundary of the RIM extents. Satellites that experienced this failure were flagged with a zero-valued slant delay and excluded from the positioning filter until valid data were retrieved from the map. In addition, 29 negative STEC values were computed using the RIM product and the corresponding satellites were therefore excluded from the filter at the affected epochs.

5.2.2 Satellite and receiver bias effects

Ionosphere-free code and carrier phase measurements for GPS L1 and L2 signals at a 60-second epoch rate were processed for all user stations and network station PISR (9° 1'S, 42° 42'W) using the custom RIM and standard CODE GIM products. If an undifferenced and uncombined model were used instead, then the precise satellite clock product, which contains the true satellite clock offset and ionosphere-free satellite code hardware delays, as shown in Equations 2.7 and 2.8, would require additional correction. However, in an ionosphere-free model, only satellite specific P1-C1 code bias corrections are required for receivers that store C1 measurements to maintain compatibility with the satellite clock products (Kouba 2015). Therefore, the CODE monthly satellite DCB products were applied following the Bernese user guide (Dach et al. 2015) to eliminate satellite specific P1-C1 code biases from the individual measurements.

After satellite hardware delay corrections are applied to code measurements, the Equation 2.11 slant ionospheric delay remains biased by an unknown geometry-free bias, $b^{s}_{r,GF}$, that consists of both satellite and receiver bias components. However, because satellite-dependent biases were accounted for, the satellite superscript can be removed leaving only an unknown geometry-free receiver bias, that is, $b_{r,GF}$. Although both satellite and receiver differential P1-P2 bias information is provided for receivers involved in the GIM estimation process (Hernández-Pajares et al. 2009), none of the stations used in this study contained *a priori* receiver hardware delay information regardless of which ionospheric map product was used. This bias effect can be observed in the Figure 5.4 pre-fit pseudorange residuals using uncombined processing of pseudorange measurements with GIM and RIM ionospheric corrections applied.

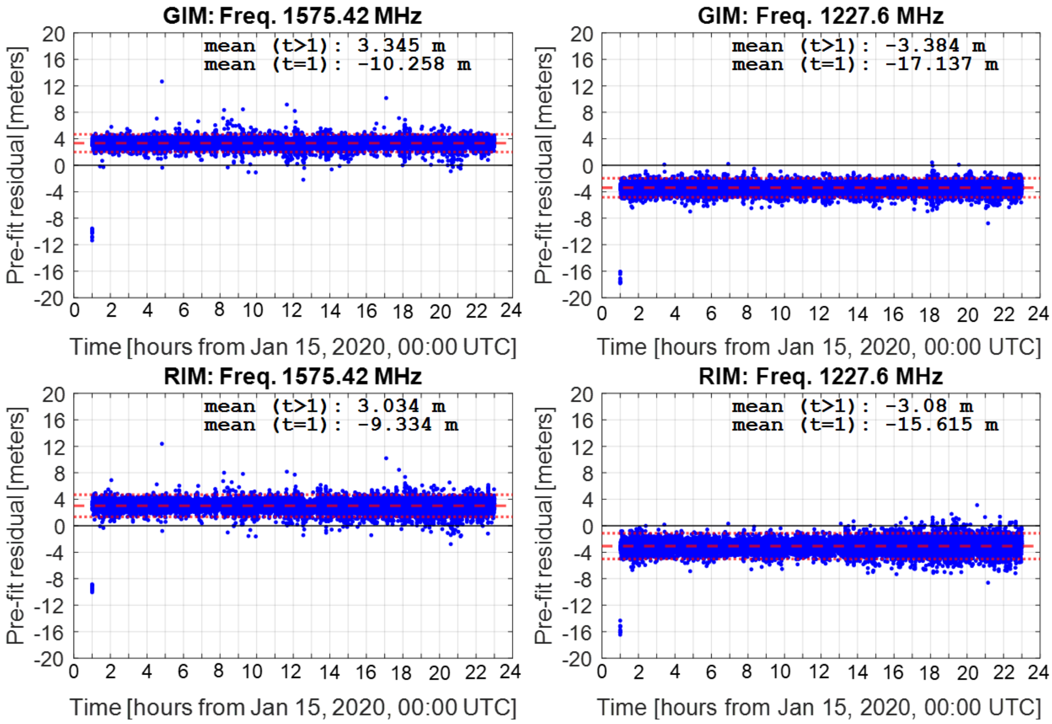

Figure 5.4. Ionosphere-fixed, bias-affected station PISR GIM (top row) and RIM (bottom row) constrained pseudorange pre-fit residuals (blue markers), with mean (red dashed line) ±3σ (red dotted lines) for GPS L1 (left column) and L2 (right column) signals at (t=1) and after (t>1) the first epoch.

According to Equation 3.3, a frequency-dependent bias between two measurements in measurement vector z_k will appear as an offset at the first epoch in the corresponding pre-fit residuals. Then, if the biases are assumed to be time-constant, the combined bias effect appears as a constant offset for pre-fit and post-fit residuals in the following epochs due to least-squares residual minimization. These effects are visible in Figure 5.4 for GIM- and RIM-fixed processing at the first epoch and afterward, with similar plots available for other stations in Appendix C. In the following, this time-constant nature of the internal bias present in the external ionospheric products enables the application of a modified ionosphere-weighted stochastic model for PPP without the need to consider the bias effects that are absorbed in the ionospheric map data.

5.2.3 Modified stochastic model

Stochastic modelling is a critical component of parameter estimation that assigns measurement weights based on the modelled measurement quality. For example, an accurate stochastic model assigns low quality measurements less weight which contribute less to the related parameter estimation. Conventionally, the following stochastic model, formulated using the satellite elevation angle (E), is typically applied to GNSS parameter estimation:

$$\sigma_E^2 = \frac{\sigma_0^2}{\sin^2(E)} \tag{5.1}$$

where σ_0^2 is the *a priori* pseudorange or carrier phase measurement variance, E represents the satellite elevation angle, and σ_E^2 is the elevation-based variance component. The Equation 5.1 stochastic model is then used to compute measurement weights equal to the inverse of the variance. However, high elevation satellites, even above 50-degrees, that would normally receive a large weight value in Equation 5.1 may produce more noisy measurements than lower elevation satellites in the presence of strong ionospheric activity (Luo et al. 2018).

The rate of total electron content index (ROTI) characterizes the severity of ionospheric disturbances and is defined by Pi et al. (1997) as:

$$ROTI = \sqrt{< ROT^2 > - < ROT >^2} \tag{5.2}$$

where the < > operator is the average value within a period of time, for example, 5-minutes for GNSS data stored at a 30-second epoch rate. Thus, Equation 5.2 represents the rate of TEC (ROT) change expressed in units of TECU/minute. In terms of an external ionospheric map product, the following expression can be used to compute the ROT for a satellite-receiver link at time *t*:

$$ROT_r^s(t) = STEC_r^s(t) + b_{GF} - (STEC_r^s(t - \Delta t) + b_{GF}) \tag{5.3}$$

where $STEC_r^s$ is the slant TEC, interpolated from either global or regional ionospheric map products that are contaminated by a time-constant geometry-free receiver bias term b_{GF}. Due to the time-constant nature of the bias parameter, only the time-difference of the $STEC_r^s$ term remains after Equation 5.3 is evaluated. Therefore, internal biases within the GIM and RIM products can be ignored if Equation 5.3 is used to compute the ROT at each epoch.

Precise ROT can be computed at each epoch for dual-frequency GNSS users that apply Equation 2.9 to carrier phase measurements (Cai et al. 2013; Cherniak et al. 2018; Luo et al. 2022). However, this method fails if carrier phase cycle slips are not detected or remain uncorrected because cycle slips artificially increase the computed TEC rate. This is especially problematic during periods of increased ionospheric activity as cycle slips are more frequent and can be further amplified in the presence of geomagnetic storms. Thus, the following ionospheric component, σ_I^2, of a modified elevation-angle stochastic model was developed by Luo et al. (2022) to amplify measurement variance using ROT:

$$\sigma_I^2 = \cos^2\left(\frac{ROT - T_{min}}{T_{max}} \cdot \frac{\pi}{2}\right); T_{min} \leq ROT < T_{max} \tag{5.4}$$

where T_{min} and T_{max} are minimum and maximum ROT thresholds equal to 0.5- and 15-TECU/minute, respectively. Note that in Luo et al. (2022), approximately 99.9% of ROT data evaluated for 240 IGS stations were below T_{max} and remaining data greater than T_{max} were removed from the PPP solution. In this thesis, ROT is set equal to T_{max} when ROT exceeds T_{max} to reduce the amount of rejected measurement data that may weaken the positioning solution if removed data worsen the satellite geometry.

Although Equation 5.4 was originally developed to use ROT derived from dual-frequency measurements for a single receiver, this thesis innovatively applies the same approach to ROT derived from externally provided GIM and RIM data. This approach eliminates artificial ROT amplification that is caused by carrier phase cycle slips, as the user's carrier phase measurements are not used to compute ROT. The new method modifies the stochastic model by Luo et al. (2022) using the following combination of stochastic model components:

$$\begin{gathered} \sigma^2 = \sigma_E^2 + \sigma_E^2 \cdot \sigma_I^2; ROT_{max} < T_{min} \\ \sigma_I^2 = 0; ROT < T_{min} \text{ or } ROT \geq T_{max} \end{gathered} \tag{5.5}$$

where ROT_{max} is the maximum ROT for all usable satellites in an epoch and σ^2 is the code or carrier phase measurement variance comprised of both elevation-based (σ_E^2) and ionospheric-based (σ_I^2) variance components. The Equation 5.5 modified stochastic model was developed to become active only when $ROT_{max} \geq T_{min}$. Thus, the standard elevation-based stochastic model in Equation 5.1 is applied without modification when the condition $ROT_{max} < T_{min}$ is met. In other words, the modified stochastic model is only active when the ionosphere is active. When the ionospheric noise component is active in Equation 5.5, the standard elevation-based stochastic model becomes modified with the addition of an amplification factor based on the ionospheric noise component scaled by the elevation-based factor.

The modified stochastic model components are represented by the Figure 5.5 measurement weights, computed as the inverse of the respective measurement variance functions, for valid ranges of satellite elevation angles and ROT values. It can be seen from Figure 5.5 that this strategy amplifies the *a priori* zenith measurement variance (σ_0^2) by a factor of two relative to the elevation-only approach when the ionospheric variance component (σ_I^2) is at its maximum. Note that this scale factor is nearly the same as the empirically derived factor used by Luo et al. (2022).

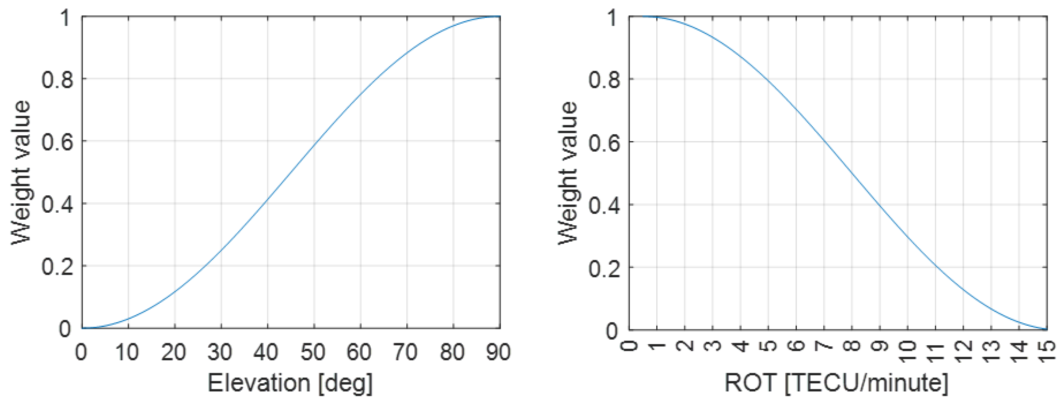

Figure 5.5. Elevation (left) and ionospheric (right) weighting values as respective functions of satellite elevation angle and ROT.

The Equation 2.7 and Equation 2.8 ionosphere-free PPP functional models were used for respective carrier phase and pseudorange measurement processing. These models were used along with the Table 5.1 configurations and default Table 3.2 strategies to process 22h of measurements at each user station and at station PISR, which was used in the generation of the RIM product. Therefore, the RIM-based processing for station PISR is not affected by interpolation errors and offers the best possibility of success when using the experimental RIM product.

Table 5.1. Ionosphere-corrected POINT software configurations and estimation strategies.

GNSS processing	Configurations/strategies
Constellation: signals	GPS: L1C/A, L2P or L2C
Measurement weighting	Standard: elevation-based (Mohammed 2017)
	Modified: elevation- and ROT-based
Satellite code biases	CODE P2C2 and P1C1 DCB products
A priori pseudorange precision	L1C/L2P: 30.0/30.0 cm
A priori carrier phase precision	L1/L2: 0.01/0.01 cycles (2.0/2.5 mm)

5.2.4 Positioning performance and evaluation

The standard elevation-based and the modified stochastic models were used for kinematic PPP processing of GPS L1 and L2 measurements observed at stations BAPA, PILF, PITN, and PISR during the 22-hour period from 01:00 to 23:00 UTC on January 15, 2020. Although this time interval is not aligned with a solar or geomagnetic storm event (Kp index ≤ 2), the region is near the geomagnetic equator and is affected by large ionospheric gradients due to the local EIA ionization crests. Ionospheric scintillation effects were not studied in this evaluation, though the region is frequently affected by moderate to strong scintillation beginning near the post-sunset period each day. To eliminate large errors that occur during the initial convergence period, only data after 2-hours of processing, i.e., 03:00 UTC, were used in the following analysis and statistics. Thus, post-convergence positioning accuracy is evaluated for the standard and modified stochastic models. However, positioning errors during the initial convergence period were found to be similar regardless of the stochastic model applied.

The Figure 5.6 positioning error time-series for station BAPA shows that achievable positioning accuracy is nearly identical, at the mm-level, regardless of which stochastic model is used. In both cases, the maximum 3D positioning error occurs at 15:30 UTC and is equal to 13.8-cm. Additionally, the mean 3D positioning error is equal to 3.0-cm in both cases and individual positioning error components are also in agreement at the mm-level or better. Therefore, it can be concluded from Figure 5.6 that the modified stochastic model did not improve the overall or worst-case positioning performance at station BAPA. On the other hand, the consistency between positioning performance for each stochastic method indicates that the modified model approach does not hinder the user when compared to the standard model.

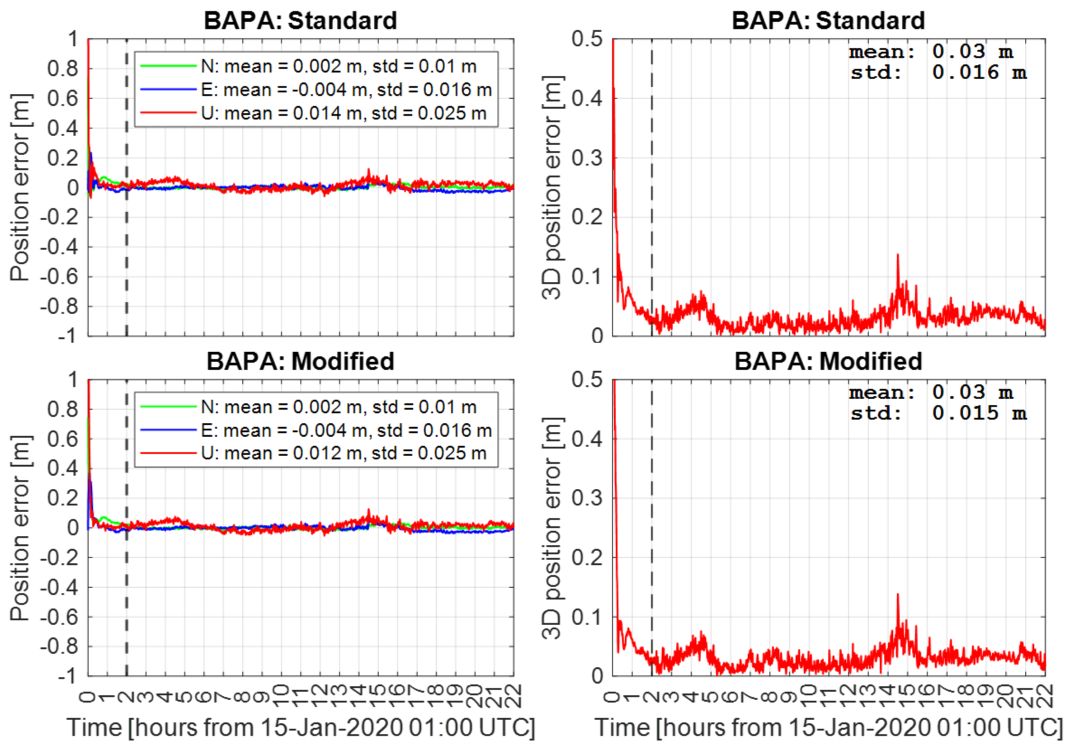

Figure 5.6. Station BAPA standard (top row) and modified (lower row) stochastic model positioning error component (left column) and 3D positioning error (right column) time series.

For station PIFL, the positioning error time-series in Figure 5.7 shows that the modified stochastic model is superior to the standard stochastic model in terms of worst-case positioning accuracy. For example, the post-convergence 3D positioning error reached a maximum of 29.7-cm at 15:40 UTC using the standard stochastic model, while the modified model reached only 14.1-cm error at the same epoch. This 15.6-cm difference corresponds to a 52.5% improvement in the 3D positioning error at the otherwise worst epoch and indicates that the modified approach helps to reduce the large errors that may occur when the stochastic model is based exclusively on satellite elevation angle. In addition, the slight overall positioning performance improvement of 6.1%, in terms of mean 3D position error, indicates that the modified stochastic approach did not degrade the achievable positioning accuracy at a daily resolution.

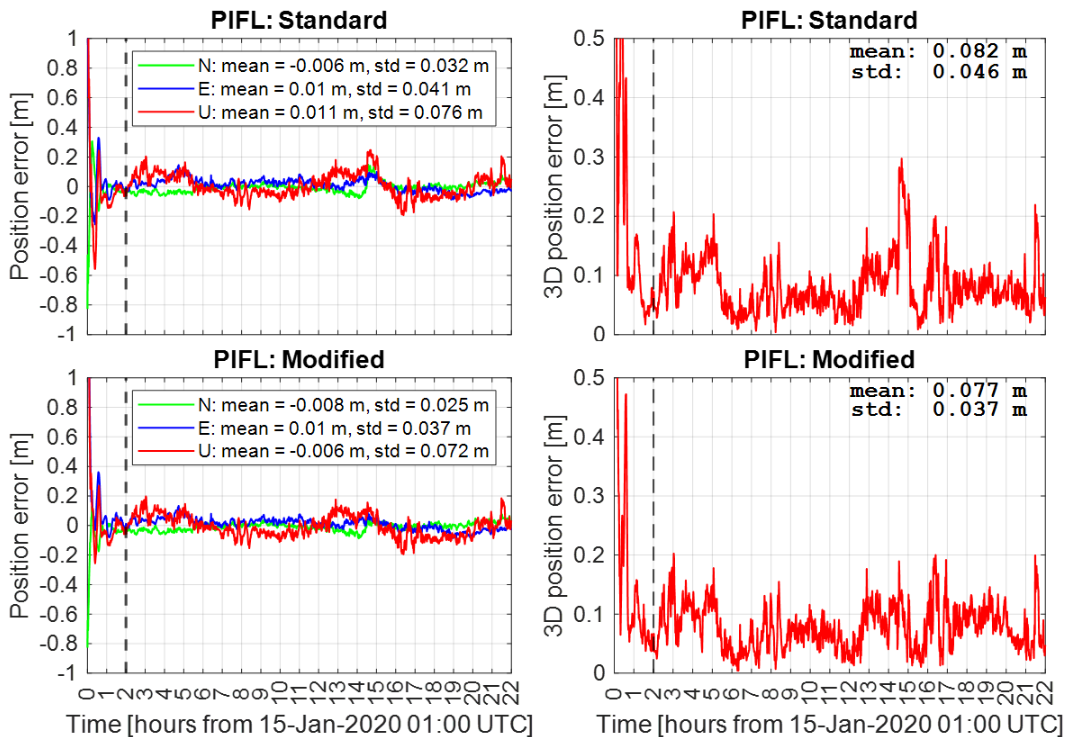

Figure 5.7. Station PIFL standard (top row) and modified (lower row) stochastic model positioning error component (left column) and 3D positioning error (right column) time series.

The station PITN positioning error time-series in Figure 5.8 is similar to the station PIFL performance, where the modified stochastic model outperforms the standard stochastic model at the maximum 3D error epoch. In this case, the post-convergence 3D positioning error reached a maximum of 26.4-cm at 20:51 UTC using the standard stochastic model, while the modified model reached only 15.1-cm 3D error at the same epoch. This 11.3-cm 3D position error improvement corresponds to a 42.8% improvement at the worst epoch of the elevation-based processing. In terms of overall positioning performance, the mean 3D positioning error was 3-mm better for the standard stochastic model configuration. Therefore, the modified approach reduced the large errors that occurred using only satellite elevation in the stochastic model, while increasing the overall 3D positioning error by a negligible mm-level.

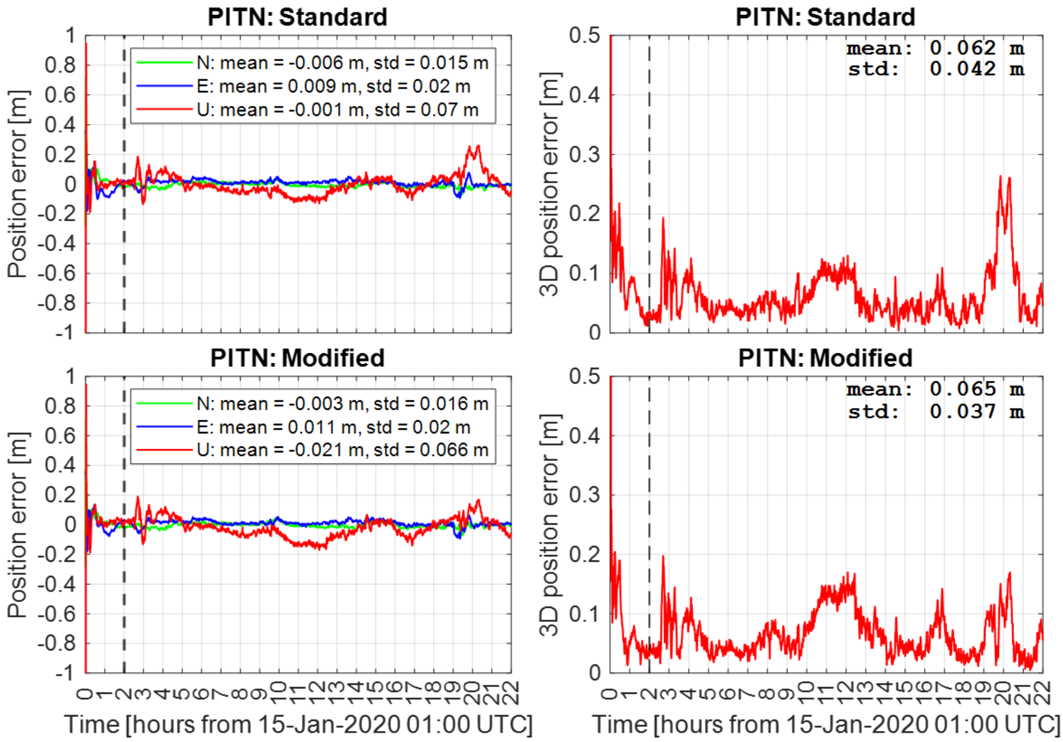

Figure 5.8. Station PITN standard (top row) and modified (lower row) stochastic model positioning error component (left column) and 3D positioning error (right column) time series.

Contrary to the previously evaluated stations, the positioning performance for station PISR degraded slightly in terms of maximum and overall positioning accuracy using the modified stochastic model approach. However, at the worst-case epoch (21:54 UTC), the modified stochastic method increased the 3D positioning error by only 2.0-cm. This slight degradation is within the tolerance reported by Luo et al. (2022) which reported worse positioning accuracy, up to 5.0-cm, for approximately 14% of the evaluated stations when smoothed geometry-free carrier phase measurements were used in a modified stochastic model. Therefore, the implemented stochastic model based on ionospheric map ROT data and with further modifications are in agreement with previous research outcomes, where only a cm-level worsening of positioning performance may occur. The modified approach increased the mean positioning error by 3.0-mm compared to the standard stochastic model due to a cm-level error amplification during the 10:30-12:00 UTC period.

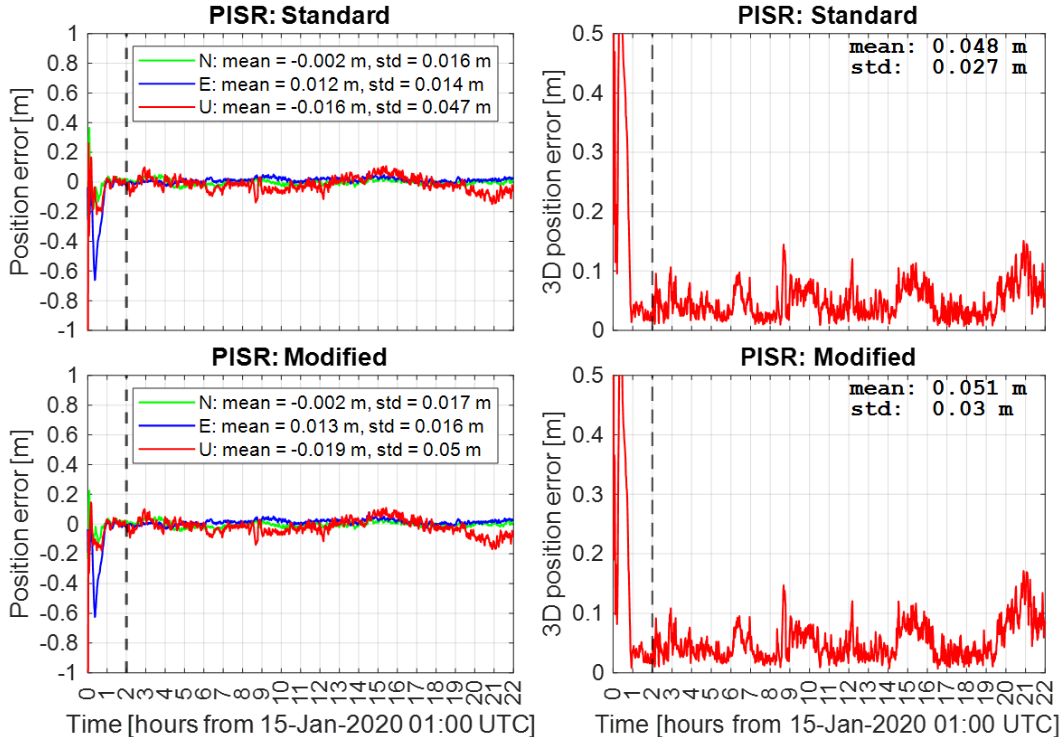

Figure 5.9. Station PISR standard (top row) and modified (lower row) stochastic model positioning error component (left column) and 3D positioning error (right column) time series.

Standard and modified stochastic model performance is compared in Table 5.2 using the mean and maximum 3D positioning error after 2-hours of processing, to large remove errors that may occur during the initial convergence interval. Additionally, the Table 5.2 maximum 3D error refers to the maximum single-epoch 3D positioning error during the 20-hour post-convergence period. Therefore, the maximum 3D error does not necessarily occur at the same epoch for each stochastic approach at each station.

For all four stations evaluated in Table 5.2, the mean 3D positioning error is consistent between stochastic methods at the mm-level, with a maximum difference equal to 0.5-mm. This indicates that the achievable daily 3D positioning performance is similar for both the standard and modified stochastic models. However, both stations PIFL and PITN achieved respective 3D positioning error improvements up to 9.3-cm (31.6%) and 6.7-cm (25.4%) in terms of the maximum single-epoch error for the entire (post-convergence) interval when the modified stochastic model was used. For station BAPA, no improvement was found for either the mean or worst-case epoch regardless of the stochastic model. Lastly, 3D positioning error for the modified stochastic model was 2.0-cm worse (-13.2%

improvement) at the single worst epoch for station PISR, which is within the accepted general tolerance (Luo et al. 2022). These improvements demonstrate that the modified stochastic approach did not simply shift the worst-case positioning accuracy to a new epoch. In addition, the modified GIM-based ionosphere-weighted stochastic model can successfully reduce maximum kinematic 3D positioning error under large ionospheric gradients.

Table 5.2. 3D kinematic PPP error comparison for standard elevation-based and ionosphere-weighted stochastic models.

	Mean / maximum 3D error [cm]		
Station	Standard model	Modified model	Improvement [%]
BAPA	3.0 / 13.8	3.0 / 13.8	0.0 / 0.0
PIFL	8.2 / 29.7	7.7 / 20.3	+6.1 / +31.6
PITN	6.2 / 26.4	6.5 / 19.7	-4.8 / +25.4
PISR	4.8 / 15.1	5.1 / 17.1	-6.3 / -13.2

The GNSS measurement data were reprocessed for each station using the RIM product data as input to the modified stochastic model. Extreme ROT variability, up to 45 TECU/minute, of the experimental high-resolution RIM product exceeded the upper ROT limit in the modified stochastic model for 88.8% of all epochs. Thus, this highly variable ROT deactivated the ionospheric variance component of the modified stochastic model for most epochs resulting in estimation that used primarily the standard elevation-based stochastic model. For this reason, the 3D position error time-series in Figure 5.10 shows that the RIM-based stochastic model performs similar to the standard model, with nearly identical worst-case positioning accuracies. Although the highly experimental RIM product was unable to fully use the modified stochastic model, the 3D positioning results demonstrate that the new method is robust and can achieve similar performance as an elevation-based approach when noisy ROT data are used as inputs.

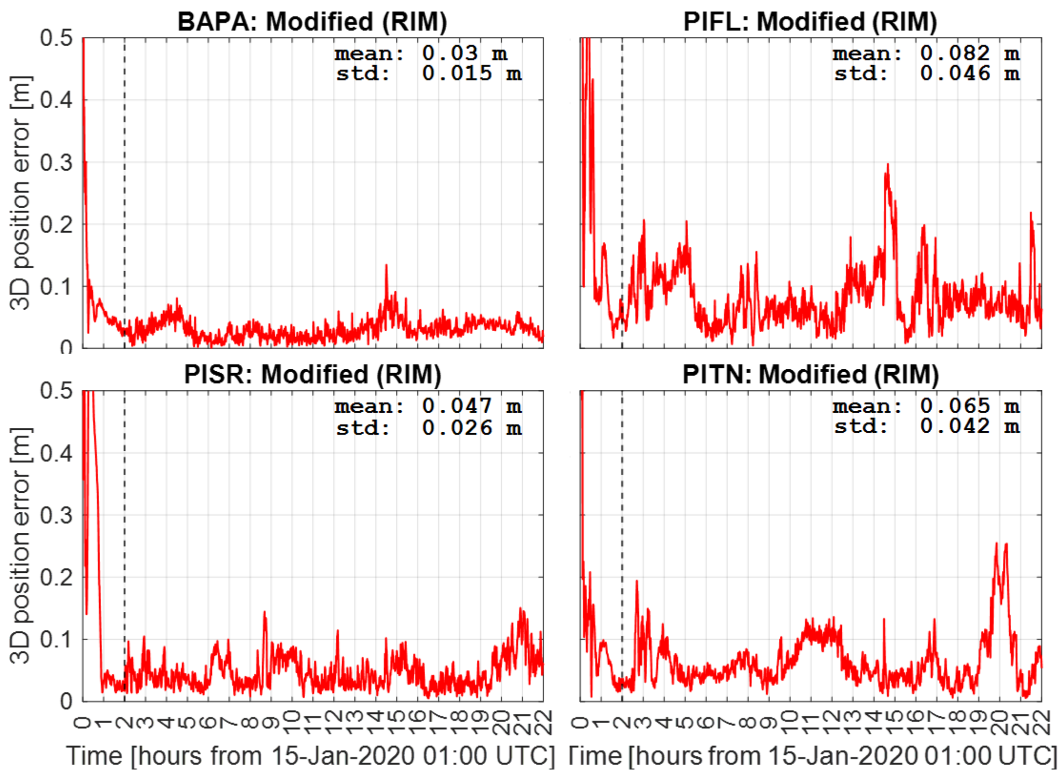

Figure 5.10. Station BAPA (top-left), PIFL (top-right), PISR (lower-left), and PITN (lower-right) 3D position error using the modified stochastic model with RIM product data.

The experimental RIM product was generated at the highest possible temporal resolution to match ionospheric data to the GNSS measurement epoch rate. For comparison, the RIM product with a 60-second update rate did not require temporal interpolation at any epoch while the GIM data required interpolation at 98.3% of all epochs due to the 10-minute update interval. In summary, the RIM product data is available at 60 times and up to 5 times more respective temporal and spatial resolution than the GIM product data. Thus, the highly variable ROT computed using the RIM data is likely caused by the extreme temporal update rate that reduces any smoothing effects caused by interpolation of the relatively sparse GIM data. Alternatively, unknown errors in the experimental RIM product, as indicated by the negative TEC values, may also amplify the computed ROT that caused deactivation of the modified stochastic model.

5.2.5 Remarks

An alternative modified stochastic model was developed using the Luo et al. (2022) framework that adapted the standard GNSS measurement stochastic model using ionospheric information. The new approach presented herein amplifies GNSS measurement uncertainty according to the ROT computed from GIM or RIM product data instead of using ROT computed from dual-frequency carrier phase measurements. This approach eliminates possible artificial ROT discontinuities that occur in the presence of carrier phase cycle slips that are especially frequent and problematic for high-accuracy GNSS positioning at low latitudes.

Kinematic PPP performance was evaluated for four low latitude GNSS reference stations using the new stochastic model and a standard satellite elevation-based model. The worst-case 3D positioning error was improved by 52.5% and 42.8% at stations PIFL and PITN, respectively, using the GIM-based modified stochastic model, while the mean positioning accuracy agreed to the mm-level for both stochastic models. Furthermore, the maximum 3D positioning error for all epochs using the modified stochastic model improved by 9.3- and 6.7-cm, respectively, for stations PIFL and PITN. Therefore, the modified stochastic model that used GIM-based noise amplification successfully reduced the overall and single-epoch maximum positioning error and did not degrade the overall positioning performance. For comparison, the alternative technique given by Luo et al. (2022) achieved approximately 13% improvement in overall 3D position error under geomagnetic storm conditions globally.

The positioning performance was nearly unchanged when the GIM-based modified stochastic model was used for stations BAPA and PISR. The high-precision cm-level positioning performance for station BAPA, located beyond 20-degrees geomagnetic latitude, achieved mm-level consistency for all positioning error components regardless of which stochastic model was used. Meanwhile, station PISR positioning performance degraded by 2.0- and 3.0-cm at the respective worst-case epoch and for the mean 3D error, which is below the Luo et al. (2022) tolerance. Therefore, it can be concluded that the ionospheric-map-based modified stochastic model is best suited for reducing large positioning errors that may occur during kinematic PPP processing. In addition, although positioning performance degraded by a few centimetres for one station, the alternative GIM-based modified stochastic approach improved the worst-case 3D positioning error up to tens of centimetres.

The same modified stochastic approach was used to reprocess data for each station using ROT derived from RIM product data. This strategy revealed that the experimental ROT was highly variable, up to 45 TECU per minute, which resulted in deactivation of the modified stochastic approach for an average of 88.8% of all epochs for all evaluated stations. Therefore, positioning performance using the RIM product was nearly identical to the standard elevation-based model in terms of both worst-case and mean positioning accuracy. Furthermore, the enhanced spatial and temporal resolution of RIM-based products, and potential unknown errors, likely amplified the ROT and caused the deactivation of the modified stochastic model.

Future research may reveal benefits for multi-epoch smoothing of ROT computed from ionospheric map data, especially if highly variable ROT is computed from experimental RIM data products. The effect of spatial and temporal resolution of ionospheric map products on ROT may help optimize RIM product generation. Although the Luo et al. (2022) modified stochastic method requires dual-frequency measurements to compute ROT, the new modified stochastic model uses ROT computed via ionospheric map products and therefore does not restrict usage to dual-frequency users. Thus, future research may evaluate the modified stochastic model for single-frequency positioning users or extend to undifferenced and uncombined functional models that do not contain GNSS measurements at multiple frequencies for all epochs due to partial loss of lock.

5.3 Troposphere-corrected positioning

This section evaluates kinematic PPP accuracy using tropospheric corrections estimated by a reference GNSS network. Chapter 2 introduced strategies to reduce tropospheric effects and identified challenges of positioning under active tropospheric conditions. Then, Chapter 3 presented to estimation method that incorporates dynamic model time constraints into the GNSS functional model. To study the performance of troposphere-corrected PPP, data from a GNSS reference network were selected to correspond with a strong tropospheric storm event that passed over the Netherlands. These reference stations were separated into network and user categories and network stations were used to estimate precise zenith wet tropospheric delays that were later used as corrections for user stations. In this framework, deterministic, partially stochastic, and fully stochastic correction configurations are developed and positioning accuracy is evaluated to demonstrate the benefits and disadvantages of each method.

5.3.1 Data and approach

Strategies to reduce tropospheric effects typically use *a priori* hydrostatic (i.e., dry) correction models (Saastamoinen 1972; Leandro et al. 2006) and estimation of zenith and horizontal gradient of wet delay components (Bar-Sever et al. 1998). However, rapid changes in atmospheric water vapor caused by heavy rainfall can amplify tropospheric asymmetry effects (Ma and Verhagen 2020) and reduce positioning accuracy (Ma et al. 2021). Therefore, data were selected to correspond with a tropospheric storm event that passed over the Netherlands on June 22, 2017. The cloud map in Figure 5.11 shows that the storm approached from the northwest at 14h UTC and travelled uniformly across the Netherlands by 20h UTC. This storm was accompanied by heavy rainfall and caused a sudden change in the atmospheric water vapor, as conditions were clear and calm prior to the arrival of the storm.

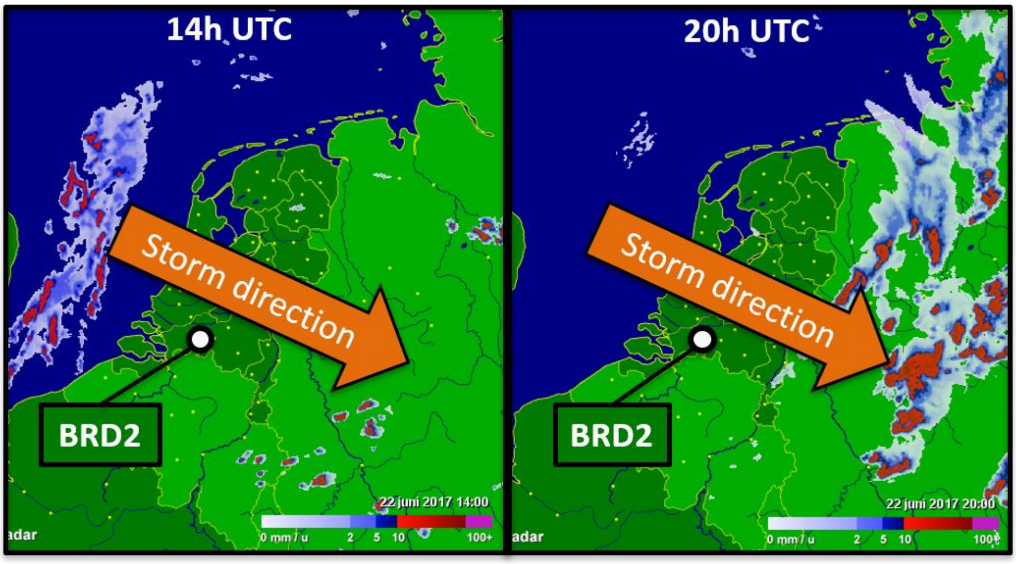

Figure 5.11. Tropospheric storm event (orange arrow) passing over the Netherlands on June 22, 2017, from 14h to 20h UTC, with station BRD2 from the Netherlands GNSS network annotated.

To study the sudden change in the tropospheric state and effects of kinematic PPP performance, RINEX data for a GNSS reference network in the Netherlands were downloaded from the Dutch Kadaster online database (http://gnss1.tudelft.nl/dpga/rinex/). The 16 stations shown in Figure 5.12 were selected and 24h RINEX data files containing measurements of GPS L1 and L2 signals were downloaded from 00h-24h UTC on the same day as the storm event. Although more stations are available in the reference network, the respective 19-km and 50-km minimum and maximum inter-station spacing of Figure 5.12 stations enabled evaluation under a range of correction conditions.

The processing strategy in Figure 5.13 was applied to the 12 network and 4 user stations in Figure 5.12 to estimate, interpolate, then apply *a priori* tropospheric zenith wet delay corrections for the user stations using deterministic, partially, and fully stochastic configurations. Results were then compared to standard kinematic PPP that operates without external information related to the troposphere. For the network processing component, precise ZWD was independently estimated at each network station using the Equation 2.12 ionosphere-free functional model configured for static PPP. It is assumed that the network has access to meteorological data or weather forecast information and can adjust parameter estimation constraints accordingly. Therefore, in this study, the static PPP estimation uses a loose ZWD time constraint equal to one thousand times the value typically used for kinematic

PPP processing in preparation for the approaching storm. This relatively loose ZWD constraint does not weaken the static PPP model to the same extent as a kinematic PPP model, as the estimated positioning components are modelled as time-constant (static) parameters, which strengthens the positioning model.

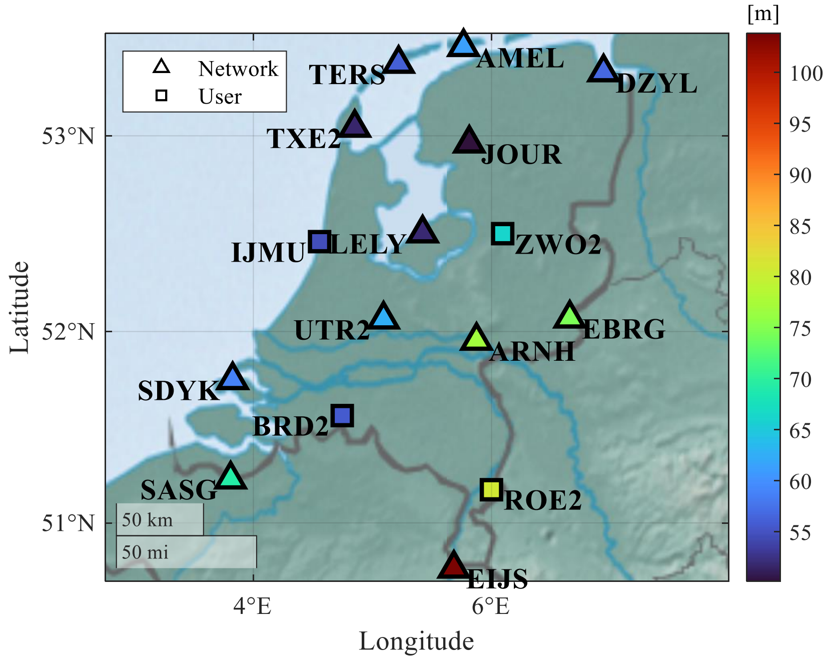

Figure 5.12. Selected GNSS reference stations in the Netherlands, where the 12 network (triangles) and 4 user (squares) stations used in the study are colored according to respective ellipsoid height values.

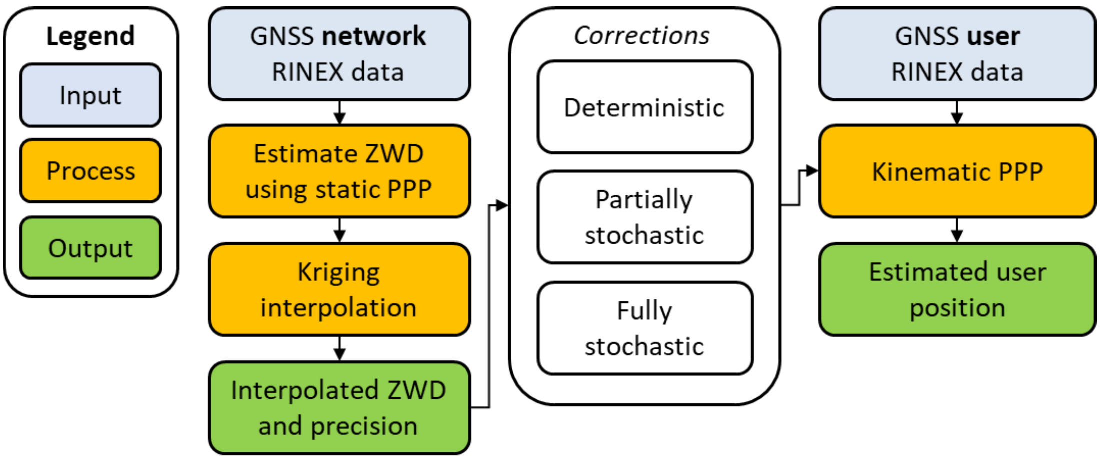

Figure 5.13. Process diagram to estimate ZWD corrections using static PPP and to apply deterministic, partially stochastic, and fully stochastic corrections for kinematic PPP.

In a kinematic PPP model, positioning components are modelled as time-dynamic parameters that are not constrained in the time domain. Therefore, the relatively weak kinematic PPP model is unable to loosen additional parameter time constraints without further weakening the overall model. For this reason, kinematic PPP users typically apply tight ZWD parameter constraints and assume that the representative atmospheric water vapor changes slowly in time. In addition, it is assumed that the standard kinematic PPP user does not have access to meteorological information that could potentially be used to adjust ZWD constraints.

After precise ZWD estimation, Kriging (Oliver and Webster 1990) interpolation was used to estimate ZWD and propagate ZWD uncertainties at the user positions. The interpolation was done in collaboration with Hongyang Ma of Delft University of Technology, as part of the TREASURE project. The Kriging algorithm uses a weighted average approach to interpolate data from known locations to unknown locations. Although other weighted average interpolation algorithms are available, for example, inverse-distance weighting, the Kriging technique estimates weights using covariance information computed from distance data. In this case, the distance data used to estimate weighting values were computed from respective network-user and inter-network station separations. The resulting weight values were then used to interpolate the network-estimated ZWD to the user stations using a weighted average calculation. Interpolation uncertainties were also estimated as part of the Kriging interpolation processing and were provided along with the interpolated ZWD data.

The four user station positions were estimated using standard kinematic PPP and with the three Figure 5.13 correction strategies applied. Interpolation of tropospheric parameters between network stations accumulates errors when station height differences increase, as the tropospheric ZWD and ZHD components depend on respective station ellipsoid heights. However, the largest ellipsoidal height difference between any two stations in Figure 5.12 is 53.6-meters, while the maximum height difference between adjacent stations is 22.9-meters (stations EIJS-ROE2). Therefore, it is assumed that differences between modelled and estimated tropospheric delay caused by station elevation differences is much smaller than the interpolation errors due to the relatively small station height variability for the GNSS stations in the region. In all processing configurations, aside from the deterministic approach, a residual tropospheric parameter is estimated and is assumed to absorb residual effects caused by station elevation differences. The same mapping functions that convert from slant to zenith directions of the reference stations as part of the network estimation were used to convert from zenith of users to slant directions to compute measurement corrections.

The kinematic PPP configurations for user stations are organized in Table 5.3 in terms of complexity for both the network and user processing requirements. All configurations in Table 5.3 begin with the Equation 2.12 ionosphere-free PPP model and vary based on the definition of the estimated ZWD parameter and the ZWD time constraint. For the standard kinematic PPP user that does not use any *a priori* network-estimated ZWD information (i.e., without corrections), the Equation 2.12 model is used directly with a tightly constrained ZWD parameter. In the remaining Table 5.3 configurations, the network-estimated ZWD is applied in the user processing.

Table 5.3. Application of network-estimated ZWD corrections for a kinematic PPP user in terms of the estimated user ZWD parameter and dynamic model constraint.

Configuration	ZWD definition	Process uncertainty [m^2/hour]	ZWD constraint
Standard	ZWD	$6.0 \cdot 10^{-4}$	Tight
Deterministic	-	-	Not estimated
Partially stochastic	Residual ZWD	$6.0 \cdot 10^{-4}$	Tight
Fully stochastic	Residual ZWD	$6.0 \cdot 10^{-4} – 4.5 \cdot 10^{-3}$	Variable

The deterministic configuration in Table 5.3 removes the ZWD parameter in Equation 2.12 from the user's model, as the network-estimated ZWD is assumed to be free from errors. For the partially stochastic configuration, the user assumes that the interpolated ZWD contains errors, yet no uncertainty information is provided by the network. Therefore, the ZWD parameter must remain in the user model and is interpreted as a residual ZWD parameter that represents ZWD errors due to interpolation and other modelling effects. The partially stochastic configuration does not use any information regarding the network-estimated ZWD precision. Thus, the same time constraint that is used for the standard kinematic PPP model is applied to tightly constrain the residual ZWD in the partially stochastic configuration.

The fully stochastic configuration extends the partially stochastic approach by incorporating network-estimated ZWD precision information in the user model. For this technique, the time constraint of the user's residual ZWD parameter becomes variable to represent the time-dependent nature of the network-estimated ZWD precision. The original ZWD precision data were multiplied by a scale factor equal to $1 \cdot 10^{-4}$ that converted the average network-estimated ZWD precision within the first hour of processing to approximately equal the tightly constrained ZWD parameter value used for standard kinematic PPP processing. Consequently, the fully stochastic technique estimates a residual ZWD parameter with a similar average process uncertainty as the ZWD parameter in the PPP model during the first hour of processing when tropospheric conditions are stable. However, the variable residual ZWD parameter uncertainty is approximately seven times larger, at maximum, compared to the average value during the first hour. Thus, the residual ZWD parameter constraint is relaxed in the fully stochastic model when the network-estimated ZWD precision is low.

Although each configuration in Table 5.3 estimates horizontal tropospheric gradients, only the fully stochastic approach applies modification to the associated gradient parameter process uncertainty values. In this case, a new scale factor that is equal to the ratio between the standard PPP ZWD and gradient parameter uncertainty values (i.e., $3 \cdot 10^{-6}:1 \cdot 10^{-5}$) is applied to the network-estimated ZWD precision data. Therefore, the average process uncertainty for tropospheric gradient parameters is nearly identical for the fully stochastic and other configurations during the first hour, i.e., many hours prior to the arrival of the storm.

5.3.2 Positioning performance evaluation

The same network estimation approach was applied to process the user stations and estimate reference ZWD values at each epoch. The ZWD time-series at each user station in Figure 5.14 indicates agreement between estimated and interpolated ZWD. Note that the ZWD estimated by static PPP for the user stations was not used in any of the processing steps other than the Figure 5.14 evaluation. The tropospheric storm effects are evident by the ZWD fluctuations in Figure 5.14 after approximately the first four hours where conditions are relatively stable. Then, large ZWD variations begin at approximately 04h UTC and end around 22h UTC, with slightly different timing depending on the station location relative to the approach or departing stormfront. A similar pattern occurs at each station during the 16h-22h UTC interval, where the estimated ZWD value rapidly changes, up to 15-cm in a two-hour time interval at station BRD2.

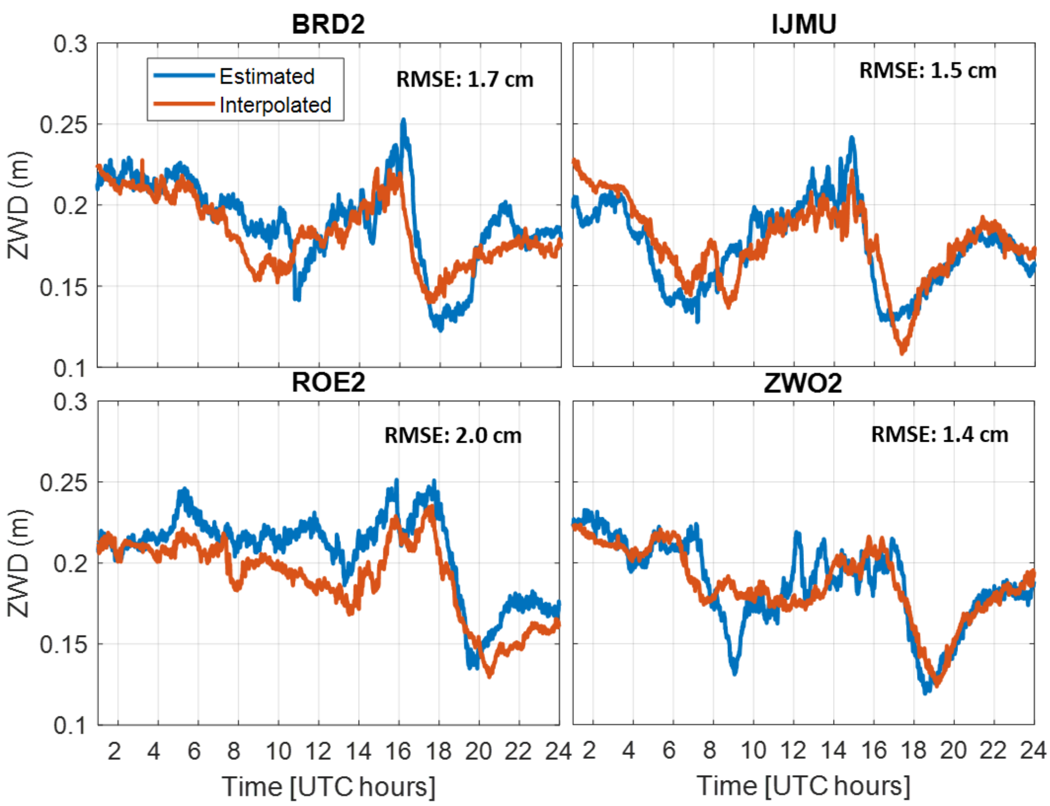

Figure 5.14. Estimated (blue) and interpolated (orange) ZWD time-series and RMS error at user stations: BRD2 (top-left), IJMU (top-right), ROE2 (lower-left), and ZWO2 (lower-right).

The overall interpolated ZWD agreement, in terms of RMS error with respect to the estimated ZWD, is 1.4-cm to 2.0-cm for the entire time interval in Figure 5.14 at each of the four user stations. This 6-mm difference in overall correction accuracy indicates that ZWD correction quality is nearly the same for each user station when evaluated over the entire interval. However, each station contains shorter periods where the instantaneous interpolated ZWD error reaches up to at least 4.0-cm, with the largest absolute error in a single epoch equal to 5.5-cm at stations BRD2 and ZWO2. These larger single-epoch errors are likely due to interpolation limitations, as the ZWD estimated using static PPP is typically at a mm-level precision, in terms of formal uncertainty.

The Figure 5.15 positioning error time-series for station BRD2 demonstrates the per-epoch kinematic PPP performance without corrections and with deterministic, partially stochastic, and fully stochastic corrections. All configurations achieve 5-cm initial convergence of the horizontal positioning component errors within one hour of processing. Furthermore, all positioning error components remain below 5-cm error for the first five hours of processing. For these reasons, the positioning performance evaluations do not use any data within the first two hours of processing to exclude the initial convergence period and to focus on positioning performance affected by the storm event.

It can be observed from Figure 5.15 that the tightly constrained tropospheric parameter used for kinematic PPP at station BRD2 without tropospheric corrections does not allow sufficient variability in the estimated ZWD parameters when a sudden change in tropospheric conditions occurs. However, if the user is not aware of nearby storms or is unable to modify their ZWD parameter constraint, then the tightly constrained ZWD parameter deteriorates the achievable kinematic PPP user accuracy and precision. This is demonstrated in Figure 5.15 where the initial cm-level positioning accuracy begins to worsen at approximately 05h UTC due to the arrival of the storm, as indicated by the increased ZWD variability in Figure 5.14.

The worst single-epoch, non-corrected vertical positioning error for station BRD2 in Figure 5.15 reaches -16.3-cm during 16h-18h UTC, while the vertical positioning error range is 28-cm in the same interval. This time period corresponds to the sudden 15-cm decrease in the estimated ZWD in Figure 5.14 for the same station. A similar abrupt 10-cm worsening of vertical positioning accuracy is also found in the 10h-12h UTC interval where the reference ZWD rapidly decreases by nearly 6-cm within one hour. Additionally, horizontal positioning accuracy also deteriorates to worse than 5-cm during the same rapidly changing ZWD time intervals.

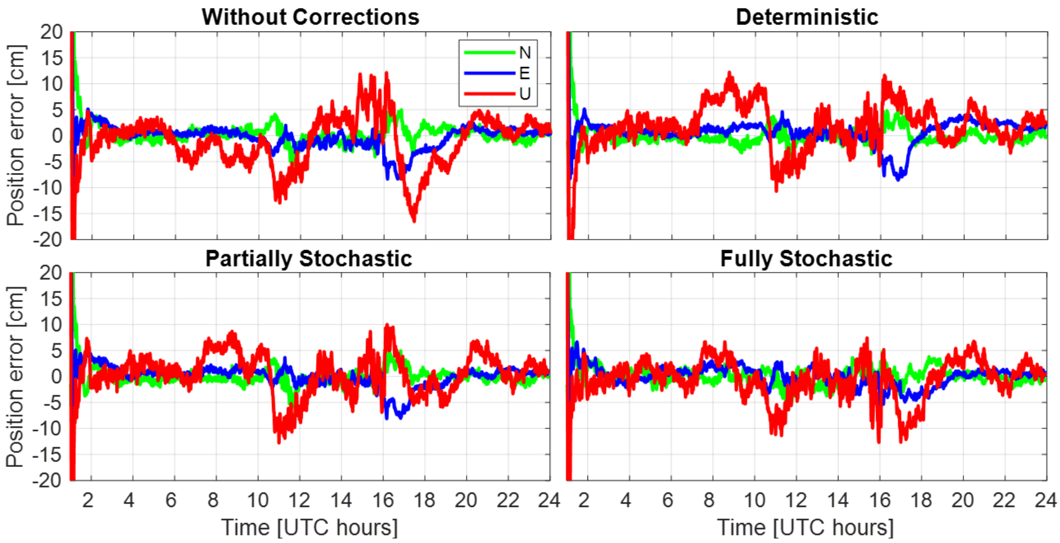

Figure 5.15. Kinematic PPP north (green), east (blue), and up (red) positioning component errors at user station BRD2, without (top-left), deterministic (top-right), partially stochastic (lower-left) and fully stochastic (lower-right) corrections.

Hourly RMS for 2D and vertical positioning errors was computed for each user station and configuration to evaluate time intervals, as opposed to per-epoch positioning performance. The maximum of hourly RMS errors is summarized for each user station and processing configuration in Figure 5.16 for both horizontal and vertical positioning error components. In Figure 5.16, only data from 03h to 24h UTC were evaluated to focus on the post-convergence interval where PPP performance is affected by the storm event. Furthermore, because maximum RMS errors are shown in Figure 5.16, the accuracies emphasize the worst-case positioning scenarios during storm conditions. For the fully stochastic configuration, the worst-case hourly horizontal RMS error remained below 4-cm, while the vertical RMS errors remained below 10-cm for all four user stations. For comparison, the worst hourly RMS error for configurations without corrections was 7.2-cm at station BRD2 and 16.2-cm at station ROE2 for respective horizontal and vertical components.

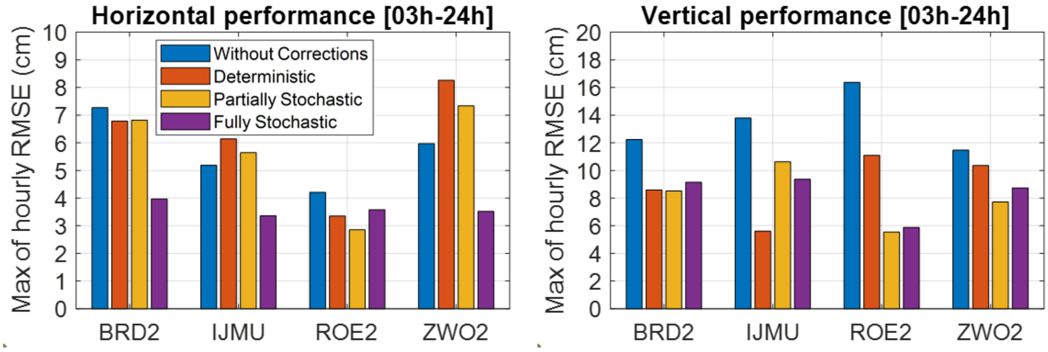

Figure 5.16. Maximum of horizontal (left) and vertical (right) hourly RMS error from 03h-24h UTC for user stations using each processing configuration.

The Figure 5.16 results were used to generate horizontal and vertical worst-case hourly RMS improvements in Table 5.4 with respect to the configuration that did not use ZWD corrections. Deterministic and partially stochastic configurations were unable to consistently improve the worst-case horizontal accuracy and, in some cases, increased the RMS errors by 1- to 2-cm, resulting in negative improvement at two stations. However, the fully stochastic configuration reduced horizontal errors at all stations, resulting in at least 15.0% and up to 45.5% improvement. This indicates that the variable tropospheric gradient process noise implemented for the fully stochastic approach is a key factor to improve horizontal performance. Moreover, the stochastic properties of tropospheric corrections can be used to improve not only vertical but also horizontal positioning accuracy if the network-estimated ZWD precision is incorporated in the user's ZWD and gradient parameter process uncertainty.

Table 5.4. Improvements of the maximum hourly RMS error for horizontal and vertical positioning components for troposphere-corrected configurations with respect to the non-corrected configuration for each user station.

	Horizontal/vertical maximum hourly RMS improvement [%]		
User station	Deterministic	Partially Stochastic	Fully Stochastic
BRD2	6.7/29.8	6.2/30.4	45.5/25.3
IJMU	-18.4/59.3	-8.8/22.9	35.1/32.1
ROE2	20.3/32.2	32.3/66.2	15.0/64.1
ZWO2	-38.4/9.6	-23.0/32.7	41.0/23.8

Regardless of the tropospheric-corrected configuration in Table 5.4, all user stations achieve better vertical positioning accuracy compared to the non-corrected configuration, resulting in 9.6% to 66.2% improvement. This indicates that errors associated with the user's ZWD parameter primarily affect the vertical positioning error component, which is reasonable, as the ZWD parameter maps tropospheric wet delay to the zenith direction. The most consistent improvements in Table 5.4 are for station ROE2, where horizontal and vertical accuracy improved by at least 15.0% and 32.2%, respectively, for all troposphere-corrected configurations. This initially seems inconsistent with the maximum RMS error in the Figure 5.14 corrections being for station ROE2. However, the overall correction quality is less important than the per-epoch accuracy when the worst-case positioning accuracy is evaluated. For example, although the correction RMS error for station ZWO2 is the minimum of the four user stations, during the 08h-10h UTC interval the correction error reaches up to 5.5-cm. This is supported by the relatively poor performance in Table 5.4 for station ZWO2. Finally, the positioning errors for each configuration were found to be in agreement at a nominal cm-level during the initial three hours of processing. Therefore, because this period was prior to the arrival of the storm, it is concluded that the modified processing does not harm the kinematic PPP user's performance under calm tropospheric conditions.

5.3.3 Remarks

In order to study troposphere-corrected kinematic PPP performance, GPS L1 and L2 signal data from a GNSS reference station network in the Netherlands that coincided with a rapidly developing storm event were evaluated relative to standard kinematic PPP results. Stations were first separated into network and user components, where static PPP was used to estimate precise ZWD and ZWD precision at each station using time constraints that were three orders of magnitude more relaxed than the tight constraints typically applied for standard kinematic PPP processing. Kriging interpolation of network-estimated ZWD data was then used to estimate precise ZWD and ZWD uncertainty at user stations, in collaboration with Hongyang Ma of Delft University of Technology.

The interpolated tropospheric corrections were evaluated relative to network processing applied for the user stations. The resulting interpolation errors were found to be from 1.4-cm to 2.0-cm, in terms of overall RMS, and up to 5.5-cm instantaneous error. In addition, the sudden storm event caused the previously stable ZWD at the user stations to change by up to 7.2-cm in a one-hour time interval, with similar trends and ZWD variability throughout the day. For the standard kinematic PPP processing that uses a tight ZWD parameter uncertainty constraint, horizontal and vertical positioning errors achieved a cm-level positioning accuracy after initial convergence and prior to the arrival of the storm. Then, respective horizontal and vertical positioning errors increased to more than 5-cm and 15-cm as the storm arrived.

To reduce the tropospheric storm effects, data for the user stations were processed using three proposed troposphere-corrected configurations: (1) deterministic, (2) partially stochastic, and (3) fully stochastic. The deterministic correction method assumes that corrections completely represent the user’s ZWD without error, while partially stochastic uses a typical time-constant process noise to estimate a residual ZWD parameter. The fully stochastic approach estimates a residual ZWD parameter and additionally uses a variable process noise equal to the correction precision multiplied by a scale factor that converts the nominal ZWD precision to equal the tightly constrained ZWD parameter uncertainty applied in the standard PPP configuration. The network-estimated ZWD precision was also incorporated in the horizontal gradient parameter uncertainty for the fully stochastic method using a similar scaling procedure.

Hourly RMS of horizontal and vertical positioning errors were computed for each configuration to evaluate the achievable accuracy under the challenging conditions. For horizontal positioning accuracy, only the fully stochastic configuration improved performance at all user stations, with at least 15.0% improvement. This indicates that the stochastic properties of the network-estimated ZWD corrections used in the horizontal gradient parameter time constraint can improve horizontal positioning accuracy under active tropospheric conditions. For vertical positioning accuracy, all troposphere-corrected configurations outperformed the configuration without corrections, resulting in improvements from 9.6% to 66.2%. Therefore, the standard PPP user can achieve better worst-case vertical positioning accuracy if precise *a priori* tropospheric wet delay information is available. If ZWD precisions are available, then it is recommended that the fully stochastic approach is used to achieve both the horizontal and vertical positioning accuracy benefits.

In the future, data from more GNSS reference station networks with a different configuration of network and user stations shall be studied to evaluate new reference and user station geometry. Also, the effect of absolute ZWD correction accuracy and precision on kinematic PPP performance requires further investigation. Research using similar troposphere-corrected strategies in an integer ambiguity resolution PPP model would be a valuable contribution, as the troposphere is estimable in an absolute sense and is therefore less complex for users to directly incorporate in their model.

5.4 Summary

This chapter develops ionosphere-weighted and troposphere-corrected processing methods and evaluates kinematic PPP performance with respect to the standard approaches. To achieve these objectives, a new modified ionosphere-based stochastic model was developed and tested using standard GIM product data and experimental RIM data using a low-latitude GNSS reference station network in Brazil. Then, kinematic PPP accuracy was evaluated relative to a standard elevation-based stochastic approach to investigate positioning performance of the modified model under highly active equatorial ionospheric conditions. For troposphere-corrected processing, precise ZWD corrections were generated from a network of GNSS reference stations affected by a tropospheric storm event in the Netherlands. The ZWD corrections were then interpolated at user locations and kinematic PPP performance was evaluated using correction strategies that rely on progressively more information provided by the reference network that includes dynamic model constraints on estimated tropospheric components.

Chapter 6

Conclusions, Suggestions and Future Research

6.1 Summary

Over the past twenty years, high-accuracy positioning users have preferred PPP when nearby reference stations are unavailable or are not feasible to deploy. Thus, many commercial and scientific applications have recently explored multi-constellation PPP and benefitted from the gradual accuracy and precision improvements of externally provided satellite clock and orbit products to achieve cm-level global positioning accuracy. Aside from these well-known advantages, PPP accuracy may be jeopardized in the presence of strong atmospheric disturbances, as the typical PPP user does not receive any external information regarding atmospheric conditions. Therefore, this thesis aims to improve kinematic PPP performance under the effects of ionospheric scintillation, strong ionospheric gradients, and extreme tropospheric events by using external atmospheric information.

This thesis extends the improved multi-GNSS positioning performance achieved by Marques et al. (2018) and Dabove et al. (2020) to include the state-of-the-art Galileo constellation in the functional model and reduce kinematic PPP errors under low latitude ionospheric scintillation conditions. The approach quantitatively evaluates single- and multi-GNSS GPS, GLONASS, and Galileo combinations in terms of positioning accuracy, reliability, and precision for a low latitude GNSS reference station for days in March 2019 and 2020. In the experiment, ionospheric scintillation conditions are categorized as weak, moderate, and strong using nearby ISMR data outputs. One of the contributions for this thesis is the superior kinematic

PPP performance under low latitude ionospheric scintillation when Galileo measurements are included in the multi-GNSS functional model.

The modified stochastic model approach by Aquino et al. (2009) was originally developed for GPS-only processing to mitigate ionospheric scintillation effects by using Conker et al. (2000) tracking error model outputs as measure uncertainties. This thesis develops improvements to the mitigation strategy and uses the Conker et al. (2000) outputs for multi-GNSS processing. To support the methods develop herein, the worst multi-GNSS positioning scenarios identified in the evaluation experiment were processed using the modified mitigation strategy. The main modifications to the Aquino et al. (2000) method first disregards the signal that is most likely to fail at the tracking loop level and then set limits on the output tracking error model values. Then, relative tracking jitter information is developed using normalization and scaling so that a non-specialized GNSS receiver user can apply a mixed stochastic model to mitigate ionospheric scintillation effects.

Although the ionosphere-free combination of dual-frequency GNSS measurements eliminates 99.9% of the ionospheric delay, positioning performance may degrade under harsh ionospheric conditions due to carrier phase cycle slips and data outages caused by receiver tracking loop failures. Therefore, Luo et al. (2022) developed a modified stochastic model that amplifies measurement uncertainty based on the ROTI computed from the geometry-free combination of dual-frequency carrier phase measurements. In this thesis, an ionospheric-weighted approach is developed using the Luo et al. (2022) methods with ROT computed from GIM and RIM data products. The major innovation for the new strategy demonstrates an alternative method to improve kinematic PPP performance that is not affected by carrier phase cycle slips and is suitable for measurements on any number of frequencies. In addition, challenges of using an experimental RIM-based product are discussed and strategies are presented to avoid problems that will possibly be encountered when a high-rate ionospheric product is used.

Finally, a tropospheric storm event that rapidly changed the atmospheric water vapor was studied to investigate the reduced positioning accuracy that can occur under these effects (Ma and Verhagen 2020; Ma et al. 2021). The study first estimated precise tropospheric zenith wet delay corrections and correction precision using static PPP processing for GNSS reference stations in the Netherlands with relatively loose tropospheric time constraints. Then, the correction and precision data were spatially interpolated at user station locations using Kriging interpolation, which is a weighted average estimation technique that relies on inter-station distances to compute weights. Afterward, horizontal and vertical kinematic PPP accuracy was evaluated using a standard ionosphere-free model and with deterministic, partially stochastic, and fully stochastic tropospheric corrections. The main innovation was to incorporate correction precision data into the ZWD and horizontal tropospheric gradient parameters estimated by the user.

In this chapter, the conclusions of the thesis are presented with quantitative support of the method developed herein referenced to the appropriate sections. Major contributions to the experiments and scientific community developed throughout the thesis conclude this chapter.

6.2 Conclusions on multi-GNSS ionospheric scintillation evaluation and mitigation

Methods to reduce errors caused by ionospheric scintillation effects generally fit at least one of the following categories: (1) using multi-GNSS processing to increase the number of satellites and strengthen the positioning model (Dabove et al. 2020; Liu et al. 2018; Marques et al. 2018), (2) modification of cycle slip thresholds to reduce false detections (Zhang et al. 2014; Luo et al. 2020), and (3) apply a modified stochastic model that provides more realistic measurement noise under scintillation conditions (Aquino et al. 2009; Guo et al. 2021; Vani et al. 2019). In this thesis, the multi-GNSS approach is used to evaluate and reduce kinematic PPP errors caused by low latitude ionospheric scintillation by using high-power, low-noise Galileo measurements. Then, the modified stochastic model method is extended to include multi-GNSS measurements for ionospheric scintillation mitigation. In addition, the standard mitigation technique using tracking jitter in a modified stochastic model is modified to use relative tracking jitter data that addresses the upper and lower modelled measurement noise limits and can be used together with a standard elevation-based stochastic approach.

6.2.1 Single- and multi-GNSS PPP performance under low-latitude scintillation

Low latitude ionospheric scintillation conditions recorded at a ISMR station were used to verify local post-sunset scintillation conditions at a nearby station located in Brazil where kinematic PPP was performed. Multi-GNSS measurement configurations using GPS and either GLONASS or Galileo, or both, were processed to evaluate kinematic PPP performance under low latitude ionospheric scintillation with respect to GPS-only processing. Horizontal and vertical reliability, accuracy and precision evaluations revealed degraded GPS-only positioning at post-sunset hours and positive improvement, on average, for all multi-GNSS configurations for all evaluation metrics compared to GPS-only.

The overall respective maximum daily reliability, accuracy and precision improvements were: 14.8% vertically using GPS+GLO+GAL, 39.8% vertically using GPS+GAL and 52.7% vertically using GPS+GAL configurations, respectively. In addition, configuration that included Galileo measurements differed in improvement by up to only 5.3% for all evaluation metrics. The GPS+GLO configuration provided up to 20% less accuracy and precision improvement when compared to the corresponding GAL configurations.

Improved multi-GNSS performance is theoretically supported by the increased number of usable satellites, thus improving the model redundancy for multi-GNSS configurations. Therefore, with a similar number of usable satellites available, the better improvements for GPS+GAL compared with GPS+GLO processing is due to the superior noise properties of the Galileo E5 signal used in the E1/E5 combined observable, as opposed to the noisy GLONASS R1/R2 measurements.

6.2.2 Multi-GNSS ionospheric scintillation mitigation at low latitude

GPS L1C/A and L2P with Galileo E1C and E5 measurements for six periods in March 2019, beginning at 20:00 UTC, were processed for elevation-based (non-mitigated) and tracking jitter (mitigated) stochastic models. The resulting 3D positioning error time-series showed the elevation-based model performed worse than the tracking jitter-based method, in terms of maximum position error, for each of the six periods. In the two best cases, the post-convergence maximum 3D positioning error for the mitigated technique improved by 16.6-cm (46.7% improvement) and 13.6-cm (37.4% improvement) relative to the elevation-based method. Furthermore, four of six periods achieved at least 29.5% improvement at the single worst-case epoch when the tracking jitter method was used, with small positive improvements for the remaining periods.

In terms of overall performance, represented by the mean 3D positioning error, the mitigated GPS+Galileo positioning accuracy was consistent with the elevation-based approach at an approximate cm-level. The reliability, represented by the standard deviation of the 3D positioning error, improved by at least 25.6% for five of the six evaluated intervals when the mitigated GPS+Galileo was used, with only 2-mm worse reliability for the remaining interval. In summary, when the elevation-based stochastic model was used, the tracking jitter mitigated approach performed at either a comparable level or offered improvements in the worst-case relative to the non-mitigated elevation-based model.

In the future, the repaired tracking jitter and relative approach would benefit from evaluation under other scintillation conditions, including geomagnetic storms and at high latitude. The techniques developed were also shown to mitigate scintillation for a non-ISMR user and shall therefore be studied in the context of tracking jitter maps that can possibly extend coverage to additional users or for low-cost receivers such as smartphones.

6.3 Conclusions on positioning with external atmospheric delay information

Tropospheric effects are typically addressed in GNSS processing by *a priori* hydrostatic (i.e., dry) correction models (Saastamoinen 1972; Leandro et al. 2006) and estimation of zenith and horizontal gradient of wet delay components (Bar-Sever et al. 1998). However, rapid changes in atmospheric water vapor caused by heavy rainfall is especially problematic and can amplify tropospheric asymmetry effects (Ma and Verhagen 2020) and reduce positioning accuracy (Ma et al. 2021). Therefore, GNSS data were selected to correspond with a tropospheric storm event to evaluate standard PPP against the developed deterministic, partially stochastic, and fully stochastic methods under the extreme storm conditions.

The well-known ionosphere-free functional model that enables high-accuracy PPP lacks ionospheric information, which may be important for applications such as atmospheric monitoring or for use in a modified stochastic model (Luo et al. 2022). Ionospheric information can typically be derived directly from dual-frequency GNSS measurements or indirectly from GIM data products. The modified stochastic approach developed by Luo et al. (2022) uses the direct method which relies on continuous carrier phase measurements that are free from cycle slip effects. However, in challenging ionospheric environments, these conditions are not guaranteed and single-frequency GNSS users are unable to form the required measurement combination to estimate ionospheric information. Therefore, an alternative modified stochastic model strategy, based on the Luo et al. (2022) method, was developed to reduce PPP error using GIM-based and RIM-based data products.

6.3.1 Ionosphere-weighted processing

The Luo et al. (2022) framework was used to develop an alternative modified stochastic model that uses ionospheric information from either GIM or RIM data products. This new method amplifies GNSS measurement uncertainty using the ROT computed from the externally available ionospheric map data and therefore does not rely on the dual-frequency carrier phase measurements observed by the user receiver. This approach eliminates possible artificial ROT discontinuities that occur in the presence of carrier phase cycle slips.

The new stochastic model and a standard satellite elevation-based model were evaluated to study kinematic PPP performance. In the best case, the GIM-based modified stochastic model approach improved the maximum 3D positioning error by up to 52.5% (9.3-cm). In all cases, the average 3D positioning error was consistent at an approximate mm-level regardless of the stochastic method applied. For two stations, the positioning performance was nearly unchanged using the GIM-based model and any minor accuracy reductions were within the Luo et al. (2022) tolerance. Therefore, it can be concluded that the ionospheric-map-based modified stochastic model is best suited for reducing large positioning errors.

The same evaluations were repeated using ROT computed from an experimental RIM product using the alternative modified stochastic model. The RIM product had much larger ROT values, up to 45 TECU per minute, which deactivated the modified model for an average of 88.8% of all epochs. This was caused by the noisy ROT data within the RIM product, compared to a relatively smooth GIM product. Therefore, positioning performance using the RIM product was nearly identical to the standard elevation-based model in terms of both worst-case and mean positioning accuracy. This indicates the external correction information needs to be smoothed and verified to be in good quality to reduce time-variability and local spikes in order to be used in the modified ionosphere-weighted stochastic model.

6.3.2 Troposphere-corrected processing

A rapidly developing storm event that passed over the Netherlands was selected to study troposphere-corrected kinematic PPP performance. GNSS reference stations were separated into network and user categories, where network stations estimated precise ZWD corrections and correction precision using static PPP processing with relatively loose time-constraints for the ZWD parameter uncertainty. Then, Kriging interpolation was used to estimate precise ZWD and ZWD precision at user station locations. The RMS of the interpolated tropospheric corrections with respect to the user-estimated versions were found to be 1.4-cm to 2.0-cm and up to 5.5-cm instantaneous error.

The storm event caused the previously stable ZWD at the user stations to suddenly change by up to 7.2-cm in a one-hour time interval, which is much greater than the typical ZWD parameter constraint allows in standard PPP processing. Thus, for standard PPP without any external tropospheric information, horizontal and vertical positioning errors achieved a cm-level positioning accuracy after initial convergence and prior to the arrival of the storm. Then positioning errors degraded to more than 15-cm upon the arrival of the storm. To mitigate these errors, GPS L1 and L2 measurement data for the user stations were processed using three proposed troposphere-corrected configurations: (1) deterministic, (2) partially stochastic, and (3) fully stochastic. The deterministic configuration assumes that the network-estimated ZWD information is free from error, while the stochastic configurations estimate a residual ZWD parameter to account for remaining errors. The fully stochastic approach further incorporates network-estimated ZWD correction precision in the user's stochastic model for the residual ZWD and horizontal tropospheric gradient parameters' time constraints.

For horizontal positioning accuracy, in terms of hourly RMS, only the fully stochastic configuration improved performance at all user stations, from 15.0% to 45.5%. This indicates that the stochastic properties of the network-estimated tropospheric corrections used in the ZWD gradient time constraint can consistently improve horizontal positioning accuracy under tropospheric storm conditions. For vertical positioning accuracy, all troposphere-corrected configurations outperformed the configuration without corrections, resulting in improvements from 9.6% to 66.2%. Therefore, the standard PPP user can achieve better worst-case vertical positioning accuracy if *a priori* tropospheric wet delay information is provided by the network. If ZWD precisions are available, then it is recommended that the fully stochastic approach is used to achieve both the horizontal and vertical positioning accuracy benefits.

6.4 Key innovations and contributions to knowledge

The critical findings, innovations, and contributions to the scientific knowledge base are as follows:

1. **Demonstrated benefits of using multi-GNSS processing with modernized Galileo signals to combat low latitude ionospheric scintillation effects on kinematic PPP.** A thorough evaluation of kinematic PPP performance affected by low latitude ionospheric scintillation was presented. The quantitative evaluation of positioning accuracy, reliability, and precision revealed that GPS+Galileo configurations achieved comparable performance as the GPS+GLONASS+Galileo combination. Furthermore, the multi-GNSS combinations that included Galileo successfully reduced the large positioning errors caused by the harsh low latitude ionospheric scintillation environment.
2. **Mitigated low-latitude ionospheric scintillation effects for a non-specialized GNSS user using repaired receiver tracking error in a mixed stochastic model.** Receiver tracking error model outages were identified and repaired, then outputs were extended for multi-GNSS processing using Galileo signals. The modified stochastic model approach was extended to a

non-specialized GNSS user using an innovative relative tracking jitter approach, which was used simultaneously with a standard elevation-based strategy in a mixed stochastic model. Despite excellent improvement when multi-GNSS configurations are used, results showed that further mitigation of ionospheric scintillation effects can be achieved using the new approach that was developed to be suitable for non-ISMR users.

3. **Mitigated ionospheric gradient effects using a new modified stochastic model that incorporates GIM product data to amplify measurement uncertainty.** An alternative approach to amplify measurement uncertainty using GIM-based data was developed and tested to eliminate the dependency on potentially problematic GNSS measurement data. In addition to the standard GIM data, an experimental RIM data product was also tested and found to be problematic for the modified stochastic method due to highly variable ROT at most epochs, as a result of the noisy experimental RIM data. These findings helped to set limits on the activation of the modified stochastic model in order to avoid potential degradation and restore positioning performance similar to the standard elevation-based model.
4. **Enhanced kinematic PPP accuracy under extreme tropospheric storm conditions using network-estimated tropospheric corrections and correction precision for affected users.** The rapidly varying and highly asymmetric tropospheric state was evaluated using progressively more external tropospheric information. For the first time, a fully stochastic approach was developed and tested, where precise ZWD corrections and correction precision were incorporated into the kinematic PPP functional model. The estimable tropospheric parameter time constraints of the user, as part of the Kalman filter dynamic model, were modified using the network-estimated corrections precision in a so-called fully stochastic strategy. This approach allowed the otherwise tightly constrained tropospheric parameters to become more variable based on the correction precision and thus improve positioning accuracy during the storm event.

6.5 Recommendations for future studies

In the scope of this thesis and the research conducted herein, the recommendations and outlooks for future studies are as follows:

1. **Evaluation of multi-frequency and undifferenced/uncombined functional model performance under low latitude ionospheric scintillation conditions.** The research carried out in this thesis used dual-frequency measurements to form an ionosphere-free functional model for kinematic PPP configurations. However, triple- or multi-frequency ionosphere-free combinations are available to study in the current multi-GNSS environment.
2. **Ionospheric scintillation mitigation using undifferenced/uncombined multi-GNSS functional model.** The standard Conker et al. (2000) tracking error model outputs are available for dual-frequency GPS L1 and L2 pseudorange and carrier phase measurements. Therefore, the mitigation strategy introduced by Aquino et al. (2009) is possibly more suitable to use in an undifferenced/uncombined functional model where measurements are treated independently, unlike the ionosphere-free model that requires uncertainty propagation from the individual measurement noise to the combined noise. This strategy may help eliminate some of the problems that occur when the Conker et al. (2000) outputs amplify the measurement uncertainty to many orders of magnitude beyond the typical values output by an elevation-based stochastic model.
3. **Enhanced RIM data products.** The RIM data used in this thesis for ionosphere-weighted processing was generated as requested with an extremely high temporal resolution. In the future, other RIM products generated using different temporal and spatial resolutions can be tested with the modified stochastic strategy to investigate interpolation effects on the positioning performance. Lastly, smoothing of the RIM data in the time domain will likely improve the achievable positioning accuracy, as the resulting ionospheric slant delays would approach the smoothness of the GIM data.
4. **Enhanced tropospheric storm mitigation.** In this thesis, the tropospheric storm event was selected to study due to the extreme, and difficult to find, asymmetry and rapidly increasing ZWD conditions. Further research would

benefit by studying more storm events and using different reference station spacing and geometry. Furthermore, tuning of the fully stochastic method may result in improved mitigation if more realistic tropospheric correction information is provided to the user. Different interpolation techniques, other than Kriging, may improve positioning performance and require additional testing and validation. Lastly, a dedicated horizontal tropospheric gradient product estimated by the network processing and interpolated to user locations may further improve the horizontal positioning accuracy under asymmetric tropospheric conditions.

References

Alkan, R.M. (2001). GPS-single point positioning without selective availability. In: Proceedings of US Hydrographic Conference, Norfold, US.

Aquino, M., Moore, T., Dodson, A., Waugh, S., Souter, J., and Rodrigues, F. S. (2005). Implications of ionospheric scintillation for GNSS users in Northern Europe, Journal of Navigation, 58(2), pp. 241-256. https://doi.org/10.1017/S037346330500321

Aquino, M., Monico, J. F. G., Dodson, A. H., Marques, H., De Franceschi, G., Alfonsi, L., Romano, V., Andreotti, M. (2009). Improving the GNSS positioning stochastic model in the presence of ionospheric scintillation. Journal of Geodesy, 83(10), pp. 953-966. https ://doi.org/10.1007/s00190-009-0313-6

Arbesser-Rastburg, B. (2006). The Galileo Single Frequency Ionospheric Correction Algorithm. European Space Weather Week, Brussels.

Ashby, N. (2003). Relativity in the Global Positioning System. Living Reviews in Relativity, 6(1). https://doi.org/10.12942/lrr-2003-1

Bar-Sever, Y. E., Kroger, P. M., Borjesson, J. A. (1998). Estimating horizontal gradients of tropospheric path delay with a single GPS receiver. Journal of Geophysical Research: Solid Earth, 103(B3), pp. 5019-5035. https://doi.org/10.1029/97JB03534

Basile, F., Moore, T., Hill, C. (2019). Analysis on the Potential Performance of GPS and Galileo Precise Point Positioning using Simulated Real-Time Products. Journal of Navigation, 72(1), pp. 19-33. https://doi.org/10.1017/S0373463318000577

Bassiri, S., Hajj, G. A. (1993). Higher-order ionospheric effects on the global positioning system observables and means of modeling them. Manuscripta geodaetica, 18(5), pp. 280-280.

Basu, S., K. M. Groves, Su. Basu, and P. J. Sultan (2002). Specification and forecasting of scintillations in communication/navigation links: Current status and future plans, Journal of Atmospheric and Solar-Terrestrial Physics, 64, pp. 1745–1754. https://doi.org/10.1016/S1364-6826(02)00124-4.

BDS-SIS-ICD (2013). BeiDou navigation satellite system signal in space interface control document—open service signal (version 2.0). China Satellite Navigation Office.

Beutler G., Schildknecht T., Hugentobler U., Gurtner W. (2003). Orbit determination in satellite geodesy. Advances in Space Research, 31(8), pp. 1853-1868

Bisnath, S., Gao, Y. (2009). Precise point positioning: A powerful technique with a promising future. GPS World, 20(4), pp. 43-50.

Bisnath, S., Aggrey, J., Seepersad, G., Gill, M. (2018). Innovation: Examining precise point positioning now and in the future. GPS World, March 19, 2018.

Blewitt, G. (1990). An automatic editing algorithm for GPS data, Geophysical Research Letters, 17(3), pp. 199–202. https://doi.org/10.1029/GL017i003p00199

Blewitt, G. (2008). Fixed point theorems of GPS carrier phase ambiguity resolution and their application to massive network processing: Ambizap. Journal of Geophysical Research, 113(B12), p. B12410. https://doi.org/10.1029/2008JB005736

Bock H., Dach R., Jaggi A., Beutler G. (2009). High-rate GPS clock corrections from CODE: Support of 1 Hz applications. Journal of Geodesy, 83(11), pp. 1083-1094. https://doi.org/10.1007/s00190-009-0326-1

Boehm J., Niell A.E., Tregoning P., Schuh H. (2006). The Global Mapping Function (GMF): A new empirical mapping function based on data from numerical weather model data. Geophysical Research Letters, 33(L07304). https://doi.org/10.1029/2005GL025546

Bouin, M.N., Ballu, V., Calmant, S., Bore, J.M., Folcher, E., Ammann, J. (2009). A kinematic GPS methodology for sea surface mapping, Vanuatu. Journal of Geodesy, 83(12), pp. 1203-1217. https://doi.org/10.1007/s00190-009-0338-x

Briggs, B., Parkin, I. (1963). On the variation of radio star and satellite scintillations with zenith angle. Journal of Atmospheric and Solar-Terrestrial Physics, 25(6), pp. 339-366. https://doi.org/10.1016/0021-9169(63)90150-8

Cai, C., Gao, Y. (2007). Performance analysis of precise point positioning based on combined GPS and GLONASS. In: Proceedings of ION GNSS 20th International Technical Meeting of the Satellite Division, Fort Worth, US, pp. 858-865.

Cai, C., Liu, Z., Xia, P., & Dai, W. (2013). Cycle slip detection and repair for undifferenced GPS observations under high ionospheric activity. GPS Solutions, 17(2), pp. 247-260. doi:10.1007/s10291-012-0275-7

Cao, W., Hauschild, A., Steigenberger, P., Langley, R.B., Urquhart, L., Santos, M., Montenbruck, O. (2010). Performance evaluation of integrated GPS/GIOVE precise point positioning. In: Proceedings of ION International Technical Meeting, San Diego, US, pp. 540-552

Chadwell, C.D., Spiess, F.N. (2008). Plate motion at the ridge-transform boundary of the south Cleft Segment of the Juan de Fuca Ridge from GPS-acoustic data. Journal of Geophysical Research, 113(B04415). doi:10.1029/2007JB004936

Chen, G. and Herring, T. A. (1997). Effects of Atmospheric Azimuthal Asymmetry on the Analysis of Space Geodetic Data, Journal of Geophysical Research, 102(B9), pp. 20,489-20,502. https://doi.org/10.1029/97JB01739

Chen, H-Y., Ikuta, R., Hsu, Y-J., Tsujii, T., Ando, M., Tu, Y., Kohmi, T., Takemoto, K., Mizuno, K., Tung, H., Ku, C-S., and Lin, C-H. (2021). A Decade of Global Navigation Satellite System/Acoustic Measurements of Back-Arc Spreading in the Southwestern Okinawa Trough. Frontiers in Earth Science, 9, p. 601138. doi: 10.3389/feart.2021.601138

Cherniak, I., Krankowski, A., & Zakharenkova, I. (2018). ROTI Maps: a new IGS ionospheric product characterizing the ionospheric irregularities occurrence. GPS Solutions, 22(3), pp. 1-12. https://doi.org/10.1007/s10291-018-0730-1

Choi, B.-K., Cho, C.-H., Cho, J. H., Lee, S. J. (2015). Multi-GNSS Standard Point Positioning using GPS, GLONASS, BeiDou and QZSS Measurements Recorded at MKPO Reference Station in South Korea. Journal of Positioning, Navigation, and Timing, 4(4), pp. 205–211. https://doi.org/10.11003/JPNT.2015.4.4.205

Ciraolo, L., Azpilicueta, F., Brunini, C., Meza, A., & Radicella, S. M. (2007). Calibration errors on experimental slant total electron content (TEC) determined with GPS. Journal of geodesy, 81(2), pp. 111-120. https://doi.org/10.1007/s00190-006-0093-1

Collins, J. P., and Langley, R. B. (1997). A tropospheric delay model for the user of the wide area augmentation system. Fredericton, NB, Canada: Department of Geodesy and Geomatics Engineering, University of New Brunswick.

Colombo OL (2006). A zenith delay model for precise kinematic aircraft navigation. In: Proceedings of ION GNSS 19th International Technical Meeting of the Satellite Division, Fort Worth, US, pp. 68-76

Dabove, P., Linty, N., Dovis, F. (2020). Analysis of multi-constellation GNSS PPP solutions under phase scintillations at high latitudes. Applied Geomatics, 12(1), pp. 45-52. https://doi.org/10.1007/s12518-019-00269-4

Dai, L. (2000). Dual-frequency GPS/GLONASS real-time ambiguity resolution for medium-range kinematic positioning. In: Proceedings of ION GPS 13th International Technical Meeting of the Satellite Division, Salt Lake City, US, pp. 1071-1079.

Dai, L., Eslinger, D., Sharpe, T. (2007). Innovative algorithms to improve long range RTK reliability and availability. In: Proceedings of ION National Technical Meeting, San Diego, US, pp. 860-872.

Defraigne, P., Bruyninx, C. (2000). Frequency transfer using GPS codes and phases: short and long term stability. In: Breakiron LA (ed) Proceedings of the 31st PTTI meeting, Dana Point, California, December 1999, pp. 471–478.

Defraigne, P., Bruyninx, C. (2007). On the link between GPS pseudorange noise and day-boundary discontinuities in geodetic time transfer solutions. GPS Solutions, 11, pp. 239–249. https://doi.org/10.1007/s10291-007-0054-z

Defraigne, P., Aerts, W., Cerretto, G., Cantoni, E. and Sleewaegen, JM. (2014). Calibration of Galileo signals for time metrology. IEEE transactions on Ultrasonics Ferroelectrics and Frequency control, 61(12), pp. 1967-75.

De Franceschi, G., Alfonsi, L., Romano, V., Aquino, M., Dodson, A., Mitchell, C.N., Spencer, P., Wernik, A.W. (2008). Dynamics of high latitude patches and associated small scale irregularities during the October and November 2003 storms. Journal of Atmospheric and Solar-Terrestrial Physics, 70, pp. 879–888.

Dixon, K. (2006). StarFire: A global SBAS for sub-decimeter precise point positioning. In: Proceedings of ION GNSS 19th International Technical Meeting of the Satellite Division, Fort Worth, US, pp. 2286-2296.

Doherty, P.H., Delay, S.H., Valladares, C.E., Klobuchar, J.A. (2003). Ionospheric scintillation effects on GPS in the equatorial and auroral regions. Navigation, 50, pp. 235–245. https://doi.org/10.1002/j.2161-4296.2003.tb00332.x

Douša, J., Dick, G., Kačmařík, M., Brožková, R., Zus, F., Brenot, H., Stoycheva, A., Möller, G., and Kaplon, J. (2016). Benchmark campaign and case study episode in central Europe for development and assessment of advanced GNSS tropospheric models and products. Atmospheric Measurement Techniques, 9(7), pp. 2989-3008. https://doi.org/10.5194/amt-9-2989-2016

Dyrud, L., Jovancevic, A., Brown, A., Wilson, D. and Ganguly, S. (2008). Ionospheric measurement with GPS: Receiver techniques and methods, Radio Science, 43(6). doi:10.1029/2007RS003770.

Eckl, M.C., Snay, R.A., Soler, T., Cline, M.W., Mader, G.L. (2001). Accuracy of GPS-derived relative positions as a function of interstation distance and observing-session duration. Journal of Geodesy, 75(12), pp. 633-640. https://doi.org/10.1007/s001900100204

Elmas, Z. G. (2013). Exploiting new GNSS signals to monitor, model and mitigate the ionospheric effects in GNSS. PhD thesis, University of Nottingham. http://eprints.nottingham.ac.uk/28418/

European GNSS Agency (2018). Using GNSS raw measurements on Android devices, White paper, Publications Office. Accessed February 2021. https://data.europa.eu/doi/10.2878/449581

European GNSS Agency (2019). GSA GNSS market report – Issue 6. Accessed January 2021. doi:10.2878/031762

European GNSS Agency (2020). GSA GNSS user technology report – Issue 3. Accessed January 2021. doi:10.2878/565013.

Evans, E.L., Minson, S.E., Chadwell, C.D. (2022). Imaging the next Cascadia earthquake: optimal design for a seafloor GNSS-A network, Geophysical Journal International, 228(2), pp. 944–957. https://doi.org/10.1093/gji/ggab360

Gebbers, R. and Adamchuk, V.I. (2010). Precision agriculture and food security. Science, 327(5967), pp. 828-831. doi:10.1126/science.1183899

Geng, J., Meng, X., Teferle, F.N., Dodson, A.H. (2010a). Performance of precise point positioning with ambiguity resolution for 1- to 4-hour observation periods. Survey Review, 42(316), pp. 155-165. https://doi.org/10.1179/003962610X12572516251682

Geng, J., Teferle, F.N., Meng, X., Dodson, A.H. (2010b). Kinematic precise point positioning at remote marine platforms. GPS Solutions, 14, pp. 343-350 https://doi.org/10.1007/s10291-009-0157-9

Geng J., Jiang E., Li G., Xin S., Wei N. (2019). An Improved Hatch Filter Algorithm towards Sub-Meter Positioning Using only Android Raw GNSS Measurements without External Augmentation Corrections. Remote Sensing, 11(14), p. 1679. https://doi.org/10.3390/rs11141679

Ghilani, C. D. (2017). Adjustment computations: spatial data analysis. John Wiley & Sons.

Gjevestad, J.G.O., Ovstedal, O., Kjorsvik, N.S. (2007). The contribution of GLONASS and Galileo to kinematic GPS precise point positioning. In: Proceedings of ION GNSS 20th International Technical Meeting of the Satellite Division, Fort Worth, US, pp. 876-882

Gong, X., Gu, S., Lou, Y., Zheng, F., Ge, M., & Liu, J. (2018). An efficient solution of real-time data processing for multi-GNSS network. Journal of Geodesy, 92(7), pp. 797–809. https://doi.org/10.1007/s00190-017-1095-x

GPS S/A Announcement (2000). Announcement of U.S. White House, Office of the Press Secretary: statement by the president regarding the U.S. decision to stop degrading GPS accuracy. U.S. Department of Homeland Security, U.S. Coast Guard, Navigation Center. Accessed: December 2021. https://www.navcen.uscg.gov/?pageName=gpsSelectiveAvailability#

Gregorius, T. (1996). GIPSY-OASIS II: how it works. Department of Geomatics, University of Newcastle upon Tyne, p. 109.

Grzesiak, M., Cesaroni, C., Spogli, L., De Franceschi, G., & Romano, V. (2018). Regional short-term forecasting of ionospheric TEC and scintillation. Radio Science, 53(10), pp. 1254-1268. https://doi.org/10.1029/2017RS006310

Guo, F., Li, X., Zhang, X., Wang, J. (2016). The contribution of Multi-GNSS Experiment (MGEX) to precise point positioning. Advances in Space Research, 59(11), pp. 2714-2725.

Guo, K., Aquino, M., Veettil, S. V., Liu, Z., Chen, W., Marques, H. A. (2019). Analysis of Ionospheric Scintillation and its Impact on PPP at Low Latitudes. Proc. ION Pacific PNT, Institute of Navigation, Honolulu, Hawaii, USA, April 8-11, pp. 835-845. https://doi.org/10.33012/2019.16842

Guo, K., Veettil, S. V., Weaver, B. J., Aquino, M. (2021). Mitigating high latitude ionospheric scintillation effects on GNSS Precise Point Positioning exploiting 1-s scintillation indices. Journal of Geodesy, 95(30). https://doi.org/10.1007/s00190-021-01475-y

Han, S. (1997). Quality-control issues relating to instantaneous ambiguity resolution for real-time GPS kinematic positioning. Journal of Geodesy, 71(6), pp. 351-361. https://doi.org/10.1007/s001900050103

Han, S., Rizos, C. (2000). Airborne GPS kinematic positioning and its application to oceanographic mapping. Earth Planets Space, 52(10), pp. 819-824. https://doi.org/10.1186/BF03352288

Hatch, R. R. (1982). The synergism of GPS code and carrier measurements. Proceedings of the Third International Geodetic Symposium on Satellite Doppler Positioning, New Mexico, II, pp. 1213-1232.

Hauschild, A., Montenbruck, O. (2009). Kalman-filter-based GPS clock estimation for near real-time positioning. GPS Solutions, 13, pp. 173–182. https://doi.org/10.1007/s10291-008-0110-3

Hauschild, A. (2017). Combinations of Observations. In: Teunissen P.J., Montenbruck O. (eds) Springer Handbook of Global Navigation Satellite

Systems. Springer Handbooks. Springer, Cham. https://doi.org/10.1007/978-3-319-42928-1_20

Hernández-Pajares, M., Juan, J. M., Sanz, J., Orus, R., Garcia-Rigo, A., Feltens, J., Komjathy, A., Schaer, S. C., Krankowski, A. (2009). The IGS VTEC maps: a reliable source of ionospheric information since 1998. Journal of Geodesy, 83(3-4), pp. 263-275. https://doi.org/10.1007/s00190-008-0266-1

Hide, C., Pinchin, J., Park, D. (2007). Development of a low cost multiple GPS antenna attitude system. In Proceedings of the 20th International Technical Meeting of the Satellite Division of The Institute of Navigation 2007 ION GNSS 2007, Fort Worth, TX, USA, 25–28 September, Volume 1, pp. 88–95.

Hill, E.M., Davis, J. L., Elosegui, P., Wernicke, B. P., Malikowski, E., Niemi, N. A. (2009). Characterization of site-specific GPS errors using a short-baseline network of braced monuments at Yucca Mountain, southern Nevada. Journal of Geophysical Research, 114(B11402). doi:10.1029/2008JB006027

Hochegger, G., Nava, B., Radicella, S., Leitinger, R. (2000). A family of ionospheric models for different uses. Physics and Chemistry of the Earth Part C: Solar, Terrestrial & Planetary Science, 25, pp. 307–310.

Hopfield, H. S. (1969). Two-quadratic tropospheric refractivity profile for correction satellite data. Journal of Geophysical Research, 74(18), pp. 4487-4499

Hoque, M. M., & Jakowski, N. (2007). Higher order ionospheric effects in precise GNSS positioning. Journal of Geodesy, 81(4), pp. 259-268. https://doi.org/10.1007/s00190-006-0106-0

Hoque, M. M. and Jakowsi, N. (2008). Estimate of higher order ionospheric errors in GNSS positioning, Radio Science, 43(RS5008), pp. 1–15. https://doi.org/10.1029/2007RS003817

Hoque, M. M., & Jakowski, N. (2015). An alternative ionospheric correction model for global navigation satellite systems. Journal of Geodesy, 89(4), pp. 391-406. https://doi.org/10.1007/s00190-014-0783-z

Humphreys, T. (2005). GPS carrier tracking loop performance in the presence of ionospheric scintillations. In: Proceedings of ION GNSS 2005, Institute of Navigation, Long Beach, CA, September 2005, pp. 156–167.

Hunsucker, R. D., and Hargreaves, J. K. (2003). The high-latitude F region and the trough. The high-latitude ionosphere and its effects on radio propagation, pp. 227-281.

ICD GLONASS (2008). Global Navigation Satellite System GLONASS, Interface Control Document, Navigational Radio Signal in bands L1, L2. Moscow, Russia

International Telecommunication Union (2016). Ionospheric propagation data and prediction methods required for the design of satellite services and systems. ITU Radiocommunication Sector, Radiowave Propagation technical report, Recommendation ITU-R P.531-13, Geneva, Switzerland. http://www.itu.int/publ/R-REC/en

IS-GPS-200G (2012). Global positioning system directorate systems engineering and integration: interface specification IS-GPS-200. https://www.gps.gov/technical/icwg/IS-GPS-200G.pdf

Jiao Y., Morton Y. T. (2015). Comparison of the effect of high-latitude and equatorial ionospheric scintillation on GPS signals during the maximum of solar cycle 24. Radio Science, 50(9), pp. 886–903. https://doi.org/10.1002/2015RS005719.

Jefferson D.C., Heflin M. B., Muellerschoen R. J. (2001). Examining the C1-P1 pseudorange bias. GPS Solutions, 4(4), pp. 25-30. https://doi.org/10.1007/PL00012862

Jensen A. B. O., Ovstedal O. (2008). The effect of different tropospheric models on precise point positioning in kinematic mode. Survey Review, 40(308), pp. 173-187.

Jia, M., Dawson, J., & Moore, M. (2014). AUSPOS: Geoscience Australia’s on-line GPS positioning service. In Proceedings of the 27th International Technical Meeting of The Satellite Division of the Institute of Navigation (ION GNSS+), pp. 315-320.

Juan, J. M., Aragon-Angel, A., Sanz, J., González-Casado, G., Rovira-Garcia, A. (2017). A method for scintillation characterization using geodetic receivers operating at 1 Hz. Journal of Geodesy, 91(11), pp. 1383-1397. https://doi.org/10.1007/s00190-017-1031-0

Kalman, R. E. (1960). A new approach to linear filtering and prediction problems. Journal of Basic Engineering, 82(1), pp. 35-45. https://doi.org/10.1115/1.3662552

Kato, T., Terada, Y., Ito, K., Hattori, R., Abe, T., Miyake, T., Koshimura, S., Nagai, T. (2005). Tsunami due to the 2004 September 5th off the Kii peninsula earthquake, Japan, recorded by a new GPS buoy. Earth Planets Space, 57(4), pp. 297-301.

King, M. A. (2009). The GPS contribution to the error budget of surface elevations derived from airborne LIDAR. IEEE Transactions on Geoscience and Remote Sensing, 47(3), pp. 874-883.

King, M. A., Williams S. D. P. (2009). Apparent stability of GPS monumentation from short-baseline time series. Journal of Geophysical Research, 114(B10403). doi:10.1029/2009JB006319

Kinrade, J., Mitchell, C. N., Yin, P., Smith, N., Jarvis, M. J., Maxfield, D. J., et al. (2012). Ionospheric scintillation over Antarctica during the storm of 5–6 April 2010. Journal of Geophysical Research: Space Physics, 117(A5). https://doi.org/10.1029/2011JA017073

Kintner, P. M., Kil, H., Beach, T. L., de Paula, E. R. (2001). Fading timescales associated with GPS signals and potential consequences. Radio Science, 36, pp. 731–743. doi:10.1029/1999RS002310

Kintner, P. M., Ledvina, B. M., & De Paula, E. R. (2007). GPS and ionospheric scintillations. Space Weather, 5(9). https://doi.org/10.1029/2006SW000260

Klobuchar, J. (1987). Ionospheric Time-Delay Algorithms for Single-Frequency GPS Users. IEEE Transactions on Aerospace and Electronic Systems, 3, pp. 325-331.

Kouba, J., Heroux, P. (2001). Precise point positioning using IGS orbit and clock products. GPS Solutions, 5(2), pp. 12-28. https://doi.org/10.1007/PL00012883

Kouba, J., Springer, T. (2001). New IGS Station and Satellite Clock Combination. GPS Solutions, 4, pp. 31–36. https://doi.org/10.1007/PL00012863

Kouba, J. (2009). Testing of global pressure/temperature (GPT) model and global mapping function (GMF) in GPS analyses. Journal of Geodesy, 83(3), pp. 199-208. https://doi.org/10.1007/s00190-008-0229-6

Kouba J. (2015). A guide to using International GNSS Service (IGS) products. Geodetic Survey Division, Natural Resources Canada. https://igs.org/wp-content/uploads/2019/08/UsingIGSProductsVer21_cor.pdf

Lan, Y., Shengde, C., Fritz, B.K. (2017). Current status and future trends of precision agricultural aviation technologies. International Journal of Agricultural and Biological Engineering, 10(3), pp. 1-17. http://ijabe.org/index.php/ijabe/article/view/3088

Landau H., Chen X., Klose S., Leandro R., Vollath U. (2007). Trimble's RTK and DGPS solutions in comparison with precise point positioning. In: Sideris MG (ed) Observing our changing Earth, Springer-Verlag, Berlin Heidelberg, pp. 709-718

Larson, K. M., Bilich, A., Axelrad, P. (2007). Improving the precision of high-rate GPS. Journal of Geophysical Research, 112(B05422). doi:10.1029/2006JB004367

Laurichesse D., Mercier F. (2007). Integer ambiguity resolution on undifferenced GPS phase measurements and its application to PPP. In: Proceedings of the 20th international technical meeting of the satellite division of the Institute of Navigation (ION GNSS 2007), pp. 839–848.

Leandro, R. F., Santos, M. C., Langley, R. B. (2006). UNB neutral atmosphere models: development and performance. Proc. ION NTM, Institute of Navigation, Monterey, California, USA, 18–20 January 2006, pp. 564-573. https://www.ion.org/publications/abstract.cfm?articleID=6562

Leandro R., Langley R. B., Santos M. C. (2007a). Estimation of P2-C2 biases by means of precise point positioning. In: Proceedings of the 63rd Annual Meeting of The Institute of Navigation, Cambridge, US, pp. 225-231.

Leandro, R. F., Santos M. C., and Langley R. B. (2007b). GAPS: The GPS Analysis and Positioning Software – A Brief Overview. Proceedings of the 20th International Technical Meeting of the Science for a Sustainable Planet, International Association of Geodesy Symposia, 139.

Leandro, R., Landau, H., Nitschke, M., Glocker, M., Seeger, S., Chen, X., Deking, A., BenTahar, M., Zhang, F., Ferguson, K., et al. (2011). RTX positioning: the next generation of cm-accurate real-time GNSS positioning. In: Proceedings of the 24th International Technical Meeting of the Satellite Division of the Institute of Navigation (ION GNSS), Portland, OR, Sept 19–23, pp. 1460–1475.

Leick, A. (1995). GPS satellite surveying, 2nd Ed., Wiley, New York.

Levy, L. J. (1997). The Kalman filter: navigation's integration workhorse. GPS World, 8(9), pp. 65-71.

Li, G., Ning, B., Ren, Z., Hu, L. (2010). Statistics of GPS ionospheric scintillation and irregularities over polar regions at solar minimum. GPS Solutions, 14(4), pp. 331–341. doi:10.1007/s10291-009-0156-x

Li, P., Zhang, X., Ren, X. et al. (2016). Generating GPS satellite fractional cycle bias for ambiguity-fixed precise point positioning. GPS Solutions, 20, pp. 771–782. https://doi.org/10.1007/s10291-015-0483-z

Li, X., Ge, M., Dai, X., Ren, X., Fritsche, M., Wickert, J., & Schuh, H. (2015). Accuracy and reliability of multi-GNSS real-time precise positioning: GPS, GLONASS, BeiDou, and Galileo. Journal of Geodesy, 89(6), pp. 607-635. https://doi.org/10.1007/s10291-019-0852-0

Liu, T., Chen, H., Chen, Q., Jiang, W., Laurichesse, D., An, X., & Geng, T. (2021). Characteristics of phase bias from CNES and its application in multi-frequency and multi-GNSS precise point positioning with ambiguity resolution. GPS Solutions, 25, pp. 1-13. https://doi.org/10.1007/s10291-021-01100-7

Liu, T., Zhang, B., Yuan, Y., Li, Z., & Wang, N. (2019). Multi-GNSS triple-frequency differential code bias (DCB) determination with precise point positioning (PPP). Journal of Geodesy, 93(5), pp. 765-784. https://doi.org/10.1007/s00190-019-01229-x

Liu, Y., Lou, Y., Ye, S., Zhang, R., Song, W., Zhang, X., Li, Q. (2017). Assessment of PPP integer ambiguity resolution using GPS, GLONASS and BeiDou (IGSO, MEO) constellations. GPS Solutions, 21(4), pp. 1647-1659. https://doi.org/10.1007/s10291-017-0641-6

Liu, Z. (2011). A new automated cycle slip detection and repair method for a single dual-frequency GPS receiver. Journal of Geodesy, 85(3), pp. 171–183. https://doi.org/10.1007/s00190-010-0426-y

Lou Y., Zheng F., Gu S., Wang C., Guo H., Feng Y. (2016). Multi-GNSS precise point positioning with raw single-frequency and dual-frequency measurement models. GPS Solutions, 20(4), pp. 849-862. http://doi.org/10.1007/s10291-015-0495-8

Loyer, S., Banville, S., Geng, J., & Strasser, S. (2021). Exchanging satellite attitude quaternions for improved GNSS data processing consistency. Advances in Space Research, 68(6), pp. 2441-2452. https://doi.org/10.1016/j.asr.2021.04.049

Luo, X., Lou, Y., Xiao, Q., Gu, S., Chen, B., Liu, Z. (2018). Investigation of ionospheric scintillation effects on BDS precise point positioning at low-latitude regions. GPS Solutions, 22(63). https://doi.org/10.1007/s10291-018-0728-8

Luo, X., Gu, S., Lou, Y., Chen, B., Song, W. (2020). Better thresholds and weights to improve GNSS PPP under ionospheric scintillation activity at low latitudes. GPS Solutions, 24(17). https://doi.org/10.1007/s10291-019-0924-1

Luo, X., Du, J., Galera Monico, J. F., Xiong, C., Liu, J., & Liang, X. (2022). ROTI‐Based Stochastic Model to Improve GNSS Precise Point Positioning Under Severe Geomagnetic Storm Activity. Space Weather, 20(7), e2022SW003114. https://doi.org/10.1029/2022SW003114

Ma, H., Zhao, Q., Verhagen, S., Psychas, D., Liu, X. (2020). Assessing the Performance of Multi-GNSS PPP-RTK in the Local Area. Remote Sensing, 12(20), p. 3343. https://doi.org/10.3390/rs12203343

Ma, H., Psychas, D., Xing, X., Zhao, Q., Verhagen, S., & Liu, X. (2021). Influence of the inhomogeneous troposphere on GNSS positioning and integer ambiguity resolution. Advances in Space Research, 67(6), pp. 1914-1928. https://doi.org/10.1016/j.asr.2020.12.043

Madore, B., Imahori, G., Kum, J., White, S., Worthem, A. (2018). NOAA's use of remote sensing technology and the coastal mapping program. OCEANS 2018 MTS/IEEE Charleston, pp. 1-7, doi:10.1109/OCEANS.2018.8604932

Malys, S., Jensen, P. A. (1990). Geodetic Point Positioning with GPS Carrier Beat Phase Data from the CASA UNO Experiment. Geophysical Research Letters, 17(5), pp. 651-654. https://doi.org/10.1029/GL017i005p00651

Mannucci, A. J., Wilson, B. D., Yuan, D. N., Ho, C. H., Lindqwister, U. J., & Runge, T. F. (1998). A global mapping technique for GPS-derived ionospheric total electron content measurements. Radio Science, 33(3), pp. 565-582. https://doi.org/10.1029/97RS02707

Marques, H. A. S., Monico, J. F. G., Marques, H. A. (2016). Performance of the L2C civil GPS signal under various ionospheric scintillation effects. GPS Solutions, 20(2), pp. 139-149. https://doi.org/10.1007/s10291-015-0472-2

Marques, H. A., Marques, H. A. S., Aquino, M., Veettil, S. V., Monico, J. F. G. (2018). Accuracy assessment of Precise Point Positioning with multi-constellation GNSS data under ionospheric scintillation effects. Journal of Space Weather and Space Climate, 8(A15). https://doi.org/10.1051/swsc/2017043

Masoumi, S., McClusky, S., Koulali, A., & Tregoning, P. (2017). A directional model of tropospheric horizontal gradients in Global Positioning System and its application for particular weather scenarios. Journal of Geophysical Research: Atmospheres, 122(8), pp. 4401-4425. https://doi.org/10.1002/2016JD026184

McDonald K.D. (2002). The modernization of GPS: Plans, new capabilities and the future relationship to Galileo. Journal of Global Positioning System, 1(1), pp. 1-17.

Meggs, R. W., Mitchell, C. N., Honary, F. (2008). GPS scintillation over the European arctic during the November 2004 storms. GPS Solutions, 12, pp. 281–287. doi:10.1007/s10291-008-0090-3

Melbourne, W. G. (1985). The case for ranging in GPS-based geodetic systems. In Proceedings of the first international symposium on precise positioning with the Global Positioning System, US Department of Commerce Rockville, Maryland, pp. 373-386.

Mitchell, C. N., Alfonsi, L., De Franceschi, G., Lester, M., Romano, V., Wernik, A.W. (2005). GPS TEC and scintillation measurements from the polar ionosphere during the October 2003 storm. Geophysical Research Letters, 32(L12S03). doi:10.1029/2004GL021644

Mohammed, J. (2017). Precise Point Positioning (PPP): GPS vs. GLONASS and GPS+GLONASS with an alternative strategy for Tropospheric Zenith Total Delay (ZTD) Estimation. Ph.D. thesis, University of Nottingham. http://eprints.nottingham.ac.uk/45468/

Montenbruck, O., and Gill, E. (2000). Real-time estimation of sgp4 orbital elements from gps navigation data. In International Symposium Space Flight Dynamics, pp. 26-30. Biarritz, France.

Montenbruck, O., Gill, E., & Lutze, F. (2002). Satellite orbits: models, methods, and applications. Applied Mechanics Reviews, 55(2), pp. B27-B28. https://doi.org/10.1115/1.1451162

Moraes, A., Costa, E., de Paula, E., Perella, W., Monico, J. (2014). Extended ionospheric amplitude scintillation model for GPS receivers. Radio Science, 49(5), pp. 315-329. https://doi.org/10.1002/2013RS005307

Nakagami, M. (1960). The m-distribution: a general formula of intensity distribution of rapid fading. In: Hoffman WC (ed) Statistical methods in radio wave propagation. Pergamon, New York, pp. 33–36.

Nava, B., Coisson, P., Radicella, S.M. (2008). A new version of the NeQuick ionosphere electron density model. Journal of Atmospheric and Solar-Terrestrial Physics, 70, pp. 1856–1862.

Niell A. E. (1996). Global mapping functions for the atmosphere delay at radio wavelengths. Journal of Geophysical Research, 101(B2), pp. 3227-3246.

Nischan, Thomas (2016). GFZRNX - RINEX GNSS Data Conversion and Manipulation Toolbox. GFZ Data Services. http://dx.doi.org/10.5880/GFZ.1.1.2016.002

Noll, C., Bock, Y., Habrich, H. Moore, A. (2009). Development of data infrastructure to support scientific analysis for the International GNSS Service. Journal of Geodesy, 83(3-4), pp. 309–325. https://doi.org/10.1007/s00190-008-0245-6

Odijk, D., Zhang, B., Khodabandeh, A., Odolinski, R., Teunissen, P. J. G. (2016). On the estimability of parameters in undifferenced, uncombined GNSS network and PPP-RTK user models by means of S-system theory. Journal of Geodesy, 90(1), pp. 15-44. https://doi.org/10.1007/s00190-015-0854-9

Oliver, M. A., and Webster, R. (1990). Kriging: a method of interpolation for geographical information systems. International Journal of Geographical Information System, 4(3), pp. 313-332.

OS-SIS-ICD (2021). European GNSS (Galileo) OpenService. Signal in space interface control document. Issue 2.0. https://www.gsc-europa.eu/sites/default/files/sites/all/files/Galileo_OS_SIS_ICD_v2.0.pdf. European Union.

Pan, L., Zhang, X., Li, X., Li, X., Lu, C., Liu, J. (2019). Satellite availability and point positioning accuracy evaluation on a global scale for integration of GPS, GLONASS, BDS and Galileo. Advances in Space Research, 63(9), pp. 2696-2710. https://doi.org/10.1016/j.asr.2017.07.029

Park, J., Veettil, S. V., Aquino, M., Yang, L., Cesaroni, C. (2017). Mitigation of ionospheric effects on GNSS positioning at low latitudes. NAVIGATION: Journal of the Institute of Navigation, 64(1), pp. 67–74. https://doi.org/10.1002/navi.177

Paziewski, J., & Sieradzki, R. (2020). Enhanced wide-area multi-GNSS RTK and rapid static positioning in the presence of ionospheric disturbances. Earth, Planets and Space, 72(1), pp. 1-16. https://doi.org/10.1186/s40623-020-01238-7

Penna, N., Dodson, A., & Chen, W. (2001). Assessment of EGNOS tropospheric correction model. The Journal of Navigation, 54(1), pp. 37-55. https://doi.org/10.1017/S0373463300001107

Petovello, M. G. (2003). Real-time integration of a tactical-grade IMU and GPS for high-accuracy positioning and navigation. Ph.D. thesis, University of Calgary. https://www.ucalgary.ca/engo_webdocs/GL/03.20173.MGPetovello.pdf

Pi, X., Mannucci, A. J., Lindqwister, U. J., Ho, C. M. (1997). Monitoring of global ionospheric irregularities using the worldwide GPS network. Geophysical Research Letters, 24(18), pp. 2283-2286. https://doi.org/10.1029/97GL02273

Pi, X, Iijima, B. A., Lu, W. (2017). Effects of ionospheric scintillation on GNSS-Based positioning. NAVIGATION: Journal of the Institute of Navigation, 64(1), pp. 3-22. https://doi.org/10.1002/navi.182

Picot, N., Case, K., Desai, S., & Vincent, P. (2003). AVISO and PODAAC user handbook, Issue 5, Revision 1. IGDR and GDR Jason products. SMM_MU_M5_OP_13184_CN (AVISO) JPL D_21352 (PODAAC).

Píriz, R., Mozo, A., Navarro, P., & Rodríguez, D. (2008). MagicGNSS: Precise GNSS products out of the box. In Proceedings of the 21st International Technical Meeting of the Satellite Division of The Institute of Navigation (ION GNSS), pp. 1242-1251.

Prieto-Cerdeira, R., Orús-Pérez R., Breeuwer E., Lucas-Rodríguez R., and Falcone M. (2014). Innovation: The European Way. Performance of the Galileo Single-Frequency Ionospheric Correction During In-Orbit Validation. In: GPS World, pp. 53–58.

Prikryl, P., Jayachandran, P. T., Mushini, S. C., Chadwick, R. (2011a). Climatology of GPS phase scintillation and HF radar backscatter for the high-latitude ionosphere under solar minimum conditions. Annales Geophysicae, 29, pp. 377–392. doi:10.5194/angeo-29-377-2011

Prikryl, P., Spogli, L., Jayachandran, P. T., Kinrade, J., et al. (2011b). Interhemispheric comparison of GPS phase scintillation at high latitudes during the magnetic-cloud-induced geomagnetic storm of 5–7 April 2010. Annales Geophysicae, 29, pp. 2287–2304. doi:10.5194/angeo-29-2287-2011

Psychas, D., Verhagen, S. (2020). Real-Time PPP-RTK Performance Analysis Using Ionospheric Corrections from Multi-Scale Network Configurations. Sensors, 20(11), p. 3012. https://doi.org/10.3390/s20113012

Revnivykh S. (2008). Glonass status and progress. In: Proceedings of ION GNSS 21st International Technical Meeting of the Satellite Division, Savannah, GA, pp. 431-452.

Rizos, C. (2007). Alternatives to current GPS-RTK services and some implications for CORS infrastructure and operations. GPS Solutions, 11, pp. 151–158. https://doi.org/10.1007/s10291-007-0056-x

Roman, D. R., Childers, V. A. (2013). The GRAV-D Project: Focus on Alaska. ISCORD 2013: Planning for Sustainable Cold Regions, Anchorage, Alaska, United States. Journal of Surveying Engineering - ASCE. https://doi.org/10.1061/9780784412978.028

Saastamoinen, J. (1972). Atmospheric Correction for the Troposphere and Stratosphere in Radio Ranging of Satellites, The Use of Artificial Satellites for Geodesy, Geophysical Monograph Series, AGU, Washington, D.C., 15, pp. 247-251. https://doi.org/10.1029/GM015p0247

Saastamoinen J. (1973). Contribution to the theory of atmospheric refraction: Refraction corrections in satellite geodesy. Bulletin Géodésique, 107(1), pp. 13-34.

Schwarz, C. R. (2008). Heuristic weighting and data conditioning in the National Geodetic Survey rapid static GPS software. Journal of Surveying Engineering – ASCE, 134(3), pp. 76-82. https://doi.org/10.1061/(ASCE)0733-9453(2008)134:3(76)

Septentrio (2015). PolaRxS Application Manual v2.5.0. Septentrio Satellite Navigation, Leuven, Belgium.

Shi, C., Guo, S., Gu, S., Yang, X., Gong, X., Deng, Z., Ge, M., & Schuh, H. (2018). Multi-GNSS satellite clock estimation constrained with oscillator noise model in the existence of data discontinuity. Journal of Geodesy, 93(4), pp. 515–528. https://doi.org/10.1007/s00190-018-1178-3

Shi, C., Zhao, Q., Geng, J., Lou, Y., Ge, M., Liu, J. (2008). Recent development of PANDA software in GNSS data processing. Proceedings of SPIE 7285, International Conference on Earth Observation Data Processing and Analysis (ICEODPA), 72851S, https://doi.org/10.1117/12.816261

Silva, H. A., Camargo, P. O., Monico, J. F. G., Aquino, M., Marques, H. A., De Franceschi, G., Dodson, A. (2010). Stochastic modelling considering ionospheric scintillation effects on GNSS relative and point positioning. Advances in Space Research, 45(9), pp. 1113-1121. https://doi.org/10.1016/j.asr.2009.10.009

Skone, S., Kundsen, K., de Jong, M. (2001). Limitation in GPS receiver tracking performance under ionospheric scintillation conditions. Physics and Chemistry of the Earth (A), 26, pp. 613–621. https://doi.org/10.1016/S1464-1895(01)00110-7

Smith, D. A., & Roman, D. R. (2010). How NOAA's GRAV-D project impacts and contributes to NOAA science. NOAA, April 2010.

Soycan, M. A. (2012). Quality Evaluation of Precise Point Positioning within the Bernese GPS Software Version 5.0. Arabian Journal for Science and Engineering, 37, pp. 147–162. https://doi.org/10.1007/s13369-011-0162-5

Spogli, L., Alfonsi, L., De Franceschi, G., Romano, V., Aquino, M., Dodson, A. (2009). Climatology of GPS ionospheric scintillations over high and mid-latitude European regions. Annales Geophysicae, 27, pp. 3429–3437.

Spogli, L., Alfonsi, L., Romano, V., De Franceschi, G., Joao Francisco, G. M., Hirokazu Shimabukuro, M., Bougard, B., Aquino, M. (2013). Assessing the GNSS scintillation climate over Brazil under increasing solar activity. Journal of Atmospheric and Solar-Terrestrial Physics, 105, pp. 199-206. https://doi.org/10.1016/j.jastp.2013.10.003

Sreeja, V., Aquino, M., Elmas, Z. G. (2011). Impact of ionospheric scintillation on GNSS receiver tracking performance over Latin America: Introducing the concept of tracking jitter variance maps. Space Weather, 9(10), p. S10002. https://doi.org/10.1029/2011SW000707

Sreeja, V., Aquino, M., Elmas, Z. G., Forte, B. (2012). Correlation analysis between ionospheric scintillation levels and receiver tracking performance. Space Weather, 10(6), S06005. https://doi.org/10.1029/2012sw000769

Sreeja, V. (2016). Impact and mitigation of space weather effects on GNSS receiver performance. Geoscience Letters, 3(24). https://doi.org/10.1186/s40562-016-0057-0

Steigenberger, P., Thölert, S., Montenbruck, O. (2018). GNSS satellite transmit power and its impact on orbit determination. Journal of Geodesy, 92, pp. 609-624. https://doi.org/10.1007/s00190-017-1082-2.

Subirana, J. S., Zornoza, J. M. J., Hernández-Pajares, M. (2013). Global Navigation Satellite Systems: Volume I: Fundamentals and Algorithms. Fletcher, K. (ed), ESA Communications, Leiden, the Netherlands.

Susi, M., Andreotti, M., Aquino, M., Dodson, A. (2017). Tuning a Kalman filter carrier tracking algorithm in the presence of ionospheric scintillation. GPS Solutions, 21, pp. 1149-1160. https://doi.org/10.1007/s10291-016-0597-y

Tavasci, L., Vecchi, E., & Gandolfi, S. (2021). Performance of Atlas GNSS Global Correction Service for High-Accuracy Positioning. Journal of Surveying Engineering-ASCE, 147(4), 05021005.

Teferle, F. N., Orliac, E. J., Bingley, R. M. (2007). An assessment of Bernese GPS software precise point positioning using IGS final products for global site velocities. GPS Solutions, 11(3), pp. 205-213. https://doi.org/10.1007/s10291-006-0051-7

Teunissen, P. J. G., De Jonge, P. J., & Tiberius, C. C. J. M. (1995). The LAMBDA method for fast GPS surveying. In International Symposium GPS Technology Applications, Bucharest, Romania (September).

Teunissen, P. J. G. (1998). Quality control and GPS. In GPS for Geodesy. Springer, Berlin, Heidelberg, pp. 271-318.

Teunissen, P. J. G., Joosten, P., & Odijk, D. (1999). The reliability of GPS ambiguity resolution. GPS Solutions, 2(3), pp. 63-69. doi:10.1007/PL00012758

Teunissen, P. J. G., and Khodabandeh A. (2015). Review and principles of PPP-RTK methods. Journal of Geodesy, 89(3), pp. 217–240. https://doi.org/10.1007/s00190-015-0854-9

United Nations (2019). Department of Economic and Social Affairs, Population Division, World Population Prospects 2019: Highlights, ST/ESA/SER.A/423. Accessed: October 2021. https://population.un.org/wpp/Publications/Files/WPP2019_Highlights.pdf

Van Dierendonck, A. J., Klobuchar, J., Hua, Q. (1993). Ionospheric scintillation monitoring using commercial single frequency C/A code receivers. Proceedings of ION ITM Satellite Division, Institute of Navigation, Salt Lake City, Utah, USA, September 22-24, pp. 1333-1342. https://www.ion.org/publications/abstract.cfm?articleID=4318

Vani, B. C., Shimabukuro, M. H., Monico, J. F. G. (2017). Visual exploration and analysis of ionospheric scintillation monitoring data: The ISMR Query Tool. Computers & Geosciences, 104, pp. 125-134. https://doi.org/10.1016/j.cageo.2016.08.022

Vani, B. C., Forte, B., Monico, J. F. G., Skone, S., Shimabukuro, M.H., Moraes, A.O., Portella, I.P., Marques, H.A. (2019). A novel approach to improve GNSS Precise Point Positioning during strong ionospheric scintillation: theory and demonstration. IEEE Transactions on Vehicular Technology, 68, pp. 4391–4403. https://doi.org/10.1109/TVT.2019.2903988

Verhagen, S., Teunissen P. J. G. (2017). Least-Squares Estimation and Kalman Filtering. In Springer Handbook of Global Navigation Satellite Systems, 1st ed., Teunissen, P. J. G., Montenbruck, O. (eds.), Springer International Publishing: Cham, Switzerland, pp. 639-660. https://doi.org/10.1007/978-3-319-42928-1_22

Veettil S.V., Aquino M., Marques H. A., Moraes A. (2020). Mitigation of ionospheric scintillation effects on GNSS precise point positioning (PPP) at low latitudes. Journal of Geodesy, 94(15). https://doi.org/10.1007/s00190-020-01345-z

Welch, G., & Bishop, G. (1995). An introduction to the Kalman filter. Department of Computer Science University of North Carolina at Chapel Hill Chapel Hill, NC. Updated: Monday, July 24, 2006.

Weng, D., Ji, S., Chen, W., Liu, Z. (2014). Assessment and mitigation of ionospheric disturbance effects on GPS accuracy and integrity. The Journal of Navigation, 67(3), pp. 371–384. https://doi.org/10.1017/S0373463314000046

Wieser, A., & Brunner, F. K. (2000). An extended weight model for GPS phase observations. Earth, Planets and Space, 52(10), pp. 777-782. https://doi.org/10.1186/BF03352281

Wübbena, G., Schmitz, M., & Bagge, A. (2014). PPP with ambiguity resolution (AR) using RTCM-SSR. In: IGS Workshop.

Wübbena G., Schmitz M., Bagg A. (2005). PPP-RTK: precise point positioning using state-space representation in RTK networks. In: Proceedings of ION GNSS, pp. 13–16.

Wübbena, G., Hannover, U. (1985). SOFTWARE DEVELOPMENTS FOR GEODETIC POSITIONING WITH GPS. In Positioning with GPS-1985: Proceedings, First International Symposium on Precise Positioning with the Global Positioning System, Rockville, Maryland, April 15-19, 1985 (Vol. 1, p. 403). US Department of Commerce, National Oceanic and Atmospheric Administration, National Ocean Service.

Xia, F., Ye, S., Xia, P., Zhao, L., Jiang, N., Chen, D., Hu, G. (2019). Assessing the latest performance of Galileo-only PPP and the contribution of Galileo to Multi-GNSS PPP. Advances in Space Research, 63(9), pp. 2784-2795. https://doi.org/10.1016/j.asr.2018.06.008

Xu, R., Liu, Z., Chen, W. (2015). Improved FLL-assisted PLL with in-phase pre-filtering to mitigate amplitude scintillation effects. GPS Solutions, 19, pp. 263-276. https://doi.org/10.1007/s10291-014-0385-5

Yacoub, M.D. (2007). The α–μ distribution: a physical fading model for the Stacy distribution. IEEE Transactions on Vehicular Technology, 56, pp. 24–27. https://doi.org/10.1109/TVT.2006.883753

Yang, Y., Mao, Y. & Sun, B. (2020). Basic performance and future developments of BeiDou global navigation satellite system. Satellite Navigation, 1(1), pp. 1-8. https://doi.org/10.1186/s43020-019-0006-0

Yeh, C., Chao-Han, L. (1982). Radio wave scintillations in the ionosphere. Proceedings of IEEE, 70(4), pp. 324-360. https://doi.org/10.1109/PROC.1982.12313

Yousif H., El-Rabbany A. (2007). Assessment of several interpolation methods for precise GPS orbit. The Journal of Navigation, 60(3), pp. 443-455. https://doi.org/10.1017/S0373463307004250

Zaminpardaz, S., Teunissen, P. J. G. (2017). Analysis of Galileo IOV + FOC signals and E5 RTK performance. GPS Solutions, 21(4), pp. 1855-1870. https://doi.org/10.1007/s10291-017-0659-9

Zhang, L., Morton, Y. (2009). Tracking GPS signals under ionosphere scintillation conditions. In: Proceedings of ION-GNSS-2009, Institute of Navigation, Savannah, GA, USA, September 2009, pp. 227–234.

Zhang, X., Guo, F., Zhou, P. (2014). Improved precise point positioning in the presence of ionospheric scintillation. GPS Solutions, 18, pp. 51–60. https://doi.org/10.1007/s10291-012-0309-1

Zumberge, J. F., Heflin, M. B., Jefferson, D. C.,Watkins, M. M. and Webb, F. H. (1997). Precise point positioning for the efficient and robust analysis of GPS data from large networks. Journal of Geophysical Research: Solid Earth, 102, pp. 5005-5017. https://doi.org/10.1029/96JB03860

Zuo, X., Jiang, X., Li, P., Wang, J., Ge, M., Schuh, H. (2021). A square root information filter for multi-GNSS real-time precise clock estimation. Satellite Navigation, 2(1), pp. 1-14. https://doi.org/10.1186/s43020-021-00060-0

Appendix A: PPP correction model effects

The following figures show the positioning effect of correction models that are commonly applied to single-receiver positioning such as PPP. In these examples, the vertical positioning error component is given for static PPP over a 24-hour period with individual correction models disabled.

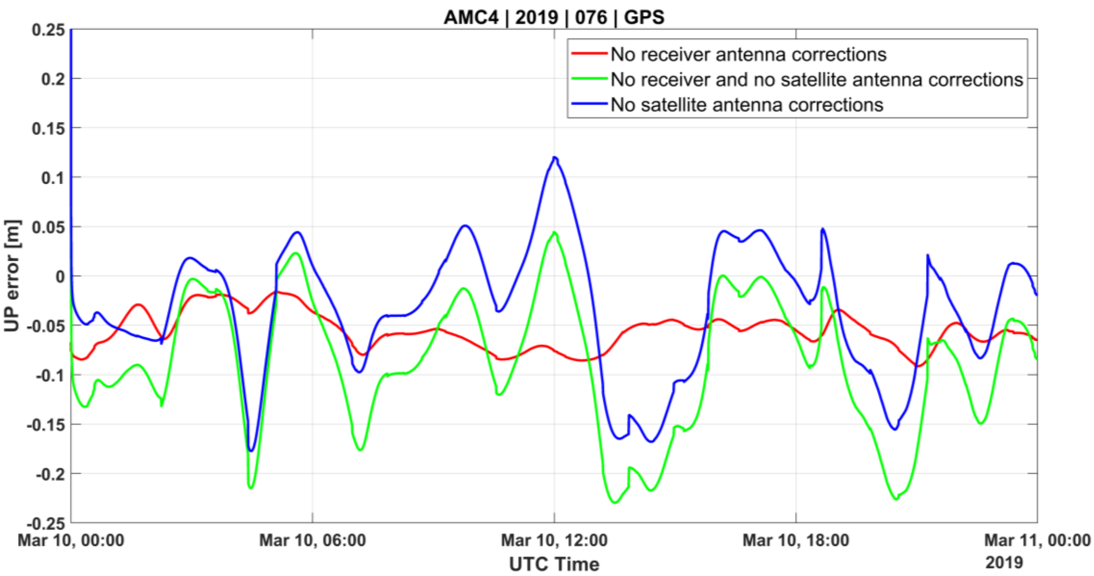

Figure A.1. Vertical kinematic PPP errors wrt. full-model processing over a 24-hour period with satellite and receiver PCO and PCV corrections enabled and disabled.

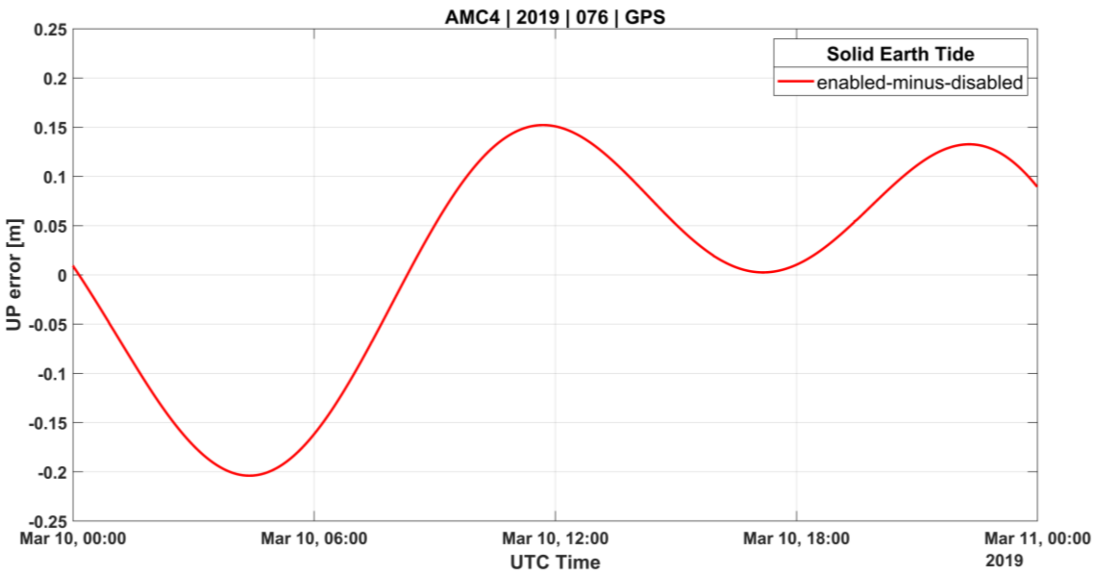

Figure A.2. Vertical kinematic PPP errors wrt. full-model processing over a 24-hour period with solid earth tide corrections enabled and disabled.

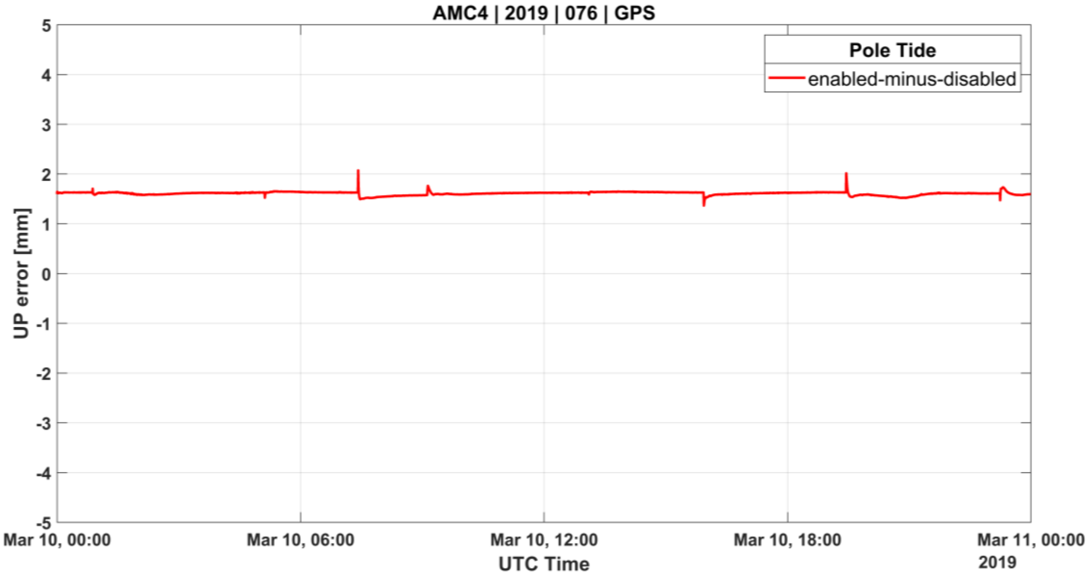

Figure A.3. Vertical kinematic PPP errors wrt. full-model processing over a 24-hour period with pole tide corrections enabled and disabled.

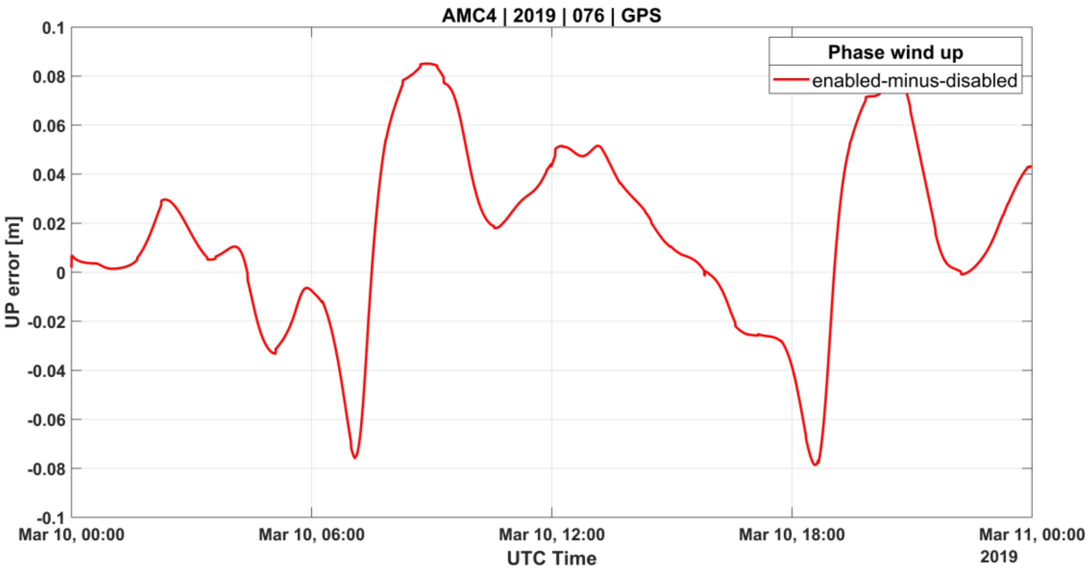

Figure A.4. Vertical kinematic PPP errors wrt. full-model processing over a 24-hour period with carrier phase wind up corrections enabled and disabled.

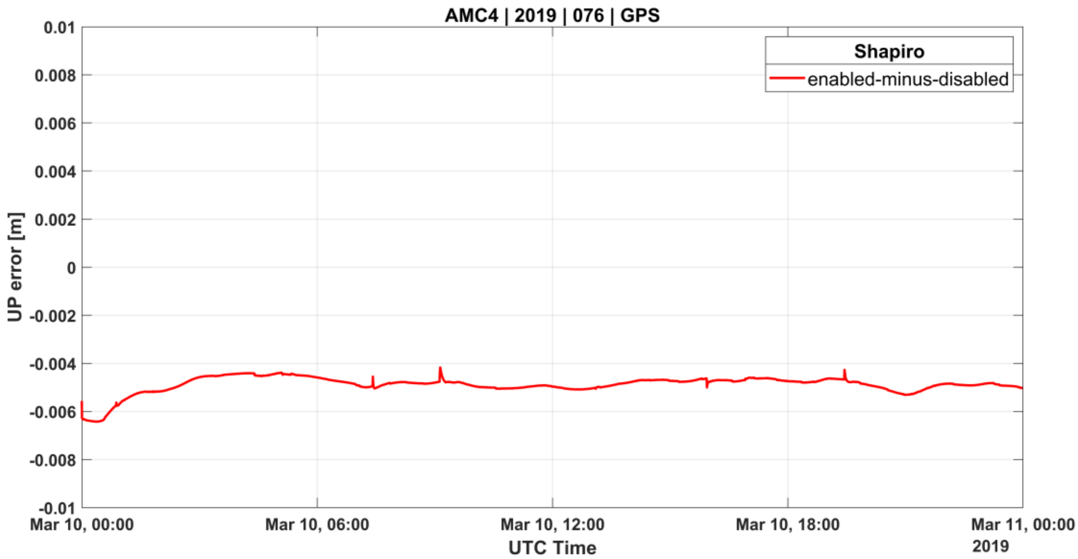

Figure A.5. Vertical kinematic PPP errors wrt. full-model processing over a 24-hour period with relativistic corrections enabled and disabled.

Appendix B: Professional development and accomplishments during this PhD

TREASURE secondments

Collaboration among TREASURE partners occurred during TREASURE secondments that took place during the PhD:

- Hosted by Alezi Teodolini, February-March, 2018, São Paulo, Brazil
- Hosted by Curtin University, August-September, 2018, Perth, Australia
- Hosted by Oregon State University, May-July, 2019, Oregon, United States

TREASURE workshops

Stages of this research were presented at the following TREASURE workshops during the development of this PhD:

- *Initial Developments and Interaction with Academia and Industry*, April 17-18, 2018, Rome, Italy
- *A response to user needs in PPP and RTK*, May 21-22, 2019, Toulouse, France
- *Appraisal of scientific and technological output*, May 11-13, 2020, Webinar
- *The Ultimate Real Time EGNSS Solution: achievements and the near future*, October 19-21, 2020, Webinar.

TREASURE training

Training opportunities organized by TREASURE provided key technical developments and discussions with academic and industry leaders in GNSS technologies:

- *GNSS, EGNSS and related high accuracy positioning techniques and applications*, September 11-15, 2017, Nottingham, United Kingdom
- Transferable skills week, November 12-16, 2018, Nottingham, United Kingdom

- *PPP and RTK error modelling: the challenges for ambiguity resolution*, November 19-22, 2018, Bath, United Kingdom
- *State of the art of EGNSS high accuracy positioning: what can Galileo bring to the table?*, December 4-8, 2019, Torino, Italy

Other achievements

Conference presentation

- AGU Fall Meeting, December 9-13, 2019, San Francisco, US
    - Weaver, B., Aquino, M., Vadakke-Veettil, S. (2019). G13A-04 - Exploiting Multi-GNSS Measurements to Improve Precise Point Positioning (PPP) Performance Under Scintillation Conditions.

Dissemination

- Farming by Satellite competition runner-up, in collaboration with TREASURE fellows, December 4-6, 2018 Marseille, France.
- I’m an engineer get me out of here! Space zone winner (2019).

Appendix C: Pseudorange bias effects using GIM- and RIM-fixed processing

The following figures show the time-constant pseudorange bias effects for user stations that constrained the GIM and RIM data products in the ionosphere-weighted experiment.

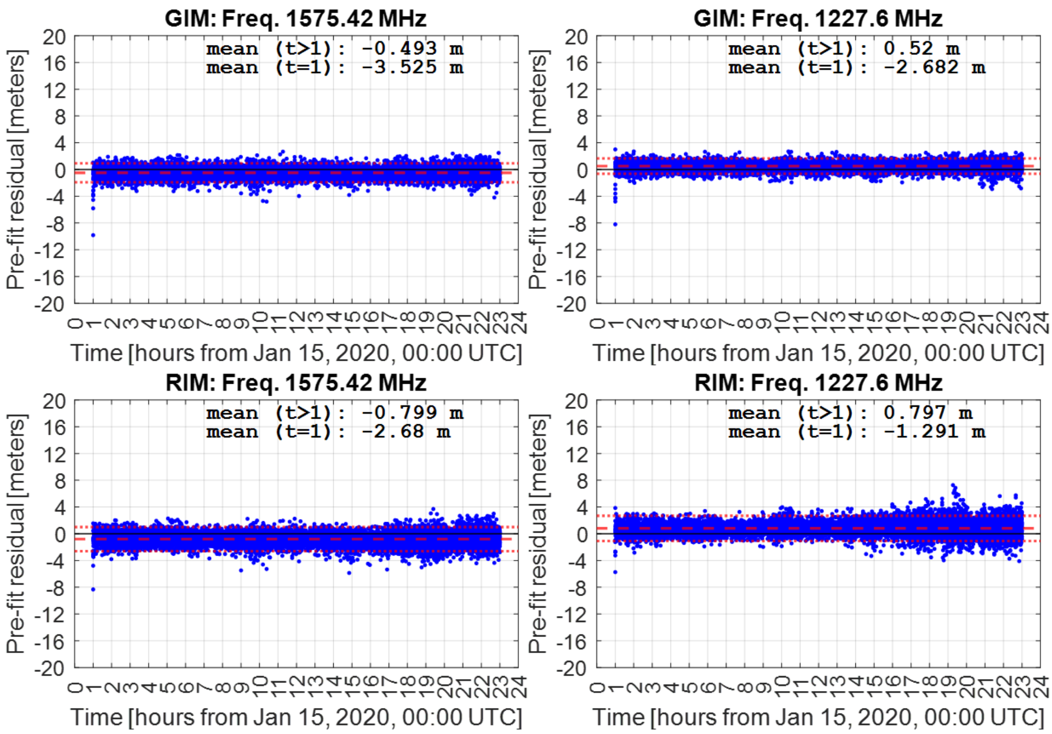

Figure C.1. Station BAPA GIM (top row) and RIM (bottom row) constrained pseudorange pre-fit residuals (blue markers), with mean (red dashed line) ±3σ (red dotted lines) for GPS L1 (left column) and L2 (right column) signals at the first (t=1) and all other (t>1) epochs.

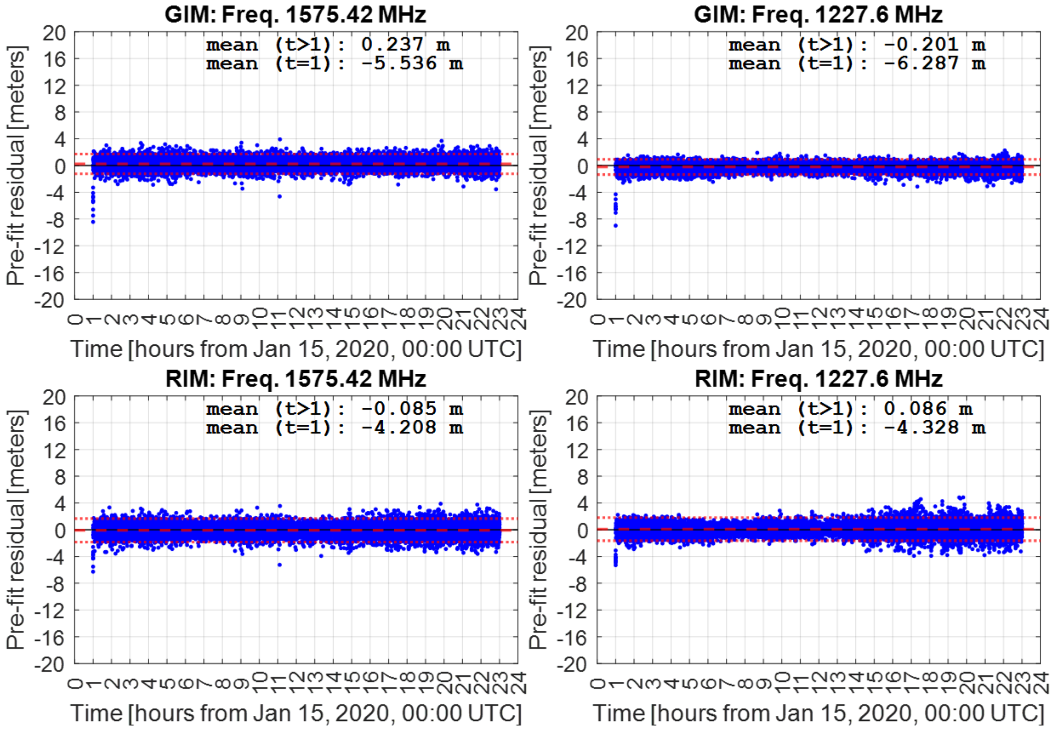

Figure C.2. Station PITN GIM (top row) and RIM (bottom row) constrained pseudorange pre-fit residuals (blue markers), with mean (red dashed line) ±3σ (red dotted lines) for GPS L1 (left column) and L2 (right column) signals at the first (t=1) and all other (t>1) epochs.

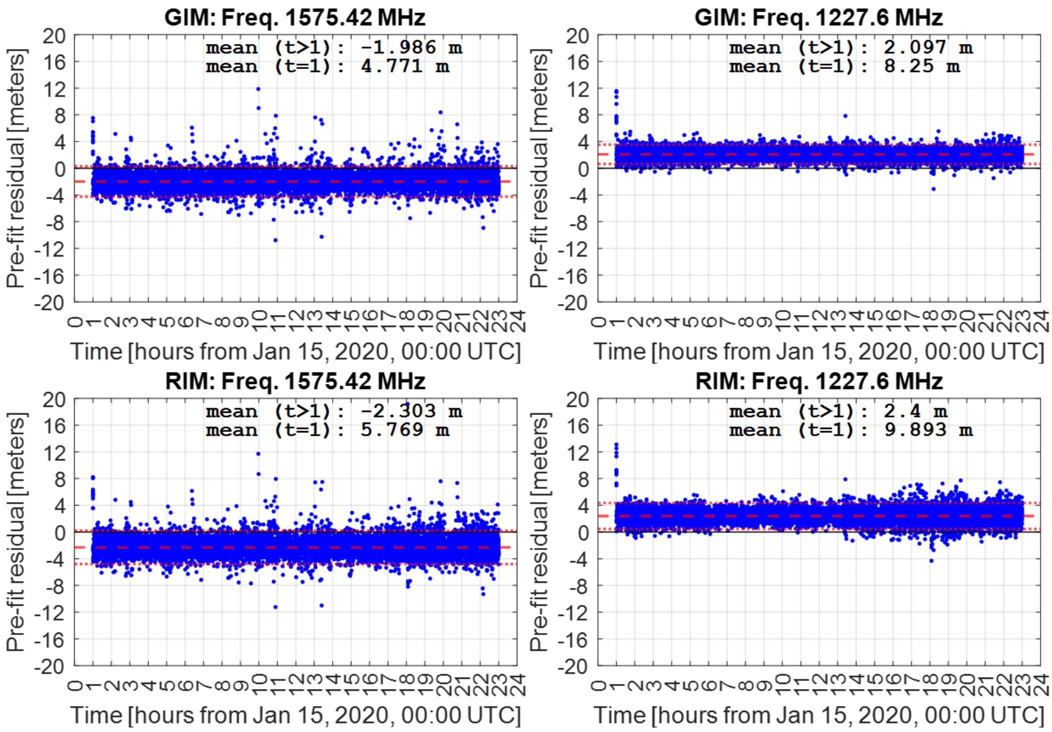

Figure C.3. Station PIFL GIM (top row) and RIM (bottom row) constrained pseudorange pre-fit residuals (blue markers), with mean (red dashed line) ±3σ (red dotted lines) for GPS L1 (left column) and L2 (right column) signals at the first (t=1) and all other (t>1) epochs.

Appendix D: Multi-GNSS ionospheric scintillation mitigation positioning error component time-series

The following figures show local north (green lines), east (blue lines), and up (red lines) positioning error component time-series for tracking jitter mitigated (right columns) and elevation-based non-mitigated (left columns) stochastic models for low-latitude station PPTE during six intervals identified as having strong scintillation in March 2019. Note that positioning error mean and standard deviation shown in the legend of each figure are computed after two hours of processing (black dashed line) to exclude initial convergence errors.

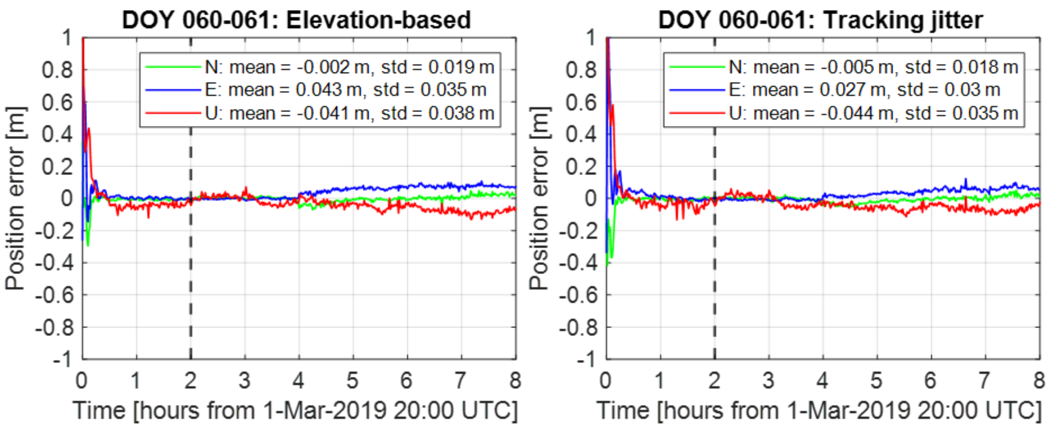

Figure D.1. Elevation-based (left) and tracking jitter (right) stochastic models used for kinematic PPP processing of GPS+Galileo measurements observed at station PPTE beginning on March 1, 2019, 20:00 UTC.

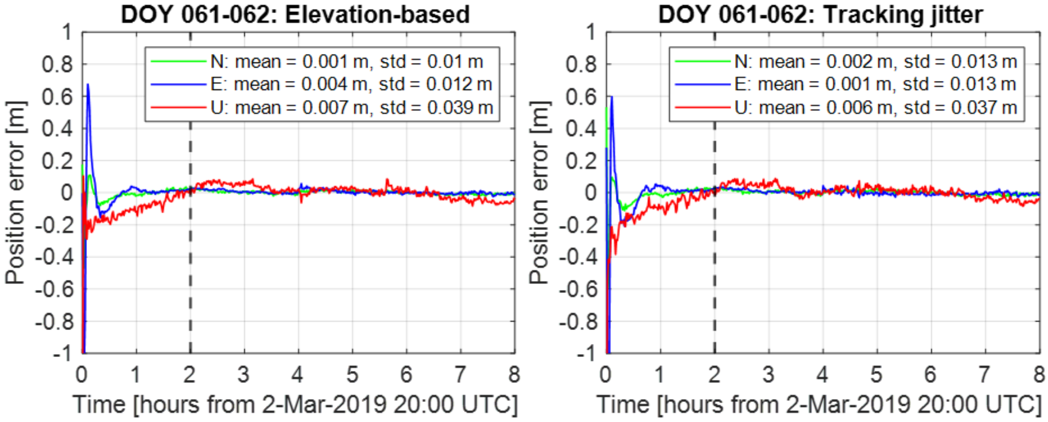

Figure D.2. Elevation-based (left) and tracking jitter (right) stochastic models used for kinematic PPP processing of GPS+Galileo measurements observed at station PPTE beginning on March 2, 2019, 20:00 UTC.

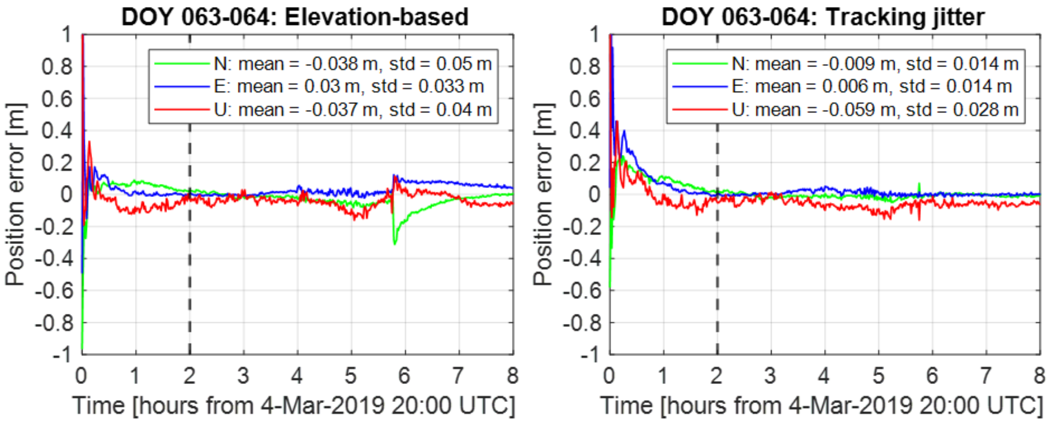

Figure D.3. Elevation-based (left) and tracking jitter (right) stochastic models used for kinematic PPP processing of GPS+Galileo measurements observed at station PPTE beginning on March 4, 2019, 20:00 UTC.

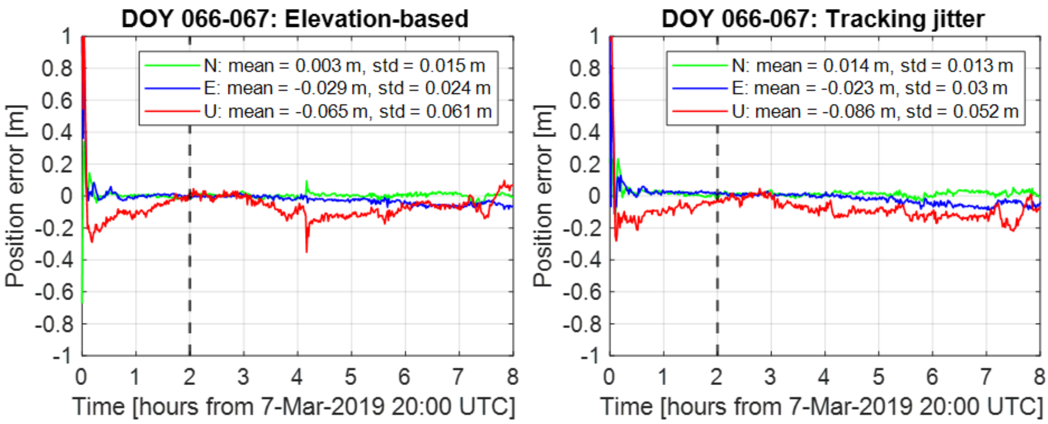

Figure D.4. Elevation-based (left) and tracking jitter (right) stochastic models used for kinematic PPP processing of GPS+Galileo measurements observed at station PPTE beginning on March 7, 2019, 20:00 UTC.

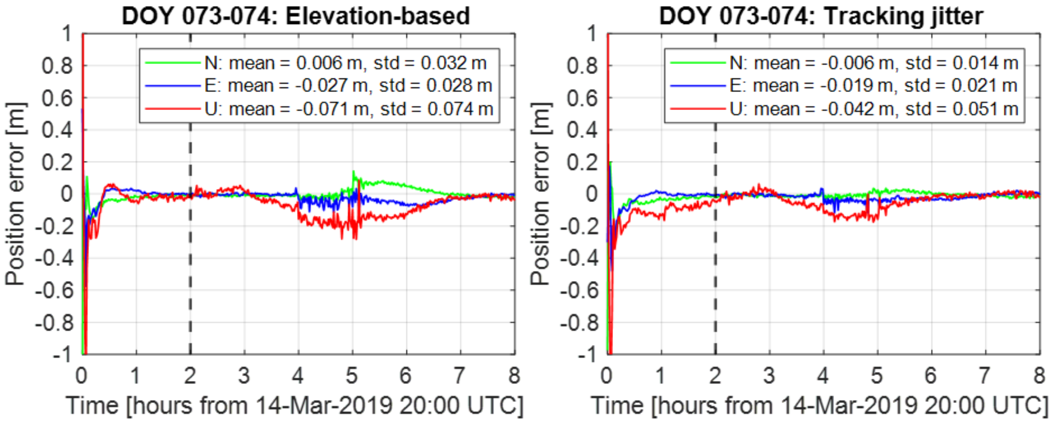

Figure D.5. Elevation-based (left) and tracking jitter (right) stochastic models used for kinematic PPP processing of GPS+Galileo measurements observed at station PPTE beginning on March 14, 2019, 20:00 UTC.

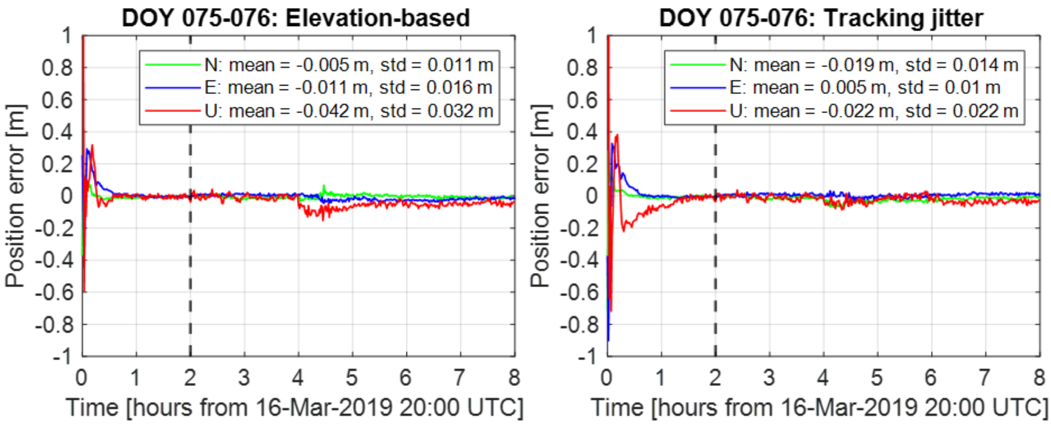

Figure D.6. Elevation-based (left) and tracking jitter (right) stochastic models used for kinematic PPP processing of GPS+Galileo measurements observed at station PPTE beginning on March 16, 2019, 20:00 UTC.

Appendix E: Integer ambiguity resolution and the LAMBDA method

This appendix provides details related to integer ambiguity resolution and the LAMBDA method, adapted from Teunissen et al. (1999). First, double differenced GNSS models are presented, in terms of geometry-preserving and geometry-free combinations, as these models are typically used in relative positioning techniques such as RTK. The corresponding variance-covariance matrix and mixed integer model is then provided. Lastly, the key steps and techniques for integer ambiguity resolution using decorrelation and estimation are given, as these steps are critical components of the LAMBDA technique.

Double-differenced GNSS models

Double-differenced short baseline GNSS models eliminate the receiver and satellite dependent errors, along with atmospheric effects. In the case of a geometry-free model, the ranges are estimated and satellite coordinates are not needed. The double-differenced, geometry-free model for one epoch and *m* satellites is:

$$\begin{pmatrix}\varphi_1\\ \varphi_2\\ p_1\\ p_2\end{pmatrix} = \left(\begin{bmatrix}\lambda_1 I_{m-1} & \\ & \lambda_2 I_{m-1}\\ & \\ & \end{bmatrix}\begin{bmatrix}I_{m-1} & -\mu_1 I_{m-1}\\ I_{m-1} & -\mu_2 I_{m-1}\\ I_{m-1} & \mu_1 I_{m-1}\\ I_{m-1} & \mu_2 I_{m-1}\end{bmatrix}\right)\begin{pmatrix}\begin{bmatrix}a_1\\ a_2\end{bmatrix}\\ \begin{bmatrix}\rho\\ \iota_1\end{bmatrix}\end{pmatrix} + \begin{pmatrix}\varepsilon_1\\ \varepsilon_2\\ \epsilon_1\\ \epsilon_2\end{pmatrix}$$

where the ionospheric parameter (ι_1) is either included or neglected for respective long- and short-baseline processing.

In the geometry-based model, user coordinates are estimated and satellite coordinates are required. The double-differenced, geometry-based model for one epoch and *m* satellites is:

$$\begin{pmatrix}\varphi_1\\ \varphi_2\\ p_1\\ p_2\end{pmatrix} = \left(\begin{bmatrix}\lambda_1 I_{m-1} & \\ & \lambda_2 I_{m-1}\\ & \\ & \end{bmatrix}\begin{bmatrix}G & -\mu_1 I_{m-1}\\ G & -\mu_2 I_{m-1}\\ G & \mu_1 I_{m-1}\\ G & \mu_2 I_{m-1}\end{bmatrix}\right)\begin{pmatrix}\begin{bmatrix}a_1\\ a_2\end{bmatrix}\\ \begin{bmatrix}g\\ \iota_1\end{bmatrix}\end{pmatrix} + \begin{pmatrix}\varepsilon_1\\ \varepsilon_2\\ \epsilon_1\\ \epsilon_2\end{pmatrix}$$

where the parameter *G* is a matrix contains the unit direction (line-of-sight) vectors, between the receiver and satellite.

Variance-covariance matrix

The variance-covariance (VCV) matrix of the double differenced GNSS model can be easily found from the well-known propagation of error in a series of *n* observations: $\sigma_A = \sigma_B\sqrt{n}$ (Ghilani 2017). This simplified version of errors in a sum relies on the assumption that errors for each observed value are identical. Given the following double differenced observation vector *y*, the resulting VCV matrix (Q_{yy}) is expressed as:

$$y = \begin{pmatrix} \varphi_1 \\ \varphi_2 \\ p_1 \\ p_2 \end{pmatrix};\ Q_{yy} = \begin{pmatrix} 2\sigma_{\phi_1}^2 C & & & \\ & 2\sigma_{\phi_2}^2 C & & \\ & & 2\sigma_{p_1}^2 C & \\ & & & 2\sigma_{p_2}^2 C \end{pmatrix}$$

where the matrix C, size (m-1) x (m-1), is due to double differencing. The following expression expands the contents of the double differencing matrix:

$$C_{(m-1)x(m-1)} = \begin{pmatrix} 2 & 1 & \cdots & 1 \\ 1 & 2 & \cdots & 1 \\ \vdots & \vdots & \ddots & \vdots \\ 1 & 1 & \dots & 2 \end{pmatrix}$$

Mixed-integer GNSS model

Unmodeled and random errors in the GNSS model result in an estimated real-valued number of full wavelengths, therefore, the integer number becomes ambiguous. If the integer ambiguity can be determined and removed from the GNSS model, then the extremely precise carrier phase measurements become equivalent to extremely precise pseudorange measurements. Therefore, the following mixed-integer GNSS observation model separates integer and real-valued parameters:

$$y = Aa + Bb + e,\ \ a \in Z^n,\ \ Q_{yy}$$

In this model, the integer-valued ambiguities (*a*) are separated from the real valued baseline coordinates and other unknowns (*b*). This mix-integer model is typically a critical step in integer ambiguity resolution process for both PPP-RTK and RTK models.

Integer ambiguity resolution

Ambiguities successfully resolved to integer values achieve the highest precision of estimable parameters in the underlying GNSS model. Although integer ambiguity resolution can become quite complex, the general process can be described with three straightforward steps:

1. **Float solution.** Estimate the position and carrier phase (float) ambiguities.
$$\begin{pmatrix}\hat{a}\\ \hat{b}\end{pmatrix};\ \begin{pmatrix}Q_{\hat{a}\hat{a}} & Q_{\hat{a}\hat{b}}\\ Q_{\hat{b}\hat{a}} & Q_{\hat{b}\hat{b}}\end{pmatrix}$$
2. **LAMBDA method.** Estimate integer ambiguities ($\breve{a}$) using the stochastic properties of the float ambiguities ($\hat{a}$) and real-to-integer ($R^n \rightarrow Z^n$) mapping function, *S*.
$$\breve{a} = S(\hat{a});\ S: R^n \rightarrow Z^n$$
3. **Fixed solution.** Update position estimates using fixed ambiguities.
$$\breve{b} = \hat{b} - Q_{\hat{b}\hat{a}}Q_{\hat{a}\hat{a}}^{-1}(\hat{a} - \breve{a})$$

Regarding step 2, three main methods are used to fix float ambiguities to integer values: integer rounding, bootstrapping, and least squares. Each method has a probabilistic success rate that can be used to decide if ambiguities should remain as float values or can be updated to fixed values.

Integer rounding

The simplest method to fix float ambiguities to integer values is by rounding, denoted by [.], to the nearest integer: $\breve{a} = [\hat{a}]$. Therefore, in integer- (*z*-) space, $\breve{a} = z$ if the following criteria is met:

$$z - \frac{1}{2} \leq \hat{a} \leq z + \frac{1}{2}$$

The probability of successfully fixed float ambiguities using the integer rounding estimator is:

$$P(\breve{a}_R = a) = \int_{S_a} f_{\hat{a}}(x)dx = \int_{S_a} \frac{1}{\sqrt{|Q_{\hat{a}\hat{a}}|}(2\pi)^{\frac{1}{2}n}} e^{\left(-\frac{1}{2}||x-a||^2_{Q_{\hat{a}\hat{a}}}\right)}dx$$

Integer bootstrapping

Integer bootstrapping combines rounding with sequential conditional least squares and considers some of the correlation between float ambiguities. The integer bootstrapped solution is:

$$\breve{a}_i = \left[\hat{a}_i - \sum_{j=1}^{i-1} \sigma_{i,j|J}\sigma_{j|J}^{-2}\left(\hat{a}_{j|J} - \breve{a}_j\right)\right]$$

$$\breve{a}_i = \left[\hat{a}_{i|I}\right]$$

The following steps describe the general bootstrapping process:

1. Round the most precise float ambiguity to the nearest integer value.

$$\breve{a}_1 = [\hat{a}_1]$$

2. Correct the remaining real-valued estimates by their correlation with the previous (integer rounded) ambiguity.

$$\hat{a}_2 - \sigma_{\hat{a}_2,\hat{a}_1}\sigma_{\hat{a}_1}^{-2}(\hat{a}_1 - \breve{a}_1)$$

3. Round the next real-valued ambiguity to the nearest integer.

$$\breve{a}_2 = \left[\hat{a}_2 - \sigma_{\hat{a}_2,\hat{a}_1}\sigma_{\hat{a}_1}^{-2}(\hat{a}_1 - \breve{a}_1)\right]$$

4. Repeat steps 2 and 3 until all components have been adjusted.

$$\breve{a}_i = \left[\hat{a}_i - \sum_{j=1}^{i-1} \sigma_{i,j|J}\sigma_{j|J}^{-2}\left(\hat{a}_{j|J} - \breve{a}_j\right)\right]$$

When the float ambiguity VCV matrix is decomposed as $Q_{\hat{a}\hat{a}} = LDL^T$, the bootstrapped estimator can be expressed as:

$$\breve{a} = [\hat{a} + (L^{-1} - I_n)(\hat{a} - \breve{a})]$$

The probability of successfully fixed float ambiguities using the integer bootstrapping estimator is:

$$P(\breve{a}_B = a) = \prod_{i=1}^{n}\left[2\Phi\left(\frac{1}{2\sigma_{\hat{a}_{i|I}}}\right) - 1\right]$$

Note that the performance of bootstrapping is always better or equal to rounding: $P(\breve{a}_B = a) \geq P(\breve{a}_R = a)$.

Ambiguity decorrelation

The Z-transformation is necessary to improve the precision of the highly correlated float ambiguities. The simplest Z-transformations are referred to as wide-lane transformations which form carrier phase observables with long wavelengths and a modified (inflated) variance matrix.

The ambiguity variance matrix ($Q_{\hat{a}\hat{a}}$) completely controls the ambiguity success rate. Therefore, the optimal Z-transformation is the one that decorrelates the ambiguities as much as possible. The nearly diagonal transformed ambiguity matrix ($Q_{\hat{z}\hat{z}} = ZQ_{\hat{a}\hat{a}}Z^T$) increases the success rates of the integer estimators since no further optimization can be accomplished through re-parameterization.

To visualize the decorrelating Z-transformation, imagine a two-dimensional ambiguity vector and its corresponding highly correlated variance matrix which defines an extremely elongated error ellipse. In essence, a series of area-preserving

Z-transformations sequentially push the “width” and “height” of the error ellipse until it is as circular as possible.

The entries in the Z-transformation matrix must be integers. The determinant of Z must equal ± 1. The form of a two-dimensional Z-transformation is given as follows:

$$Z_i = \begin{bmatrix} \alpha_i & 1 \\ 1 & 0 \end{bmatrix}, \qquad Q^i = \begin{bmatrix} \sigma_1^2(i) & \sigma_{12}(i) \\ \sigma_{21}(i) & \sigma_2^2(i) \end{bmatrix}, \qquad \alpha_i = -[\sigma_{21}(i)\sigma_1^{-2}(i)]$$

The goal is to find the Z-transformation matrix (Z) which is a series of products of individual Z-transformations. The process to find Z is described below:

1. Construct Q^1:

$$Q_{\hat{a}\hat{a}} = Q^1 = \begin{bmatrix} \sigma_1^2(1) & \sigma_{12}(1) \\ \sigma_{21}(1) & \sigma_2^2(1) \end{bmatrix}$$

2. Compute α_1:

$$\alpha_1 = -[\sigma_{21}(1)\sigma_1^{-2}(1)]$$

3. Compute Z_1:

$$\begin{aligned} Z_1 &= \begin{bmatrix} \alpha_1 & 1 \\ 1 & 0 \end{bmatrix} \\ &= \begin{bmatrix} -[\sigma_{21}(1)\sigma_1^{-2}(1)] & 1 \\ 1 & 0 \end{bmatrix} \end{aligned}$$

4. Construct Q^2:

$$\begin{aligned} Q^2 &= Z_1 Q^1 Z_1^T \\ &= \begin{bmatrix} -[\sigma_{21}(1)\sigma_1^{-2}(1)] & 1 \\ 1 & 0 \end{bmatrix} \begin{bmatrix} \sigma_1^2(1) & \sigma_{12}(1) \\ \sigma_{21}(1) & \sigma_2^2(1) \end{bmatrix} \begin{bmatrix} -[\sigma_{21}(1)\sigma_1^{-2}(1)] & 1 \\ 1 & 0 \end{bmatrix}^T \\ &= \begin{bmatrix} \sigma_1^2(2) & \sigma_{12}(2) \\ \sigma_{21}(2) & \sigma_2^2(2) \end{bmatrix} \end{aligned}$$

5. Compute α_2

$$\alpha_2 = -[\sigma_{21}(2)\sigma_1^{-2}(2)]$$

6. Compute Z_2

$$\begin{aligned} Z_2 &= \begin{bmatrix} \alpha_2 & 1 \\ 1 & 0 \end{bmatrix} \\ &= \begin{bmatrix} -[\sigma_{21}(2)\sigma_1^{-2}(2)] & 1 \\ 1 & 0 \end{bmatrix} \end{aligned}$$

7. Compute Z-transformation matrix

$$\begin{aligned} Z &= Z_i Z_{i-1} \ldots Z_1 \\ &= Z_2 Z_1 \end{aligned}$$

$$= \begin{bmatrix} \alpha_2 & 1 \\ 1 & 0 \end{bmatrix} \begin{bmatrix} \alpha_1 & 1 \\ 1 & 0 \end{bmatrix}$$

$$= \begin{bmatrix} \alpha_2\alpha_1 & \alpha_2 \\ \alpha_1 & 1 \end{bmatrix}$$

Care must be taken to ensure the Z-transformation does not destroy the integer nature of the ambiguities, i.e. |Z| = ± 1. For example, ambiguities parameterized as wide-lane and narrow-lane are not admissible (|Z| = -2) while wide-lane and an uncombined ambiguity is admissible (|Z| = -1).

$$WL + UC = \begin{bmatrix} -1 & 1 \\ 1 & 0 \end{bmatrix} \begin{bmatrix} a_1 \\ a_2 \end{bmatrix} \rightarrow Z = \begin{bmatrix} -1 & 1 \\ 1 & 0 \end{bmatrix} \rightarrow |Z| = -1$$

$$WL + NL = \begin{bmatrix} -1 & 1 \\ 1 & 1 \end{bmatrix} \begin{bmatrix} a_1 \\ a_2 \end{bmatrix} \rightarrow Z = \begin{bmatrix} -1 & 1 \\ 1 & 1 \end{bmatrix} \rightarrow |Z| = -2$$

The decorrelating Z-transformation eliminates discontinuity in the ambiguity spectrum and helps prevent search halting. Higher dimension ambiguity spaces can be decorrelated by repeating the application of two-dimensional transformations.

Integer least squares (ILS)

Least squares applied to the mixed-integer GNSS model with integer ambiguity constraints can be solved by orthogonal decomposition, then simplification. The ILS estimator has the following properties:

- Better performance than both rounding and bootstrapping.

$$P(\breve{a}_{ILS} = a) \geq P(\breve{a}_B = a) \geq P(\breve{a}_R = a)$$

- Requires an integer search step.

$$\breve{a}_{LS} = \arg min \left|\left|\hat{a} - z\right|\right|^2_{Q_{\hat{a}\hat{a}}}$$

- Z-invariant: $\breve{z}_{ILS} = Z\breve{a}_{ILS}$.

$$P(\breve{z}_{ILS} = z) = P(\breve{a}_{ILS} = a)$$

$$\breve{b}_{ILS} = \hat{b} - Q_{\hat{b}\hat{a}}Q^{-1}_{\hat{a}\hat{a}}(\hat{a} - \breve{a}_{ILS})$$

$$\breve{b}_{ILS} = \hat{b} - Q_{\hat{b}\hat{z}}Q^{-1}_{\hat{z}\hat{z}}(\hat{z} - \breve{z}_{ILS})$$

The integer least squares solution is comprised of two main parts: (1) integer ambiguity search and (2) the ambiguity decorrelation. The ambiguity search space is ellipsoidal and bounded by a positive constant χ^2 value. When the (decorrelated) bootstrapped estimator is used to compute χ^2, the search space becomes very small and guarantees at least one ILS solution is contained within the search space.

Ambiguity decorrelation (Z-transformation) reduces the elongation of the search space and increase the search efficiency.

The ILS success rate is not easy to compute since it requires the evaluation of a multivariate integral. The approximate ILS success rate is calculated by:

$$P(\breve{z}_B = z) \leq P(\breve{a}_{ILS} = a) \leq P\left(\chi^2_{n,0} \leq \frac{c_n}{ADOP^2}\right)$$

$$ADOP = |Q_{\hat{a}\hat{a}}|^{\frac{1}{2n}}, \qquad c_n = \frac{\left(\frac{n}{2}\Gamma\left(\frac{n}{2}\right)\right)^{\frac{2}{n}}}{\pi}, \Gamma(\mathrm{x}) = \text{gamma function}$$

Appendix F: Global ionospheric map product visualization

This appendix provides global ionospheric map (GIM) product data from the Center for Orbit Determination in Europe (CODE), operated by the Astronomical Institute of the University of Bern (AIUB), for each hour on January 15, 2020. In the following figures, the map color scale corresponds to total electron content units (TECU), where 1 TECU = 10^{16} electrons per square meter, which corresponds to approximately 16-cm of range delay for the GPS L1 frequency.

Note that equatorial ionization anomaly effects are typically visible at low latitude regions, within ±20-degrees from the geomagnetic equator. In the most extreme cases, the resulting plasma fountains appear as two distinct orange and red areas on either side of the geomagnetic equator.

The figures described above are provided in time-ascending order below, where each figure corresponds to the first epoch in each UTC hour of the day:

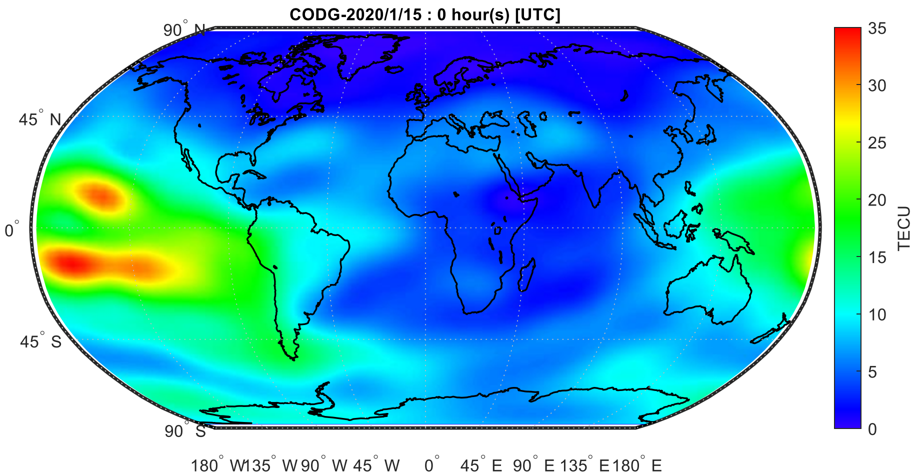

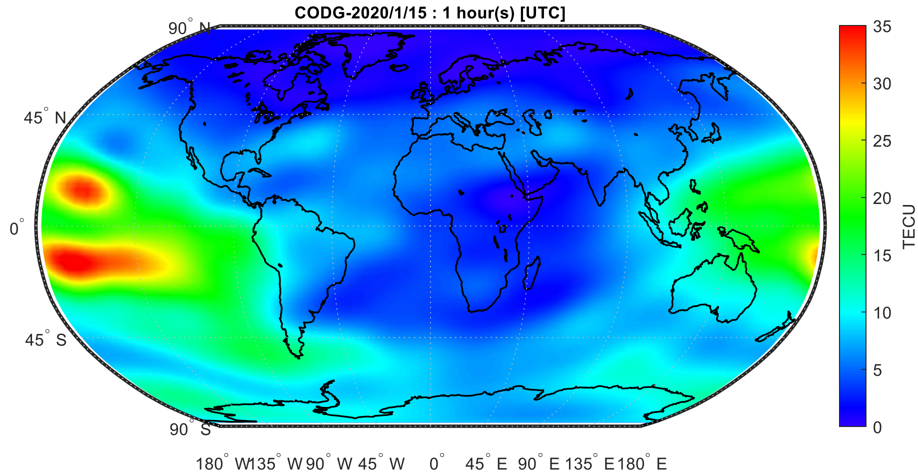

4885

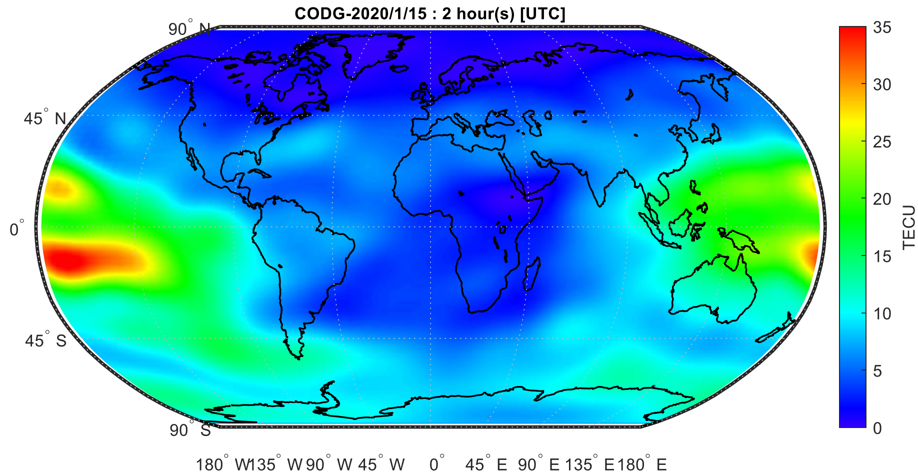

4886

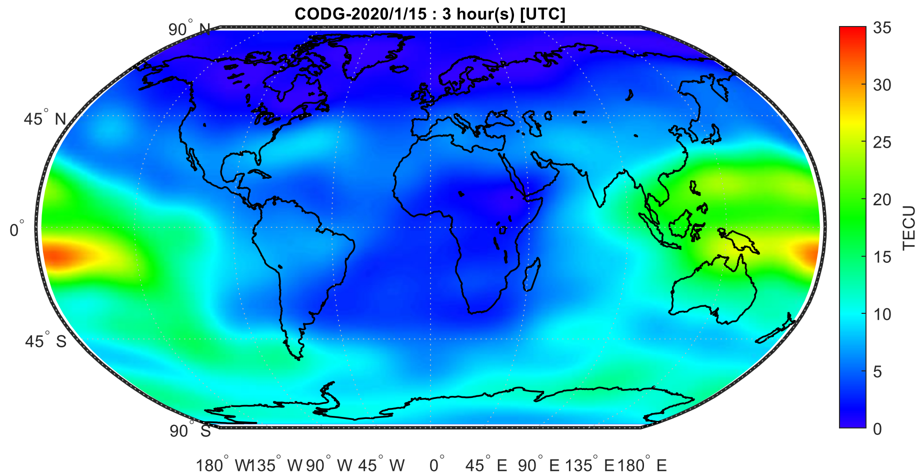

4887

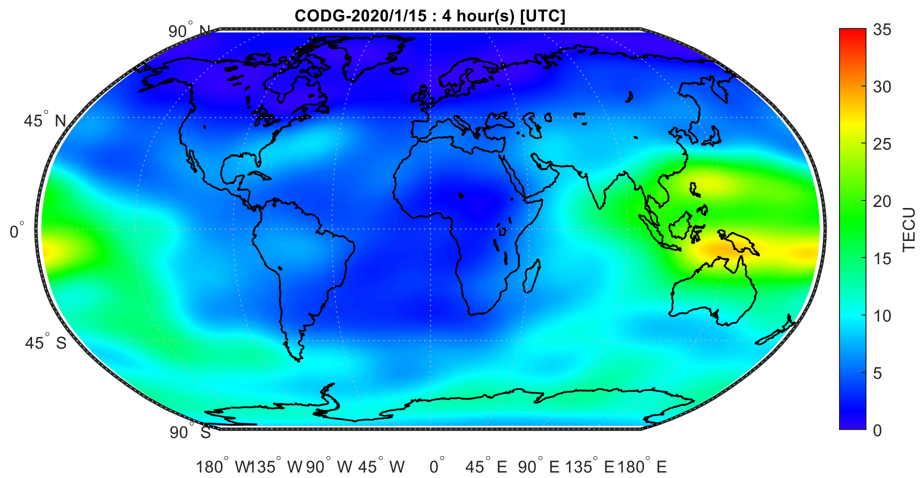

4888

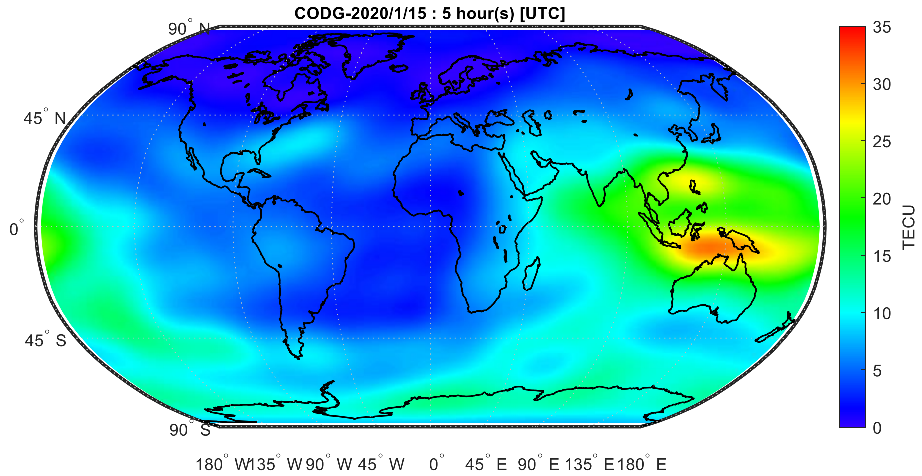

4889

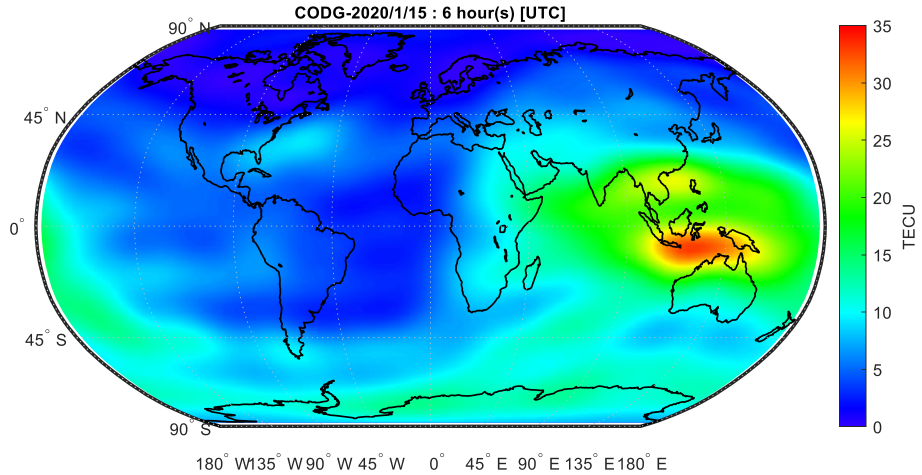

4890

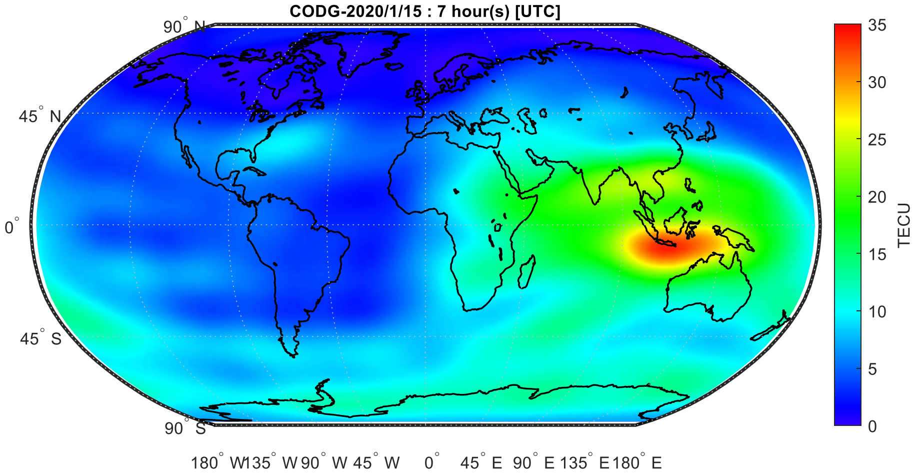

4891

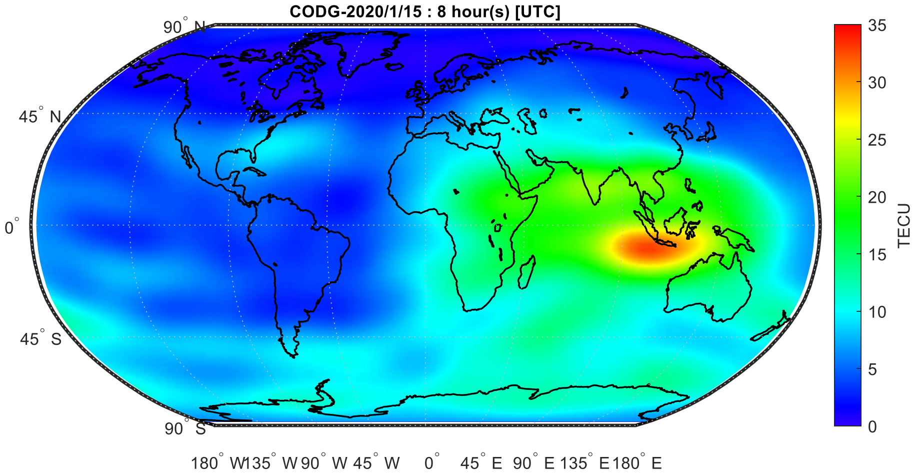

4892

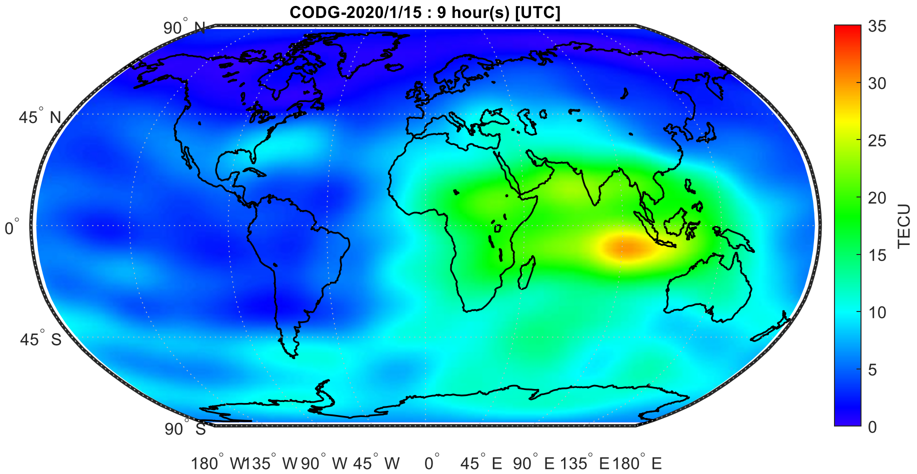

4893

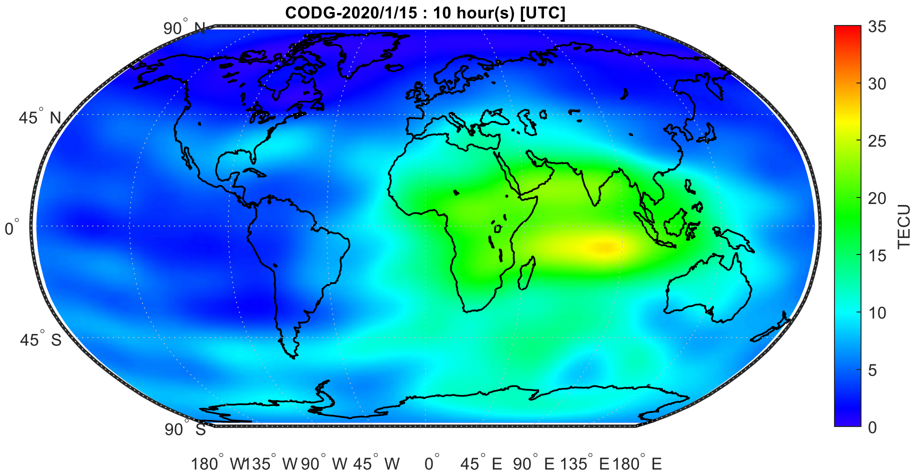

4894

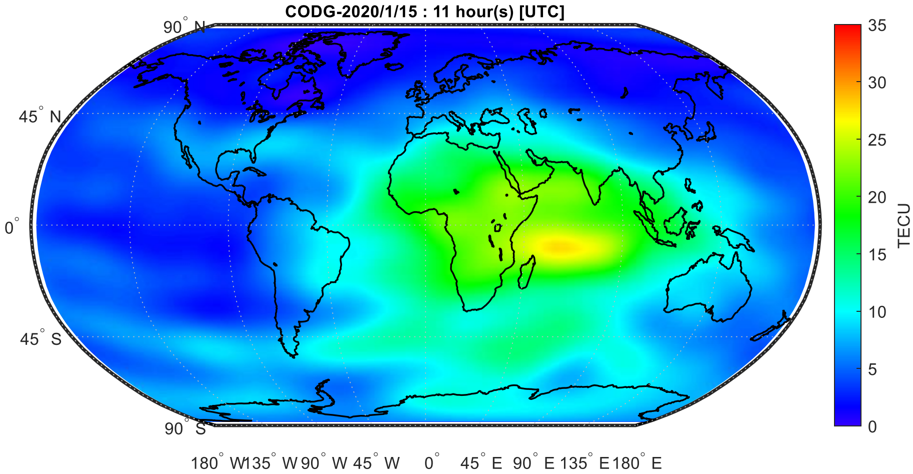

4895

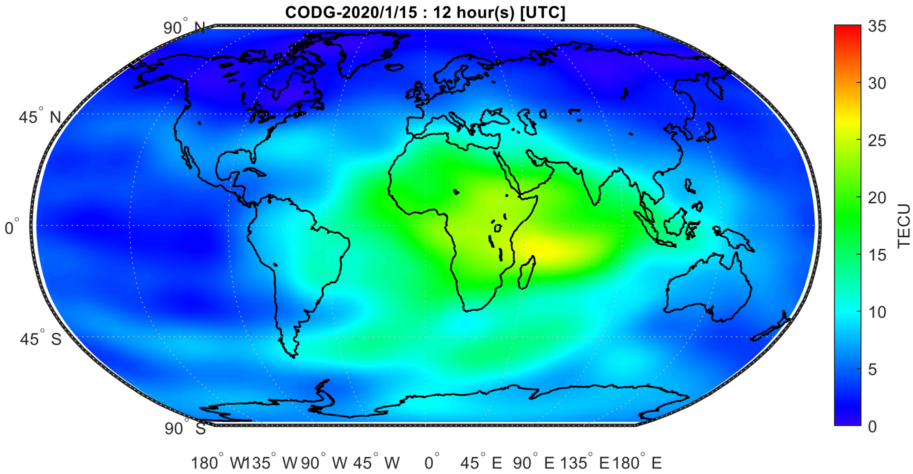

4896

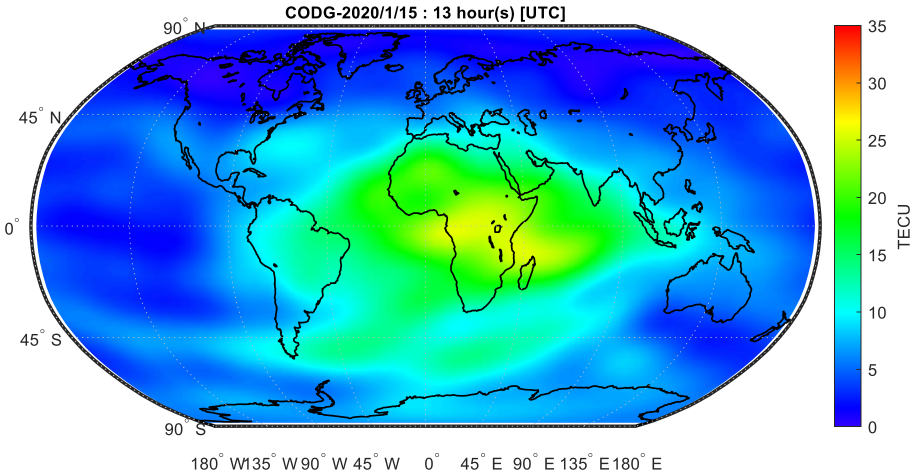

4897

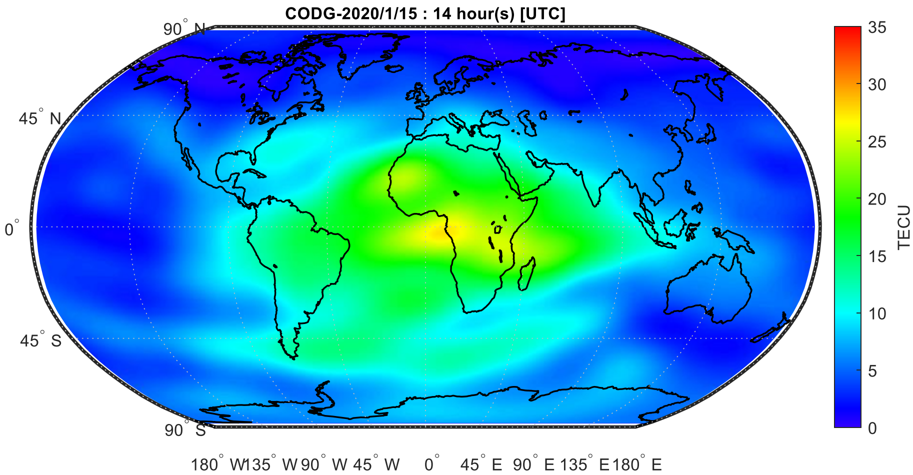

4898

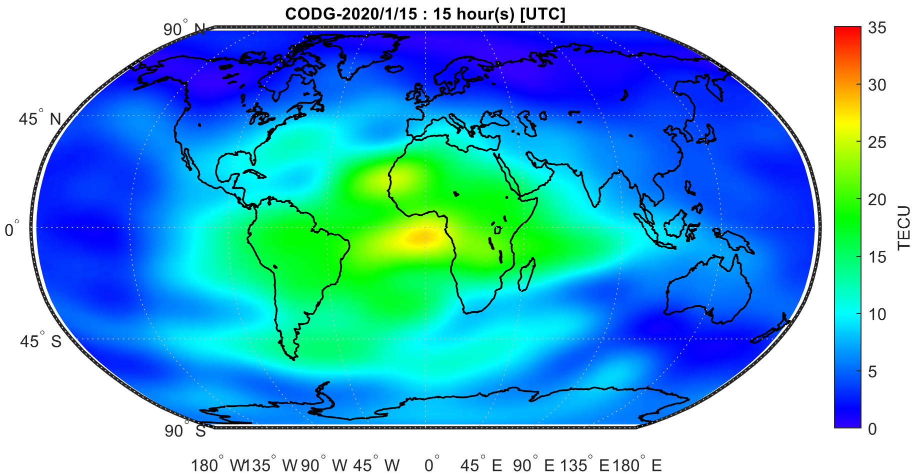

4899

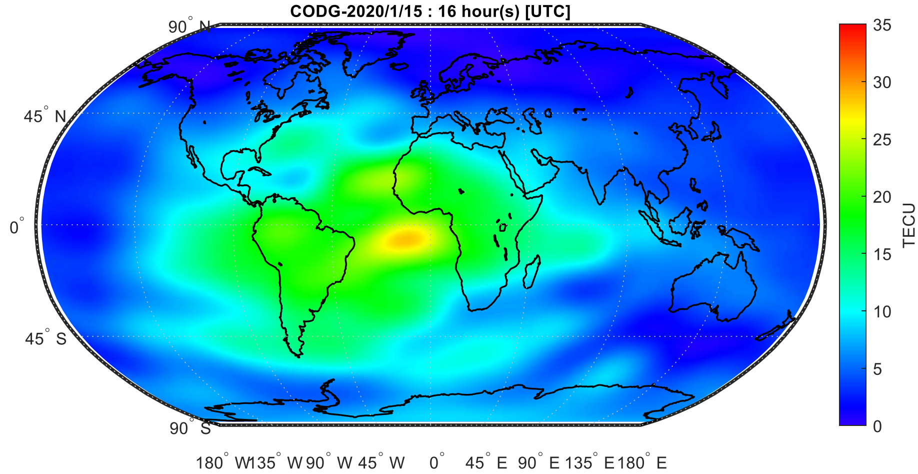

4900

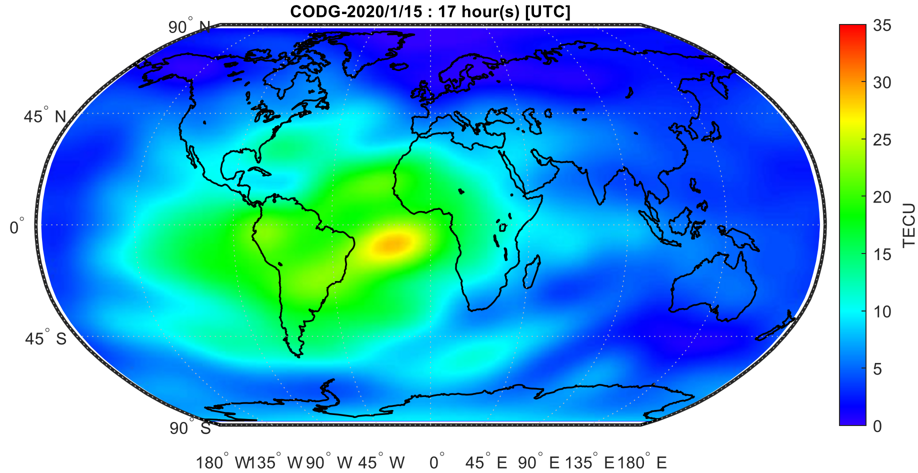

4901

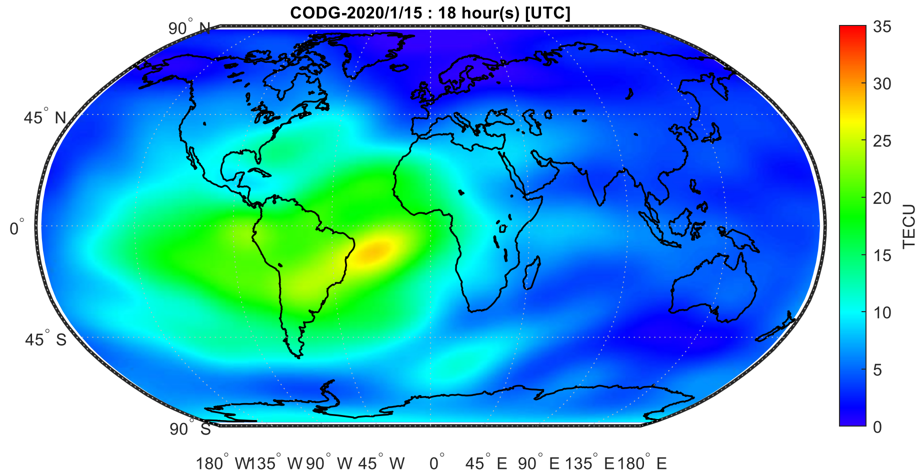

4902

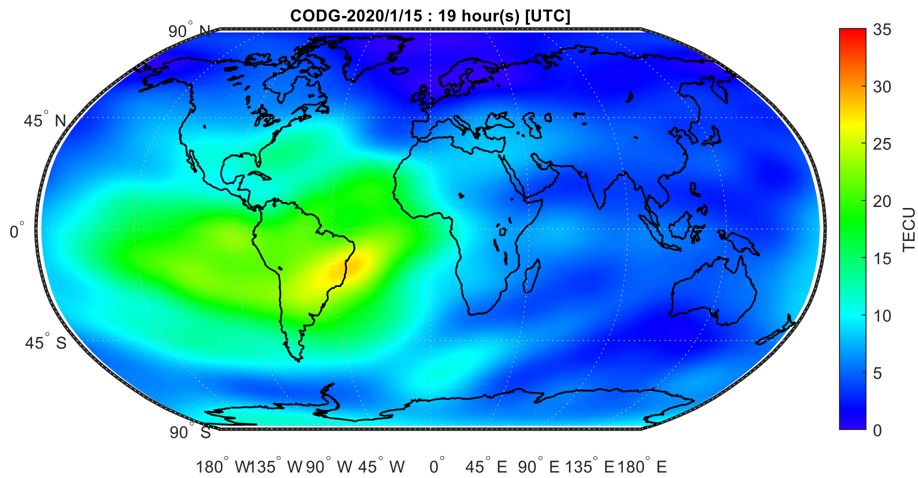

4903

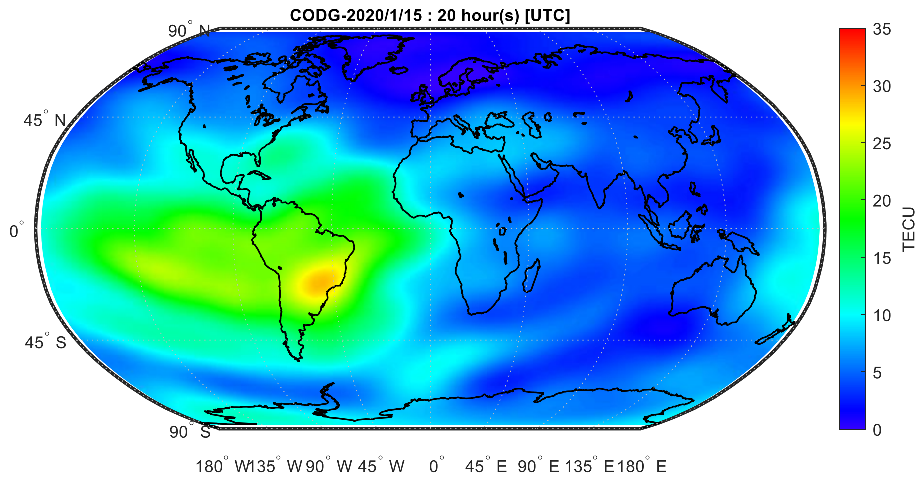

4904

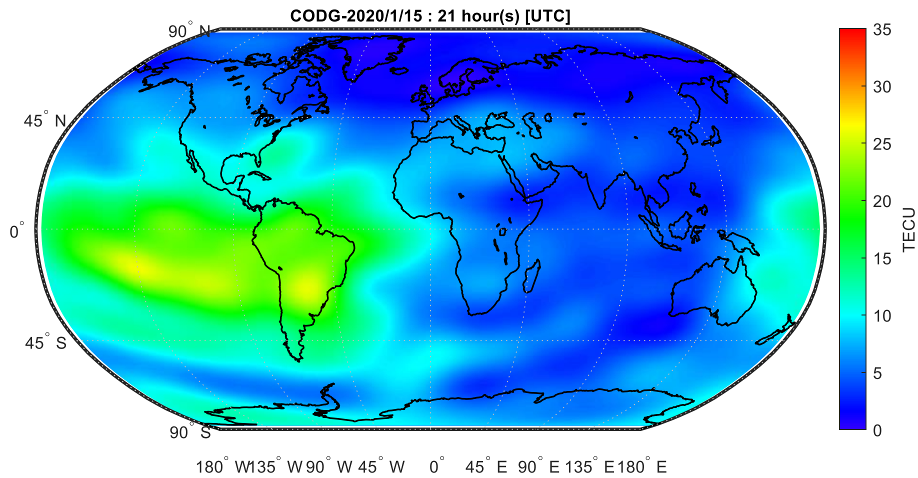

4905

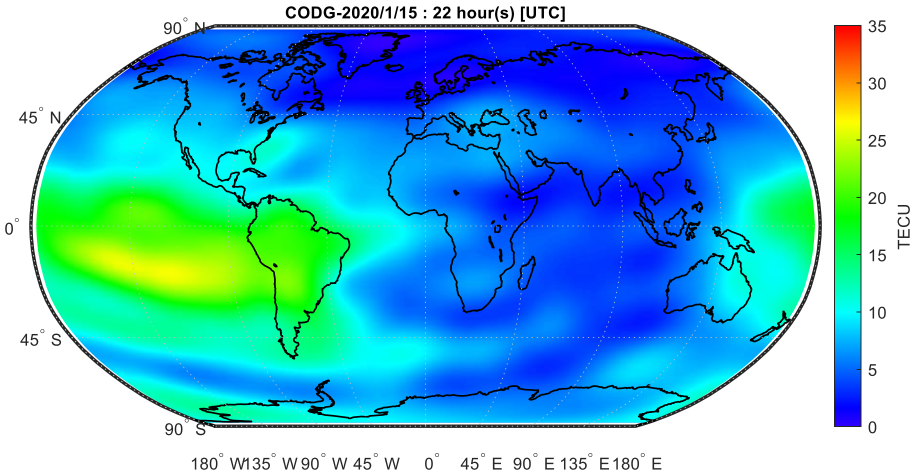
CODG-2020/1/15 : 22 hour(s) [UTC]
90° N
45° N
0°
45° S
90° S
180° W 135° W 90° W 45° W 0° 45° E 90° E 135° E 180° E
TECU
35
30
25
20
15
10
5
0

4906

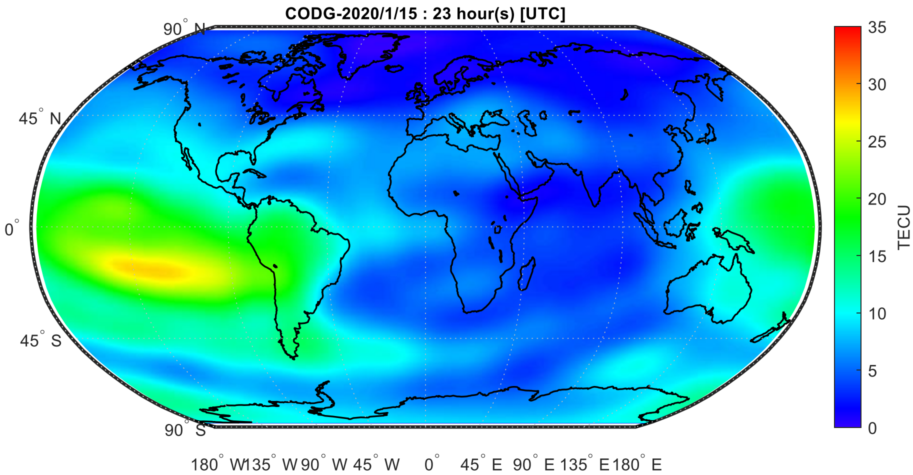
CODG-2020/1/15 : 23 hour(s) [UTC]
90° N
45° N
0°
45° S
90° S
180° W 135° W 90° W 45° W 0° 45° E 90° E 135° E 180° E
TECU
35
30
25
20
15
10
5
0

4907